THIS THESIS

HAS

RESTRICTED ACCESS

FOR

5 YEARS

FROM

THE DATE OF SUBMISSION

DATE OF SUBMISSION: 04/10/2013

TITANIUM VAULTED STRUCTURES FOR ORTHOPAEDIC APPLICATIONS

Thesis submitted in accordance with requirements of the University of Liverpool for the degree of Doctor in Philosophy

Xiaodong Song

ABSTRACT

Medical devices are used to recreate damaged or diseased joints and also to restore pain reduced mobility to patients. Devices such as hip and knee implants are fixed to the host bone by use of acrylic bone cement or by a press-fit interference technique. The surface of the press fit implants may be roughened, but non-porous, which allows new bone to form on the surface, or they may be porous to encourage bone growth into the structure. Traditionally implants are produced by machining, casting or forging, before applying any coatings that are required. More recently Additive Manufacturing (AM) techniques such as Electron Beam Manufacturing (EBM) and Selective Laser Melting (SLM) have attracted interest as they may be able to create the whole device in one operation. This thesis describes the research carried out to produce "Vaulted Structure (VS)" as a method for creating specific porosity with increased strength in porous medical devices. Unit cell structures (Wire frames) are inherently weak because of the struts. It was proposed that VSs, constructed of platelets, would have a higher specific strength and therefore extend the range of available properties while still maintaining a structure that resembles cancellous bone, a structure preferred by surgeons.

The creation of a VS begins with a computer model of the object to be created. This is then surrounded by an axis aligned bounding box, a box that has edges parallel to the x, y and z directions and just encloses the object. The bounding box is then voxelised, so it consists of many smaller cubic boxes, these boxes being the size of the required structure. The VS is then constructed by creating holed platelets on some of the surfaces of the smaller boxes, with these platelets being randomly deformed if required. The structure within the bounding box is then trimmed to the boundary of the required structure, this being accomplished using a rapid technique developed during this project. To allow manufacture of the components, the structure is sliced to create a suitable format for the SLM. By using SLM in combination with these new novel structures, a wide range of possible properties and morphologies can be generated, these being controlled by the cell size, hole size, thickness of the platelet and the level of randomisation.

A range of structures with different morphologies were produced and mechanically tested in compression. It was found that a percentage randomisation of more than 60% and a cell aspect ratio of 1:1:2, produced isotropic mechanical behaviour, while other structures produced very different behaviour. It was also observed that the failure mode in compression could be controlled by the degree of randomisation and this is discussed in the thesis. A property that is important in the medical device industry is the look of the component as this affects up take by surgeons. The preferred structures are ones that look like cancellous bone and the new structures created here match both the look and mechanical properties of this material, but with the added advantage that it is possible, by modifying the control variables, to match the structure to cancellous bone from different aged patients. The research presented in this thesis considers the inter-relationship between the process parameters, architecture, properties of the structures and why these inter relationships occur.

The research presented here extends knowledge of how to create these novel material/structure combinations, how to tailor them to a given purpose and by predicting behaviour in software produce the most suitable properties for a given medical device without extensive testing.

CONTENTS

NOMENCLATURE

A, B, C	Coordinates of vector $\vec{N}$	(-)
A_i, B_i, C_i	Vertices of triangle T_i	(-)
Ar	The total area of triangles in vaulted structure	(m^2)
$Ar0$	Area over which the pressure is applied	(m^2)
$Ar1$	The total area of low angle triangles	(m^2)
D	The diameter of a pore	(m)
Dia	The diameter of pore at the surface	(m)
E_ρ	The energy density of each spot	(J/mm^2)
E_{xp}	The amount of time that laser is exposed to the powder bed	(s)
H	The height of a unit cell	(mm)
$H0$	The height of a bounding box	(mm)
H(D)	The probability of finding a point in space with a pore size greater than or equal to *D*	(-)
I	Current	(A)
J_{qq}	The second moment of area about line *q*	(cm^4)
K_{tg}	The stress concentration factor based on the gross stress	(-)
L	The length of a unit cell	(mm)
$L0$	The length of a bounding box	(mm)
N	The normalised vector of a plane	(-)
$\vec{N}$	Vector of a plane normal	(-)
N_1	The normal vector to the plane on which the triangle lies	(-)
N_p	The number of a polygon edges	(-)
Nt	Number of triangles	(-)
Nx	Number of cells in x direction	(-)
Ny	Number of cells in y direction	(-)
Nz	Number of cells in z direction	(-)
P	Power	(W)
P_0, P_1	End points of a segment	(-)
P_{00}, P_{01}	End points of a segment	(-)
P_{0x}, P_{0y}, P_{0z}	Coordinates of the point P_0	(-)
P_{1x}, P_{1y}, P_{1z}	Coordinates of the point P_1	(-)
$P_{00x}, P_{00y}, P_{00z}$	Coordinates of the point P_{00}	(-)
$P_{01x}, P_{01y}, P_{01z}$	Coordinates of the point P_{01}	(-)
P_{12}, P_{13}	End points of a segment	(-)
$P_{12x,}P_{12y}, P_{12z}$	Coordinates of the point P_{12}	(-)
$P_{13x}, P_{13y}, P_{13z}$	Coordinates of the point P_{13}	(-)
P(D)	Pore size distribution	(-)
$Pout$	Any point out of a plane	(-)
Pre	Pressure	(Pa)
PSD	The pore size distribution	(-)
Pt	Any point on a segment	(-)
Ptx, Pty, Ptz	Coordinates of point Pt	(-)
$Pt0$	Any point on a segment	(-)
$Pt1$	Any point on a segment	(-)
Pu_0, Pu_1	Projections of points u_0, u_1	(-)

R	The radius of a hole	(mm)
$RefX, RefY, RefZ$	Coordinates of reference point of a gridded bounding box	(-)
T	Thickness of a platelet	(µm)
T_i	The $i\ th$ triangle on a solid surface	(µm)
U_0, U_1, U_2	Vertex of the triangle T_1	(-)
V_0, V_1, V_2	Vertices of a triangle.	(-)
V_{0x}, V_{0y}, V_{0z}	Coordinates of the point V_0	(-)
V_{1x}, V_{1y}, V_{1z}	Coordinates of the point V_1	(-)
V_{2x}, V_{2y}, V_{2z}	Coordinates of the point V_2	(-)
Vol	The volume of a sample	(mm^3)
$Vol1$	The volume of triangles	(mm^3)
$Vol2$	The volume of low angle triangles	(mm^3)
VP	Any point on a triangle	(-)
V_x, V_y, V_z	Coordinates of any point on triangle	(-)
W	The width of a unit cell	(mm)
$W0$	The width of a bounding box	(mm)
$Xarray$	Array of the x coordinates	(-)
X_A, Y_A, Z_A	Coordinates of the facet vertex A	(-)
X_{max}	The maximum percentage of movement in the x direction	(%)
X_{min}	The minimum percentage of movement in the x direction	(%)
$Xpoint$	Any point on a plane	(-)
$Yarray$	Array of the y coordinates	(-)
Y_{max}	The maximum percentage of movement in the y direction	(%)
Y_{min}	The minimum percentage of movement in the y direction	(%)
$Zarray$	Array of the z coordinates	(-)
Z_{max}	The maximum percentage of movement in the z direction	(%)
Z_{min}	The minimum percentage of movement in the z direction	(%)

d	Dot product of the vector $-\vec{N}$ and vector (x, y, z)	(-)
dA	An element area	(-)
dm	The dot product of the vector – $Xpoint$ and N	(-)
dn	The dot product of the vector $-N_1$ and vector U_0	(-)
du_i	The signed distance (+/-) from each vertex of a triangle to its corresponding plane	(-)
d_{u0}	The signed distance (+/-) from vertex u_0 of a triangle to its corresponding plane	(-)
d_{u1}	The signed distance (+/-) from vertex u_1 of a triangle to its corresponding plane	(-)
$error$	Accuracy	(%)
f_{Ext}	The externally applied force	(N)
f_R	The force to resist the entry of mercury	(N)
i	Subscript	(-)
$maxx$	The maximum value of element in array $Xarray$	(-)
$maxy$	The maximum value of element in array $Yarray$	(-)
$maxz$	The maximum value of element in array $Zarray$	(-)
$minx$	The minimum value of element in array $Xarray$	(-)
$miny$	The minimum value of element in array $Yarray$	(-)
$minz$	The minimum value of element in array $Zarray$	(-)
pt	Percentage of low angle triangles	(%)

r	The distance from the point $Pout$ to a plane	(-)
rand	Percentage of randomisation	(%)
r_p	The diameter of the smallest pillar	(µm)
t	A parameter defining the point position on a segment.	(-)
$t0$	A parameter defining the point position on a segment.	(-)
$t1$	A parameter defining the point position on a segment.	(-)
th	The thickness of fabricated triangles	(µm)
v, u	The parameters specifying the point position on a triangle	(-)
x, y, z	Coordinates of a point or a vertex	(-)
xc, yc, zc	Coordinates of a facet centre	(-)
$x_i\ y_i\ z_i$	Coordinates of the $i\ th$ vertex of a hexagon	(-)
xv, yv, zv	The coordinates of a vertex	(-)

α	The angle between a low angle triangle and Z plane	(°)
ß	The angle in the right triangle ACK	(-)
ε0	The angle between a triangle and Z plane	(°)
γ	The surface tension of mercury	(mNm^{-1})
θ	The liquid-solid contact angle	(°)
θ_i	Central angle of a hexagon	(-)
λ	Wavelength	(µm)
ν	The diameter of a fabricated sliced line	(µm)
π	The ratio of a circle's circumference to its diameter	(-)
ρ	Density	(kg/m^3)
ρr	Porosity	(%)
ρ_{Ti}	The density of CpTi	(kg/m^3)
σ	Compressive Strength	(MPa)
σ0	The stress on the cross section far from a hole	(MPa)
σ_{max}	The maximum stress at the edge of a hole	(MPa)
τ	Laser exposure time	(µs)
τ0	Time	(s)
Ø	Diameter of a cylinder	(mm)
ω	The radius of the applied laser beam	(mm)

GLOSSARY OF TERMS

2D	2 Dimensions
316LSS	316L Stainless Steel
3D	3 Dimensions
3DP	3 Dimensional Printing
AABB	Axis-Aligned Bounding Box
AM	Additive Manufacturing
ASTM	American Society for Testing and Materials
BSD	Berkeley Source Distribution
CAD	Computer Aided Design
Co	Cobalt
CpTi	Commercial pure Titanium
Cr	Chromium
CSG	Constructive Solid Geometry
CT	Computer Tomography
CVD	Chemical Vapour Deposition
EBM	Electron Beam Manufacturing
FDM	Fused Deposition Modelling
GUI	Graphical User Interface
HA	Hydroxyapatite
LLM	Layer Laminate Manufacturing
LOM	Laminated Object Manufacturing
LTAVD	Low Temperature Arc Vapour Deposition
Nd-YAG	Neodymium-doped Yttrium Aluminium Garnet
Ni	Nickel
NVP	N-Vinyl Pyrrolidone
PDLLA	Poly-DL-Lactide
PMMA	Polymethylmethacrylate
PVA	Polyvinyl Alcohol
PVD	Physical Vapour Deposition
RVS	Randomised Vaulted Structure
SAT	Separating Axis Theorem
SEM	Selective Electron Microscopy

SL	Stereolithography
SLM	Selective Laser Melting
SLS	Selective Laser Sintering
STL	Stereolithography (file format)
THRs	Total Hip Replacement system
Ti	Titanium
UHMWPE	Ultra High Molecular Weight Polyethylene
VS	Vaulted Structure

CHAPTER 1

INTRODUCTION

Total Hip Replacement systems (THRs) and Total Knee Replacement systems (TKRs) have been developed as a remedy for serious osteoarthritis, rheumatoid arthritis, congenital deformities and certain post-traumatic conditions [1,2]. This is a industry where almost a million people are treated each year at a cost of £billions [3]. The treatment involves the attachment of the implant to the host bone by either the use of cement mechanical fixation or by bone growth into the roughened or porous surfaces of THRs. Long-term fixation must be effective and provide a durable and reliable bond, particularly for younger, more active patients who, place significantly higher loads on the joints [4], while also having a longer life expectancy and so require the joints to last for a significantly longer time [5–7]. Revision of damage or worn implants is a significant cost and a more traumatic surgery, and these numbers are increasing [3].

The porous structure used in THRs can be fabricated either by various coating technologies such as sintered beads, plasma spraying or new methods such as Chemical Vapour Deposition (CVD) and Low Temperature Arc Vapour Deposition (LTAVD). These coatings are applied to a solid machined preform which has been cast or forged. Most of these methods are limited in controlling the geometry of pores to meet the bone ingrowth requirements. Additive Manufacturing (AM) provides more freedom to produce complex porous structures with various bio-materials. This method however relies heavily on the CAD technologies to design the porous structures and process the data for AM fabrication. Both selective laser melting (SLM) and Electron Beam Melting (EBM) are currently showing promise as production technologies, and employ a scanning strategy based upon beam overlap or unit cell constructs [8,9]. It is also believed that additive manufacture methods are a technology [10] which will disrupt the current manufacturing methods.

However, there are some issues regarding the appearance of beam overlap structures, and with the strength of unit cell structures (wire framed structures) in certain applications, and that perhaps a combination of both of these technologies could give a more favourable outcome, and consequently a plan to research this idea has been developed, notwithstanding the requirement that the process should be able to meet the volume requirements already noted. The detail of this research is fully and clearly presented in this thesis which is split into seven chapters.

In Chapter 2, the background to the research areas relevant to the work are reviewed beginning with a review of the fixation methods used in THRs and the requirements needed for structures for promoting bone ingrowth. Conventional methods for manufacturing these bone ingrowth structures are discussed and their limitations identified with reference to the bone ingrowth requirements for THRs. Chapter 2 then moves on to the fabrication methods possible using AM particularly focusing on SLM used in this research to create the bone ingrowth structures. As AM technologies are reliant on precise 3D CAD technologies, a review of the design methods of bone ingrowth structures is also undertaken. Finally in Chapter 2 the intersection test methods used to develop the software to create the structures are reviewed. At the end of Chapter 2, the project aim and objectives are derived based on the information gathered from this background material.

In order to achieve the aim and fulfil the objectives, in Chapter 3, the software development tools have been introduced to create the new structures. The process parameters are developed for fabricating these structures. Then these structures are fabricated specifically by a modified MCP Realizer SLM 100 after data processing. Based on the procedure developed by Stryker Orthopaedics, these structures are cleaned to remove residual powder and readied for measurement of the various properties.

Chapter 4 presents the development of the software to allow the creation of open celled structures that resemble cancellous bone. In order to create such a structure, four software functions are required. These functions are described in detail and

then subject to a number of processes for verification. To reduce the number of samples that had to be manufactured, functions were developed to compute the properties such as porosity and pore size distribution based on the digital model and these are also discussed in this chapter. Additionally, a function to create closed surface VSs which can be fabricated by other AM technologies is also detailed.

In Chapter 5, the creation of platelet based structures without surface deformation (regular VS) is presented and discussed. These samples were used to study how the range of properties available could be modified by changing the architecture and whether the behaviour could be controlled. The experimental results show that the range of available properties can be enlarged by altering the cell and the hole size, and that it was not possible to achieve isotropic behaviour with these regular structures.

In Chapter 6 the properties of platelet based structures with random surface deformation are discussed, with the effects of introducing randomisation being explained. These results indicate that the range of available properties can be increased by changing the cell size and the hole size, the changes affecting both compressive strength and porosity. It will also be shown that altering the laser power used during the fabrication significantly affects platelet thickness and has considerable effect on the compressive strength and porosity. Furthermore, isotropic behaviour can be achieved by using a RVS by altering the cell size aspect ratio and by using the random deformation mechanism.

The conclusions of this thesis are given in Chapter 7 where the relationships between the architecture and mechanical properties for the VSs are summarised, along with the evidence for what causes this interplay. By using the knowledge presented here, new designs of VSs tailored with application matched mechanical and structural properties will be possible, and this development is considered in the Future Work section.

CHAPTER 2

BACKGROUND

This chapter provides background to the research areas relevant to the work presented in this thesis. It begins with a review of fixation methods used in Total Hip Replacement systems (THRs) before considering the literature on the requirements for surface coatings used on THRs to allow bone ingrowth. With reference to the requirements above, conventional methods for fabricating three generations of bone ingrowth structures are reviewed. This is followed by a review of AM for fabricating bone ingrowth structures as well as the 3D CAD technologies for designing them. Following on from this, the mathematical tools for geometry manipulation and intersection test methods used for the software design are also reviewed. Finally the project aim and objectives are derived based on the summary of this background material.

2.1. THRs Fixation Systems

Total Hip Replacement systems (THRs) have been developed as a remedy for serious osteoarthritis, rheumatoid arthritis, congenital deformities and certain post-traumatic conditions [1,2]. Figure 2-1 shows the principal components of modern THRs. The femoral components consist of the femoral stem, shoulder, neck and head which may be modular or singular in construction. The acetabular components comprise the acetabular cup and a liner. The components can be attached to the host bone by various methods, the most common [11–14] being the use of Polymethylmethacrylate (PMMA) bone cement [15]. During the 1980s [6], an alternative fixation was introduced that attached the THRs directly to the host bone by bone growth into or onto the surface coating rather than by the use of bone cement [14]. Additionally screws [16], spikes [17] and pegs [18] are used to provide additional attachment when the THRs are fixed to host bone without bone cement. Over the past two decades, there have been many improvements in both the materials [19], design [20–22] and the methods [17] used to fix the femoral and acetabular components to the host bone. These improvements have lead to a high survival rate (>85%) for cemented and cementless THRs [4,15]. A debate still

remains however as to the best fixation method for THRs, which are classified into two categories, including fixation with bone cement and without bone cement [6].

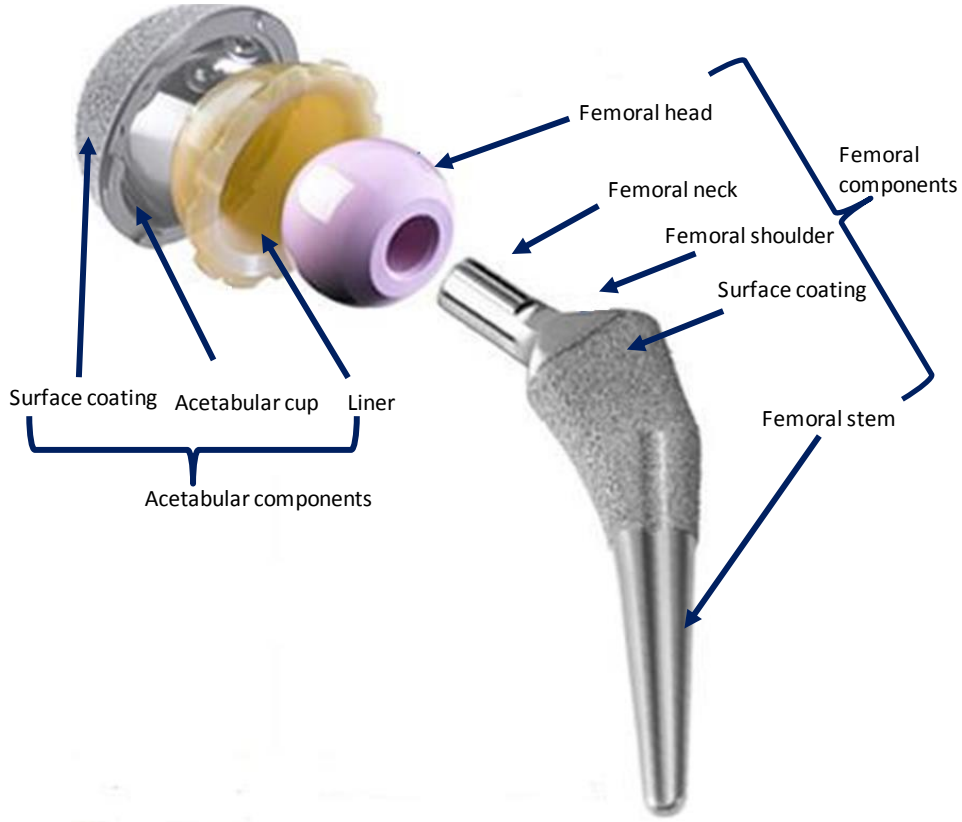

Figure 2-1 Schematic of an uncemented THRs note the surface coating [23].

2.1.1. Fixation with Bone Cement

Fixation with bone cement is achieved by a solid mechanical interlock at the bone-cement-implant interface [24,25]. However, bone cement is susceptible to cracking and this can lead to fatigue fractures and an unstable fixation [15]. Furthermore the debris released from bone cement can trigger a biological response resulting in the loss of bone around the THRs allowing loosening to occur [4,26,27]. Similarly this microscopic debris can be absorbed by cells around the implant initiating an inflammatory response causing cells to remove bone from around the joint; this is termed osteolysis [26–30] once again causing the implant to loosen [29,30]. Other

debris is released by the action of the femoral head against the polyethylene liner. They cause a similar problem as debris from bone cement [31,32]. However by changing the liner material to Ultra High Molecular Weight Polyethylene (UHMWPE), a considerable decrease in wear debris was observed by Charnley [33]. Although these failure mechanisms exist, bone cement still provides a durable and reliable fixation [5,13,24,34], particularly for older patients (>65years) [6,35,36], for patients with conditions such as rheumatoid arthritis and for patients with compromised severe trauma or poor bone quality and density [13].

2.1.2. Fixation without Bone Cement

Fixation without bone cement is provided by bone growth into or onto the textured surface [37] or surface coating of THRs [38]. In order to give a strong and durable bond between implant and host bone, the orthopaedic surgery must be performed precisely as the gap between the implant and the bone must be less than 1 to 2mm to ensure the bone can form a bridge [15,39,40]. After the THRs are implanted, a period of protected weight-bearing (using crutches or a walker) is required to avoid movement (less than 25-50μm) [39] between host bone and THRs and to enable the bone to sufficiently attach itself to the THRs, otherwise, the movement can damage the surrounding tissue, cut off the blood supply leading to necrosis, inflammation [41] and bond failure [42–44]. The healing time for uncemented THRs (up to three months) [45] is longer than that for bone cemented THRs. Although some orthopaedic surgeons are now using cementless devices for all patients [4], the cementless THRs is more suitable for younger patients [22] with good bone quality to allow sufficient bone growth into the components [7,19,37].

Fixation without bone cement is not only required to give a primary fixation, but also it must provide initial stability to avoid movement between the implant and host bone allowing sufficient bone bridging and ingrowth during the healing process. The initial stability of THRs is provided by friction between the surface and host bone [14,38,46]. Subsequently the primary fixation is given by the bone growth into or onto the implant surface coating. In some designs, screws, spikes and pegs are also used to provide additional initial stability and primary fixation [17,18,47].

2.1.3. Summary of the Types of Fixation on THRs

Fixation with or without bone cement are both effective methods to attach THRs to host bone for specified groups of patients. For younger, more active patients and patients with good bone quality, fixation without bone cement is recommended to provide a durable and reliable bond by encouraging the bone growth into the surface coating around THRs.

According to the method provided by Jamieson [38], surface coatings with structures are classified into three generations based on their fabrication methods (sintering beads, plasma spraying and Chemical Vapour Deposition (CVD). In order to identify their limitations and understand the bone ingrowth mechanism, a literature review was carried out on the requirements for bone ingrowth structures and this is presented in the following section.

2.2. Requirements for Bone Ingrowth Structures

As discussed above, bone ingrowth structures are used as the surface coating in THRs to provide fixation without bone cement, thus the material used for them must not be toxic or cause any inflammatory or allergic reaction. Furthermore in order to achieve a durable and reliable bond between the THRs and the host bone, the bone ingrowth structure should possess open and well interconnected pores for deeper bone penetration and adequate bone ingrowth. Additionally, it should be strong enough to keep a sufficient void space for bone penetration and ingrowth under initial loading conditions. Finally the requirements for bone ingrowth structure were summarised.

2.2.1. Material Choice

When the THRs is implanted, the bone ingrowth structure is exposed to human tissues and fluids. The reaction between the bone ingrowth structure and host bone indicates the acceptability. It was termed “biocompatibility” which was defined by Williams [48] and describes the ability of a material to perform with an appropriate host response in a specific application. Furthermore, due to the high

corrosion rates in the body, the released metal ions such as Nickel (Ni), Chromium (Cr) and Cobalt (Co) are found to cause allergic and toxic reactions by Wapner [49]. Currently, materials used for surgical implants include 316L Stainless Steel (316LSS), Cobalt Chromium (Co-Cr) alloys, Titanium (Ti) and its alloys and Tantalum [50]. Considering the potential risk of releasing Ni, Cr and Co from the implant, Ti, its alloys and tantalum are considered as the candidate material for bone ingrowth structures.

Tantalum shows a good safety record in the orthopaedic literature [51] and exhibits excellent corrosion-erosion resistance [52]. Bobyn et al [53] studied the bone ingrowth characteristics of acetabular components made of tantalum in a canine model for six months. In 22 cementless porous tantalum acetabular components, the depth of bone ingrowth was in a range of 0.2 to 2mm and average bone ingrowth was up to 16.8% for all sections and 25% for periphery sections. This compares with 21.5% of new bone which was found in titanium porous coated cementless canine acetabular components [54]. It indicates that the bone ingrowth in tantalum porous structure is comparable to the bone ingrowth in titanium porous structures. However, due to high cost and difficulty of fabrication, it is more cost-effective to use Ti and its alloys [55] if possible.

2.2.2. Pore Size Distribution

In general, the biomaterials with interconnected pores are superior to biomaterials containing pores with dead ends [56]. These interconnected pores allow the full penetration and vascularisation of the new bone [57,58] and promote a fast bone ingrowth [59], which is especially important for long-term tissue interface maintenance [60]. Smaller pore size (75-100µm) results in un-mineralized osteoid or fibrous tissue. The limit for the maximum pore size that produces good quality bone ingrowth is not well defined [61]. Based on a literature review on the optimum pore size of previous generations of bone ingrowth structures, the general consensus is that the optimum pore size lies in the range of 100-400µm [53,61–78]. Furthermore a literature review was also carried out for the new generation of bone ingrowth structures. The bone ingrowth structures made of commercially

pure titanium and generated by Stryker have an average pore size of 550µm, with bone ingrowth averages 23% at three months and 38% at six months [79]. Zimmer also produces bone ingrowth structures but in this case they are made of tantalum, with high porosity (75-85%) and its average pore size lies in the range of 400-600µm and achieved 80% occupation of pores with new bone in acetabular components at 1 year retrieval [80] which gives adequate time for the structure to attach itself to the host bone. Thus it is believed that the optimum pore size can be extended and lie in the range of 100 to 600µm. No evidence has been found to show that the shape of the pores affects the biological response but pore size is influential [81].

2.2.3. Porosity

Porosity is defined as the percentage of void space in a solid [82,83]. Higher porosities give more void space for transporting oxygen and nutrients to the cells and therefore allowing a sustained bone ingrowth. Higher porosity can also provide a larger porous surface area, which is instrumental in improving the mechanical interlock between THRs and the host bone.

Furthermore the compressive strength of porous material is inevitably affected by its porosity. For example, a bone ingrowth structure made of Commercial pure Titanium (CpTi) has been shown to exhibit a strong dependency between porosity 10-95% and compressive strength 350-0.5MPa respectively [9]. Considering the low compressive strength at high porosity, the consensus of opinion suggests that porosity should lie in the range of 65%-75% for promoting good levels of bone ingrowth [53,56,65,77,80,81].

2.2.4. Pore Surface

The pore surface roughness can promote the direct structural and functional connection between the living bone and the surface of a load-bearing implant being termed osteo-integration [84]. Comparing rough and polished surfaces of titanium, the rough surface can promote osteo-integration [85–87]. Further comparison was carried out on a surface varying in roughness; it indicated that R_a value of surface roughness in the range of 1 to 7µm were most suitable for promoting bone

formation [88–90]. Similar results indicate that a rough pore surface can enhance bone attachment and proliferation [91]. Additionally the oxide layer (1.5-10nm thick) on Ti and its alloys on the pore surface was found to affect the cell response as well as the number of attached osteoblast cells [92–94] which are responsible for bone formation. In vitro studies suggest that increasing the oxide layer thickness increases the attachment of attached osteoblast cells [92].

2.2.5. Compressive Strength

The bone ingrowth structure must provide adequate compressive strength to ensure sufficient void space for bone ingrowth under the loading condition. Widmer calculated (with some basic assumptions) that for a patient who was 60 years old, the maximum compressive strength in the acetabulum was (30MPa) [95]. According to the research on the relationship between compressive strength of cancellous bone and age, it was shown that the compressive strength of cancellous bone decreases by 8.5% each decade [96]. This research indicates that the maximum compressive strength in the acetabulum from a younger patient (< 60 years old) is greater than 30MPa. In order to allow the porous material to be over engineered, a safety margin needs be added to the value of maximum compressive strength in the acetabulum [97], therefore 30MPa is the minimum requirement of compressive strength.

2.2.6. Summary of Requirements for Bone Ingrowth Structures

The data on bone ingrowth structures, from the work presented in this literature review is summarised in Table 2-1. This data shows that bone will grow into materials with quite a wide range of pore sizes but that it is important to meet the minimum compressive strength to stop the implant crushing before the bone can grow into the material. Therefore, as the components where to be made from CpTi, to maximise biocompatibility, this research was driven by the requirement to achieve the maximum compressive strength with the maximum porosity, while maintaining the pore size in the desired range.

Table 2-1 Requirements for bone ingrowth structures

Material	Ti and its alloys
Optimum pore size	100μm-600μm
Minimum compressive strength	30MPa
Optimum porosity	65%-75%

2.3. General Fabrication Methods for Bone ingrowth Structures

Various conventional methods are employed for fabricating bone ingrowth structures and these can be classified based on the type of pore (closed or open) and pore distribution (homogenous, non homogenous or functionally graded) [98]. In this section the conventional methods for fabricating various generations of these ingrowth structures are examined including sintering, plasma spraying and CVD. These methods are detailed and discussed in the following section.

2.3.1. Sintering

Sintering is the simplest conventional method and was used for fabricating the first generation of bone ingrowth structures in THRs. Utilising an atomisation process, such as gas atomisation, metal powders at various diameters, are produced from a variety of materials including CoCr and Ti. Then powder or beads can be attached to a preform by glue and prepared for sintering. The sintering operation is performed in a high vacuum furnace (10^{-5}mbar) to minimise the oxidation. The sintering temperature is set to 1250°C to form the solid metallic "necks" between particles and particles to substrate. These solid metallic necks provide the strength to the surface coating. The porosity of sintered powder surface coating depends on the degree of particle interconnectivity and particle size and can be controlled by the process variables including compacted powder density, sintering temperature and time, generally the porosity is limited to less than 50% [80]. As shown in Figure 2-2, the pore size and shape is formed by the powder particle geometry. Thus the average pore size lies in the range of 100-400μm [99]. The smooth surface of the powder particles decreases the coefficient of friction of the surface coating to 0.53 which is insufficient to provide adequate initial stability.

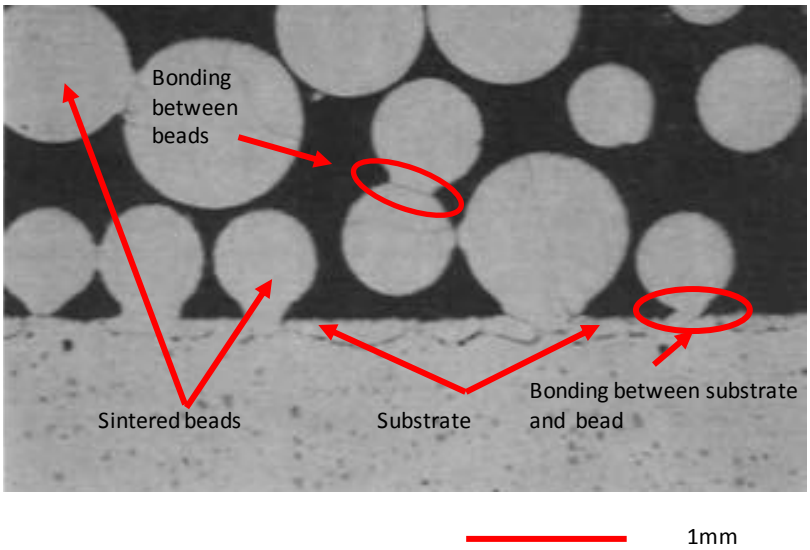

Figure 2-2 Sintered beads (Co-Cr) on substrate [100].

Metal fibre is an alternative material used for sintered bone ingrowth structures for providing uncemented fixation for THRs. The metal fibres are compacted to a shape prior to sintering. Then their contact points are bonded by a low temperature-pressure sintering (diffusion bonding) process [101]. In the sintering processes, the metal fibre is prone to spring back which may affect the bonding. The average pore size lies in the range of 100-400µm with high porosity (65-70%). As shown in Figure 2-3, the smooth surface of the metal fibre (coefficient of friction 0.63) cannot provide sufficient initial stability for THRs [57].

Figure 2-3 SEM image fibre mesh on THRs surface [102].

2.3.2. Plasma Spraying

Plasma spraying is a common method normally used to fabricate the second generation of bone ingrowth structures. In order to minimise oxidization, plasma spraying is carried out in a vacuum environment. Figure 2-4 shows the plasma spraying process. Two electrodes are utilised to generate an electric arc to heat a gas to high temperatures (up to 20,000°C) forming a plasma. The gas is accelerated through a cathode and used to melt and deliver the powder injected into a carrier gas. Finally the part melted powder is impacted onto the substrate and forms a rough, irregular structure. Functional graded porous structures can be fabricated by plasma spraying [103,104]. Here three different layers varying in pore size are produced as a single implant. The outer layer with the largest pore size (100-150µm) is to attract bone ingrowth. It is followed by a middle layer with smaller pore size and inner layer with full density. This functionally graded porous structure not only provides void space for bone ingrowth but also ensures a strong bond between bone ingrowth structure and substrate. Recently, as shown in Figure 2-5, by adjusting the plasma spraying parameters, it is possible to produce a porous structure with higher porosity and deeper pores. Pore size lies in the range of (100-1000µm) and porosity lies in the range of 40-65% [105].

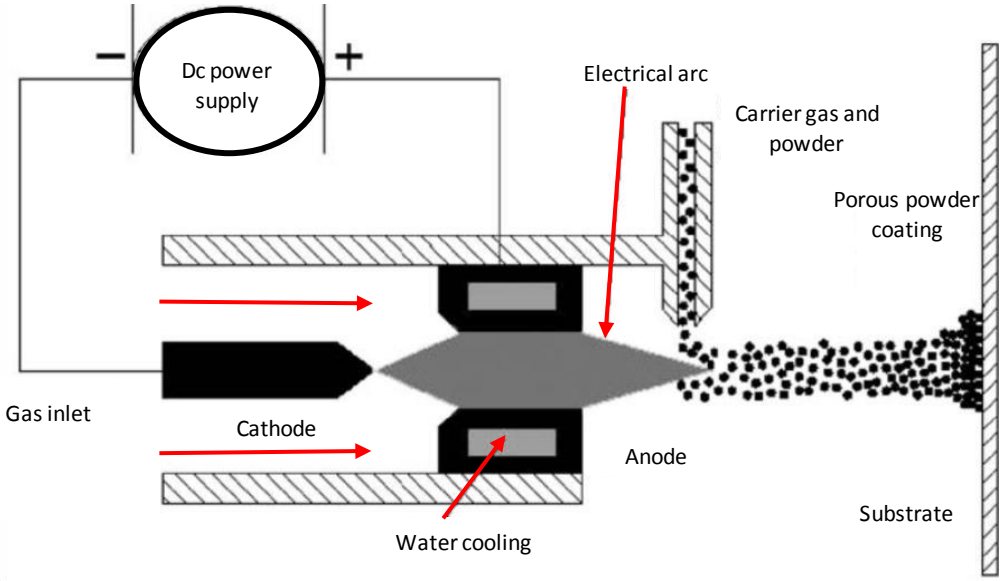

Figure 2-4 Schematic of the plasma spraying process [98].

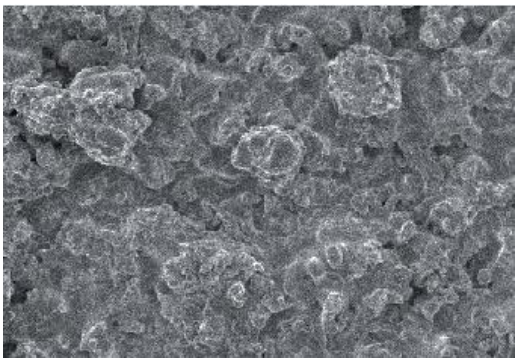

Conventional plasma spraying, average pore size 20-50 µm, porosity 10-40%, Titanium

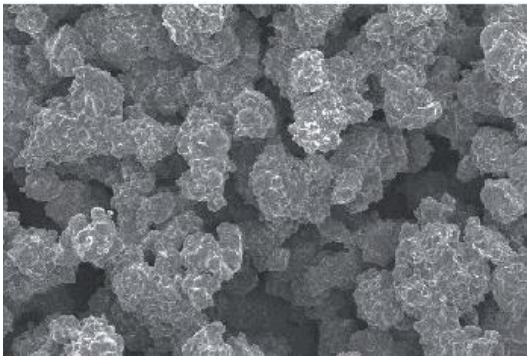

New plasma spraying (Ti-GROWTH®),average pore size 100-800 µm, porosity 40-70%,Titanium

Figure 2-5 The different surface coating in THRs fabricated by conventional plasma spraying and new plasma spraying [106].

2.3.3. Vapour Deposition Methods

The new generation of bone ingrowth structures are fabricated using various methods including Chemical Vapour Deposition (CVD) [101] and Low Temperature Arc Vapour Deposition (LTAVD). As shown in Figure 2-6, the cold source gases (at room temperature) flow into a reaction chamber where they are heated by the radiation from the heated substrate. The reactions of source gases occur at the surface of the substrate to form a coating layer and its gaseous reaction by–products are transported out of the reaction chamber. Compared with the methods previously described such as sintering beads and plasma spraying, these methods can fabricate bone ingrowth structures with higher coefficients of friction

(>0.88), and porosity (>60%), well interconnected open pores as (Figure 2-7) with a similar appearance to cancellous bone.

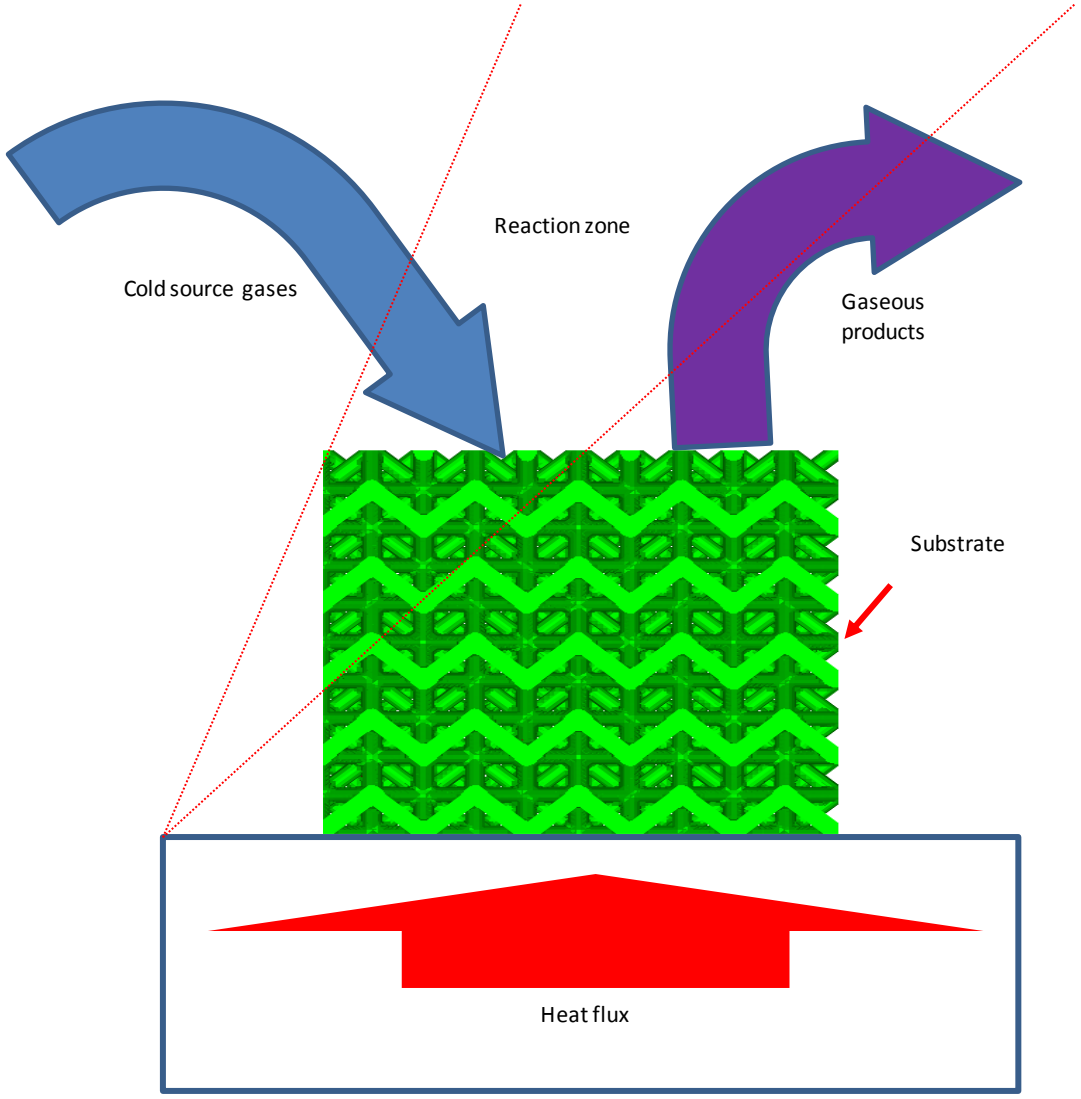

Figure 2-6 Schematic of CVD process [98].

By using this technique, the company Zimmer developed bone ingrowth structure, termed trabecular metal which is made of tantalum. Pyrolysis of polymer foam is used to form a repeating dodecahedron array of pores in a low density vitreous carbon skeleton, this skeleton is then CVD coated in CpTi [59]. Mechanical properties can be altered by changing the thickness of the deposited tantalum, while the geometry of the bone ingrowth structure can be modified by changing the carbon skeleton. The resulting material has a compressive strength of 50-70MPa, a

high porosity in the range of 75% to 85% and an average pore size of 400-600µm [59,99]. Following implantation of acetabular components, 80% of pores are found to be occupied by new bone after one year. This technique is versatile and can be used to fabricate many orthopaedic components, for example augments as shown in Figure 2-7.

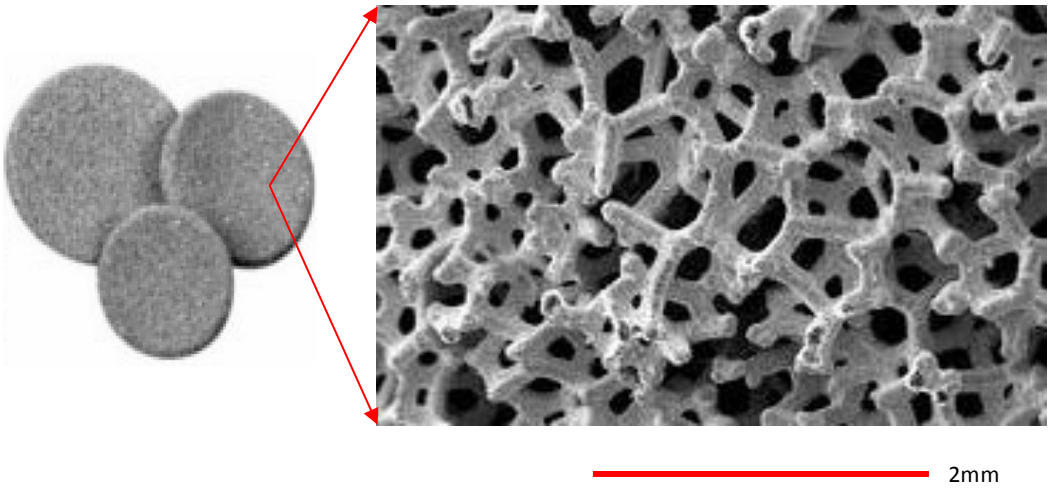

Figure 2-7 Trabecular metal acetabular augments fabricated by CVD and utilized in revision THRs [107].

Another vapour deposition method, also known as Physical Vapour Deposition (PVD), termed Low Temperature Arc Vapour Deposition (LTAVD) can be used to fabricate bone ingrowth structures (Trianium™) and has been used by Stryker to produce the Trianium™ range products. A porous polyurethane foam shell is machined to shape followed by LTAVD to deposit sufficient metal thickness onto its porous surface. Finally the polyurethane foam is burnt out and the part sintered to generate the bone ingrowth structure [99]. The bone ingrowth structure (Figure 2-8) possesses a high porosity (72%) and an average pore size of 546µm. It also possesses a high coefficient of friction which can provide adequate surface roughness for initial stability. Compared to earlier generations, this bone ingrowth structure also shows superior penetration of bone and most of its pores are filled with new bone. The bone ingrowth results were based on analysing these

acetabular surfaces in a canine total hip model [79]. At three months, the average bone ingrowth reached 23% and at 6 months improved to 38% [79]. This is much superior to the average bone ingrowth in sintered beads (6%) [108].

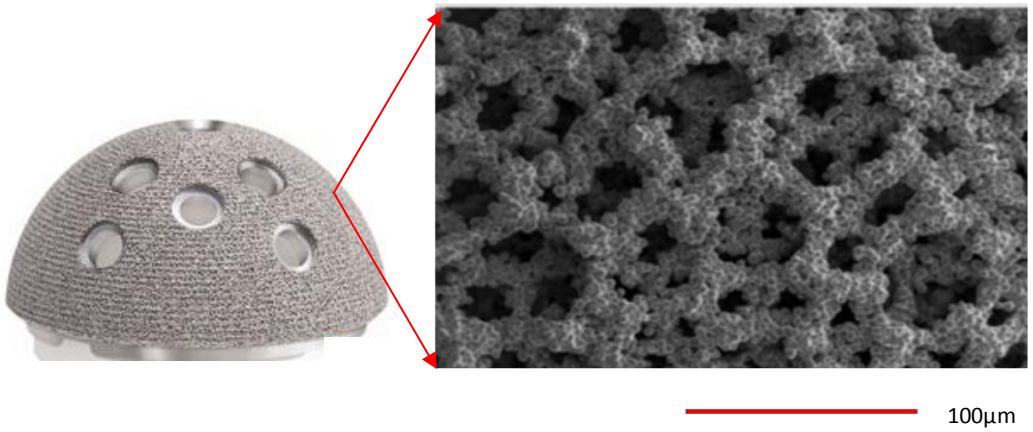

Figure 2-8 A bone ingrowth structure fabricated by LTAVD and used in titanium coated acetabular component [100].

2.3.4. Summary of Conventional Methods for Fabricating Bone Ingrowth Structures

Compared with older generation structures for bone ingrowth, new structures exhibit interconnected open pores with high porosity and bear resemblance to cancellous bone. This structure ensures a sufficient void space for deeper bone penetration allowing significant bone ingrowth. Although this new generation of structure can be fabricated by CVD and PVD, its properties rely heavily on the foam onto which the metal is deposited. The complex fabrication process of fabricating foam for CVD and the limitation in controlling the geometry of the pores [109] have driven the development of new technologies to provide more freedom to design and fabricate bone ingrowth structures.

2.4. AM for Fabricating Bone Ingrowth Structure Production

AM is an umbrella term that refers to a range of technologies that are capable of translating digital solid model data into physical parts directly [110,111]. A complex

digital 3D solid model is sliced into a series of 2D cross-sections with a specified layer thickness. The 2D cross-sections are fed into AM machines so that they can be fabricated in a layer-by-layer sequence to form a physical part. The accuracy of AM can be a few tens of microns [111] and it can be used to fabricate complex porous architecture [112] such as bone ingrowth structures.

2.4.1. Generic Steps of Data Processes for AM Fabrication

The AM processes starts with a digital solid model created by 3D CAD software. The creation of a digital model is followed by a complex data chain process, which converts the digital model to a discrete model constructed from information in the form of layers. The layer information directs the energy source to solidify raw material on each layer.

Creating the Digital Solid Model

CAD software packages such as Pro Engineer or AutoCAD can allow designers to link seamlessly to the AM machine however this is not the only way [113]. This data can also be created by reverse engineering equipment such as a CT scanner to get 2D images, which can then be reconstructed by software to create closed and continuous 3D solid models. The digital solid models cannot be used by AM directly without the following data conversion and processes.

Data Conversion

Stereolithography format (.stl) [114] is a widely accepted data format in the AM industry. It represents a digital solid model surface by a set of un-ordered triangles and most CAD systems can output such a file format [113]. The solid model with a closed and continuous surface is approximated by triangles [113], termed tessellation. The tessellated digital solid model has a major limitation [115,116], in that the intent of the original design is lost because of the first order piece-wise approximation of its surface. Figure 2-9 shows a solid model that has been tessellated and the maximum difference between the CAD surface and the tessellated surface is indicated by the maximum chord error.

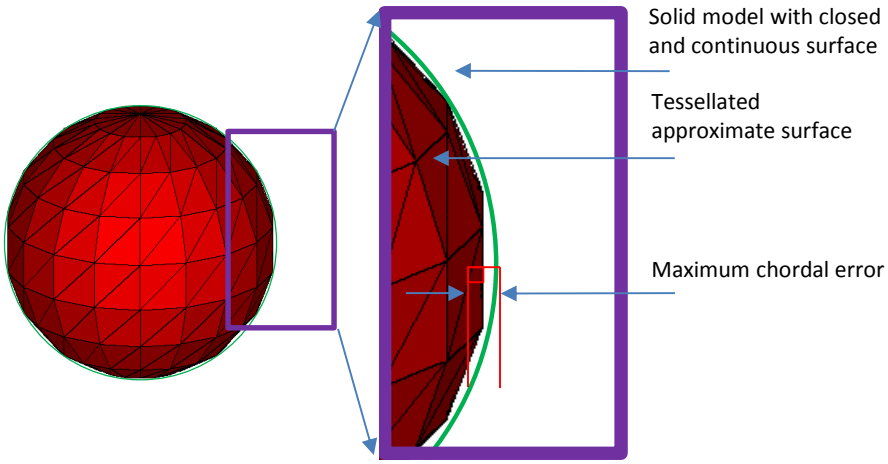

Figure 2-9 Illustration of maximum chordal error used to convert a solid model with tessellated surface [117].

A solid model is tessellated by a set of triangles with normal vectors indicating their directions and saved as a .stl file. An example of an ASCII .stl file is given in Figure 2-10, each triangle is represented by the coordinates of its vertices and the normal vector as defined by the right hand rule.

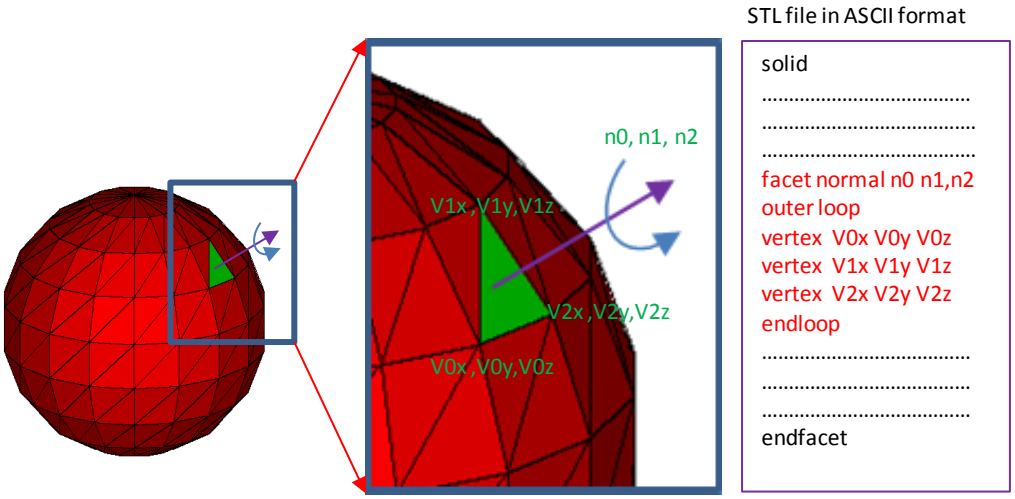

Figure 2-10 The tessellated solid model with its corresponding .stl file in ASCII format.

Data Slicing

Due to the fabrication mechanism of AM, as shown in Figure 2-11, the tessellated surface needs to be sliced by a set of Z planes with specified layer thickness. Subsequently a set of closed contours are created by joining adjacent segments in

order and each contour is hatched with a specified gap termed the hatch distance. These segments are used to form the scanning path for fabrication.

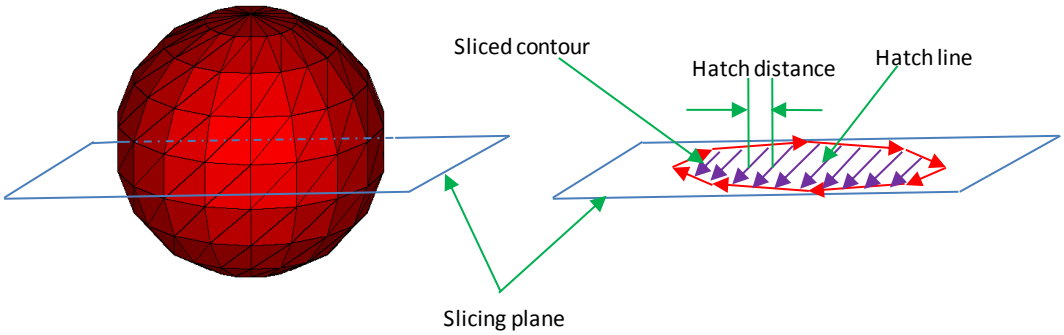

Figure 2-11 A solid model with tessellated surface is sliced and its sliced contour hatched by lines with specified hatch distance.

2.4.2. AM Processes for Manufacture

Most AM processes tend to employ an energy source to process the raw material to fabricate layers and bond them together to form the new solid parts. There are a number of methods to classify AM processes based on the initial state of the raw material, type of material, energy source and physics of the process [111]. In the following section, the various AM processes are classified into three categories based on their initial raw material state.

Liquid State Processes

Stereolithography (SL) [114] is an AM technique which uses a liquid material which is solidified by radiant energy through photopolymerisation [118,119]. Typical bio material that are already in clinical use are based on polyesters such as poly (ß-caprolactone) or poly (α-hydroxy acids) [119]. Figure 2-12 shows the schematic of SLA. An ultraviolet laser is scanned in the x-y plane curing the photo sensitive polymer and creates the layer. Figure 2-13 gives an example of a structure with well-defined architecture built by SLA. The structure is prepared from Poly-DL-Lactide (PDLLA) fumarate/ N-Vinyl Pyrrolidone (NVP) resin which supports bone cell adhesion and growth [120]. In order to promote the cell adhesion and growth, dispersed hydroxyapatite particles are added into the resin [120]. Although the bone ingrowth like structures can be fabricated by SLA with high resolution, a

specific disadvantage of this material is that its compressive strength is less than 17MPa [121] which is just over 50% of the minimum requirement of compressive strength (30MPa) [95] for bone ingrowth structures.

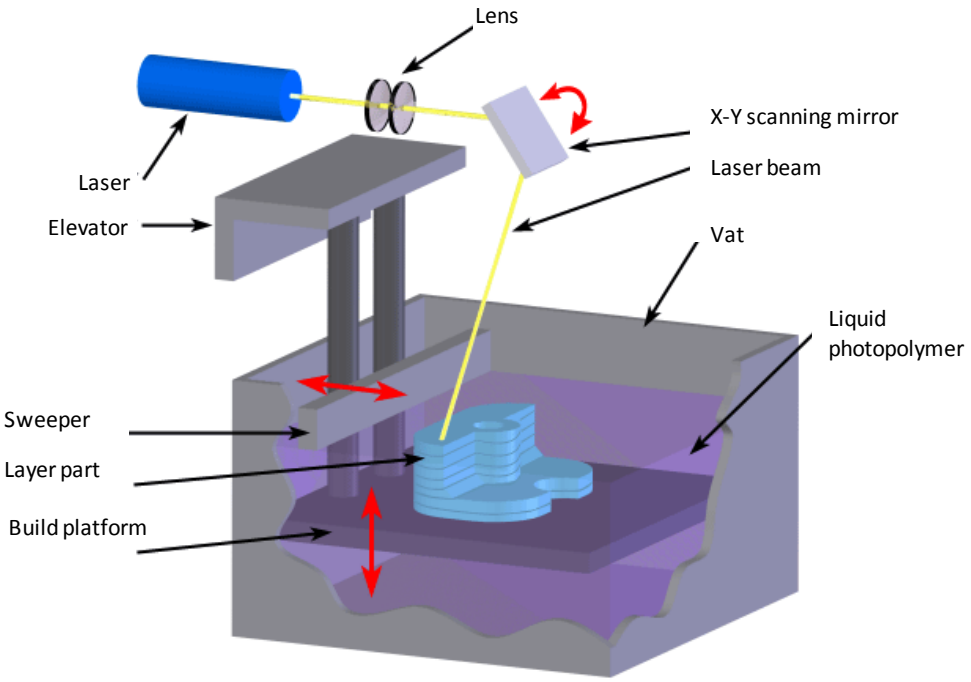

Figure 2-12 Schematic of Stereolithography (SLA) [120].

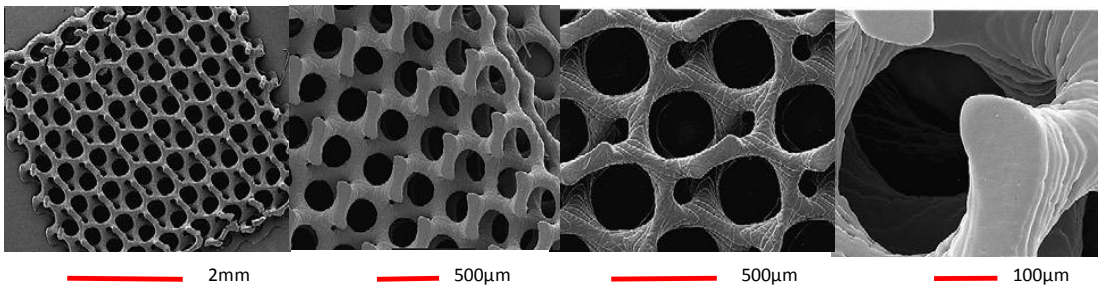

Figure 2-13 SEM image of bone ingrowth structure prepared from PDLLA fumarate and NVP as a reactive diluents and fabricated by SLA [120].

Solid State Processes

Material extrusion or Fused Deposition Modelling (FDM) [114] is an AM technique beginning with a solid state raw material. As shown in Figure 2-14, the molten material a thermoplastics such as PLA or ABS is extruded through a heated nozzle depositing onto the x y plane, subsequent layers are directly deposited onto the top

of the previous layer to fabricate a bone ingrowth structure. Typical porosity can be up to 89% [122–124] using this process, however the nozzle dimension can affect the melted thermoplastics deposition volume which is the factor that influences the resolution of the features in the structure [110].

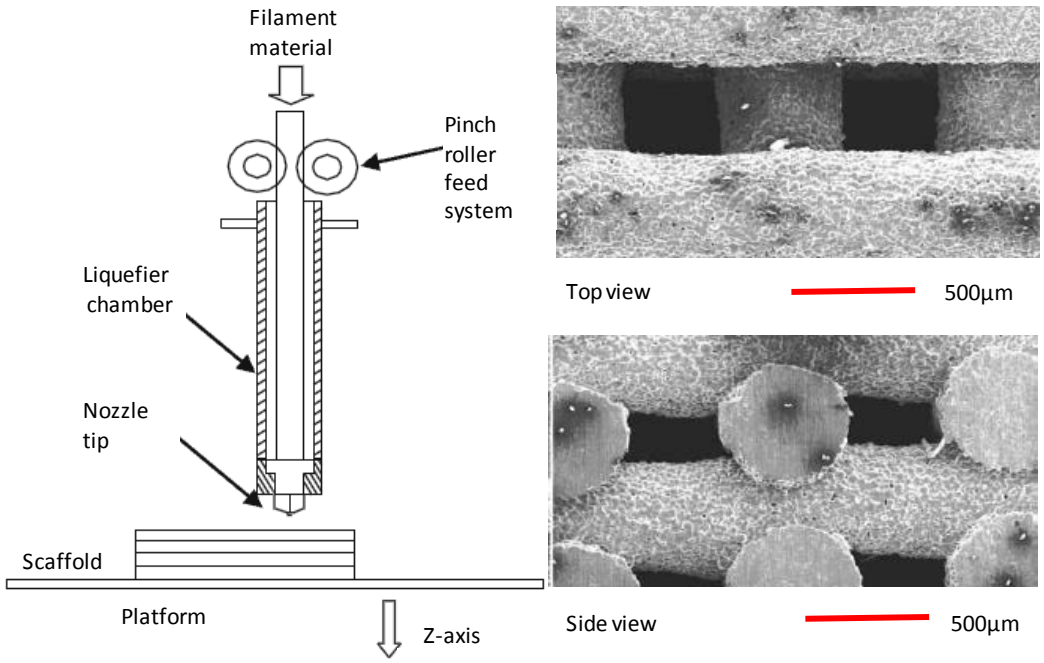

Figure 2-14 Schematics of extrusion-based systems with its fabricated bone ingrowth structure and viewed in side and top direction adapted from [125].

Sheet stacking techniques are implemented in sheet lamination manufacturing [114] which are some of the simplest AM technologies. It starts with solid state feed material, for example paper, on one surface of which a heat-activated resin is coated. A schematic of this process is shown in Figure 2-15 , in this process, the geometry of each layer is generated by cutting the sheet with a laser, hot wire or knife. The trimmed sheet of each layer is stacked on top of the previous layer to create the solid component by the application of a heated roller. Although the process has a very rapid build rate, the resultant material exhibits very high anisotropy.

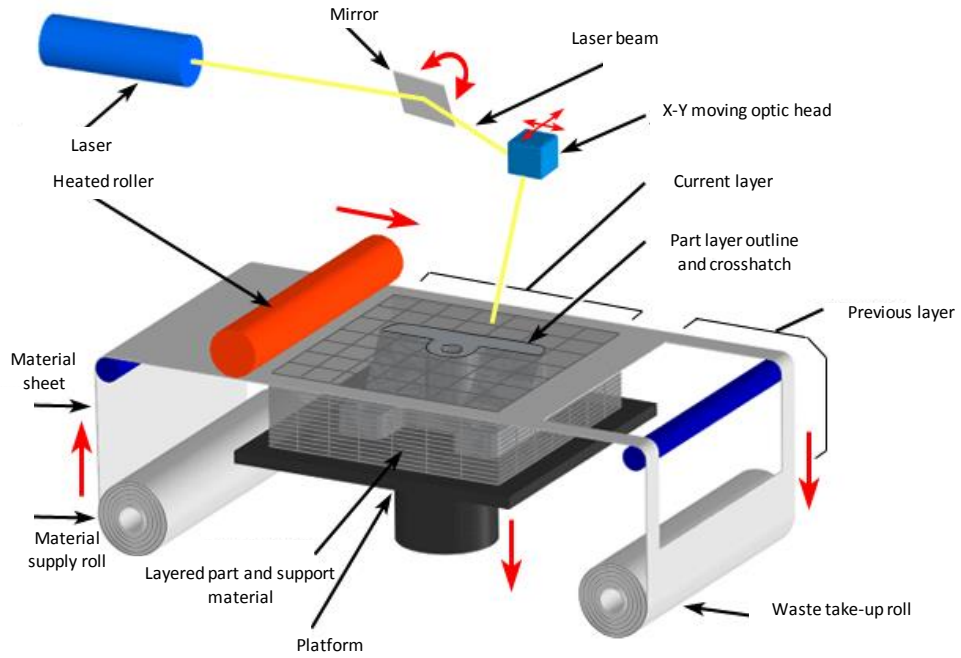

Figure 2-15 Schematic of the sheet lamination process [126].

Kusakabe et al [127] used the sheet lamination manufacturing to fabricate a bone ingrowth structure onto the surface of a THRs stem providing an uncemented fixation. The implant was prepared from wire sheets created by acid etching, having a pore size of 500-1000µm. The layers of these sheets were then sinter bonded together to form a 1mm thick 80% porous structure attached to the anterior and posterior surface of a titanium alloy hip stem as shown in Figure 2-16. As a comparison, a stem with sintered beads surface coating (porosity 35%, average pore size 300 µm and another with stacking sheets (porosity 80% and average pore size 500-1000 µm) were coated with Hydroxyapatite (HA) and then implanted into dogs. The results showed that the rate of bone ingrowth for the stack sheet was approximately twice that of the sintered bead structure. No information was released to show if the stacking sheets provided adequate compressive strength to preserve enough void space for bone ingrowth under loading. No further

information has been released to show if this technology can fabricate porous structures with high resolution directly.

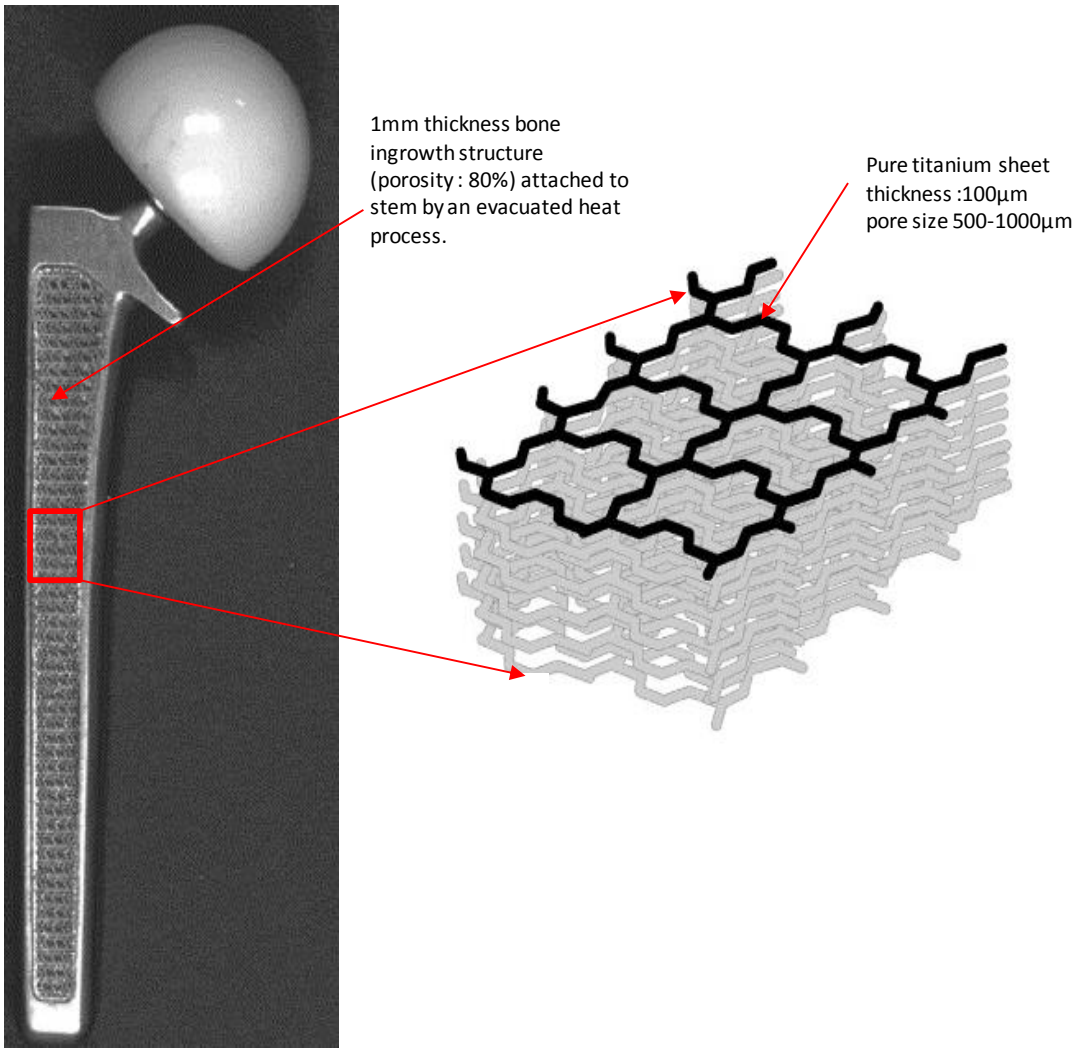

Figure 2-16 A THRs surface coating in stem is fabricated by LLM technologies (sheet stacking technology) [127].

Powder State Processes

Many AM systems use a powder feed stock, typical example being the binder jetting [114] process shown in Figure 2-17. For each layer, powder is spread evenly on the powder bed by a roller. Then an inkjet print head scans in the x y plane and injects a binder. In this way, the powder of each layer is glued to the previous one. This cycle is repeated until the part is completed. The resolution of any features in a

part is affected by the inkjet print head resolution and drop volume. Thus it is very difficult to achieve features below 500µm in size [128].

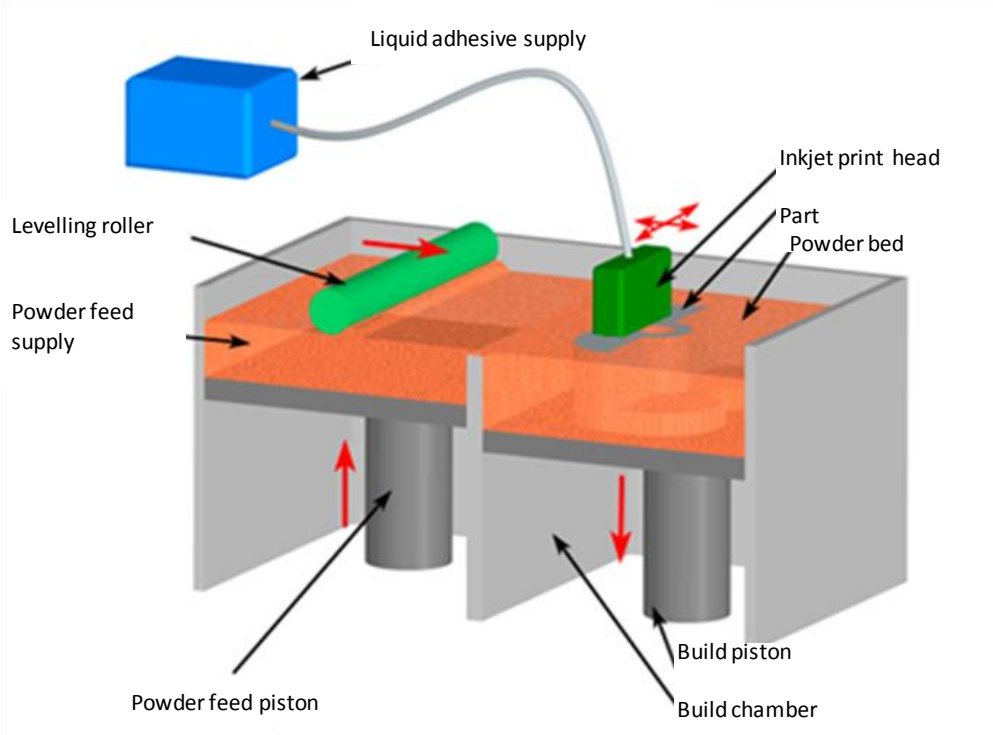

Figure 2-17 Schematic of binder jetting process [129].

When binder jetting is used for fabricating Ti bone ingrowth structures, a post-sintering process is required. The powder material was CpTi (particle size 65-106µm) and a binder of PVA solution was used in 3D printing to manufacture porous components [110]. A standard binder jetting machine (Z printer 310plus, Z corporation, Burlington, MA, US) was used to fabricate the samples (Ti cylinders of 10mm diameter and 15mm in height). The samples were removed from the powder bed and cleaned by blowing off the loose powder then placed in a furnace to burn off the PVA, followed by sintering. The final sample is shown in Figure 2-18. Although its compressive strength can be up to 159.6±6.4MPa (n=6), due to the trapped powder and process resolution, it results in a limited porosity of 34.9 ±1.4% (n=6) and there is no interconnected porosity [110].

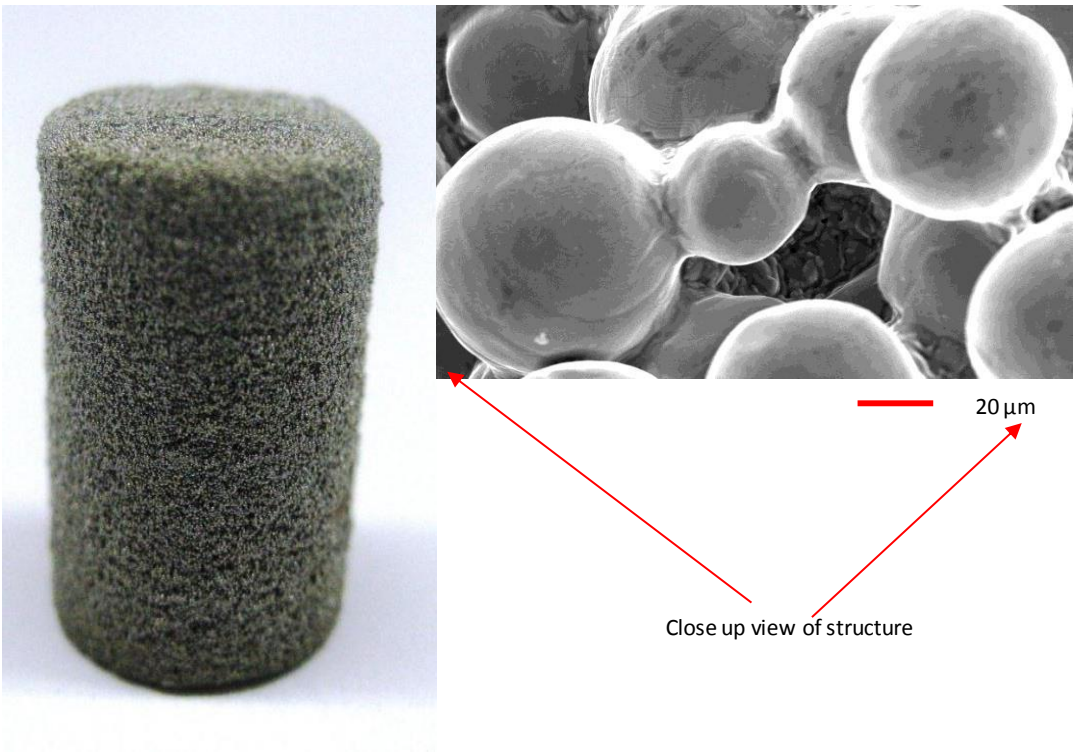

Figure 2-18 A sintered Ti cylinder formed through the 3D printing technique with its SEM image showing the necks between particles [110].

Selective Laser Sintering (SLS) [114] is another powder state based AM technique and is capable of processing polymer, metal and ceramic/glass powders, but polymers are the most widely utilised [130]. With reference to the requirements of material for bone ingrowth structure this review will however focus on metallic material fabrication. The SLS process is carried out in an inert environment to minimise oxidation [98]. Prior to the fabrication, sufficient time must be given to pre-heat the powder bed to reduce the stress caused by the sintering process. Then a continuous wavelength Neodymium-Doped Yttrium Aluminium Garnet (Nd-YAG) laser beam of wavelength (λ=1.06µm) is preferred to the CO_2 laser of wavelength (λ=10.6µm) to maximise absorption of the laser light [131]. This laser beam selective scans the powder bed to bring the temperature to just below the melting point of the powder, sintering takes place and the powder particles are fused, resulting in the reduction of particle surface energy which is proportional to the surface energy. The reduction of surface energy is the driving force for sintering in

the solid state to form a solid layer [111]. After each layer is created, as seen in Figure 2-19, a piston drops by a defined layer thickness to a new position and a new layer of powder is deposited, using a mechanical roller to level the powder bed. Finally a solid structure is fabricated with inherently porous and mechanically weak [95], although these properties may be improved by post-manufacture such as infiltration and sintering furnace consolidation to generate fully-dense parts [132]. Considering the fabrication of porous structure for bone ingrowth, the technique can sinter a metallic material such 316L with similar result to conventional sintering as seen in Figure 2-20. Although the porosity can be enhanced to 40-50% with a compressive strength of 21-32MPa respectively [133], these properties cannot meet the requirements of bone ingrowth. For the porous structure, the post-manufacture is still required. Therefore the full melting of the powder particle is necessary for both solid and porous structures.

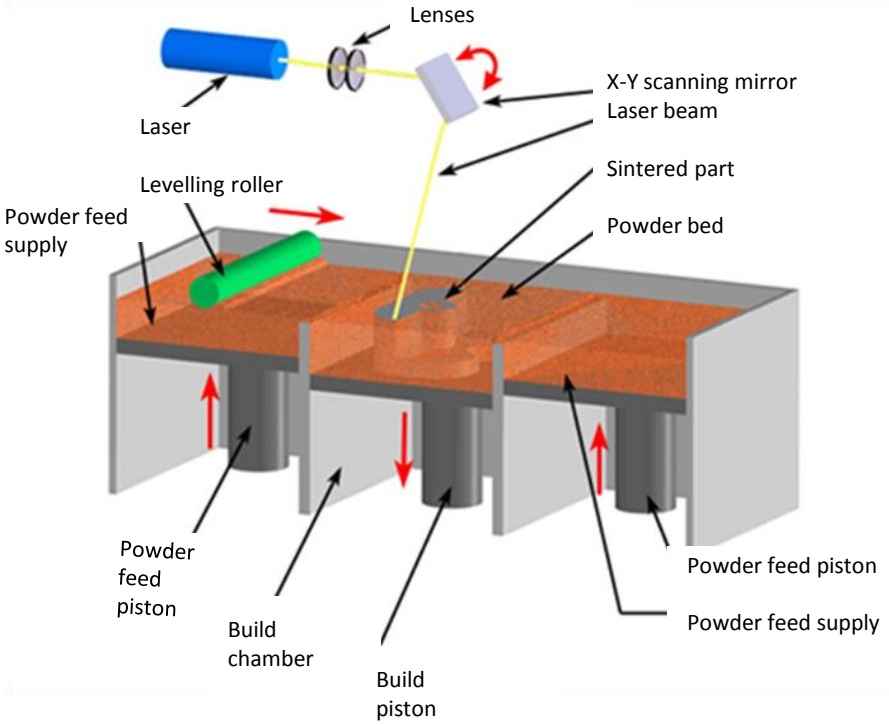

Figure 2-19 Schematic of SLS process [134].

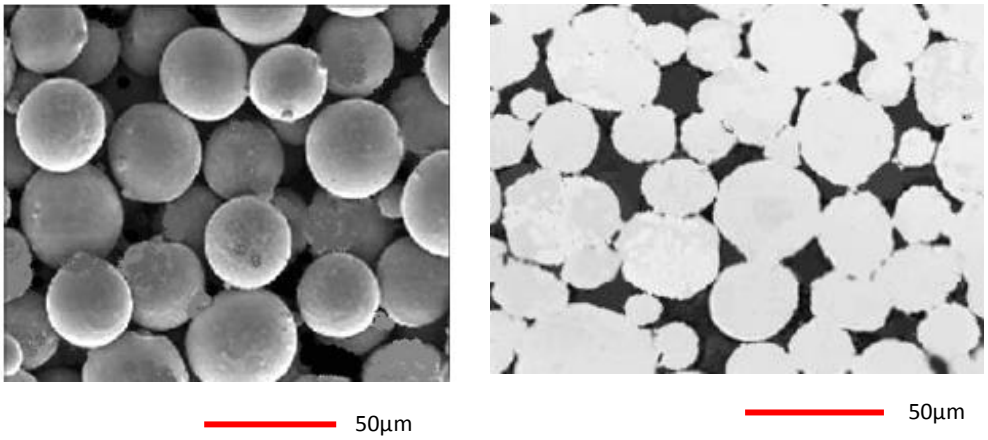

316 L stainless steel powder particles

Sintered 316 L stainless steel powder particles (porosity 29.5%) by selective laser at scan speed 800mm/s and laser power 20W and post-sintering at 1060 °C for 2 hours

Figure 2-20 316L stainless steel powder particles are sintered by selective SLS for bone ingrowth [133].

As the process moves to fully melting, a new technique emerges termed Selective Laser Melting (SLM). Although SLM is closely associated with SLS and uses similar powder delivery and laser scanning processes, it possesses a number of distinguishing features. The higher power laser (up to 400W) [135] with shorter wavelength (λ=1.06µm) is chosen to fully melt the powder particles to form melt pools [131] selectively by using the rapid movement of scanning mirrors as seen in Figure 2-21. These melt pools then rapidly cool to create a fully dense metallic layer. The rapid selectively localised heating and cooling lead to residual stresses which may be released by post-manufacture heat treatment processes [136]. After a layer is solidified, a new even layer of powder particles must be applied on top of solid layer. With reference to the metallic material (Titanium) used in this research, its processing characteristics (such as good laser absorption, flowability, etc.) makes it possible to fabricate both the pre-defined porous structure [137] and fully density solid components with levels of accuracy similar to the SLS process, however with relatively low speed (5cm^3/h) [138]. Alternatively, the solid or porous titanium components can be fabricated by Electron Beam Manufacture (EBM) which is described in detail and compared with SLM mechanism in following section.

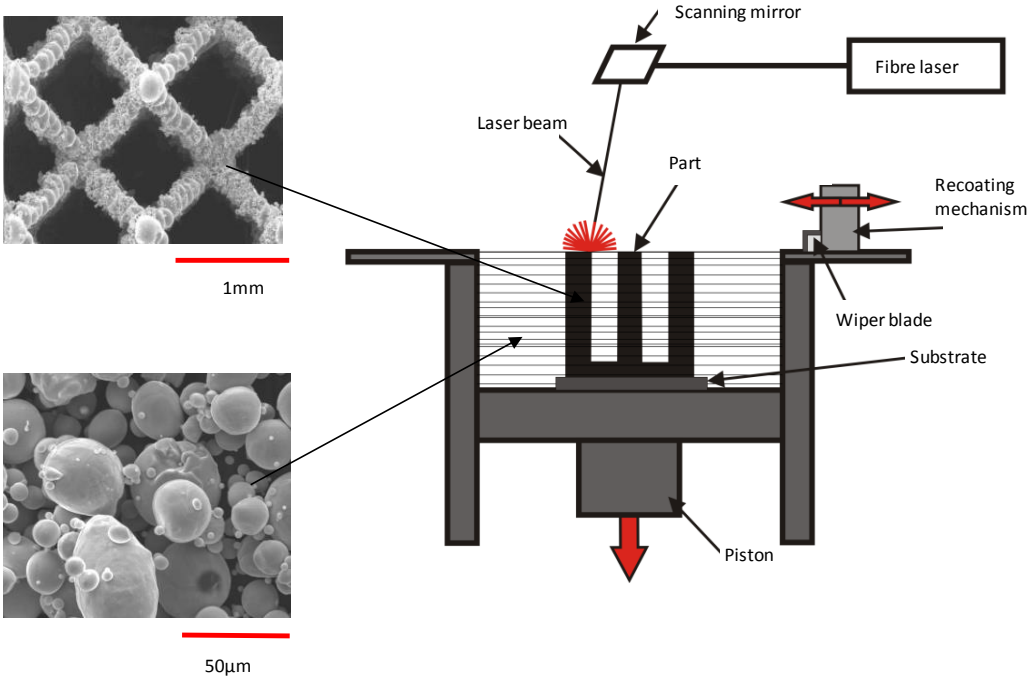

Figure 2-21 Structure [9] fabricated by SLM (schematic of SLM [138]) by melting CpTi (average powder particle size 50µm).

An electron beam is utilised by EBM and this will interact strongly with any gases present and therefore the EBM fabrication must be carried out in an evacuated environment. Prior to fabrication, the powder is pre-heated to reduce the high residual stress caused by the rapid selective heating and cooling. As seen in Figure 2-22, the electron beam can be focused by an electromagnetic focus coil and directed by an electromagnetic deflection coil respectively, which gives scanning speed of up to 10^3mm/s and directs the beam accuracy of ±50µm [139]. This electron beam with high kinetic energy enables the fabrication of fully dense parts from various materials including titanium and Co-Cr alloys with high fabrication speed (60cm^3/h) [140]. This high energy beam results in large amounts of melt powder particles attached to the part surfaces and can lead to insufficient dimensional accuracies of the order ±0.4mm [9]. Thus the final part requires further finishing. For the porous structure, the high energy beam also causes the powder particles to sinter onto the porous structure surfaces and gives smaller pore

sizes than the pre-defined size. Therefore it is necessary to incorporate the powder particles by sintering [9].

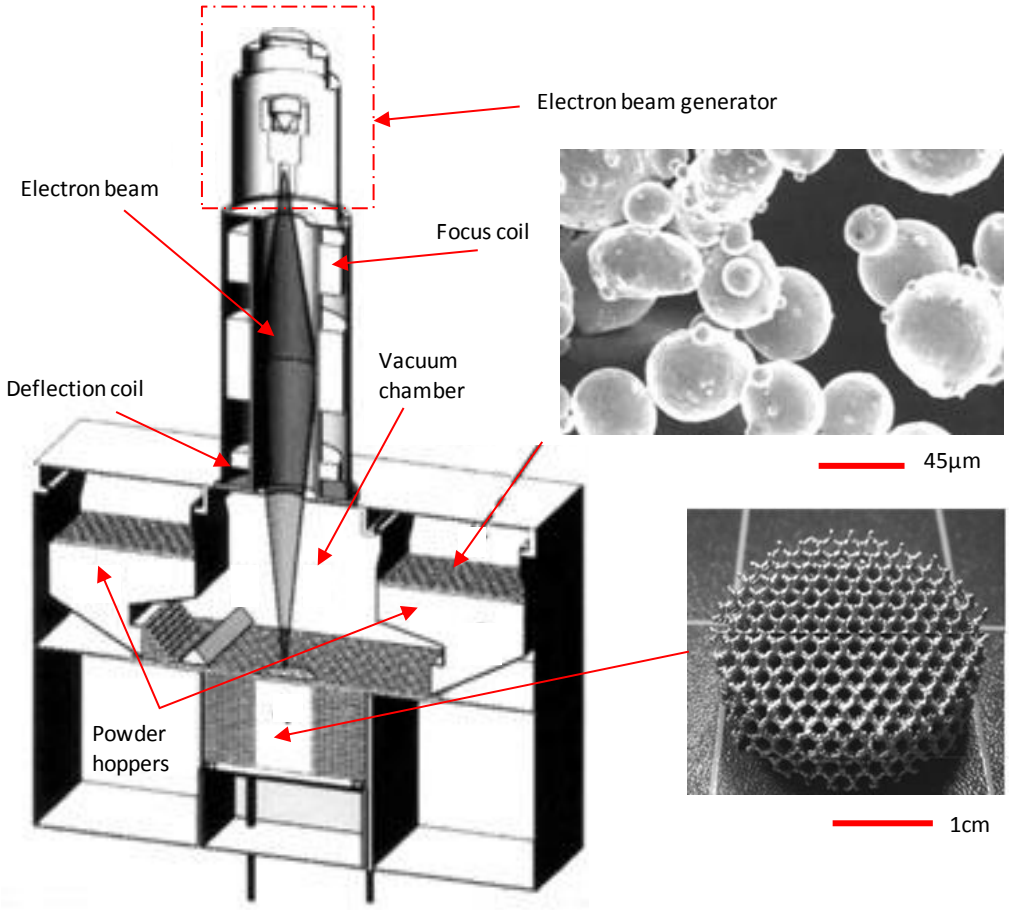

Figure 2-22 Structure fabricated by EBM (schematic of EBM [95]) by melting CpTi (average powder particle size 45µm) [141].

2.4.3. Summary of AM for Fabricating Bone Ingrowth Structures

The previous section considers a review of the literature on AM technologies; it shows that current technologies can fabricate bone ingrowth structures with high resolution and using various materials from polymers to metals. However, it also shows that the geometry of the bone ingrowth structures is quite simple and homogeneous. In order to fabricate bone ingrowth structures with complex geometry, CAD technologies are required for bone ingrowth design and AM fabrication.

2.5. CAD Technologies for Creating Bone Ingrowth Structures

The simplest method to create a block of bone ingrowth structure starts with a single design model of a pore. This single pore model design includes its geometry and type of surface (closed or open). Then the pore model can be repeated and stacked together to form a block of structure which is trimmed to obtain the desired shape. Finally the trimmed structure is sliced for AM fabrication. In the following section, the CAD technologies involved are described.

2.5.1. CAD Technologies for Creating Bone Ingrowth Structures with a Desired Shape

The bone ingrowth structure can be created by repeating a pre-designed solid model of the pore to generate a 3D block as shown in Figure 2-23. The shape of the bone ingrowth structure is achieved by using a Boolean operation between the porous block and the solid model. Due to the closed surface representation, when more than 1,000 to 2,000 surfaces or parts are modelled, the CAD systems tend to run very slowly and use many Gigabytes (GB) of memory [111]. Thus this is not a suitable method for the creation of complex bone ingrowth structures.

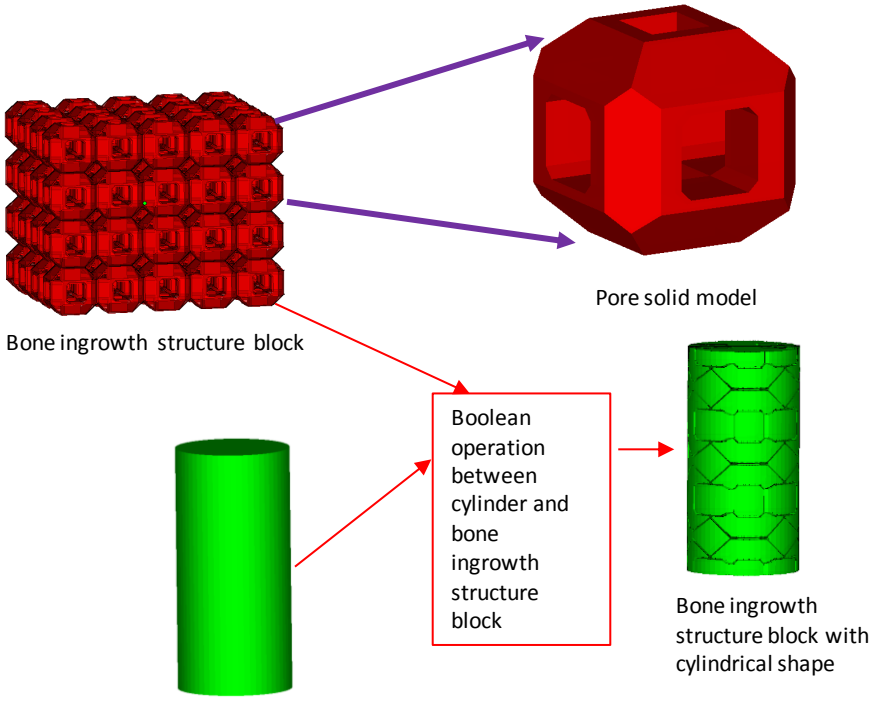

Figure 2-23 Pore with closed and continuous surface was used to construct a bone ingrowth structure block by performing a Boolean operation [175].

The above bone ingrowth structure can be built with an AM machine by fabricating cross sections of each single pore one by one. In Figure 2-24, one of the pores in the porous structure is given to explain the fabrication mechanism. A pore with a closed surface is sliced to get a set of closed contours which are then hatched with lines. These closed contour and hatch lines are used to direct the energy source scanning for AM fabrication.

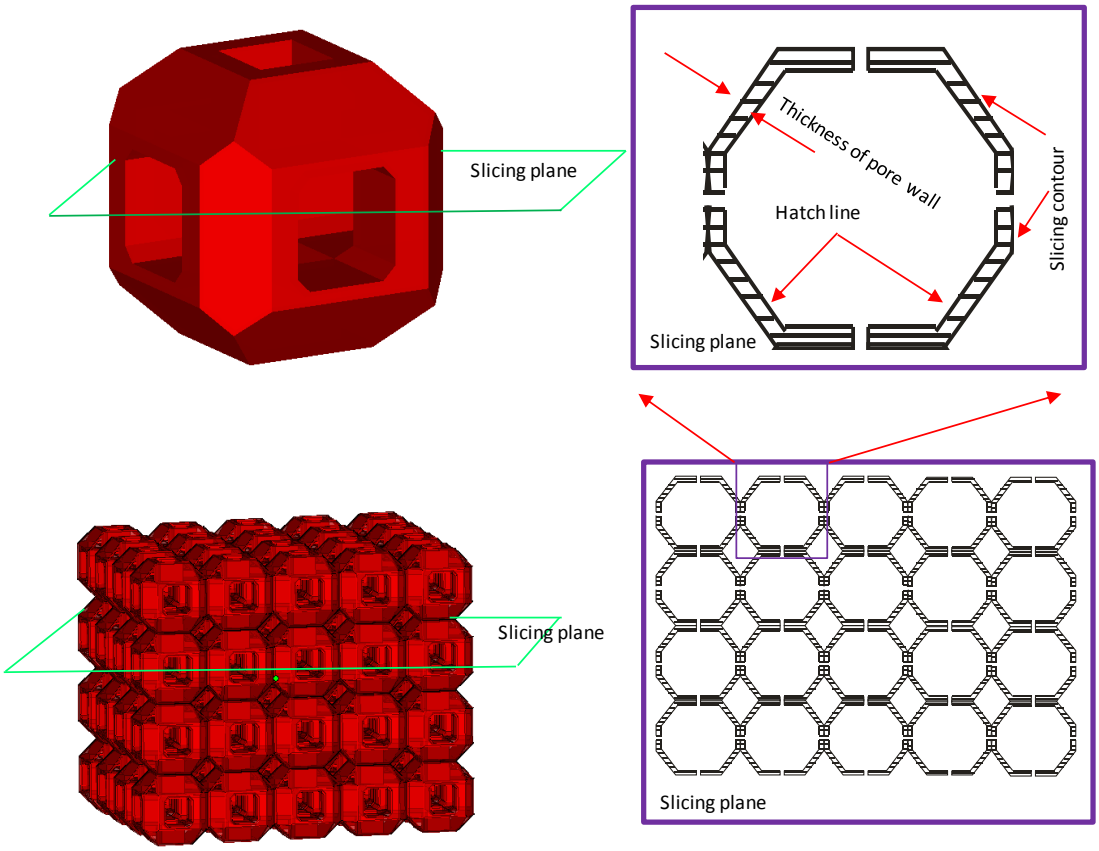

Figure 2-24 Illustration of fabrication mechanism for solid model with closed surface.

In order to decrease the memory requirements, the bone ingrowth structure block can also be created by repeating unit cells filled with pre-designed struts [142–150] as shown in Figure 2-25. These struts are represented by the coordinates of their ends rather than by a closed solid model. This results in a lower memory requirement. The desired outer shapes of the bone ingrowth structure can also be achieved by using a Boolean operation between itself and a solid model.

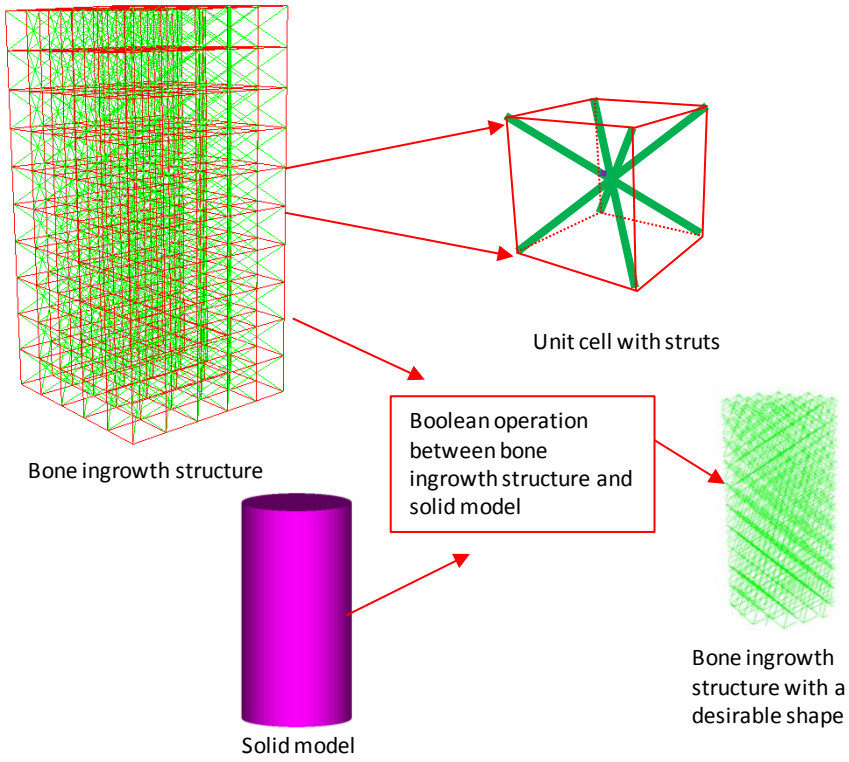

Figure 2-25 Bone ingrowth structure block was created by unit cells filled with struts and with a desired shape by using a Boolean operation between itself and a solid model. The bone ingrowth structure with a desired shape was created by using Manipulator software [151].

When this structure is sliced as shown in Figure 2-26, it produces a set of dots for each layer. These dots are represented by the coordinates which are used to direct the energy source and melt the material. So the diameters of the struts are dictated by the melt pool size which is dependent on the process parameters.

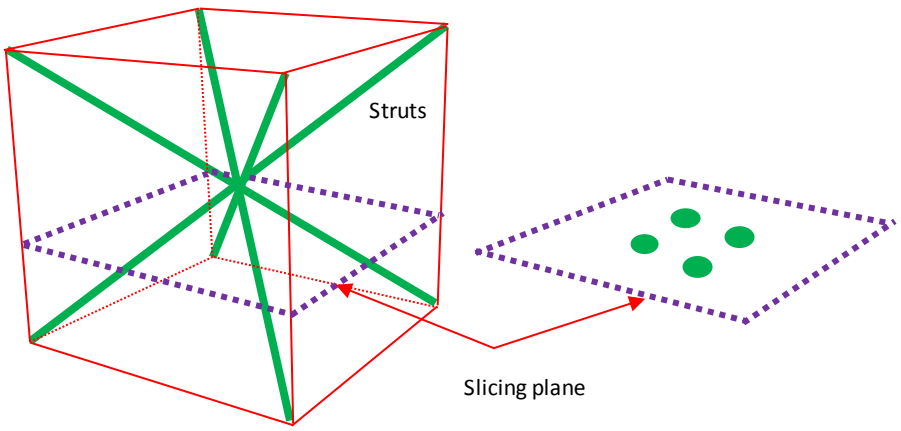

Figure 2-26 Based on the description in Brooks PhD thesis [151], struts in single unit cell are sliced by a slicing plane.

Using this basic method, a number of bone ingrowth structures can be created by the combination of strut numbers and distribution that define each cell. A bone ingrowth structure, being termed unit cell structure, was chosen for the bone ingrowth application from various bone ingrowth structures with struts [95]. This structure was later optimised by Mullen [137]. Examples of these octahedral structures made of CpTi and fabricated by SLM are shown in Figure 2-27. By altering the cell size, various unit cell structures with different strengths and porosities were obtained. Considering the requirements for bone ingrowth on porosity and compressive strength, a range of available properties was obtained. A larger range of available properties allows more options making the porous structure suitable for a wider range of patients. In order to widen the range of available properties and to ensure structural strength and incorporate the sintered powder, the structure was sintered in a vacuum furnace. Following this, its compressive strength was increased to just over 60MPa at a porosity of 75% [137]. However introducing the sintering process step significantly increases on the fabrication cost and time.

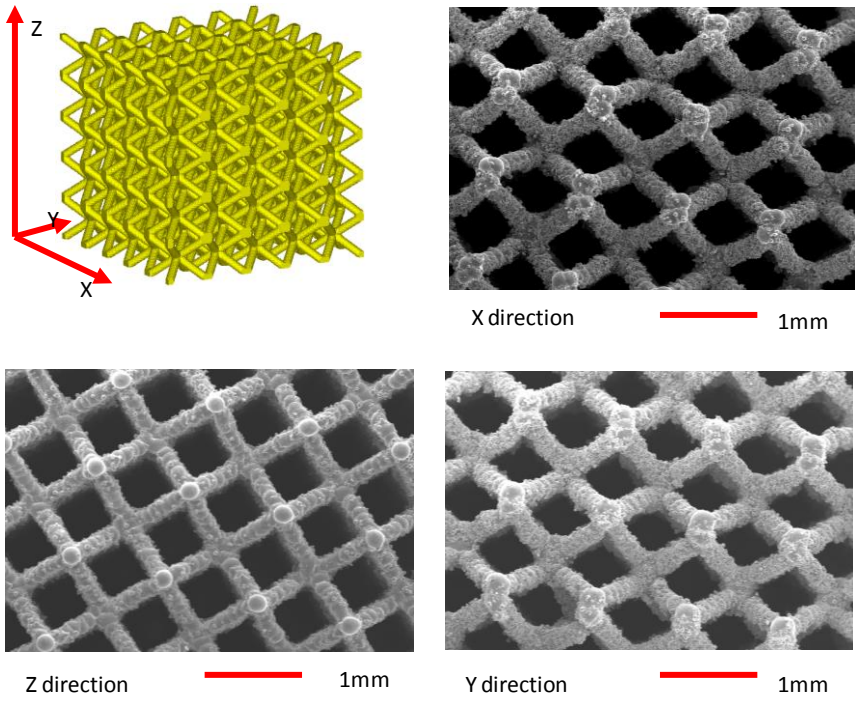

Figure 2-27 Based on the method provided by Stamp [95], a unit cell structure (octahedral) is created with Manipulator (custom software developed at the University of Liverpool) and visualised in .stl format by Magics and fabricated by SLM with Commercial pure Titanium(CpTi).

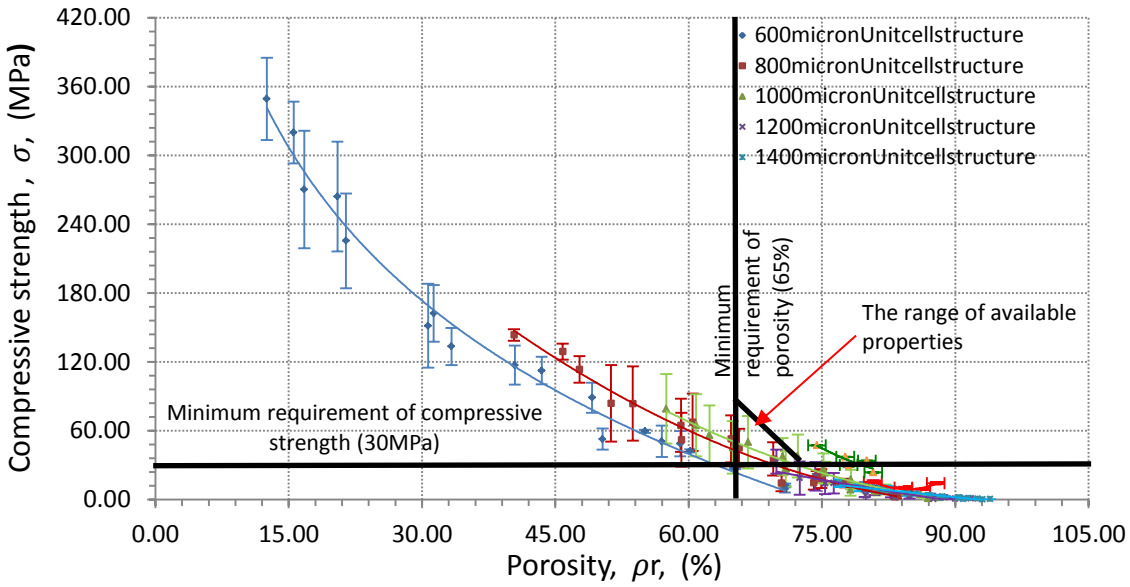

Figure 2-28 Each group of unit cell structures (CpTi) varying in cell size were fabricated by different laser energy (62W, 96W 132W and 167W) and exposure time (200 µs, 400µs, 600µs and 800µs). The unit cell structures gave different compressive strength varying with porosity [137].

In order to widen the range of mechanical properties beyond that shown in Figure 2-28, the structural elements in the bone ingrowth structure were switched from struts to platelets. An example is given in Figure 2-29. Here the platelet in each direction is fabricated by laser scanning a line (hatch line) layer by layer and its platelet thickness is dictated by the laser beam spot size and the process parameters.

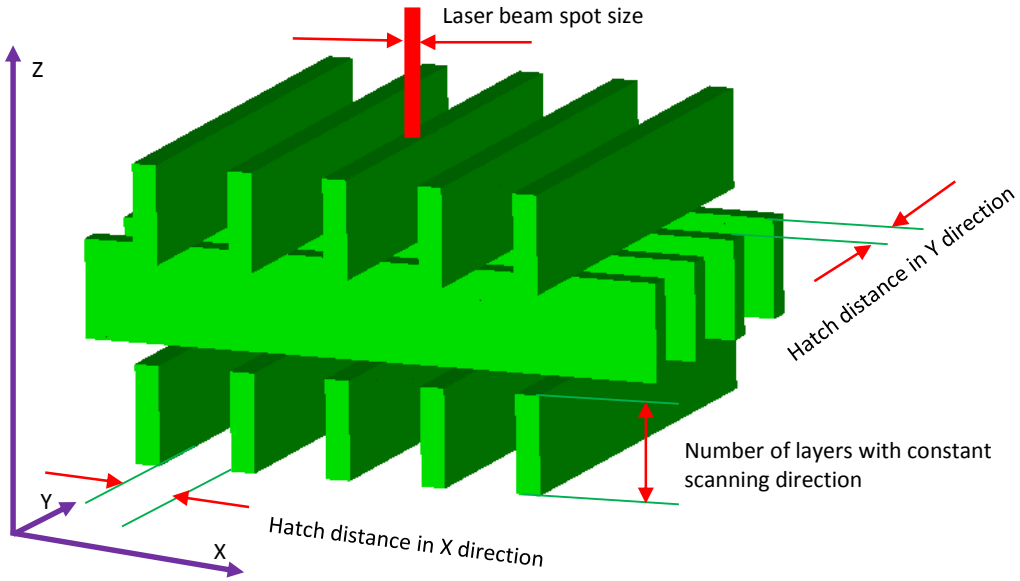

Figure 2-29 Schematic of fabricating bone ingrowth structure by hatch lines is based on the description in Mullen's PhD thesis [9].

The bone ingrowth structure with platelets can be represented in .stl format as shown in Figure 2-30. The desirable outer structure shape can be achieved by using a Boolean operation between itself and the solid model. By slicing the bone ingrowth structure, a set of hatch lines is obtained for controlling the laser. Alternatively, the bone ingrowth structure can be represented by hatch lines [8,148,149], in each layer, the lines are directly represented by the coordinates of their ends. Bone ingrowth structures in .stl format or represented by hatched lines do not need large amounts of computer memory.

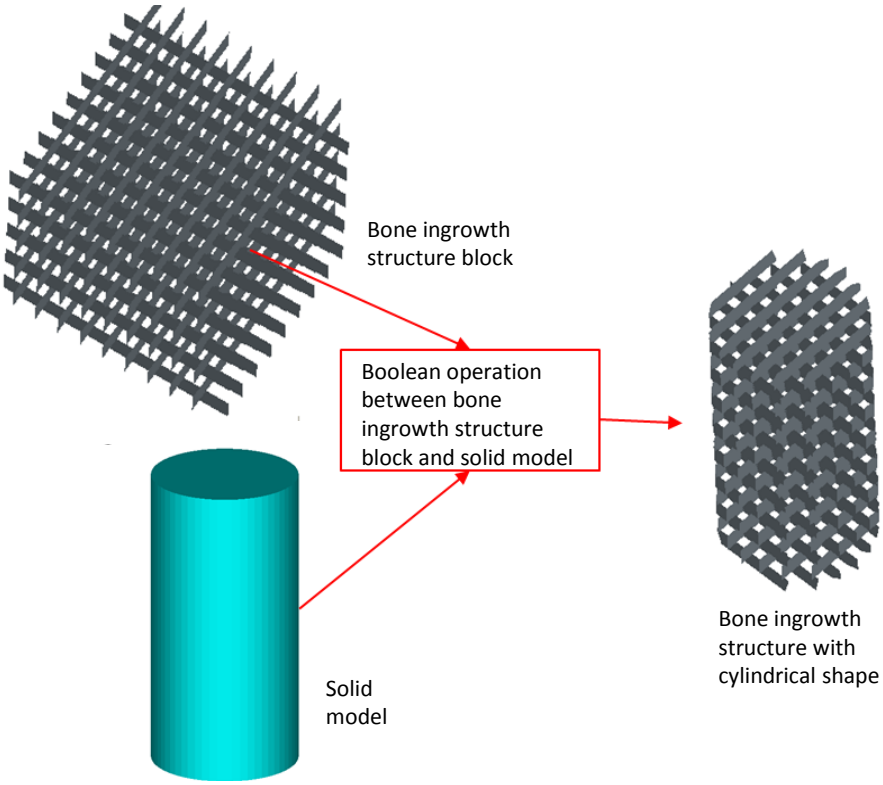

Figure 2-30 Based on the method provided by Stamp et al [8], a bone ingrowth structure is created by hatch lines and achieves a desirable shape by using a Boolean operation between itself and the solid model.

Stamp et al [8] carried out experiments using platelet based bone ingrowth structures (beam overlap) to investigate their compressive strength and porosity. This structure (Figure 2-31) was made of CpTi and fabricated by SLM. By altering the hatch distance in the x and y directions, structures with variation in porosity and compressive strength were created as shown in Figure 2-32. Considering the minimum porosity (65%) and minimum compressive strength (35MPa) requirement,

a property map was created. As compared with the range of available properties for the bone ingrowth structure with struts, the platelet based structure is stronger for a similar porosity but has a much larger cell size. However this platelet based structure is more anisotropic in behaviour [8].

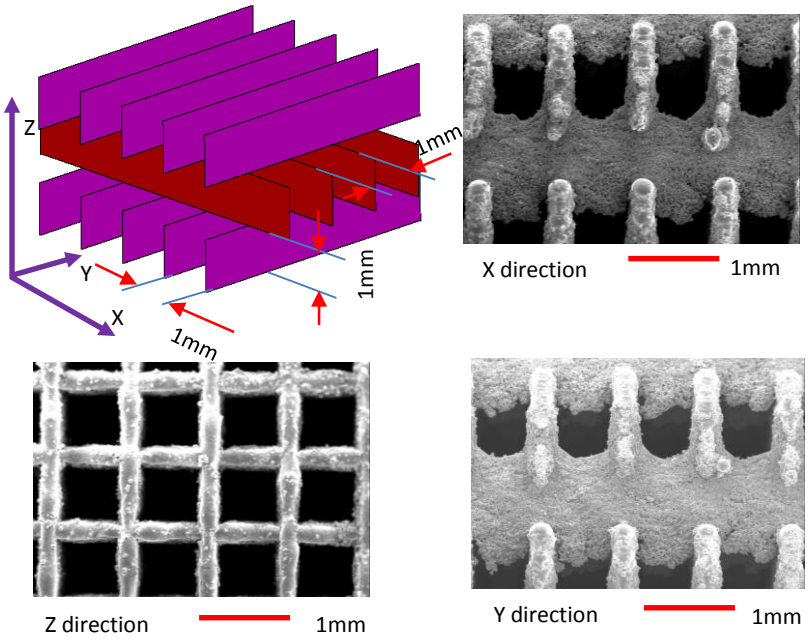

Figure 2-31 Based on the method provided by Stamp et al [8], a bone ingrowth structure (CpTi) was fabricated on a SLM Realizer 100.

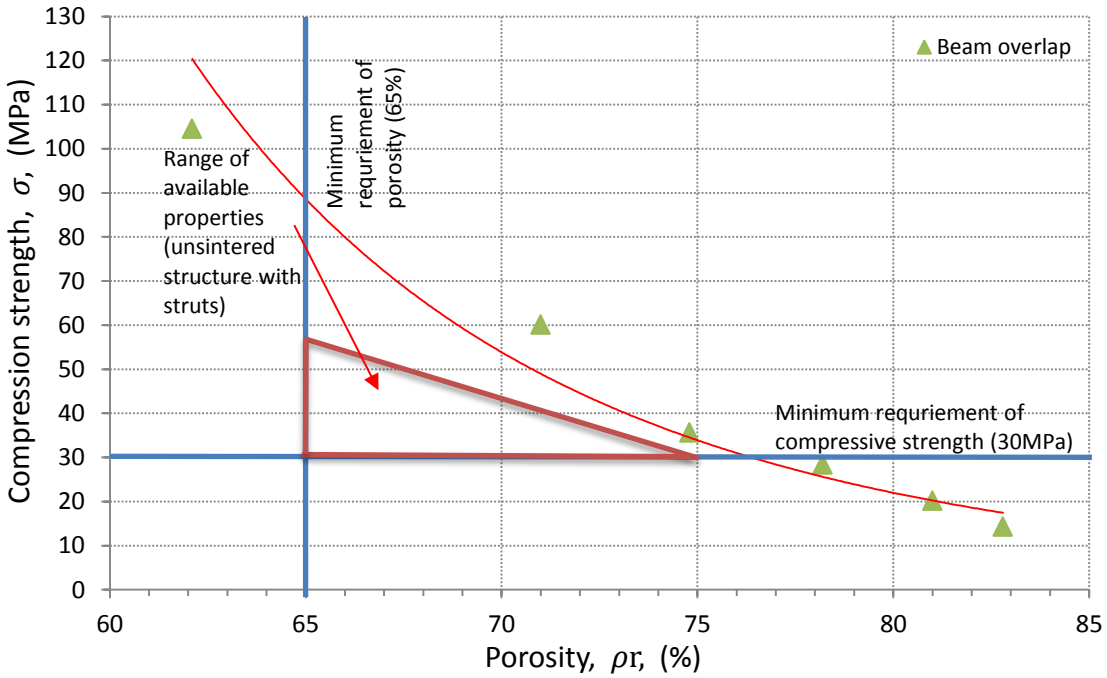

Figure 2-32 The range of mechanical properties of platelet based structure (beam overlap) and strut based structure [149].

2.5.2. CAD Technologies to Resemble the Appearance of Human Cancellous Bone

Based on the surgeon panels that Stryker carried out on the bone ingrowth structures in orthopaedic applications, bone ingrowth structures with similar appearance to cancellous bone are preferred [99]. CAD technology was developed at the University of Liverpool to create a structure that mimics the appearance of cancellous bone [9]. The bone ingrowth structure was created with struts as described previously except that the ends of the struts were moved randomly from their original location. This bone ingrowth structure was termed a randomised unit cell structure. In order to randomise the distribution of the struts, a pseudo-random function was imported into the software. As shown in Figure 2-33, by combining the randomised move direction and distance from the original points, the ends of the struts were translated to new positions [9]. Figure 2-34 shows the resultant material which has a similar appearance to cancellous bone. The compressive strength of the material is reported to be no more than 55MPa at 62% porosity and no further information has been released to show if it is isotropic in behaviour [9].

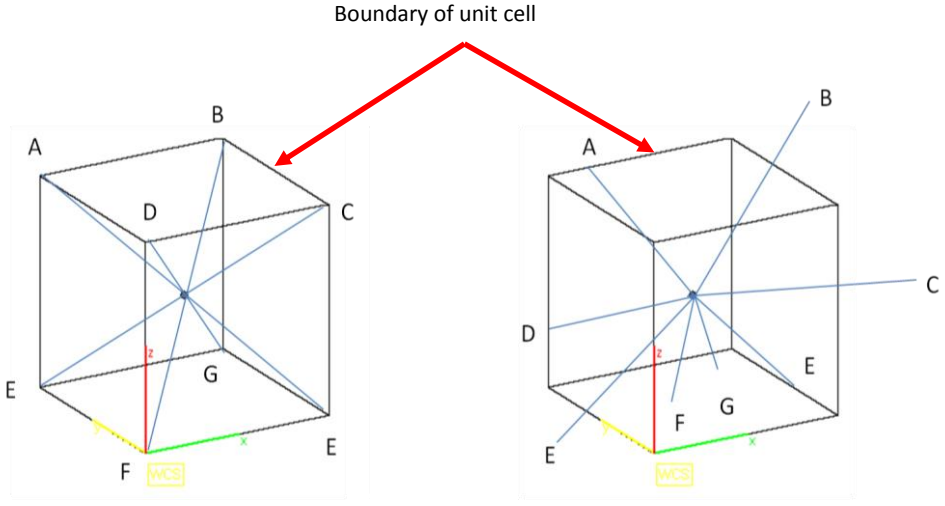

Figure 2-33 Based on the description in Brooks' PhD thesis [152], an Illustration of struts in the unit cell before randomisation (Left) and after randomisation (right) was made.

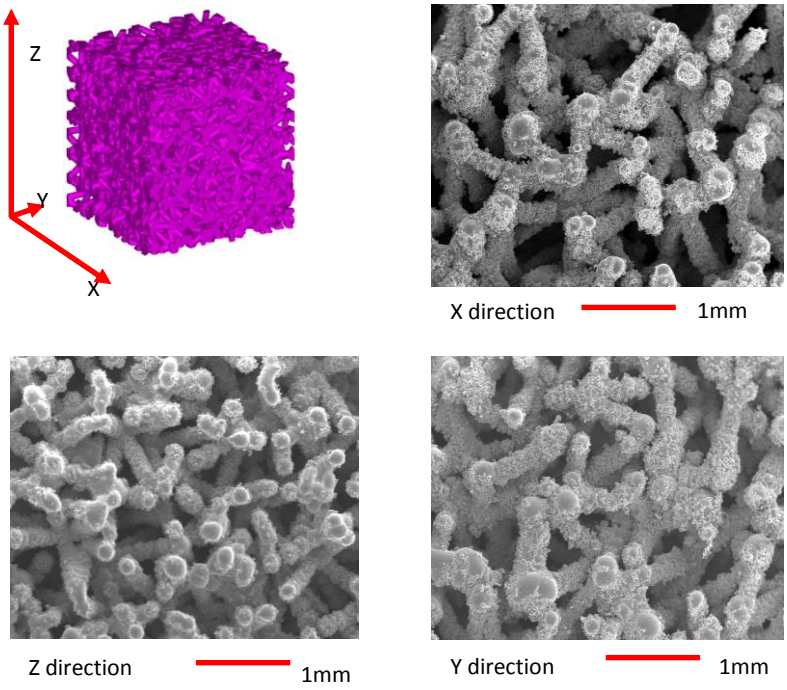

Figure 2-34 Based on the method provided by Stamp [95], a randomised unit cell structure (CpTi, cell size 600µm, randomisation percentage -30% to 30%, octahedral structure) was fabricated by SLM and its SEM image viewed in x, y and z directions.

One problem with this randomising function is that it produces a different structure each time it runs. As illustrated in Figure 2-35 and Figure 2-36, a randomised unit structure has been created six times with same parameters and as can be seen, the randomised unit cell structure is different each time. This problem affects the predictability of the properties of the randomised unit cell structure and the validation of this process in a clinical application.

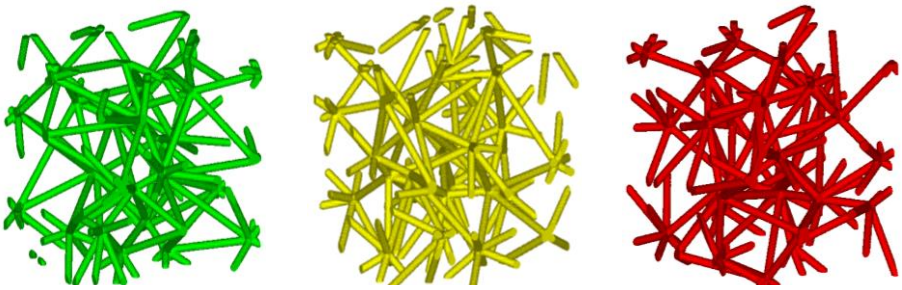

Figure 2-35 Based on the randomisation method provided by Brooks [152], a randomised unit cell structure (cell size 2mm, randomisation percentage -30% to 30%, octahedral structure) was generated by his software with the same parameters three times.

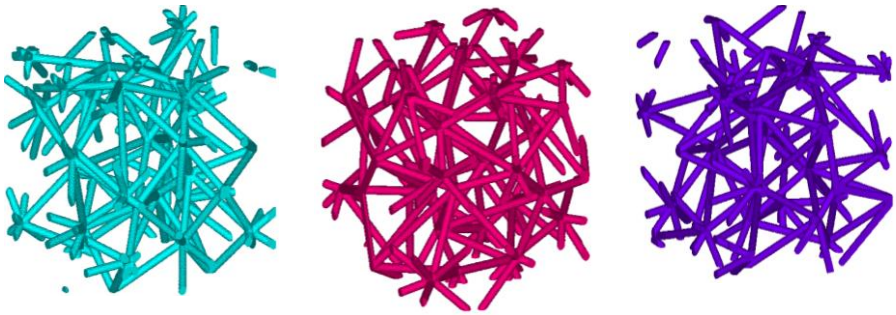

Figure 2-36 Based on the randomisation method provided by Brooks [152], a randomised unit cell structure (cell size 2mm, randomisation percentage -30% to 30%, octahedral structure) was generated by his software with the same parameters three times.

2.5.3. CAD Technologies for Slicing Bone Ingrowth Structures

The above literature review shows that bone ingrowth structures use various constructive elements such as hatch lines, triangles and closed and continuous surfaces. Correspondingly, various CAD technologies have been developed for slicing these bone ingrowth structures. In the following section these slicing methods are summarised based on the type of CAD model surface.

Slicing CAD Models with Closed Surfaces

These methods [153–156] generate slicing data directly from the original CAD model whose closed surface is represented by various methods, including boundary representation and constructive solid geometry representation. Direct slicing of CAD models was implemented first using Parasolid CAD software and user-defined routines by Jamieson and Hacker, the parts being modelled using a boundary representation [155]. Guduri et al. achieved exact contours by slicing the Constructive Solid Geometry (CSG) representation [153], which allows the modeller to create a complex surface or object by using Boolean operations to combine objects. Vuyyuru et al. obtained NURBS-based contour curves by directly slicing a solid model created in I-DEAS Software and segmented the curves using both the chordal tolerance method and the angular deviation of the tangent vector method [154]. Direct slicing of the original CAD model avoids the approximation errors resulting from tessellation. However as shown in Figure 2-37, the closed and continuous sliced contour must be approximated by a set of segments in order;

otherwise it cannot be recognized by the AM machine. In some cases, the original CAD model is converted into a .stl file and its sliced contour can be used directly without approximation.

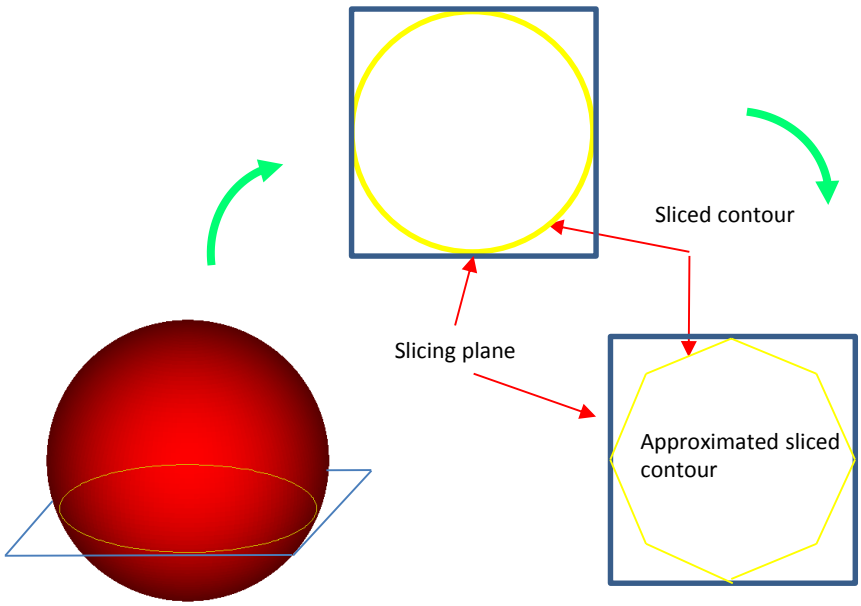

Figure 2-37 Illustration of original CAD model with closed surface was sliced and its sliced contour was approximated by segments in order for AM fabrication.

Slicing CAD Models with Open Surfaces

As discussed, struts are represented by their end coordinates rather than by closed surfaces, when they are used for constructing a bone ingrowth structure. In order to be fabricated by selective laser melting, Brooks [152] developed a method to slice this bone ingrowth structure with struts [151] producing a set of spots where the slice cuts the struts. When the struts are fabricated by SLM, the laser beam is positioned at the co-ordinates of the dots and the powder melted for a specified exposure time at set power. However as shown in Figure 2-35, the sliced spots on slicing planes A and B are different with the sliced spots on slicing plane B being very close to each other. When laser scanning onto spots that lie on slicing plane B, the average energy density on the bed is significantly increased and more powder

particles are melted and giving a larger solid block. It indicates that when designing a slicing method the fabrication mechanism should also be considered.

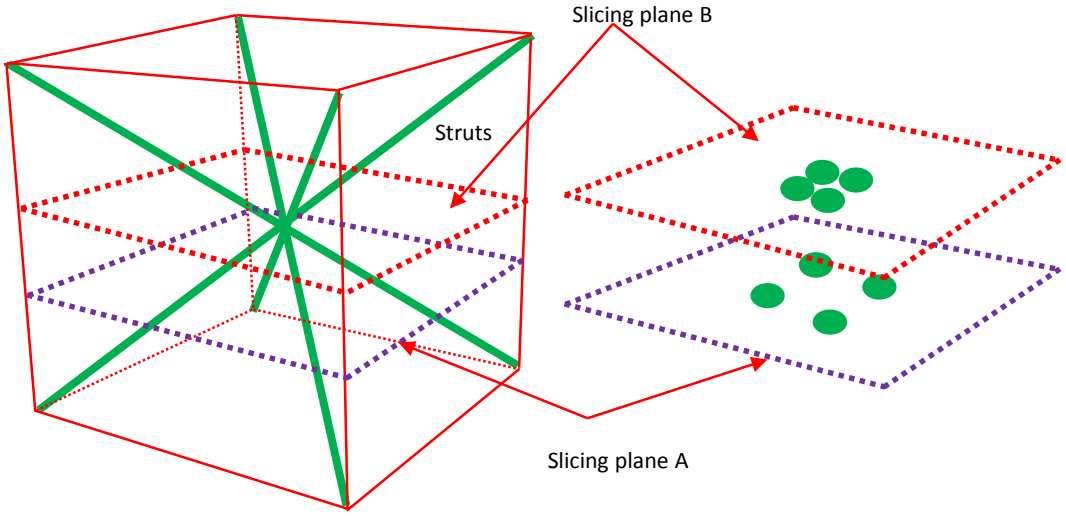

Figure 2-38 Illustration of struts in unit cell is sliced by different slicing planes based on the description in Brooks' PhD thesis [152].

2.5.4. Summary of CAD Technologies for Creating Bone Ingrowth Structures for AM Fabrication

As discussed above, bone ingrowth structures should be constructed from open and surfaces so as to reduce the requirement for computer memory to allow the construction and fabrication of more complex bone ingrowth structures with the same computing power. Comparing the possible range of properties of bone ingrowth structures fabricated with struts compared to platelets, it appears that bone ingrowth structures with platelets can provide an enlarged range of mechanical properties for similar porosity and cell size. A preferred bone ingrowth structure must have a similar appearance of cancellous bone; a CAD technology is required to create this type of structure. Finally a corresponding slicing method needs to be developed to enable AM fabrication of these structures.

2.6. Mathematical Tools for Geometry Manipulation

CAD design was performed with software that included geometric tools (mathematical tools). These geometric tools include the methods for expressing straight segments, triangles and planes and for computing the intersection between

segments, triangles and segments to triangles. Assistant tools are also discussed for checking the relative position between triangles, points to a solid model and straight segments to a solid model as well as the triangulation of polygons when involved in computing triangle intersection.

2.6.1. Straight Segment Triangle and Plane

A segment can be represented by equation (2-1) [157].

$$Pt = P_0 + t(P_1 - P_0) \qquad (2\text{-}1)$$
$$0 \leq t \leq 1$$

Where Pt is any point on the segment and P_0 and P_1 are the end points of the segment and t is a parameter defining the point position on the segment. When t is equal to 0 or 1, the point Pt is located at one end of the segment. The expanded form of equation (2-1) is shown in equation (2-2).

$$\begin{bmatrix} Pt_x \\ Pt_y \\ Pt_z \end{bmatrix} = \begin{bmatrix} P_{0x} \\ P_{0y} \\ P_{0z} \end{bmatrix} + t \begin{bmatrix} P_{1x} - P_{0x} \\ P_{1y} - P_{0y} \\ P_{1z} - P_{0z} \end{bmatrix} \qquad (2\text{-}2)$$
$$0 \leq t \leq 1$$

The triangle, a basic element for representing the VS surfaces is defined by its three non-collinear points V_0, V_1 and V_2. The parametric form of a triangle is described in equation (2-3) [157].

$$VP = V_0 + u(V_1 - V_0) + v(V_2 - V_0) \qquad (2\text{-}3)$$
$$0 \leq u \leq 1, 0 \leq v \leq 1 \; and \; u + v \leq 1$$

Where VP is any point on the triangle. V_0, V_1 and V_2 are the vertices of the triangle. u and v are the parameters specifying the point position on the triangle. For example when $u = 0$ and $v = 1$, the point VP is located on edge of the triangle. The expanded form of equation (2-3) is represented in equation (2-4).

$$\begin{bmatrix} V_x \\ V_y \\ V_z \end{bmatrix} = \begin{bmatrix} V_{0x} \\ V_{0y} \\ V_{0z} \end{bmatrix} + u \begin{bmatrix} V_{1x} - V_{0x} \\ V_{1y} - V_{0y} \\ V_{1z} - V_{0z} \end{bmatrix} + v \begin{bmatrix} V_{2x} - V_{0x} \\ V_{2y} - V_{0y} \\ V_{2z} - V_{0z} \end{bmatrix} \quad (2\text{-}4)$$

$0 \le u \le 1, 0 \le v \le 1 \; and \; u + v \le 1$

A plane is defined by equation (2-5) [157].

$$Ax + By + Cz + d = 0 \quad (2\text{-}5)$$

$A^2 + B^2 + C^2 = 1$

Vector of plane normal $\vec{N} = [A, B, C]$

$d = -\vec{N} \cdot (x, y, z)$

Where (x, y, z) defines any point on the plane.

2.6.2. Intersection Test between Straight Segment and Plane

By substituting equation (2-2) into equation (2-5), we can test if any point on the segment lies on the plane,

$$A(P_{0x} + t(P_{1x} - P_{0x})) + B(P_{0y} + t(P_{1y} - P_y)) + C(P_{0z} + t(P_{1z} - P_{0z})) + d = 0 \quad (2\text{-}6)$$

$d = -\vec{N} \cdot (x, y, z)$

and solve for parameter t:

$$t = \frac{-(AP_{0x} + BP_{0y} + CP_{0z} + d)}{A(P_{1x} - P_{0x}) + B(P_{1y} - P_y) + C(P_{1z} - P_{0z})} \quad (2\text{-}7)$$

$d = -\vec{N} \cdot (x, y, z)$

Because the dot product of two vectors $\vec{N}$ and $[P_{0x}, P_{0y}, P_{0z}]$ and the dot product of two vectors $\vec{N}$ and $\left[(P_{1x} - P_{0x}), (P_{1y} - P_y), (P_{1z} - P_{0z})\right]$ are defined as follows:

$AP_{0x} + BP_{0y} + CP_{0z} = \vec{N} \cdot P_0$

$A(P_{1x} - P_{0x}) + B(P_{1y} - P_y) + C(P_{1z} - P_{0z}) = \vec{N} \cdot (P_1 - P_0)$

the parameter t can also be represented by a vector equation as shown:

$$t = \frac{-(\vec{N} \cdot P_0 + d)}{\vec{N} \cdot (P_1 - P_0)} \quad (2\text{-}8)$$

$$d = -\vec{N} \cdot (x, y, z)$$

However t must be in the range of 0 to 1 for the point to be on the segment and hence must be true for the intersection to exist. By substituting equation (2-8) into equation (2-1), the intersection P between segment and plane can be determined .

2.6.3. Intersection Test between Segments

Suppose there are two segments, represented by following equations (2-9) and (2-10).

$$Pt0 = P_{00} + t0(P_{01} - P_{00}) \quad (2\text{-}9)$$

$$0 \leq t0 \leq 1$$

$$Pt1 = P_{12} + t1(P_{13} - P_{12}) \quad (2\text{-}10)$$

$$0 \leq t1 \leq 1$$

For the point to be the intersection of the segments then it must be the same point and therefore:

$$P_{00} + t0(P_{01} - P_{00}) = P_{12} + t1(P_{13} - P_{12}) \quad (2\text{-}11)$$

$$0 \leq t0 \leq 1 \; and \; 0 \leq t1 \leq 1$$

The expanded form of equation (2-11) is expressed by equation (2-12).

$$\begin{bmatrix} P_{00x} \\ P_{00y} \\ P_{00z} \end{bmatrix} + t0 \begin{bmatrix} P_{01x} - P_{00x} \\ P_{01y} - P_{00y} \\ P_{01z} - P_{00z} \end{bmatrix} = \begin{bmatrix} P_{12x} \\ P_{12y} \\ P_{12z} \end{bmatrix} + t1 \begin{bmatrix} P_{13x} - P_{12x} \\ P_{13y} - P_{12y} \\ P_{13z} - P_{12z} \end{bmatrix} \quad (2\text{-}12)$$

$$0 \leq t0 \leq 1 \; and \; 0 \leq t1 \leq 1$$

When equation (2-12) is solved, values for $t0$ and $t1$ can be found. If $0 \leq t0 \leq 1$ and $0 \leq t1 \leq 1$, the intersection between the segments exists. By substituting a value for $t0$ into equation (2-9), the intersection can be found.

2.6.4. Intersection Test between Segment and Triangle

The basic method to find the intersection between a segment and a triangle is to find the intersection between the segment and the plane where the triangle lies. A further test is then required to ascertain whether it is located inside the triangle. By using a method similar to that above for a segment and a plane, the intersection test between a segment and a triangle can be simplified and can be found by substituting equation (2-2) into equation (2-4) to determine if a point exists that is both within the triangle and on the segment:

$$\begin{bmatrix} P_{0x} \\ P_{0y} \\ P_{0z} \end{bmatrix} + t \begin{bmatrix} P_{1x} - P_{0x} \\ P_{1y} - P_{0y} \\ P_{1z} - P_{0z} \end{bmatrix} = \begin{bmatrix} V_{0x} \\ V_{0y} \\ V_{0z} \end{bmatrix} + u \begin{bmatrix} V_{1x} - V_{0x} \\ V_{1y} - V_{0y} \\ V_{1z} - V_{0z} \end{bmatrix} + v \begin{bmatrix} V_{2x} - V_{0x} \\ V_{2y} - V_{0y} \\ V_{2z} - V_{0z} \end{bmatrix} \quad (2\text{-}13)$$

$$0 \leq t \leq 1$$

$$0 \leq u \leq 1, 0 \leq v \leq 1 \; and \; u + v \leq 1$$

By solving equation (2-13), $t, u,$and v can be found. If $0 \leq u \leq 1, 0 \leq v \leq 1, u + v \leq 1$ and $0 \leq t \leq 1$, then the intersection point is within the triangle. Finally by substituting t into equation (2-1), the intersection point can be found.

2.6.5. Intersection Test between Triangles

The intersection between triangles cannot be directly determined by directly solving the equations for the triangles. Different strategies are used to calculate the intersection between triangles based on their relative positions including coplanar and non-coplanar. Their relative positions can be tested by the signed distance from each vertex to a plane based on equation (2-14) [158]:

$$r = N \cdot Pout + dm \quad (2\text{-}14)$$

$$dm = -Xpoint \cdot N$$

Where Xpoint is any point on the plane, r is the distance from the point Pout to the plane , N is the normalised vector of the plane, Pout is any point out of the plane.

The sign of r is positive if P is on the side of the plane toward which the normal points and negative if it is on the other side. If it is equal to zero, it is on the plane. Thus the signed distance from each vertex (U_0, U_1 and U_2) of triangle T_1 to plane π_2 on which triangle T_2(V_0,V_1 and V_2) lies can be found based on equations (2-15) to (2-18).

$$N_1 \cdot Xpoint + dn = 0 \quad (2\text{-}15)$$

$$N_1 = (U_1 - U_0) \times (U_2 - U_0) \quad (2\text{-}16)$$

$$dn = -N_1 \cdot U_0 \quad (2\text{-}17)$$

$$du_i = N_1 \cdot U_i + dn \quad (2\text{-}18)$$

N_1 is the normal vector to the plane on which the triangle lies

du_i is the signed distance from each vertex of the triangle to its corresponding plane

$i = 0,1,2$

At these stages, the relative position of the triangles can be tested by considering the following possibilities:

- If the results (value of du_i for the vertices) have the same sign (positive or negative), there is no intersection between triangles.
- If the results (value of du_i for the vertices) are zero, the triangles are co-planar.
- If the results (value of du_i for the vertices) have different signs, the intersection may exist.

At this stage the relative positions of the triangles must be determined and using the intersection tests detailed in the following section.

When the triangles are coplanar, one possibility is that one triangle is inside the other and the intersection will be the edges of the interior triangle. If not, the intersection between the triangles can be found by computing the intersections between the edges of the triangles. For all other cases, when there may be an

intersection, a further test is required by Möller's method [159]. As shown in Figure 2-39, the two planes on which the triangles lie intersect in a line L which intersects each triangle. The line L is clipped by the triangles into two segments. If there is overlap between these segments, the intersection between the triangles exists (Figure 2-39), otherwise it does not (Figure 2-40).

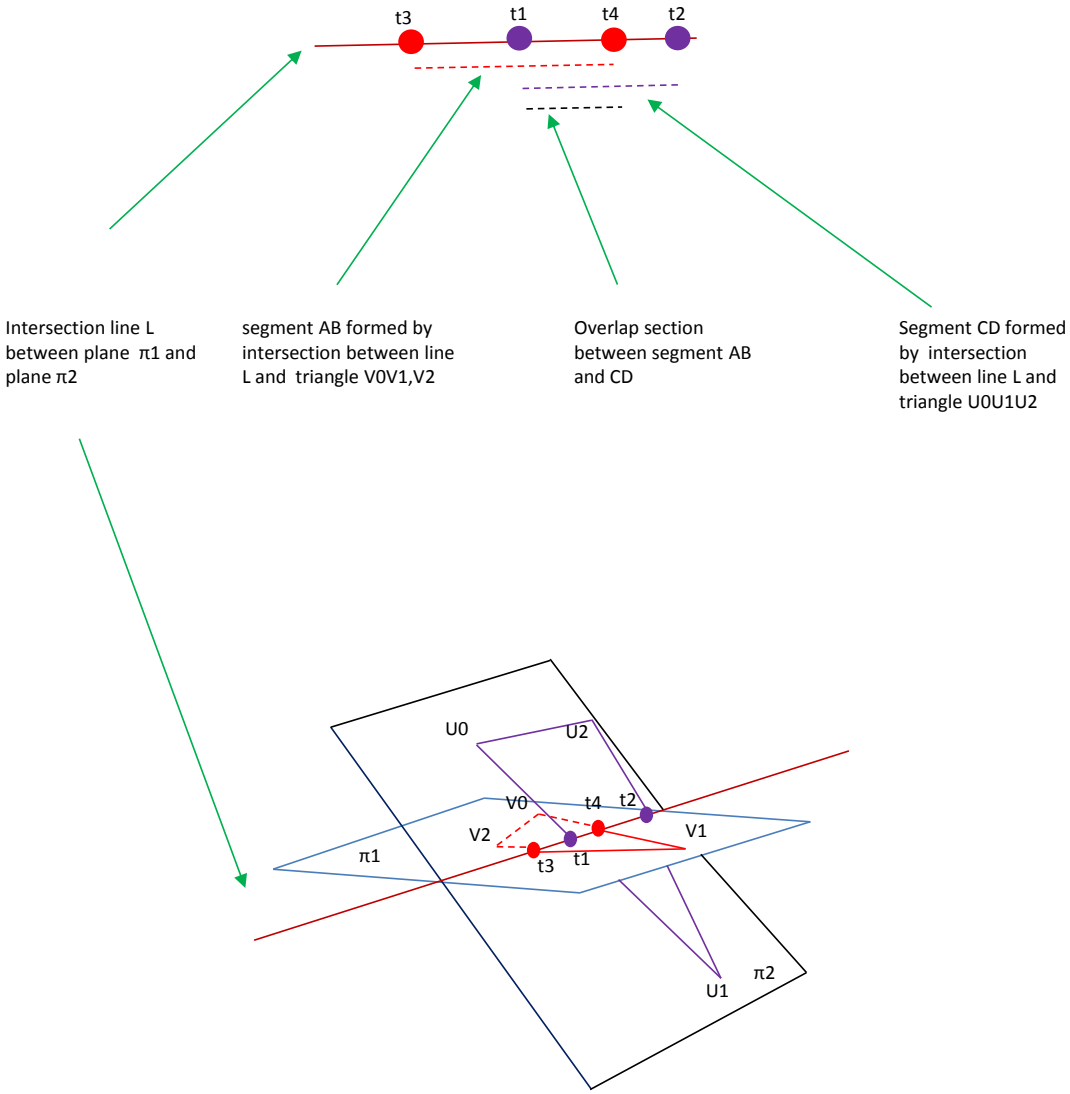

Figure 2-39 Illustration of triangles with intersections.

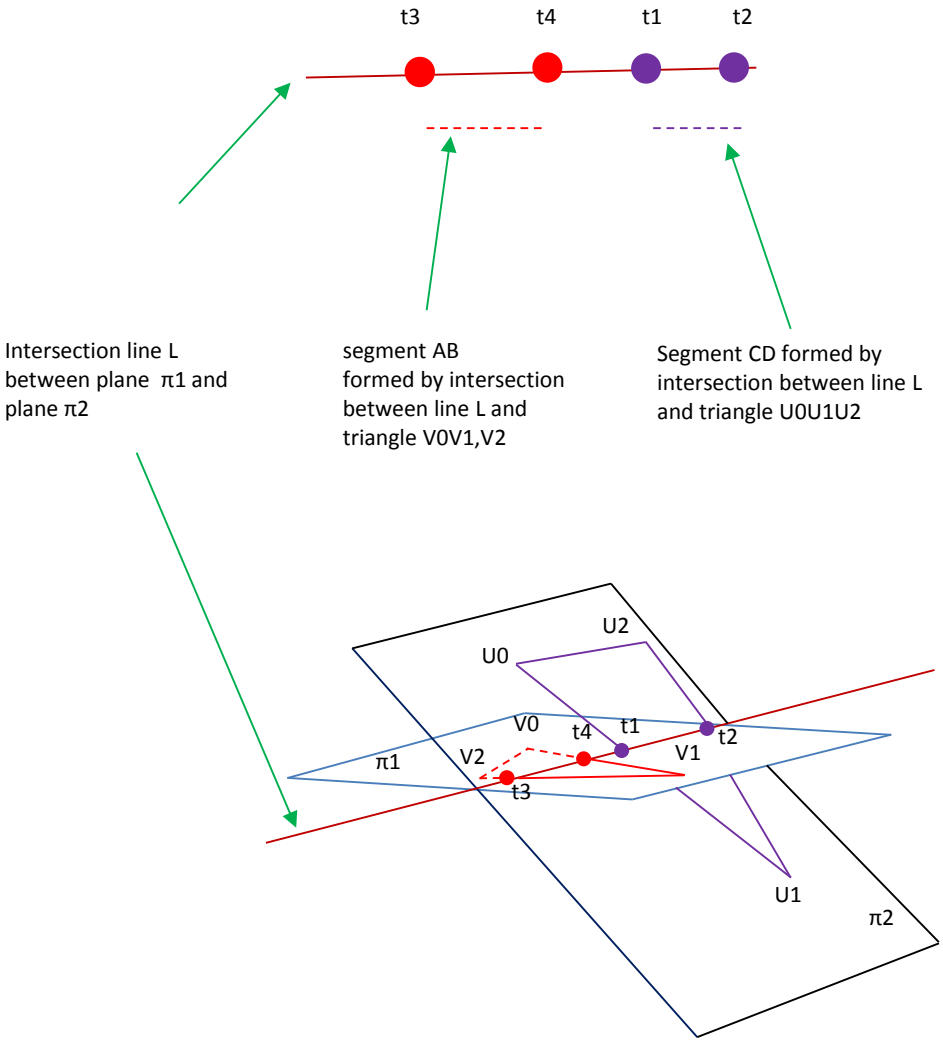

Figure 2-40 Illustration of triangles without intersections.

The intersections on line L can be found by their line parameters ($t1$, $t2$, $t3$ and $t4$) which can be determined by the use of similar triangles. In Figure 2-41, an example is given for computing the line parameter $t1$ based on equation (2-19) by the use of two similar triangles. Then the overlap section of the segments can be determined by the position of the line parameters on the line.

$$t1 = Pu_0 + (Pu_1 - Pu_0)\frac{d_{u0}}{d_{u0} - d_{u1}} \qquad (2\text{-}19)$$

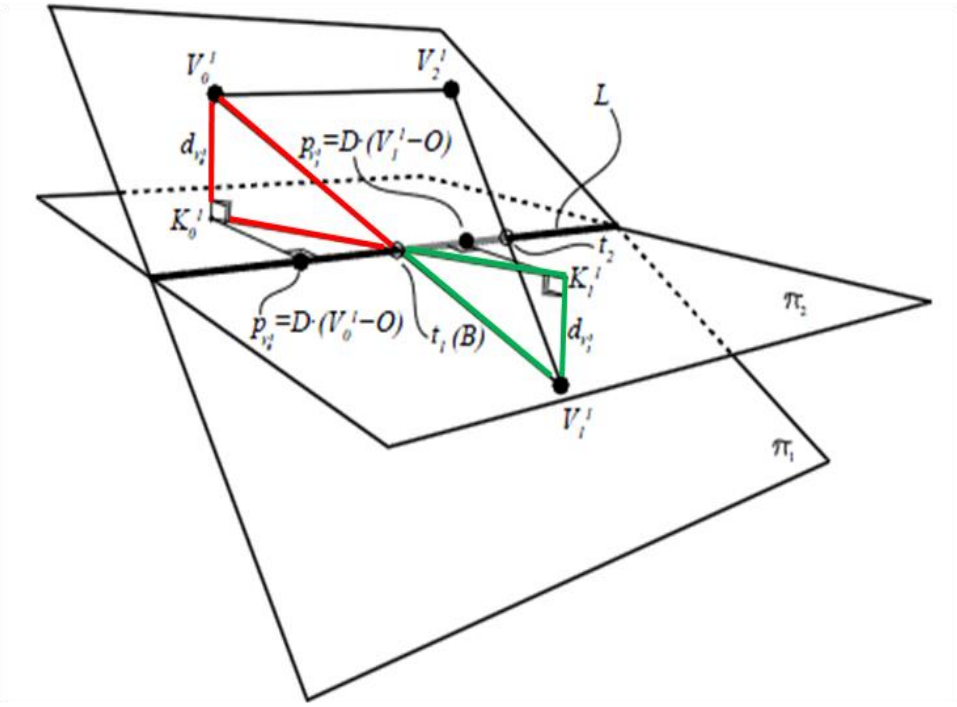

Figure 2-41 Two similar triangles marked in red and green are used for finding line parameter t1 [159].

Triangulation of Polygon

In practise, a polygon is formed by clipping one triangle with a number of others. In order to output a .stl file, any polygon needs to be triangulated. Triangulation of a polygon can be performed by using a fundamental algorithm in computational geometry. In this case, the polygon can be defined and simplified as a polygon with one boundary, without any internal holes and cannot self-intersect as seen in Figure 2-42.

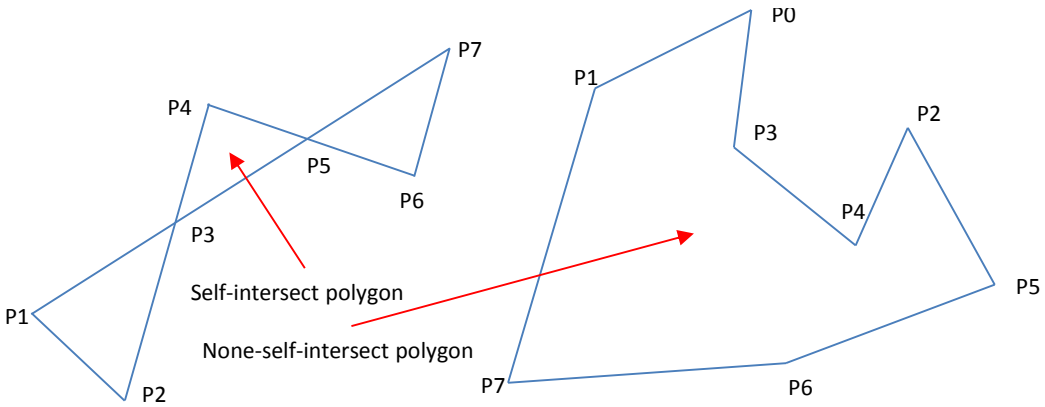

Figure 2-42 Illustration of self-intersect polygon and none-self-intersect polygon.

By implementing Seidel's algorithm [160], the polygon can be divided into trapezoids and triangles by an arbitrary ray from its vertices. Subsequently the trapezoids are subdivided by two triangles as shown in Figure 2-43 until the polygon is fully triangulated.

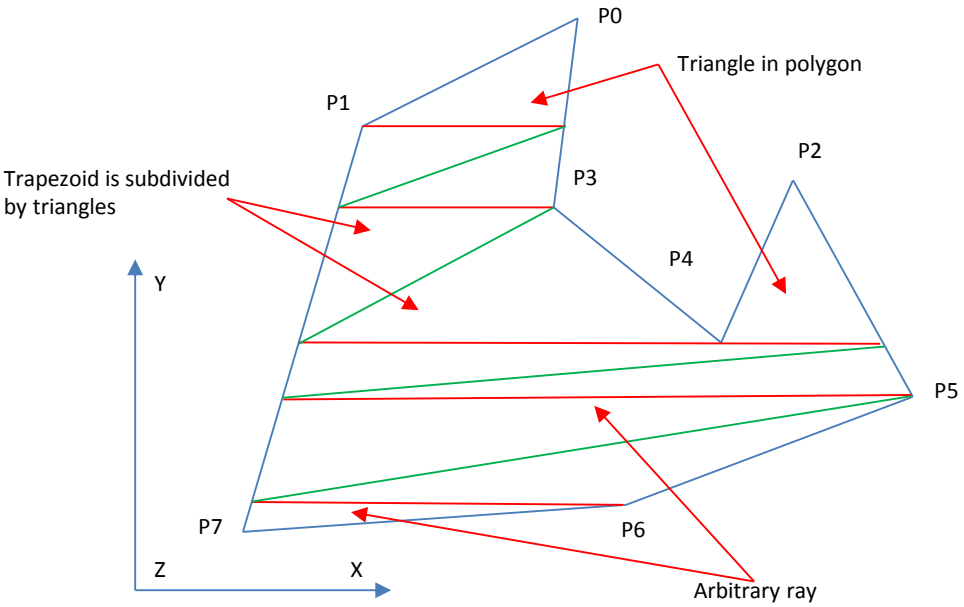

Figure 2-43 A polygon is divided by triangles and trapezoids which are subdivided by triangles.

2.6.6. Point in a Tessellated Solid Model Test

Haines [161] proposed a method termed "crossing number" to test whether a point is in a polygon or not. As shown in Figure 2-44, an arbitrary ray is generated from the test point with a direction n = (1,0). If the parity of the number of intersections between the ray and the polygon's boundary edge is odd (Case2), the test point is inside of the polygon, otherwise the point is outside the polygon (Case1).

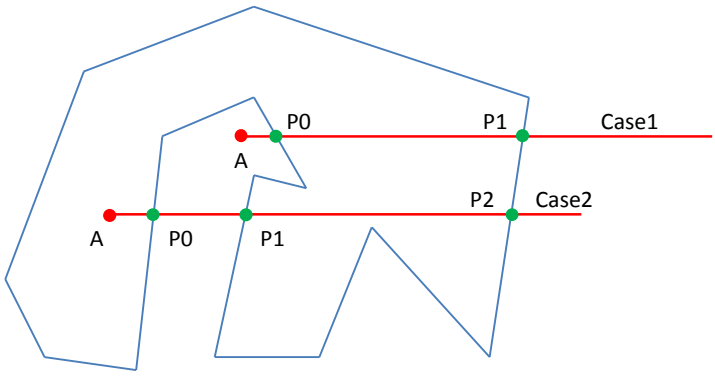

Figure 2-44 Based on the Eric Haines' method, an illustration was made for showing test points in or out of a polygon.

By extending this method from 2D to 3D, a point in a polyhedron test can be tested. However, the problem arises when the ray intersects the polyhedron at vertices or at edge points. In such cases, the parity of the number of intersections might not be correctly calculated. An example is given in Figure 2-45, where the number of intersections (A) is 1 and indicates that the test point P is inside of the solid model (its surface is tessellated by triangles) which is contradicted by its actual position.

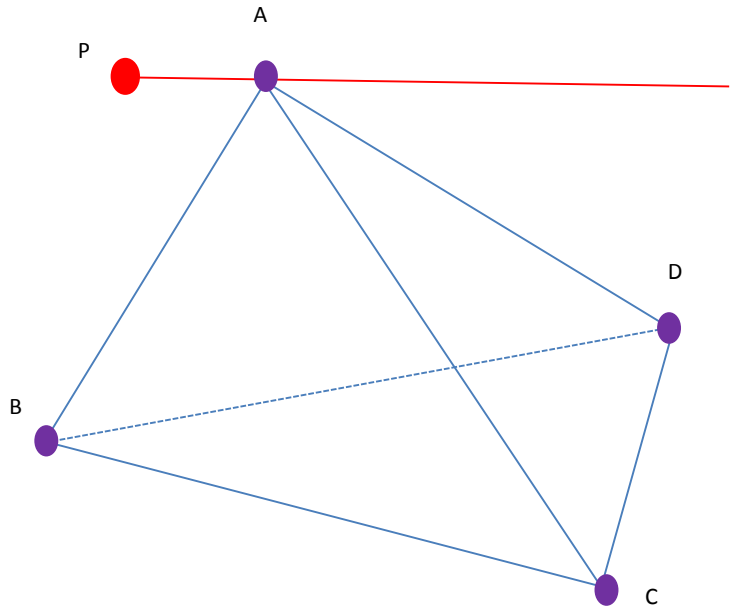

Figure 2-45 Illustration of an arbitrary ray from p intersecting with triangles (ABC, ACD and BAD) on their vertex A.

When the ray intersects at an edge point, the parity will have to be adjusted based on the local configuration (Figure 2-46) of the ray, the common edge and the faces sharing that edge. When the ray intersects at a vertex, the required test is to check whether the ray penetrates the polyhedron at the vertex or still remains in the same region. This can be done by selecting two points on the ray such that the points are located either side of the vertex. If both of them are either inside or outside, the parity is not changed otherwise it is toggled.

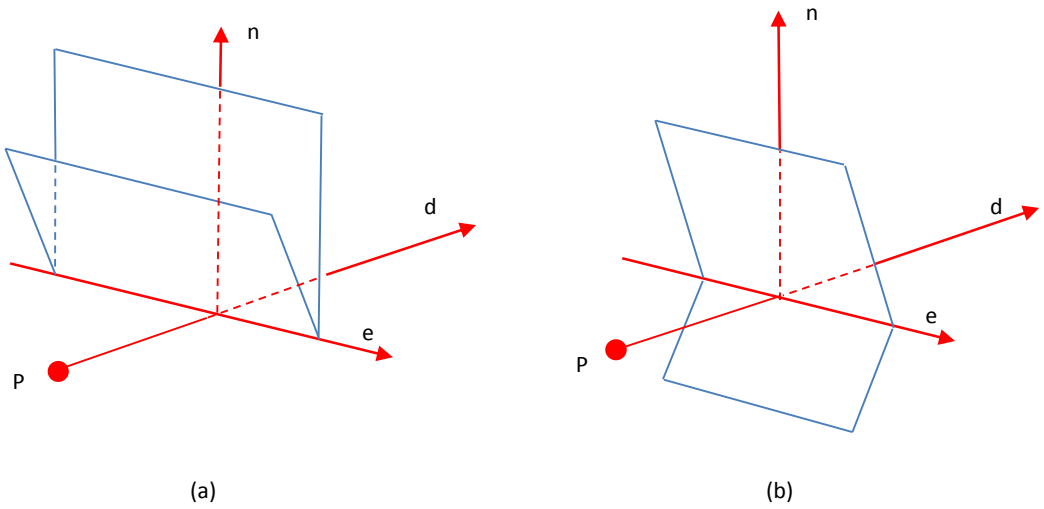

Figure 2-46 (a) The faces are on the same side of the plane formed by the edge and the ray. Parity is not changed. (b) The faces are on opposite sides. Parity is toggled [157].

2.6.7. Segment in a Tessellated Solid Model Test

In order to determine the sections of a segment that are within a tessellated solid model (Figure 2-47), an arbitrary ray is generated from the end of the segment. By checking the number of intersections between the ray and the polygon, the location of the first section can be determined. If the parity of the number of intersections is odd (Case1), the first section of segment is inside the polygon and the second section of the segment is outside the polygon and so on, and vice versa (Case2). Similarly, by extending the above method from a 2D polygon to a 3D solid model, the sections of segment can be tested. A similar issue exists in this method as discussed in section 2.6.6 and is solved similarly.

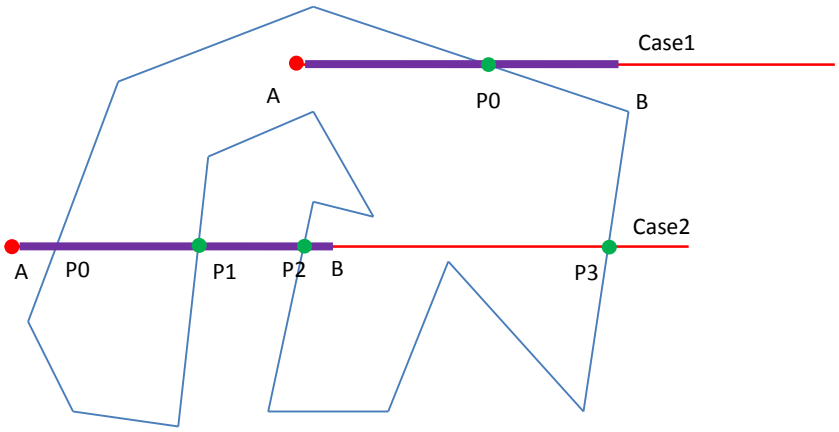

Figure 2-47 Illustration of testing various sections of a segment inside or outside of a tessellated solid model.

2.7. Fast Intersection Test Methods

In order to create a VS that has external shape, the VS block must be trimmed to a bounding .stl file. This process involves a large number of intersection tests between the triangles from the VS block and the triangles from the solid model surface. In order to reduce the computing time required for this process, a bounding box method is introduced, together with a fast testing technique to validate the box and triangle intersection method. Additionally, another method is provided to test the intersection between the triangle and sphere and this method is used to compute the pore size distribution of the structure. Both of the methods are detailed in the following section.

2.7.1. Bounding Box Method

A bounding box of a finite geometric object is a cuboid box with minimal volume that contains the object [162]. In order to illustrate this method, a triangle T_1 will be used for an intersection test among itself and a triangle T_2. Rather than implementing an intersection test between the triangles directly, the intersection test is carried out between the bounding box of the triangle T_1 and the triangle T_2. If there is no intersection between the triangle T_2 and the bounding box of the triangle T_1, there is no intersection between the triangle T_2 and the triangle T_1. The

intersection test between the triangle and the bounding box is carried out using the following method.

2.7.2. Fast Intersection Test Method on Box and Triangle

The Separating Axis Theorem (SAT) [163,164] is used to determine if two convex polyhedral A and B intersect by determining if they can be separated along either an axis parallel to a normal of a face of either A or B or along an axis formed from the cross product of an edge from A with and edge from B. Derived from this theorem, is the fast method developed by Möller [165] for testing the intersection between a triangle and an Axis-Aligned Bounding Box (AABB). An AABB is a bounding box with its edges parallel to the axes. To explain this method, an AABB and a triangle (Figure 2-48) are given. By checking whether there is overlap between the projections of AABB and the minimal AABB of the triangle on specified lines, the overlap between AABB and the triangle can be determined. These specified lines include the normal of the AABB (e0, e1 and e2), the two diagonal vertices whose direction is most closely aligned to the normal of the triangle and the lines determined by the cross product between the normal of the AABB and vectors (f1, f2 and f3) on the triangle. If there is no overlap between the projections of AABB and the minimal AABB of the triangle on each specified line, there is no intersection between AABB and the triangle.

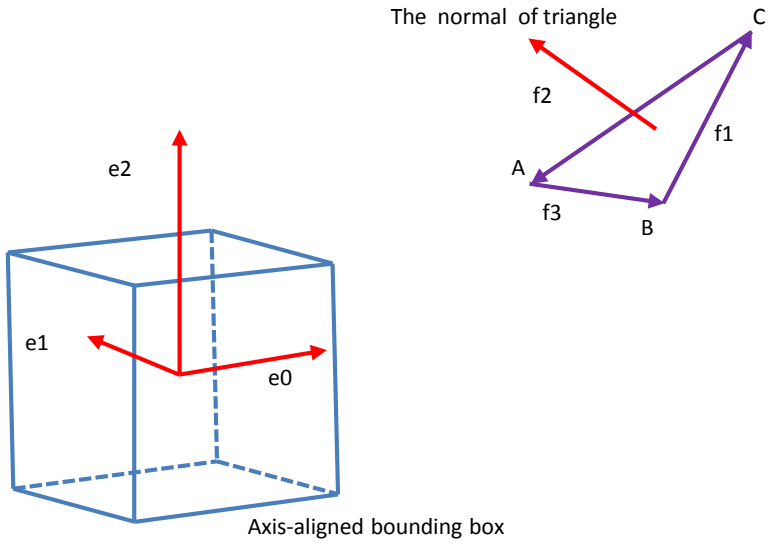

Figure 2-48 Notation used for the triangle and AABB overlap test.

2.7.3. Faster Intersection Test Method on Sphere and Triangle

Pore size distribution computing is another key function and it involves a large number of intersection tests between spheres and triangles. Ericson [166] provides a fast testing methodology for sphere and triangle intersection (Figure 2-49) based on the overlap test between the sphere and specified axes and can be summarised as following series of tests:

- Normal to the triangle plane.
- Perpendicular to AB through P.
- Perpendicular to BC through P.
- Perpendicular to CA through P.
- Through A and P.
- Through B and P.
- Through C and P.

If the outcome passes all of the above tests then there is no intersection between the sphere and triangle.

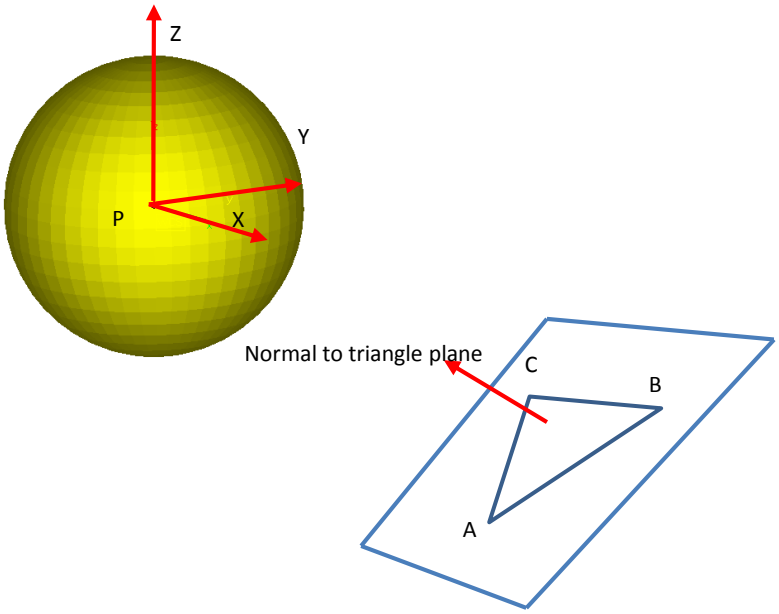

Figure 2-49 Notation used for triangle and sphere overlap test.

2.8. Summary

Orthopaedic implants can be fixed to host bone by bone cement or press fit interference technology. Both of these methods can provide a reliable and durable bond for specific patients varying in quality of bone, age and lifestyle. For the young, more active patients, fixation without bone cement is recommended and it relies on the porous structures on the implant surface, which allows the bone ingrowth. The limitation of conventional methods for fabricating bone ingrowth structure can be clearly shown with reference to the bone ingrowth requirements. These limitations may be overcome by using AM technology which provides more freedom to fabricate complex porosity with pre-defined pore size and geometry. Based on the literature review of the various AM technologies, it can clearly be seen that these technologies can be used to fabricate bone ingrowth structures if suitable CAD technologies can be developed. The review of the CAD technologies for AM indicates that the porous structure should be constructed as open surfaces such as platelets. Corresponding to these open platelets, specific methods should be developed to mimic the appearance of cancellous bone, trim the porous structure to a desirable shape and slice for AM fabrication.

According to the capability of AM technologies on various materials, specifically on metallic materials which may provide sufficient strength to resist pore deformation and give enough void space for bone ingrowth, the SLM technology was chosen for the development. With reference to previous research on SLM fabrication, the fabrication parameters have be developed for building the porous structure including wire frame structures and beam overlap etc. In this research, a new porous structure has been introduced and it is necessary to develop new fabrication parameters to build a qualified structure. The superior mechanical properties of this structure will be demonstrated by its larger range of available properties than that of current porous structures and its controllable isotropic behaviour. Its applications are illustrated by certain orthopaedic implants.

2.9. Research Aim and Objectives

The research aim for this project is to develop and test a new bone ingrowth structure that can enlarge the range of available properties for application in orthopaedics and which exhibits isotropic behaviour whilst resembling the appearance of cancellous bone. In order to achieve this aim, the following technical objectives must be met:

1. Software development
    a. Create a bone ingrowth structure with tessellated surface.
    b. Randomly deform surface of the bone ingrowth structure to resemble cancellous bone.
    c. Trim bone ingrowth structure block with the desired shape.
    d. Slice the bone ingrowth structure and output for SLM fabrication.
    e. Additional functions.
        - Computing porosity of bone ingrowth structure.
        - Computing pore size distribution of bone ingrowth structure.
        - Providing data exchange for various AMs machines.

2. Process parameter development.
    a. Laser focus.
    b. Laser power.
    c. Exposure time.

3. Testing
    a. Randomisation effect on resembling the appearance of cancellous bone.
    b. Thickness effect on the range of available properties.
    c. Hole size effect on the range of available properties.
    d. Cell size effect on the range of available properties.
    e. Aspect ratio effect on the isotropic behaviour.

4. Part production

a. Devise a new build file and output data.
b. Produce a range of typical orthopaedic implant for “show and tell”.

CHAPTER 3

METHODOLGY

In order to achieve the aim and complete the objectives set out in Chapter 2, a new bone ingrowth structure, termed “Vaulted Structure (VS)” is to be created using new custom software and fabricated by Selective Laser Melting (SLM). Thus this chapter initially sets out the software packages developed for design of the new custom software to create and characterise the VS. Then the technologies associated with SLM are detailed for fabricating VSs and finally a set of experimental methods are outlined for determining the properties of the manufactured structure.

3.1. Software Development Tools

Many functions in the custom software are provided by existing software packages. These software packages include a programming language package, a Graphical User Interface (GUI) programming package, a scientific computing package and a software distribution and maintenance package. In order to test the custom software, a PC performance profile package was imported as well. In the following section, each of these software packages is detailed.

Python was used as the programming language package because it is readily available, reasonably mature and provides access to many modules that handle diverse functions including the GUI and rendering of the 3D geometry, allowing the work to concentrate on the functional code rather than mundane tasks. The interpreter, standard and extensive library is available at http//ww.python.org/. Many third party modules, programs, tools and documents can be downloaded subject to the licence types. Python can use compiled modules that were originally written in C, C++ and Fortran. In this project, Python 2.7 was chosen as the programming platform because of its compatibility with the other packages required.

The Graphical User Interface (GUI) programming package was provided by PySide, which generates bindings to QT-based systems. QT is a cross-platform application framework that is widely used for developing application software with GUI. Because PySide (1.1.2) is compatible with Python 2.7 and open source [167], it was selected for this research.

Although MATLAB is the standard tool often used as a scientific computing package; it has a number of disadvantages, one being that it is under a commercial licence making it difficult and expensive to incorporate into any finished software. However Numpy is licensed under the Berkeley Source Distribution (BSD) license, enabling use with few restrictions [168]. Consequently Numpy 1.6.2 was chosen and it provides an extensive library for scientific computing functions that are used in the custom software design. It also provides a large library of mathematical functions for large, multi dimensional arrays and matrix operations, as well as offering random or pseudo-random number capabilities. These functions and capabilities accelerate data processing.

MATLAB also can be used to create 2D plots. It again suffers from the same problem as outlined above with cost and integration. Therefore the Matplotlib library (open source) was used as it provides the required features. The 3D computer graphics and visualization functions in the new custom software are provided by the Visualization Toolkit (VTK) which is an open source toolkit that provides visualization algorithms.

The PC performance, including CPU and memory usage, needs to be profiled when running functions in the new custom software. Although it is possible to use Python's built in function (time), the results are affected by other applications that may be running. In order to solve this issue, Psutil was used as it provides a function for retrieving information on all running processes and system utilization including CPU and memory in the Python environment.

In order to run the codes in a Microsoft Windows environment without directly installing Python 2.7 and the libraries (or modules), Py2exe (0.6.9) was used to build the code as a windows program application. This windows program application needs to be distributed and maintained during the life cycle. This maintenance can be carried out using a commercial software package such as Advanced Installer (free edition).

3.2. Solid Modelling Tools

In this research, the solid model was created and constructed as a closed and continuous surface. Then it was tessellated and converted to the .stl format, followed by any surface repair required before being orientated correctly. After this, the solid model with a tessellated surface was sliced and hatched for SLM fabrication. Alternatively the solid model surface was used to trim the VS block to the desired shape which was again sliced for SLM fabrication. Each of these actions involved the use of software packages that are detailed in the following sections.

For this research, Pro Engineer Wildfire 4 (university edition) was used to convert the solid model into the .stl format with specified deviation control including chord height and angle control. According to previous experience, the new chord height and angle control were set to 1/100 of the values (chord height and angle control) provided by Pro Engineer to minimise the loss of solid model surface geometry. Consequently the solid model was saved in .stl format and loaded into Magics (V9.5.4.7) software developed by Materialise. Using Magics, any solid model surface error caused by the conversion procedure could be repaired. Then the software was used to orientate the solid model and create support structures which are sliced and finally an .f&s file for use with the SLM machines was produced.

The MCP Realizer SLM machine has its own built-in software for slicing a solid model. It also provides functions including hatching layer contouring and the assignment of material files for generating the laser scan path and controlling laser parameters. All this information for fabricating a solid model is saved in the .f&s file.

The .f&s file path and the position of a solid model on the build platform of the SLM machine are saved in a .fas file.

3.3. Selective Laser Melting (SLM) Fabrication

The available equipment here was the MCP Realizer SLM 100 and SLM 250. The main differences between these machines are the maximum laser power and the size of the part building area. The SLM 250 has a maximum laser power of 200W (50W and 100W in the SLM 100), the higher laser power normally being used to reduce the fabrication time by reducing dwell time for the same energy input, or with the same dwell it creates a larger deeper melt pool. The build volume of the SLM 250 is up to 250mm × 250mm × 220mm (x,y,z) and for the SLM 100 is 120mm × 80mm (Ø, z). The larger maximum part building area allows more or larger parts to be fabricated at one time. The research carried out for this projection used a modified MCP Realizer SLM 100 and therefore the discussion of the methodology will refer specifically to this machine although the concept is similar to those produced by other manufacturers. The laser system in the modified SLM 100 was replaced by a 200W system in this machine to improve the fabrication time and allow the manufacture of a great range of materials. The only other modification was to the powder deposition system to produce powder layer of more consistent quality [138].

A digital solid model cannot be loaded into the SLM machine until it has been through a data processing system. Before fabrication, the powder particle size distribution must be suitable for the specified layer thickness, the output laser beam power must be calibrated and beam focus must be adjusted. Then the fabrication parameters are optimised. Once the build was finished, the used powder was recycled and a sample was cleaned for characterisation. These stages are described below.

3.3.1. Data Processing

To convert the digital model data into a form that can be used for fabrication is a complex process; parts of the process are carried out using either commercial or custom produced codes as shown in Figure 3-1. "Standard solid" (solid part) can be sliced and hatched directly using the built-in software. For more complex porous structures (porous part) however such as a lattice and VS, the structure must be generated, sliced and output as a .f&s file (detailed in APPENDIX A) by the use of specially developed software code. Once data is ready, the solid and the porous parts are merged and assigned a material file (detailed in APPENDIX B) by the Realizer built-in software. Finally the digital model is arranged on the platform and the output .fas file (detailed in APPENDIX C) is written for fabrication.

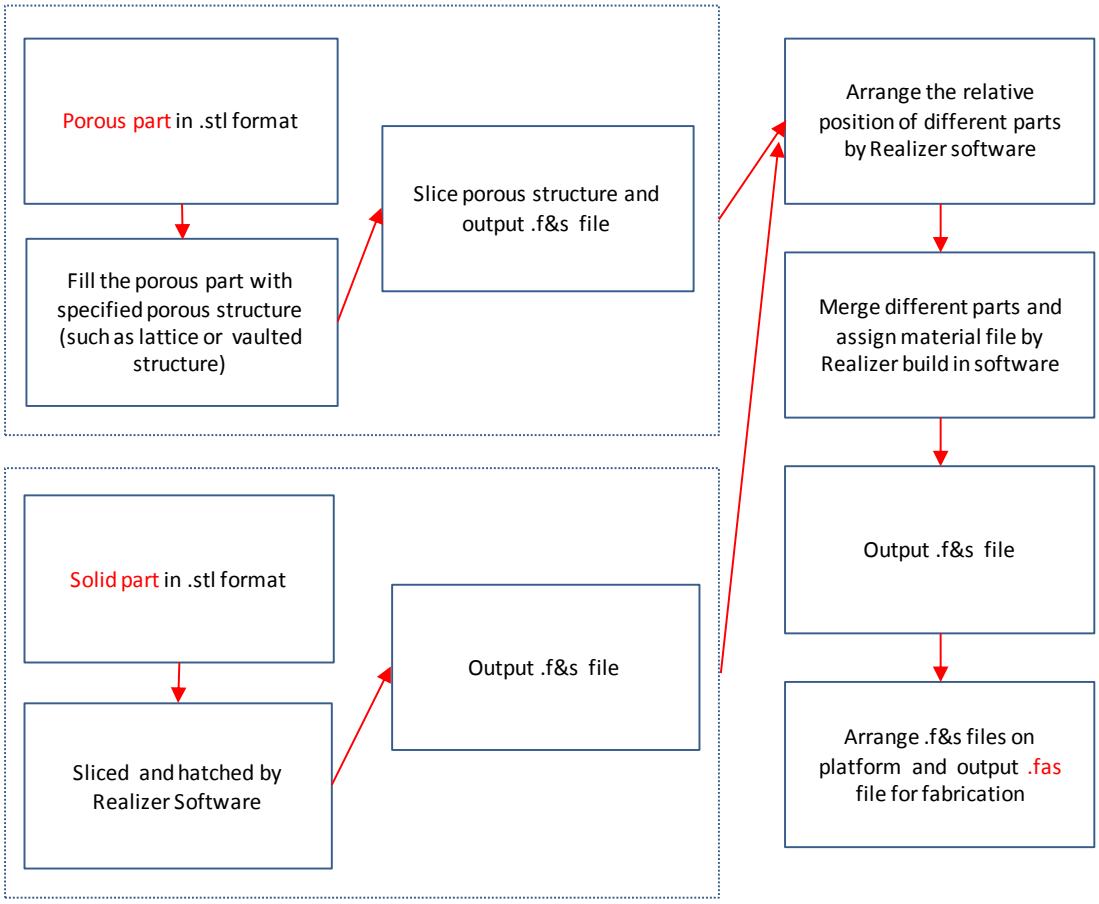

Figure 3-1 Data process for various parts of solid models in .stl format.

3.3.2. Manufacturing Equipment

In this research, an MCP Realizer SLM 100 (MTT Technologies, Renishaw, UK) was used for fabrication and detailed in Figure 3-2. Before the fabrication began, the enclosed chamber was filled with positive pressure argon. For both safety reasons and to avoid a negative effect on the build due to oxidation, the maximum oxygen level in the chamber needed to be below 0.2% which was monitored by a built in oxygen sensor. Once the oxygen concentration (< 0.2%) had been obtained, the fabrication started by deposition of the build powder onto the circular substrate (120mm) using a modified powder deposition mechanism.

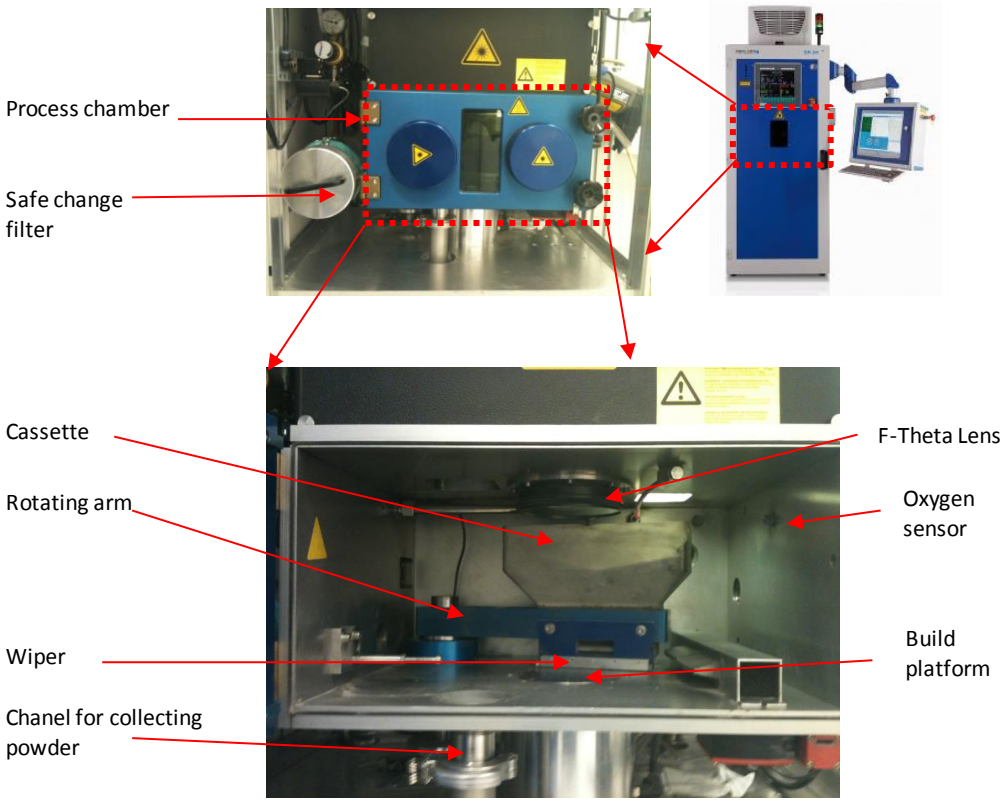

Figure 3-2 MCP SLM Realizer-100 machine details

This powder deposition mechanism is shown in Figure 3-3. A prototype cassette was manufactured by FDM (Dimension, USA) and was mounted on the rotating arm. The slider pushed against a pin attached to the chassis wall at either end of its travel. A series of slots on the slider transferred the powder from the cassette onto the substrate. The deposited powder was spread by the wiper blade to form a thin (50µm) layer, which was then selectively melted by an ytterbium fibre laser (200W,

CW, λ=1.07µm, IPG, De) under control of an optical system, with a positional accuracy up to +/-5µm. After one layer finished, the platform moved vertically downward by the specified layer thickness allowing the deposition of a further layer of powder. This process was repeated and the build fabricated layer by layer and any excess powder not in the build cylinder was collected in a container.

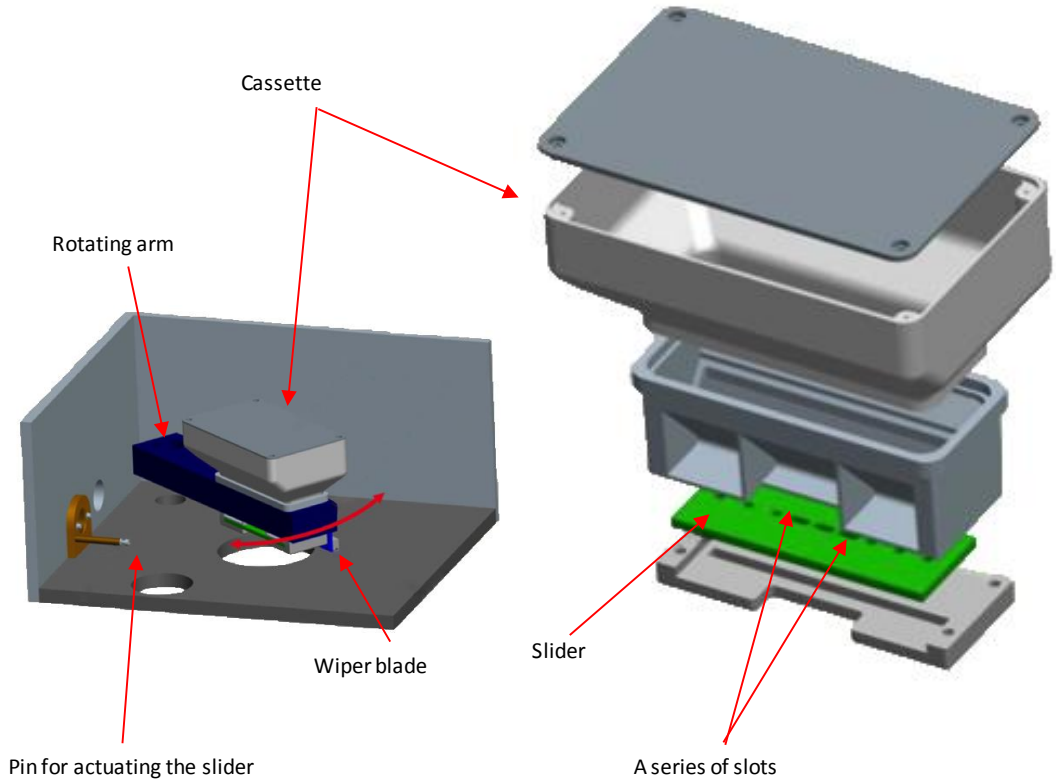

Figure 3-3 Powder Deposition Mechanism at the Realizer SLM100 [138].

The optical system is an important part of the SLM machine and has a significant effect on build quality. A schematic of the system used is shown in Figure 3-4. In this optical system, the laser beam passes through the beam focusing optics before being directed by two galvometers with reflection mirrors (Cambridge Technology, USA), it finally passes through a 250mm focal length F-Theta (Sill, De) to ensure a flat field at the image plane of the scanning system. The beam spot on the substrate is adjusted by the moveable expander lenses which are located between the laser beam and the galvanometer mirrors.

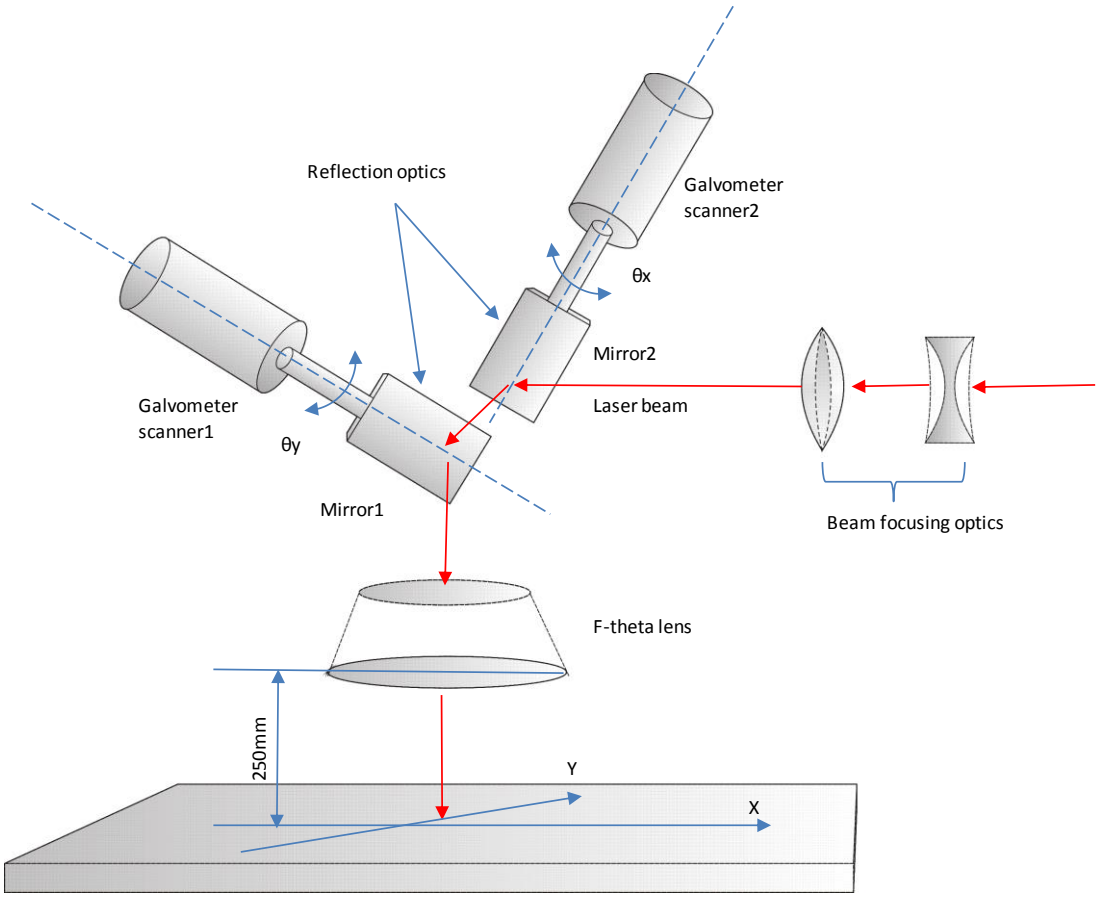

Figure 3-4 Schematic of optics system in SLM Realizer-100 [169].

As the process proceeds, the laser heats the metal powder. During this process, some of the metal is evaporated, and then condenses in the gas atmosphere and forms a nano powder. This nano powder in the atmosphere is circulated by a pump and trapped by the filter in the machine, which is changed regularly.

3.3.3. Calibration of Output Laser Beam Power

The laser beam output power after the F-theta lens can be altered by controlling the input current and then calibrating the laser power with a laser meter. In the calibration procedure, the focus and beam scanners are set on a specified position (x=0, y=0). For safety reasons, the calibration was carried out with a closed chamber, which was filled with argon, the oxygen level being below 0.2%. The recent calibration results were shown in Figure 3-5.

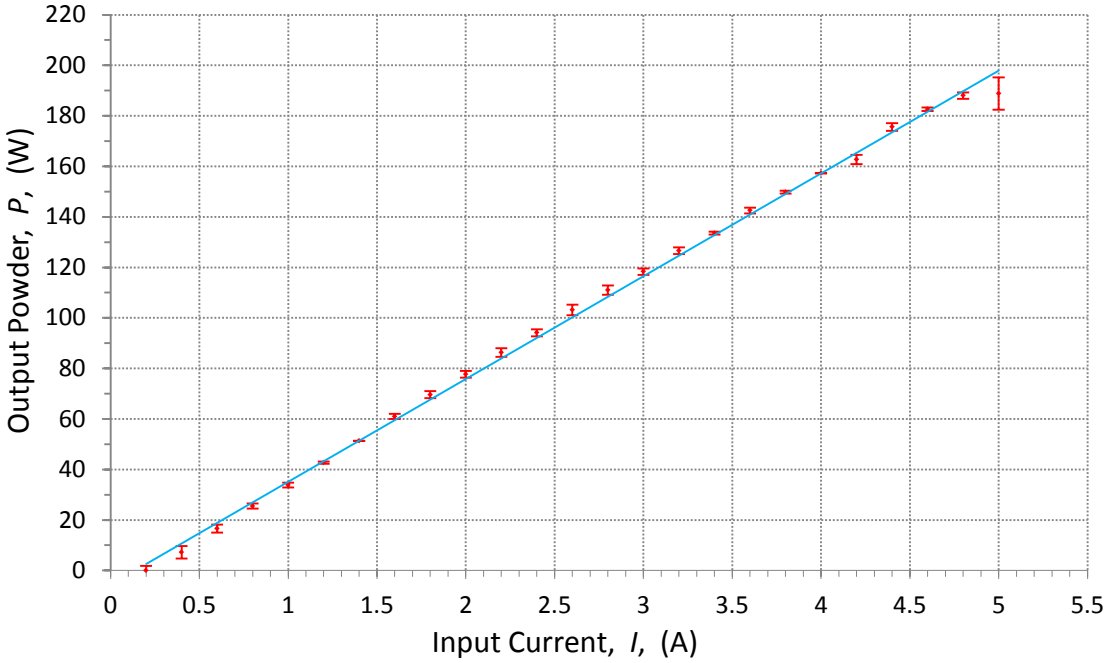

Figure 3-5 Input current with its correspondent output laser beam power measured by laser meter.

3.3.4. Determination of Laser Beam Focus

The laser energy density for any point where the laser dwells is defined by equation (3-1). However the MCP Realizer SLM 100 initially appears to scan lines rather than spots, but in reality the lines are constructed from many individual points, with the laser moving to a point before dwelling and then moving on to the next. It also has to be noted that the laser is on continuously during this process and therefore there is a small amount of additional energy that is absorbed by the bed due to the time required for the mirrors to stabilise after each movement. The effect of this extra energy is small unless the dwell time is very short. In many ways this extra energy can be seen as a minimum dwell time, so even if the dwell time was zero there would still be an actual dwell at each point. For the dwell times used here the effect is very small and can be ignored.

$$E_\rho = (P \times Exp)/\pi\omega^2 \qquad (3\text{-}1)$$

Where $\mathrm{E_\rho}$ the energy density of each spot ($\mathrm{J/mm^2}$), P is the applied laser power (W), Exp is the amount of the time (s) that laser is exposed to the powder bed, ω is the radius of the radius of the applied laser beam (mm).

The laser energy density is significantly affected by the radius of the laser beam and this is controlled by the position of the focal point relative to the powder bed. When the focus is above or below the bed the radius of the beam is increased giving a reduced power density [168] and thus it is important to control the beam radius to avoid unwanted changes in mechanical strength and part integrity. In Figure 3-6, it can be seen that the minimum spot size occurs when the focal point lies on the powder bed but by under or over focussing it can be increased by up to 1.4 times the waist diameter, by moving to either the upper or lower extremities of the raylength range. For the MCP Realizer system focussing is controlled by the relative positions of the beam expander optics and this is controlled by "laser focus position" in the Realizer software. The laser beam was scanned on to laser sensitive paper placed on the build platform using a low laser power (less than 5W), for various "laser focus positions". The shape of the spots generated on the laser sensitive paper changed from elliptical to circular and back to elliptical. Thus for these elliptical spots the spot size has to be defined by spot area rather than radius. The optimum laser focus position was found to be the smallest spot size as seen in Figure 3-7. To determine the smallest area the images on the laser sensitive paper were digitised and analysed using the public domain image analysis software, ImageJ. This created a unit-less measure of spot size by measuring the number of dark pixels.

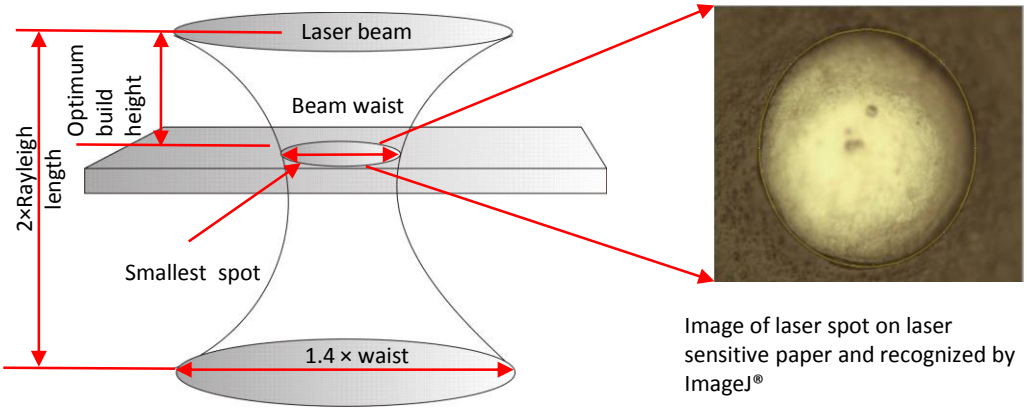

Figure 3-6 Schematic of smallest laser beam spot on optimum build height.

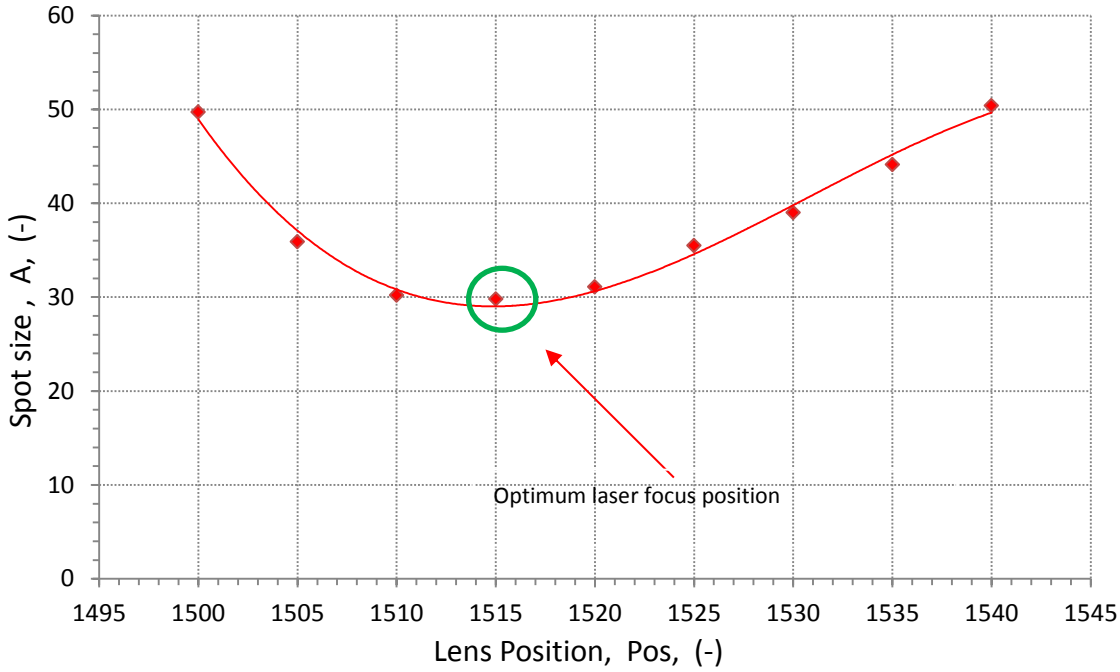

Figure 3-7 The laser spot size on laser sensitive paper varying with the position of the beam expander optics.

The above procedure requires many laser spot measurements which can be simplified using a new laboratory standard procedure. Before the experiment, a machined substrate is fixed to the platform and moves (H+h)/2 to the powder bed level (AB) as illustrated in Figure 3-8.

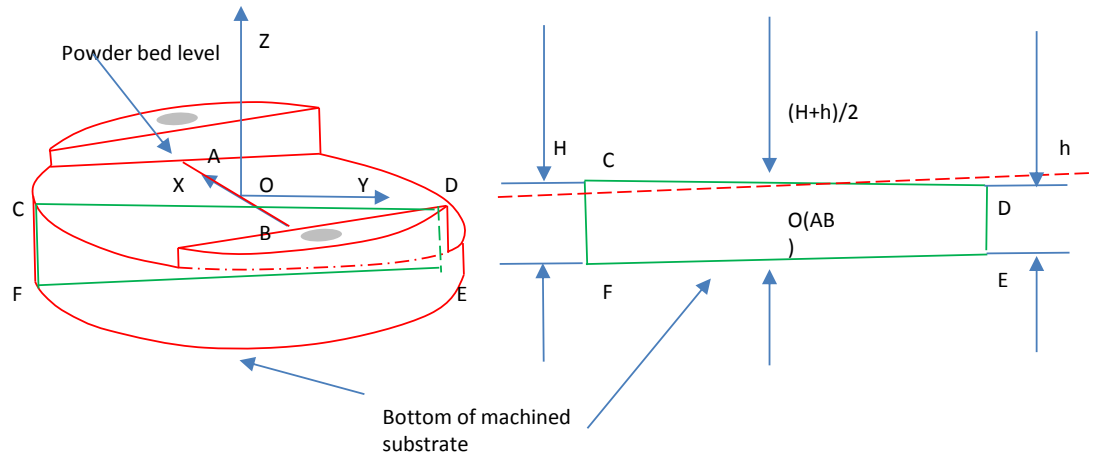

Figure 3-8 Schematic of machined substrate used for laser focus measurement.

When the laser beam scans along a line, the slope of the substrate intersects the laser beam at different positions as shown in Figure 3-9 and gives various widths along a single laser scanning line.

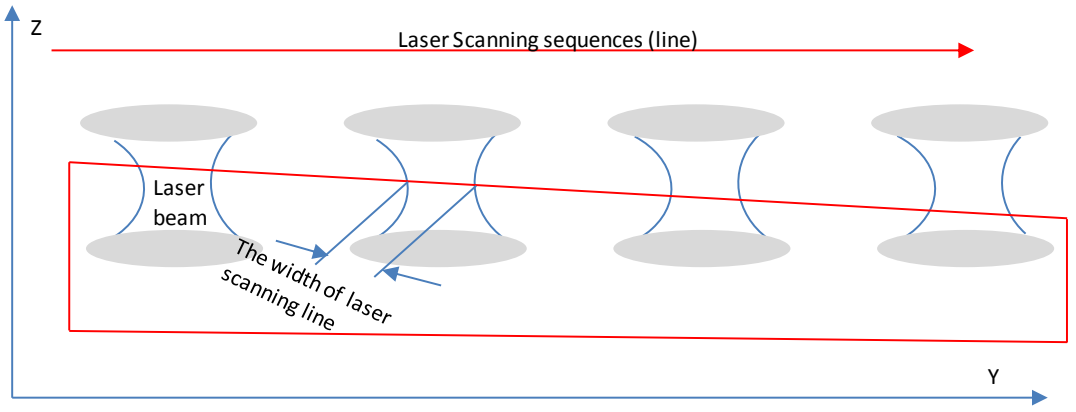

Figure 3-9 The laser scanning along a slope of the substrate and causes the change of laser scanning line width.

As the lens separation increases, the laser focus moves towards the F-theta lens, this will alter the width of line. A set of lines were scanned in the y axis direction with a various focus offset which was related to the value of lens separation as shown Figure 3-10. The minimum width of each laser scanning line forms a line (WK), intersecting the power bed level (AB). Finally the value of lens separation can be found and used for SLM fabrication.

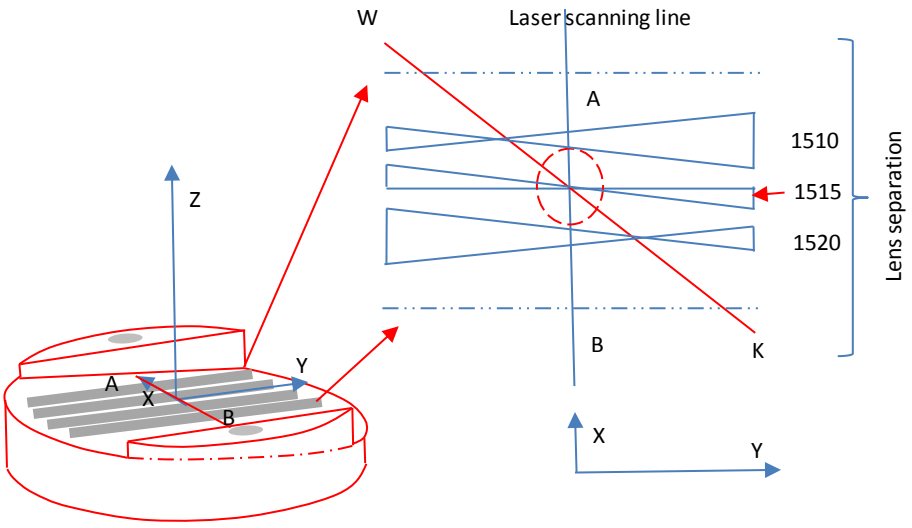

Figure 3-10 Schematic of finding the optimum value of lens expander separation.

3.3.5. Powder Particle Size

The particle size of the titanium powder (TILOP-45, OSAKA, Titanium Technologies Co Ltd, JAP) was measured using a Malvern Mastersizer 2000 (Malvern, Worcestershire, UK) that uses a laser diffraction method and is capable of measuring particle sizes in the range 0.02µm to 2000µm [169]. The particle size requires the powder to be dispersed in distilled water plus a wetting agent. It is then passed through a cell (Figure 3-11) where an incident laser beam passes through the cell filled with the dispersed powder. The density and angle of the scattered laser beam is measured by a detector and this information is translated into a particle size distribution using a computer package that uses a Mie scattering model [169].

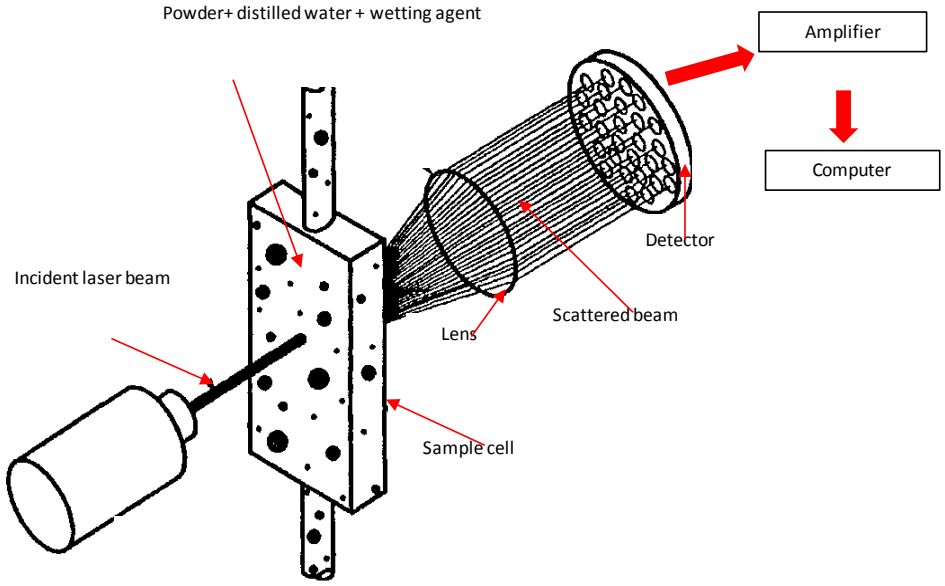

Figure 3-11 Principle of particle size analysis with the laser diffraction method [170]

A plot of the particle size distribution for the virgin powder used in this project is shown in Figure 3-12. This shows a mean particle diameter of 25µm with 90% of the particles being under 39µm. This distribution also shows a small percentage of particles larger than the specified 50µm.

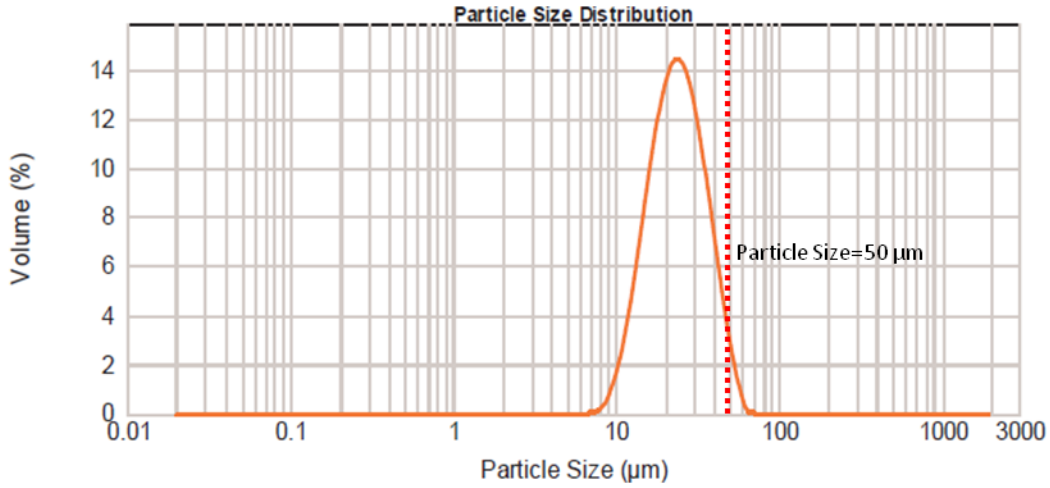

Figure 3-12 Particle size distribution of CpTi powder.

Additionally the powder particle morphology was determined using scanning electron microscopy (JEOL JSM-6610, JEOL Ltd, Tokyo, Japan). As shown in Figure 3-13, the SEM image indicates that the particle size distribution is not homogenous and the geometry of the particles is not completely spherical and but most of them are less than 45µm. In order to ensure uniform powder layer distribution, the layer thickness should be set larger than the average powder particle diameter [171]. Thus the deposited layer thickness was set to 50µm.

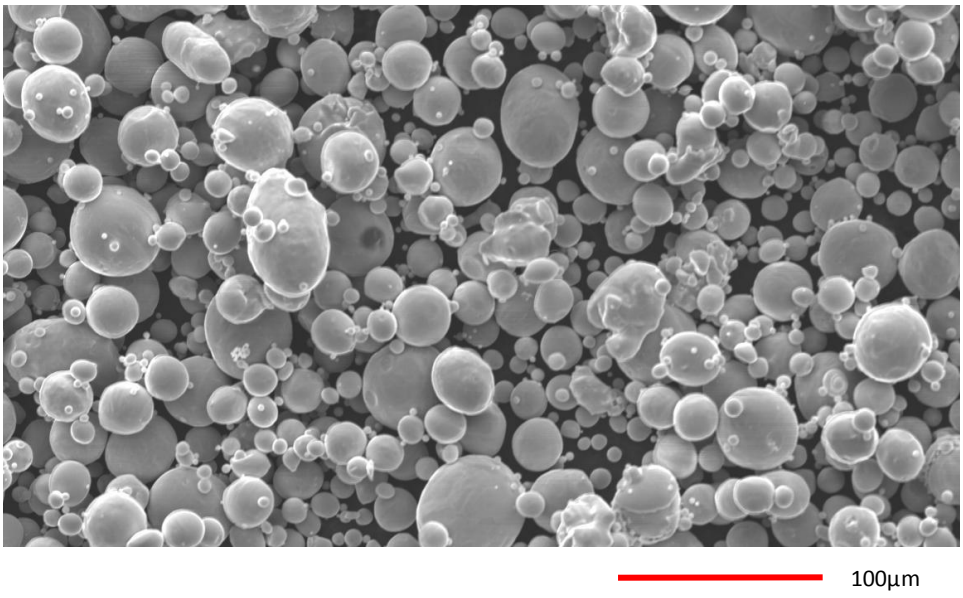

Figure 3-13 SEM image of CpTi powder.

3.3.6. Optimising Fabrication Parameters for VSs

As the VSs are constructed from platelets, it is important to optimise their integrity and to determine the effects of build parameters on their properties. This was achieved by building platelets under a range of conditions. A set of thin platelets (10mm × 10mm) [171] were fabricated and are shown in Figure 3-14. The thickness of the platelets was measured using the optical system from a micro-hardness tester (DMH-2 (MATSUZAWA, SEIKI, JAPAN)). This was used in a similar way to a travelling microscope as the optical microscope had a measuring system incorporated into it. This used two measuring bars that could be manipulated and when the two bars were aligned with the edges of the platelet the distance was determined. This distance is considered here to be the thickness of the platelet, although it is not possible by this method to determine how much of this thickness is made up of melted material and how much is sintered on powder.

According to Tsopanos et al [172] the thickness of the platelets is related to the applied beam energy which can be increased by either increasing the laser power or the exposure time. As shown in Figure 3-15, when the laser exposure time was more than 200µs, the thickness of the platelets increased as either the laser power or the exposure time increased. However when the exposure time was set at 100µs incomplete melting occurred and no platelets were fabricated fully. When the exposure time was set to 200µs and the laser power to more than 45W sound platelets were fabricated. A minimum combination of laser power (80W) and exposure time (200µs) that corresponded to the thinnest fully formed platelet was chosen. This avoided excessive melting and minimised the amount of powder sintered on to the surface.

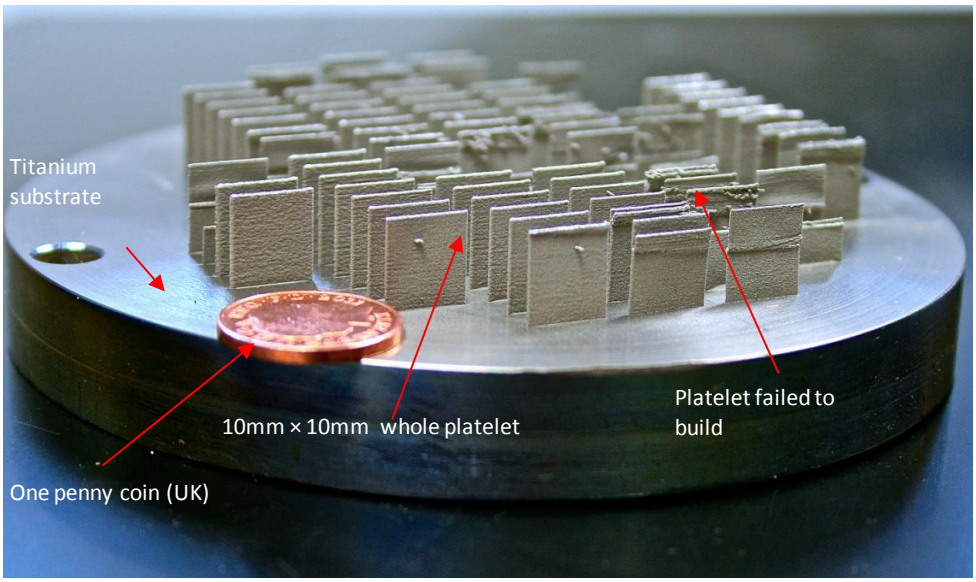

Figure 3-14 Thin platelets fabricated with various combination of laser power and exposure time.

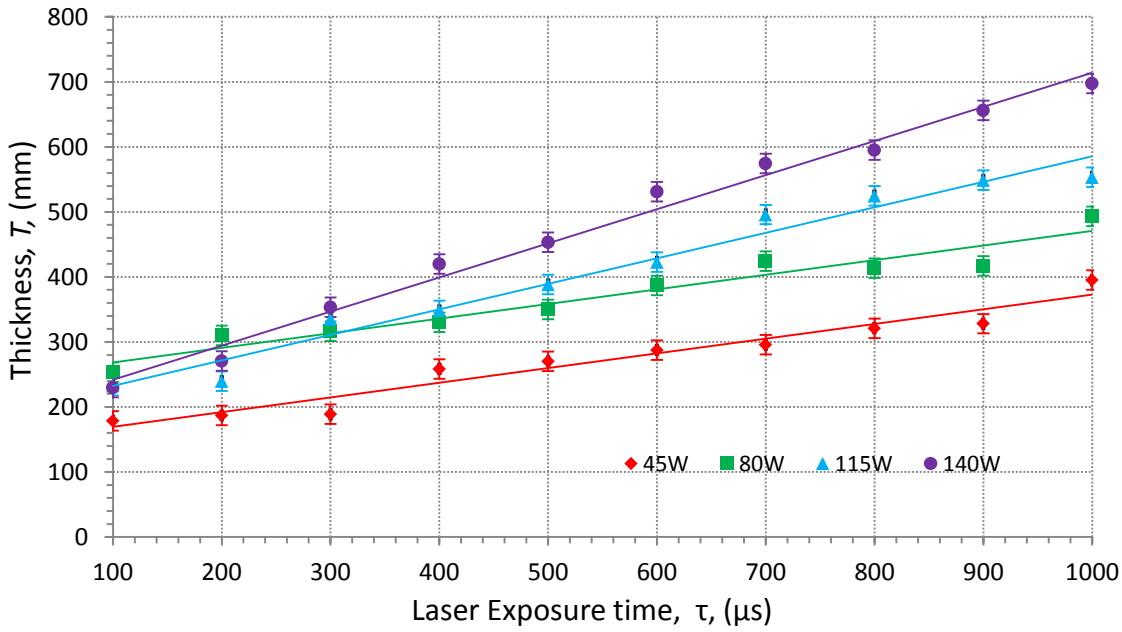

Figure 3-15 The effects of laser exposure time on the thickness of single scan line platelets at various laser parameters.

3.3.7. Powder Recycling

The used powder was recycled by removing any oversized particles that may have formed during the laser melting process. These oversized particles need removing because they affect the quality of the manufactured parts, mainly because they

disrupt the deposition of the powder bed by becoming caught in the wiper system. In this research, an automated sieving system shown in Figure 3-16 was used which comprised a Russell Finex compact sieve that vibrated to remove the particles whose size was greater than 70µm under a low frequency ultrasound. The sieved powder was collected in a bottle at the bottom of the automated sieving system. For safety reasons, the sieving process was carried out in a closed chamber filled with argon.

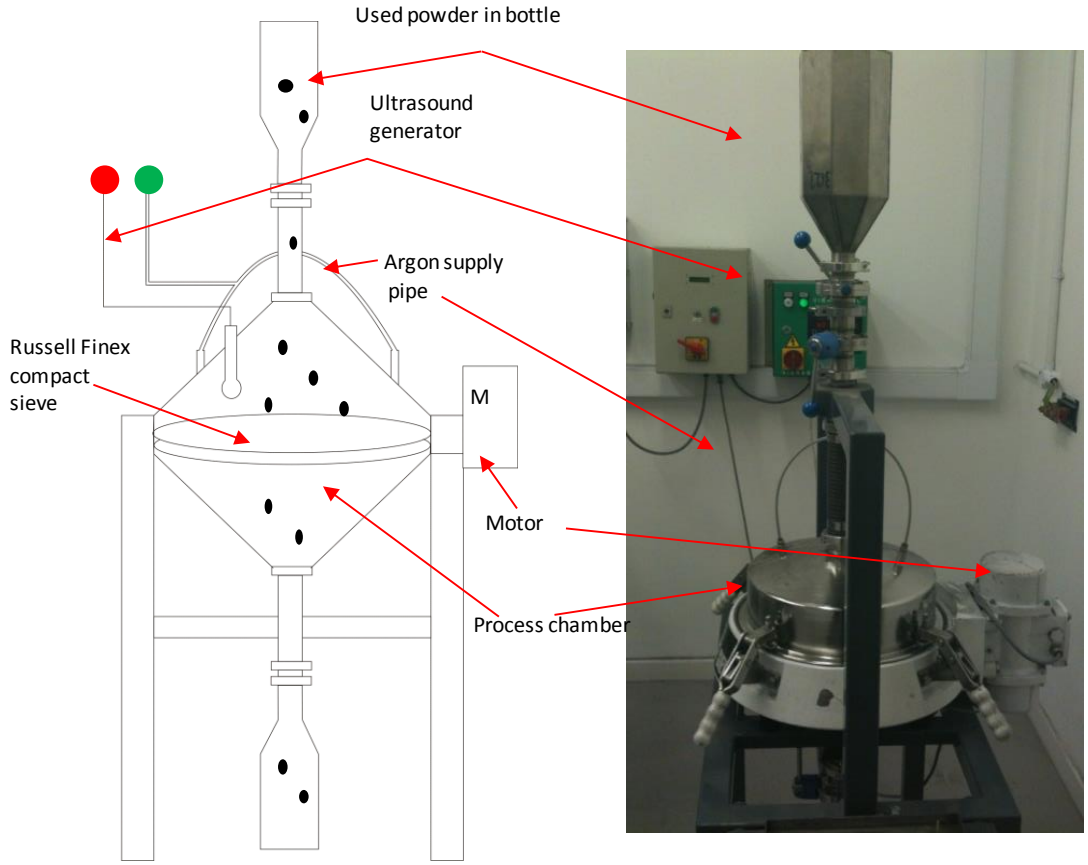

Figure 3-16 Automated sieving machine at University of Liverpool.

3.3.8. Sample Cleaning

The powder may remain in the pores of a porous structure sample which would affect the measurement of sample porosity. The sample cleaning procedure to remove the residual powder was developed by Stryker Orthopaedics as follows (private communication: Naomi Murray Stryker USA).

1. Prepare 5% decon-90 (Decon Laboratories Ltd, UK) surfactant solution and heat to 65˚C.
2. Sonicate the sample in a Branson 8200 series ultrasonic bath in the solution for 90 minutes (time depends on sample size), flip the sample if needed.
3. Rinse the sample with de-lionized water.
4. Sonicate the sample in 60˚C DI water for 1 hour.
5. Dry the sample in a drying oven (80˚C for 24 hours) and store in a desiccator.

This process was found to remove the loose residual powder from the pores and after the specified time in the ultrasonic cleaner no loose powder was observed in sectioned specimens.

3.4. Characterisation Methods for VSs

With reference to the bone ingrowth requirements listed in Chapter 2, the porosity, pore size distribution and uni-axial compressive strength of the porous structures had to be determined. The measurements of these characteristics are detailed in the follow sections.

3.4.1. Porosity of Porous Material

The porosity of a porous material is determined by measuring the amount of void space inside the structure and determining what percentage of the total volume of the material is made up of void space. The porosity can be found using equation (3-2):

$$Porosity = (1 - \frac{\frac{Mass}{Volume}}{\rho_{Ti}}) \times 100 \qquad (3\text{-}2)$$

Where mass was measured by a balance (Adam Equipment, UK) with an accuracy of ±0.01g, the volume was measured by digital callipers with an accuracy of ±0.02mm. ρTi is the density of CpTi which is 4507kg/m^3.

3.4.2. Porosimetry

Mercury porosimetry was used to measure the pore size distribution. If mercury (non wetting liquid) is placed in contact with an open pore, the surface tension of the mercury acts along the line of contact with the pore which is equal to the perimeter of the pore. This surface tension creates a force to resist the mercury entry. The magnitude of this force is proportional to the length of the contact (πDia), the surface tension (γ) of mercury, and the cosine of the contact angle (θ) as shown in Figure 3-17.

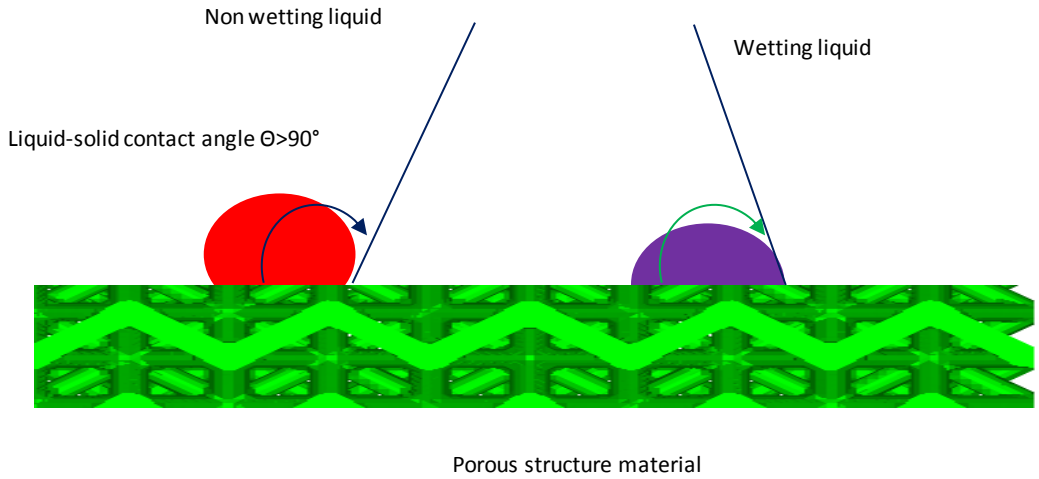

Figure 3-17 Liquid-solid contact angle for wetting and non wetting liquid.

If a circular pore is present at the surface, the force to resist the entry of mercury can be expressed as:

$$f_R = \pi\ Dia\ \gamma\ cos\theta \qquad (3\text{-}3)$$

When external pressure is applied sufficiently, it forces the mercury over the interface of the pore and bridges the pore. The externally applied force, therefore, is the product of the pressure (Pre) and area ($Ar0$) over which the pressure is applied. If a circular pore is at the surface, the externally applied force can be expressed as:

$$f_{Ext} = Pre\ Ar0 = Pre\ \pi\ Dia^2/4 \qquad (3\text{-}4)$$

When just before the force resisting the mercury entry is overcome, an equation is given as:

$$-\pi\, Dia\, \gamma\, cos\theta = Pre\, \pi\, Dia^2/4 \qquad (3\text{-}5)$$

Therefore, for a given pressure, the mercury can intrude into a pore whose diameter is greater than:

$$Dia = -4\, \gamma\, cos\theta/Pre \qquad (3\text{-}6)$$

By measuring the volume of mercury that intrudes into the porous material with each pressure change, the volume of the pore in the corresponding size is known. However, this technology cannot measure the blind pores and closed pores as shown in Figure 3-18. Even the open pore in cross-linked pores and though pores cannot be measured properly because the technique measures the largest entrance to a pore rather than the actual inner size of the pore. It therefore determines the largest connection from the sample surface to the pore rather than the pore.

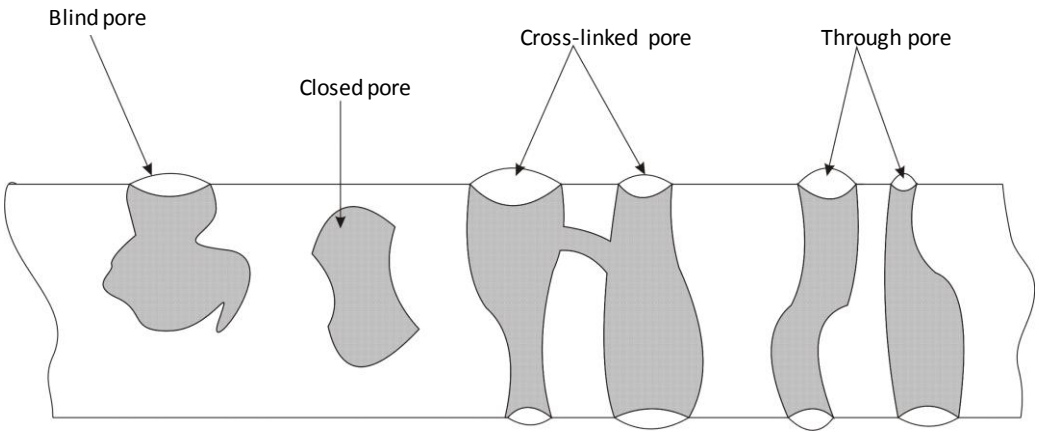

Figure 3-18 Pore classifications .

In order to overcome the limitation involved in mercury porosimetry, a new method was provided by Bhattacharya [173] with quoted accuracy greater than 99.9% was used. This method is based on a digital porous structure model which can be obtained by various methods such as CT scanning. However large computing power

and memory are required in the new method. A revised method was provided to minimise the computation of the pore size distribution and is detailed in Chapter 4.

3.4.3. Uni-axial Compressive Stress and Strain Test

Uni-axial compressive testing is the most common method for determining the mechanical properties of bone ingrowth structures [77]. The bone ingrowth structure needs to be strong enough to support the applied loads in normal use without deformation. The cylindrical samples with dimensions of Ø15mm x 30mm (±0.1mm) were used for uni-axial compressive testing. In order to avoid edge effects, a height-to-thickness ratio of at least 1.5 and at least 7 cells in each direction was used. An Instron 4505 test machine with lubricated platens, to reduce the effect of frication was used with a cross-head speed of 25.4mm/min and a total displacement of 10mm [174,175]. From the resultant graph shown in Figure 3-19, the compressive strength was determined either at the intersection between the two red lines drawn along the initial loading slope and the stress plateau or the initial peak stress if there was one following the procedure of Ashby [174].

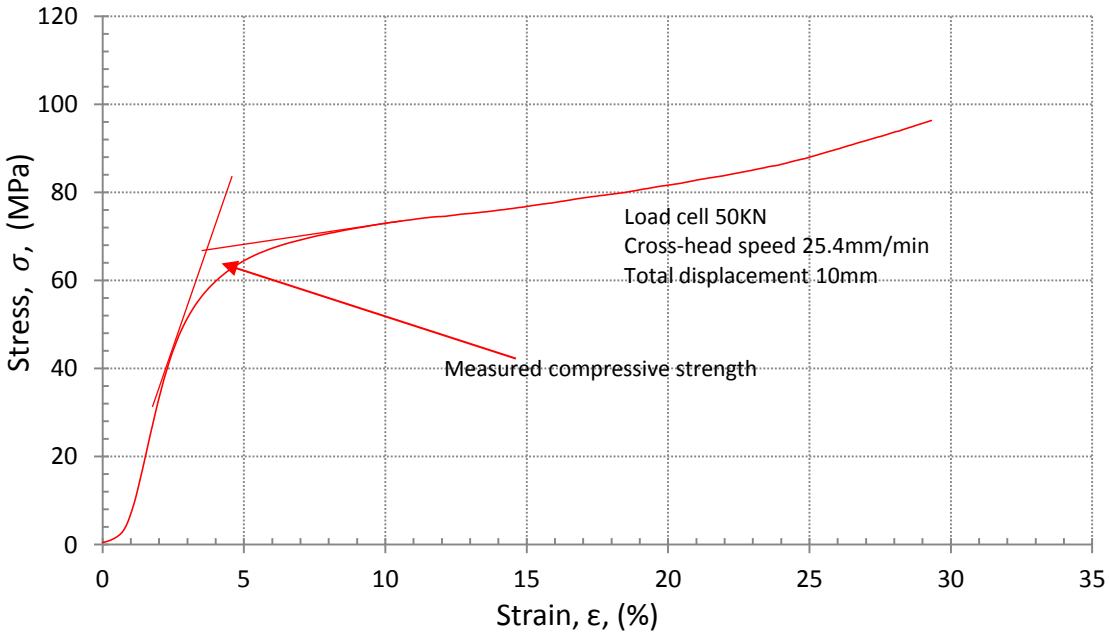

Figure 3-19 Determination of the compressive strength for components that do not exhibit an initial peak stress.

3.5. Summary

The software packages for designing the new custom software are listed in Table 3-1 and the software packages for creating, manipulating, repairing and slicing the solid model are summarised in Table 3-2. By using this software, the CAD data was converted into a version suitable for AM fabrication.

Table 3-1 Software packages

Programming language package	Python 2.7
Scientific computing package	Numpy 1.6.2
2D plot package	Matplotlib 1.1.1
Visualization package	VTK 5.6.0
GUI programming package	PySide 1.1.2
PC performance profile package	Psutil 0.6.1
Custom software distribution package	Py2exe 0.6.9

Table 3-2 Software packages used in creating, manipulating, repairing and slicing the solid model.

Creating solid model with close surface	Pro Engineer Wildfire 4
Manipulating and repairing a solid model in STL format	Magics
Slicing a solid model and hatching close contours	Realizer built-in software

The MCP SLM Realizer 100 was chosen to fabricate samples by laser melting the CpTi (average particle size 45µm) powder layer by layer. Before the fabrication, the parameters were developed and are listed in Table 3-3. The used powder was recycled and the samples were cleaned based on the method provided by Stryker Orthopaedics. The porosities of these samples were measured by gravimetric analysis and the pore size distribution was measured by mercury porosimetry. Finally uni-axial compressive testing to ASTM E9 was performed on the samples.

Table 3-3 Parameters for fabricating VSs.

Laser focus	1515	Laser input power	80W
Layer thickness	50µm	Exposure time	200µs

CHAPTER 4

PLATELET STRUCTURE DESIGN AND DEVELOPMENT

This chapter outlines the development of new custom software that allows the development of the new VS designed for orthopaedic use. It starts with the generic steps for modelling VSs. Then the four key functions are developed including construct function, deform function, trim function and slice function, considered also are the methods used for verification. In order to characterise the VSs before fabrication, the functions were developed to compute the porosity and pore size distribution. Furthermore, the new custom software provides a function for creating a VS with closed surfaces which is required by a number of AM technologies.

4.1. Processes for Creating Vaulted Structures Pre-AM Fabrication

The smallest box that can surround a 3D model is known as the bounding box and this can either be an arbitrarily oriented minimum bounding box or as used in this work an axis aligned bounding box. By the process of voxelization this bounding box can be broken down into a number of smaller unit cells [176]. In a typical example, the unit cell is represented by a cubic box. By constructing platelets with holes on some of the certain surfaces of these unit cells, the VS is created. These platelets can also be deformed to create less regular structures that can mimic the appearance of cancellous bone if required. As this creates a box of the structure which is just larger than the object it is necessary to trim the block back to the object and to do this it is necessary to break the platelets up into triangles. In the trim procedure the surface of the 3D model is introduced as a closed boundary and the triangles inside the boundary are kept and those outside rejected. Finally these triangles are sliced with a specified layer thickness for SLM fabrication.

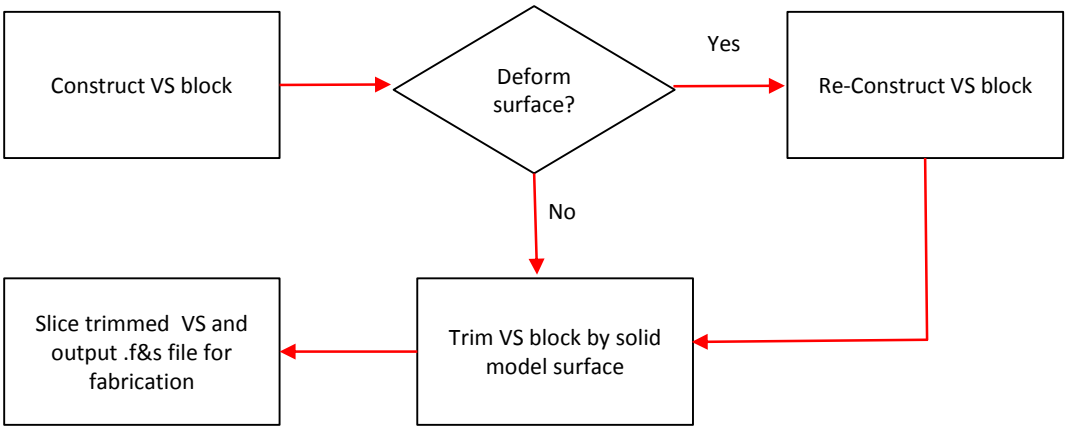

Figure 4-1 Generic steps of VS modelling.

4.2. Constructing a Vaulted Structure

The process of constructing a VS block is shown in Figure 4-2. It starts by voxelising the bounding box of a solid model (Cylinder Ø15 × 30mm in .stl format) with unit cells of a specific size (4 × 4 × 4mm). The total number of unit cells in each direction is chosen to ensure that the solid model is covered. The position of each unit cell is recorded with reference to a point detailed in 4.2.3.

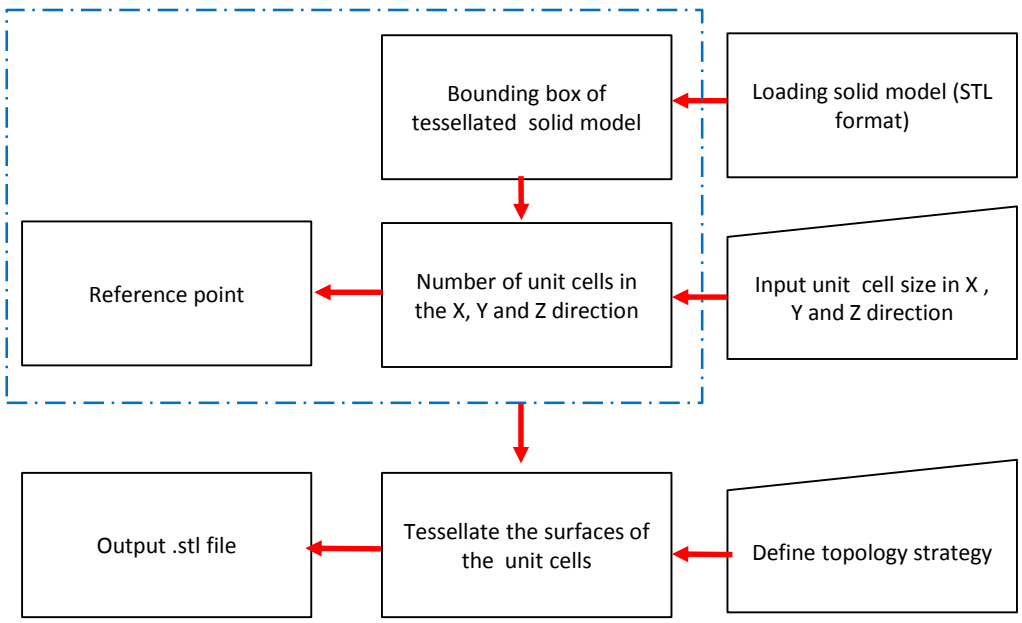

Figure 4-2 Generic steps in constructing a VS block.

4.2.1. Bounding Box of a Solid Model

A bounding box of a finite geometric solid model is a cuboid box with the minimum volume that contains the model while having its edges parallel to the coordinate

axes [162] as shown in Figure 4-3. For a solid model in .stl format in this research, its bounding box is represented by its corner coordinates and can be found using the equations (4-1) to (4-6). For this work the corner coordinates of the bounding box were also computed using Magics® so as to verify the values calculated by the software.

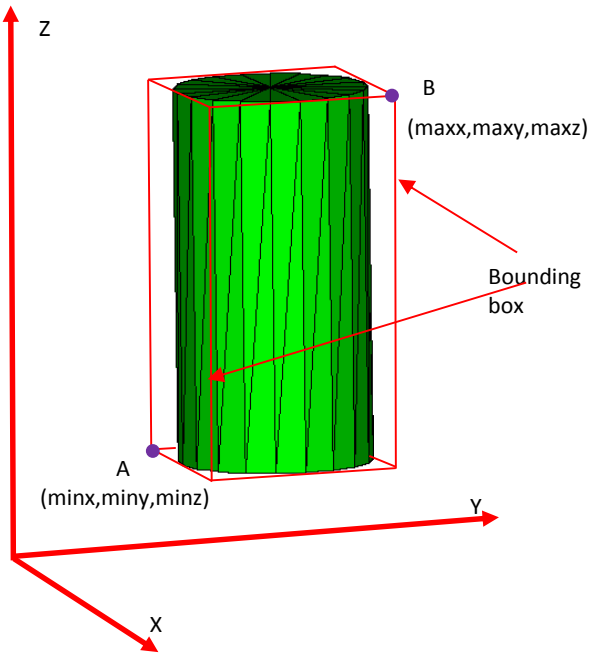

Figure 4-3 The solid model in .stl format within a bounding box.

$$minx = the\ minimum\ value\ of\ element\ in\ Xarray \quad (4\text{-}1)$$

$$maxx = the\ maxmum\ value\ of\ element\ in\ Xarray \quad (4\text{-}2)$$

$$miny = the\ minimum\ value\ of\ element\ in\ Yarray \quad (4\text{-}3)$$

$$maxy = the\ maxmum\ value\ of\ element\ in\ Yarray \quad (4\text{-}4)$$

$$minz = the\ minimum\ value\ of\ element\ in\ Zarray \quad (4\text{-}5)$$

$$maxz = the\ maxmum\ value\ of\ element\ in\ Zarray \quad (4\text{-}6)$$

T_i: *the ith triangle on the solid surface*

$$T_i = [A_i, B_i, C_i]$$

$$A_i = [xv, yv, zv], B_i = [xv, yv, zv], C_i = [xv, yv, zv]$$

$$Xarray = [A_i\,[0], B_i\,[0], C_i\,[0], A_{i+1}\,[0], B_{i+1}\,[0], C_{i+1}[0] \ldots..]$$

$$Yarray = [A_i\,[1], B_i\,[1], C_i\,[1], A_{i+1}\,[1], B_{i+1}\,[1], C_{i+1}[1] \ldots..]$$

$$Zarray = [A_i\,[3], B_i\,[3], C_i\,[3], A_{i+1}\,[3], B_{i+1}\,[3], C_{i+1}[3] \ldots..]$$

$i\ is\ integer\ from\ 0\ to\ total\ number\ of\ triangles$

4.2.2. Number of Cells in a Voxelised Bounding Box

The bounding box of the solid model was voxelised and fully filled by the required number of cells in the X, Y and Z direction. The number of cells in each directions being given by equations (4-7) to (4-9) with reference to Figure 4-4 and are rounded up to the next integer.

$$Number\ of\ cells\ in\ x\ direction = \frac{Length\ of\ bounding\ box}{length\ of\ cell} \quad (4\text{-}7)$$

$$Number\ of\ cells\ in\ y\ direction = \frac{Width\ of\ bounding\ box}{width\ of\ cell} \quad (4\text{-}8)$$

$$Number\ of\ cells\ in\ z\ direction = \frac{Height\ of\ bounding\ box}{height\ of\ cell} \quad (4\text{-}9)$$

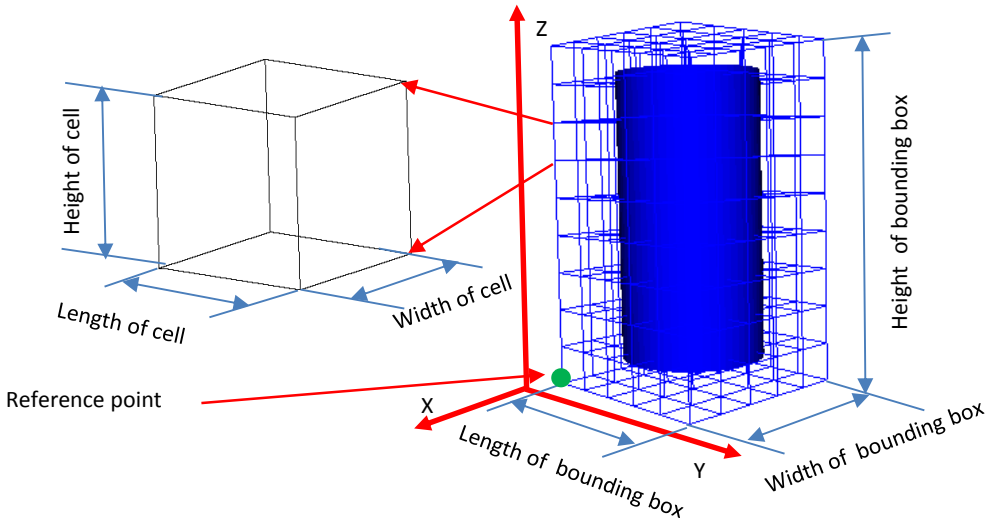

Figure 4-4 Illustration of a solid model's bounding box voxelised by a specified set of cells in x, y and z directions.

4.2.3. Reference Point of a Gridded Bounding Box

As shown in Figure 4-4, the reference point (RX, RY, RZ) of the gridded bounding box can be determined by equations (4-10) to (4-12). It ensures the solid model is filled with unit cells symmetrically and gives a uniform surface after trimming, an example is given in Figure 4-5, which compares the cylindrical solid model filled with

the unit cell structure created by the Manipulator software and that created with the new software.

$$RX = minx - \frac{Nx \times length\ of\ cell - Length\ of\ bounding\ box}{2} \quad (4\text{-}10)$$

$$RY = miny - \frac{Ny \times width\ of\ cell - Width\ of\ bounding\ box}{2} \quad (4\text{-}11)$$

$$RZ = minz - \frac{Nz \times height\ of\ cell - Height\ of\ bounding\ box}{2} \quad (4\text{-}12)$$

Nx: Number of cells in x direction, Ny : Number of cells in y direction, Nz : Number of cells in y direction.

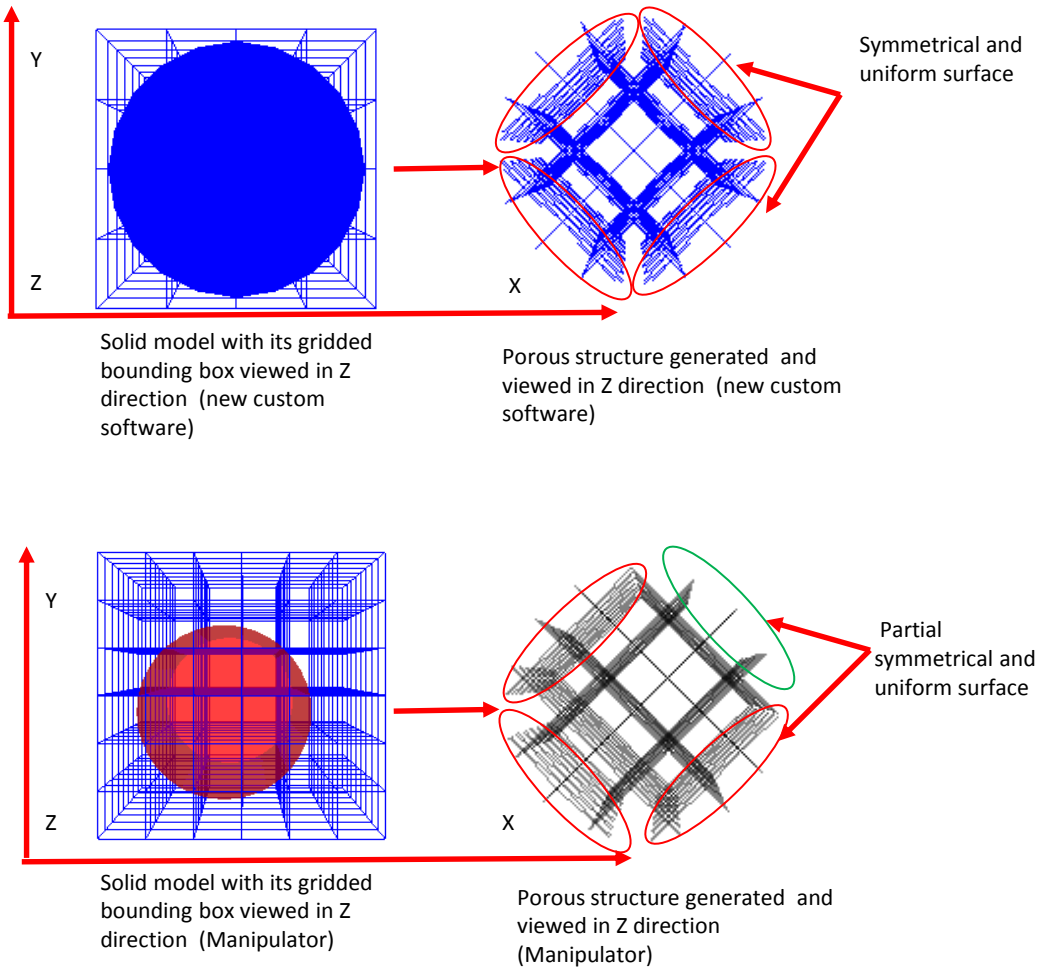

Figure 4-5 Cylindrical unit cell structures created by new custom software and Manipulator (software developed at University of Liverpool).

The analysis can be extended to the VS, as shown in Figure 4-6, which compares the cylindrical VS models generated by Plateletqt (software developed by FreeSteel®

[177]) with the software developed here, Plateletqt cannot produce a uniform surface of the VS with symmetrical shape. Additionally, the position of each unit cell does not need to be stored, when it is required it can be obtained directly based on the equations (4-10) to (4-12). This results in a reduction in the computer memory requirements.

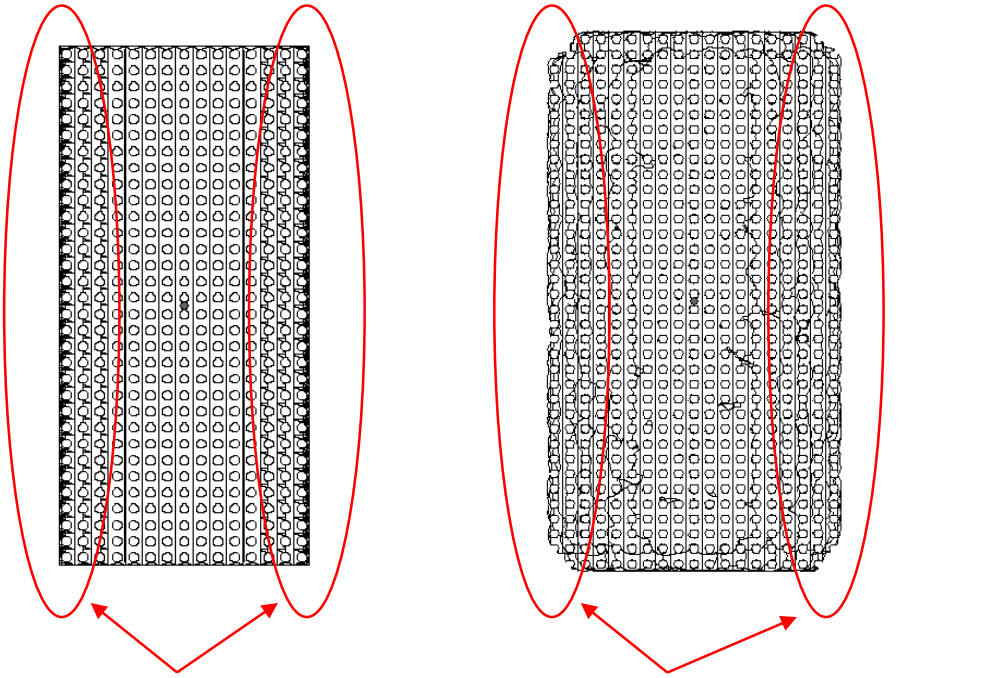

Uniform surface generated by new custom software

Non-Uniform surface generated by Plateletqt

Figure 4-6 A cylindrical VS created by the new custom software and Plateletqt.

4.2.4. Tessellating Surfaces in the Unit Cell

In order to output the models as .stl files for fabrication, the surfaces inside the cells were tessellated by triangles and their holes approximated by polygons with a specified number of edges. For demonstration of this method, a surface with a hole is tessellated and the hole is approximated by a hexagon as shown in Figure 4-7. The vertices of the hexagon are determined by equations (4-13) to (4-21).

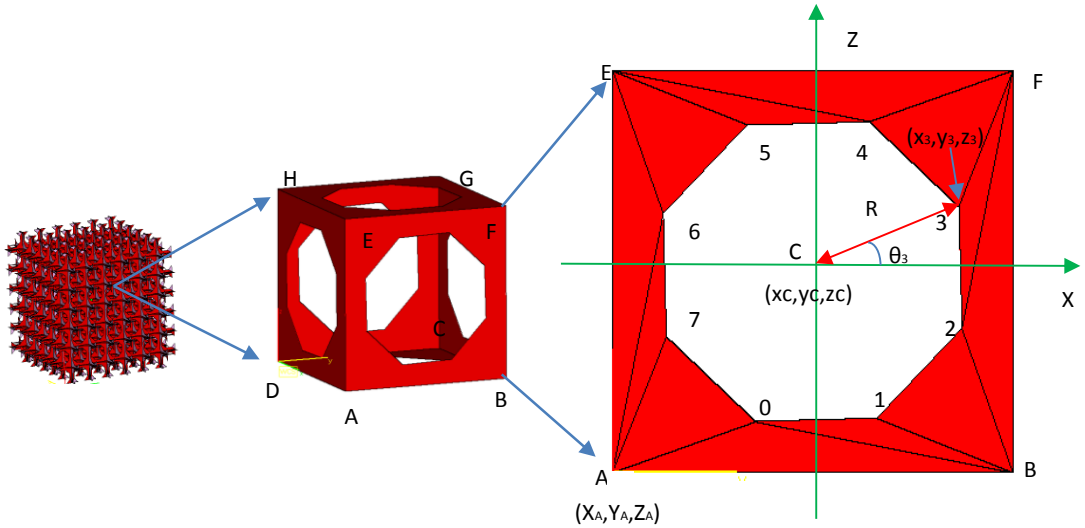

Figure 4-7 Illustration of a VS whose surfaces are tessellated and visualised by Magics.

$$X_A = RX + Number\ of\ cells\ in\ x\ direction \times length\ of\ cell \quad (4\text{-}13)$$

$$Y_A = RY + Number\ of\ cells\ in\ y\ direction \times width\ of\ cell \quad (4\text{-}14)$$

$$Z_A = RZ + Number\ of\ cells\ in\ z\ direction \times heigth\ of\ cell \quad (4\text{-}15)$$

$$centre\ of\ facet\ xc = X_A + \frac{1}{2} \times length\ of\ cell \quad (4\text{-}16)$$

$$centre\ of\ facet\ yc = Y_A \quad (4\text{-}17)$$

$$centre\ of\ facet\ zc = Z_A + \frac{1}{2} \times height\ of\ cell \quad (4\text{-}18)$$

$$x_i = centre\ of\ facet\ xc + R \times cos\theta_i \quad (4\text{-}19)$$

$$y_i = centre\ of\ facet\ yc \quad (4\text{-}20)$$

$$z_i = centre\ of\ facet\ zc + R \times sin\theta_i \quad (4\text{-}21)$$

$$\theta_i = \frac{360}{N_p} \times i - \frac{360}{N_p} \times \frac{5}{2}, i = 0,1,2,3 \ldots . N_p$$

Where N_p is the number of a polygon edges, R is the radius of a hole.

Further work was then focused on how this hole could be approximated to a polygon. By considering Figure 4-8 it can be seen that the polygon and circle are coincident at the corners while they differ most at the maximum chord error (AC) which is defined by equation (4-22)

$$AC = R - R \times \cos(\frac{360}{2 \times N_p}) \quad (4\text{-}22)$$

The projection (AK) of AC in the fabrication direction (Z direction) can be determined by equation (4-23)

$$AK = AC \times sin ß \quad (4\text{-}23)$$

Where ß is an angle in the right triangle ACK

Combining equations (4-22) to (4-23), AK can be represented by equation (4-24)

$$AK = R \times (1 - \cos(\frac{360}{2 \times N_p})) \times \sin(\frac{360}{N_p}) \quad (4\text{-}24)$$

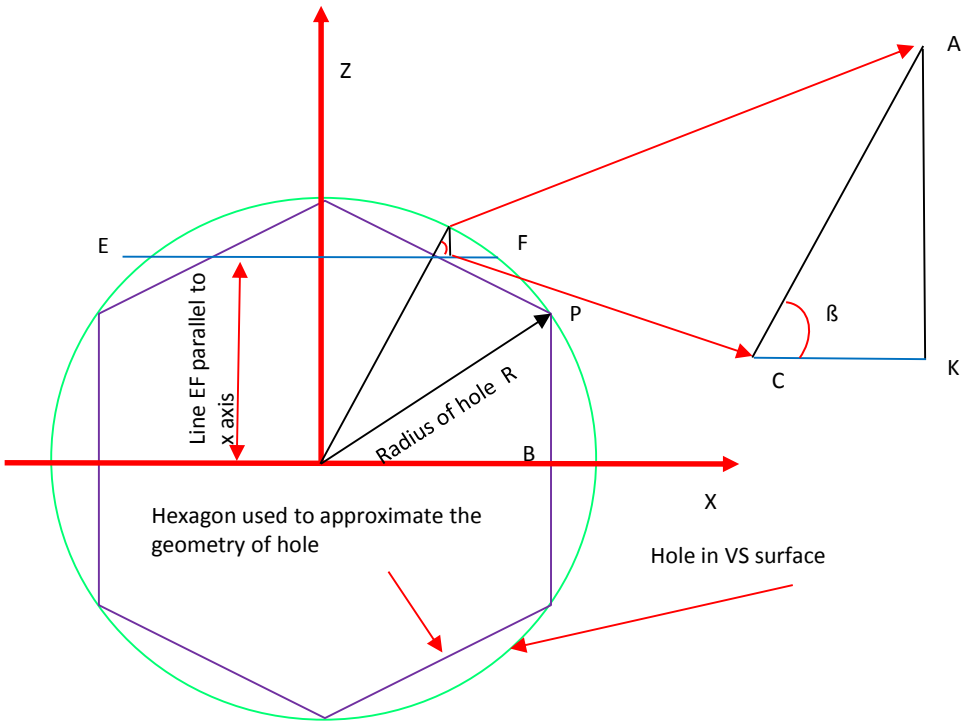

Figure 4-8 Illustration of hole in the surface of a VS approximated by polygon (six edges).

Due to the layer by layer fabrication method used in SLM and the minimum angle at which objects can be built because of the need to support overhanging structures, there are effects on the number of edges the polygon must have for a given layer

thickness and size, and the approximation of the polygon to the hole is largely controlled by the layer thickness. The projection (AK) has for a successful build to be similar or slightly larger than the layer thickness. In order to simplifying the research carried out in Chapter 5, the size of a hole on the platelet is termed hole size and defined by equation (4-25).

$$hole\ size = \frac{R}{R_p} \times 100 \qquad (4\text{-}25)$$

Where R_p is the possible maximum hole in a platelet.

Using these rules, a VS block made from a series of unit cells can be constructed as shown in Figure 4-9. Although in reality the melting and refreezing of the metal will modify the hole shape due to surface tension.

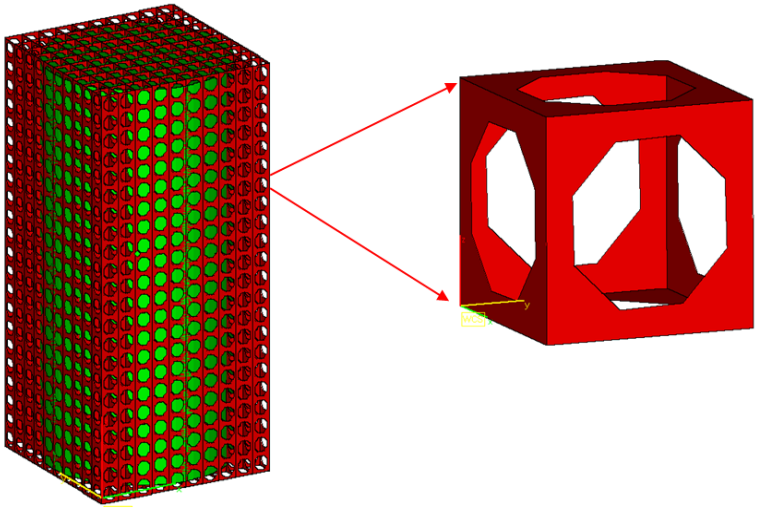

Figure 4-9 Illustration of constructing a VS block with the tessellated solid model.

4.2.5. Various Vaulted Structures

Various VSs can be created by altering the distribution in each unit cell. Three typical platelet based structures [174] were used for investigating the mechanical

properties of natural cellular structures including cancellous bone and the distribution of platelets in each unit cell can be seen in Figure 4-10.

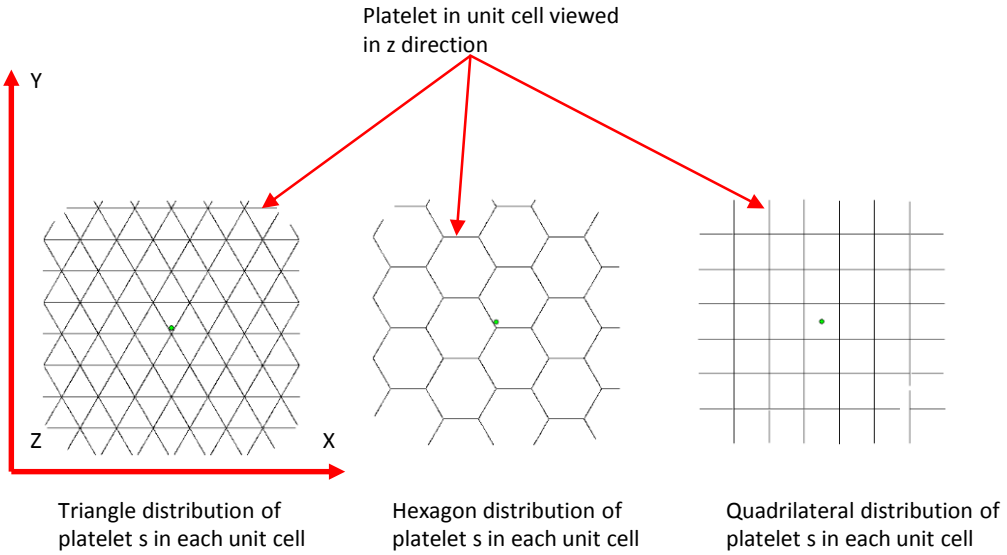

Figure 4-10 Three key porous structures mentioned by Ashby [174] used for explaining the mechanical properties of a porous structure are created by varying platelets distribution in unit cells.

Theoretically any modification to the VSs is possible, but it is critical that the cells within the VS are designed so that they are continuous and interconnected. The continuous and interconnected architecture can be achieved by adjacent cells sharing edges or platelets. As a demonstration, various VSs can be created by adding or subtracting the platelets in each unit cell. VSs can be created by a quadrilateral distribution of six platelets in each unit cell as shown in Figure 4-11. By removing the platelets from the top and bottom, a new VS with four platelets is created. By removing the platelets vertically or parallel to each other, it gives further VSs, possessing various porosities and compressive strengths and are investigated in the research in Chapter 5 and Chapter 6.

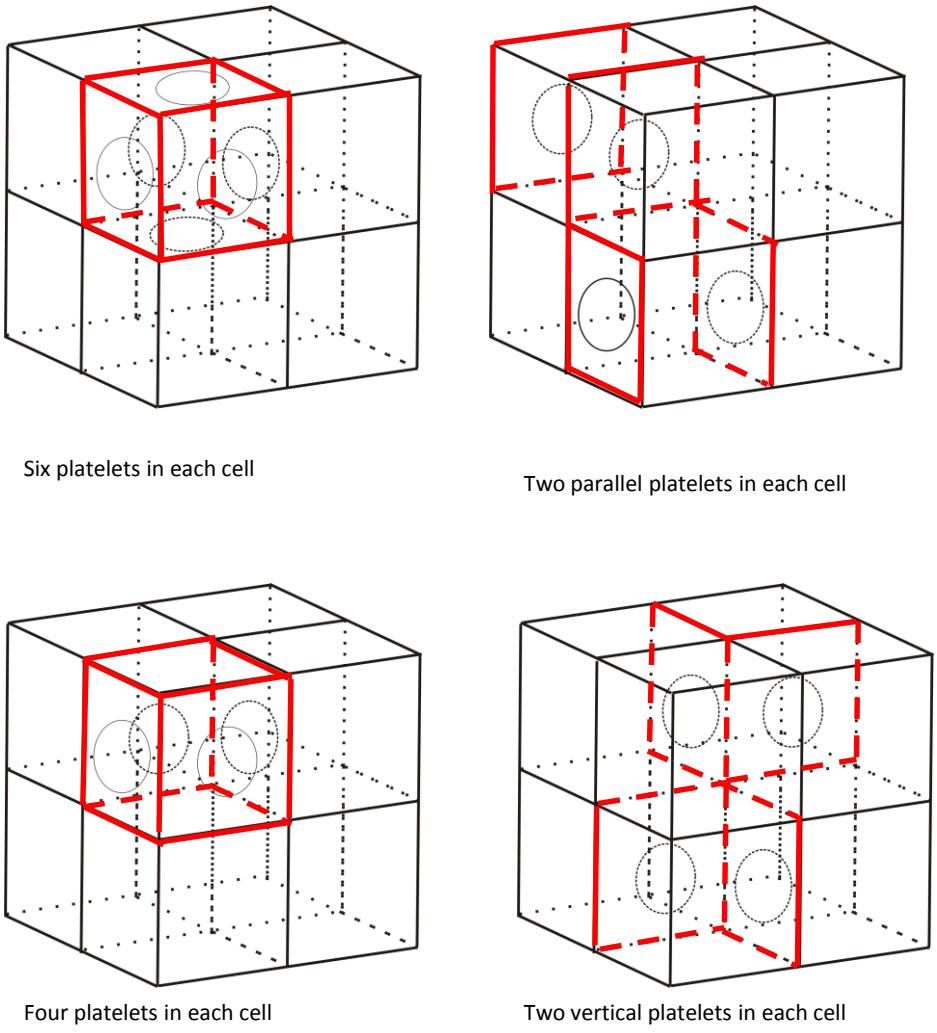

Figure 4-11 Illustration of the VSs with various topological strategies.

4.3. Random Surface Deformation

The method used to deform the surfaces is one widely used in computer graphics to mimic the appearance of a solid model when a force acts upon it [178]. Generally the process starts with a continuous model surface which is parameterised to form a set of nodes. By moving some of these nodes on the surface (termed control nodes), the motion of other nodes is controlled by an equation that defines the relationship between the position of the control nodes and the other nodes. Finally by tessellating the nodes on the discrete surface, a deformed surface is achieved. When the control nodes are moved randomly, they can give a randomised deformed structure. In order to achieve the research objectives listed in Chapter 2, a new randomised deforming mechanism was created, resembling the cancellous bone, using this technique.

4.3.1. Deformation Mechanism

The deformation mechanism is heavily reliant on the representation of the surface [179]. For AM fabrication, the surface is represented in stl format and can be derived from the surface mesh followed by a tessellation with triangles. In order to provide more freedom to construct the surfaces and limit possible deformations, a set of Bezier curves (parametric curves) were chosen to mesh the surfaces. Therefore the points for constructing any surface can be easily determined based on which curve they lie. This idea is visualised and shown in Figure 4-12. It starts with discretisation of a continuous face of each unit cell using a set of Bezier curves (continuous model) in both longitude and latitude with a specified gap between the Bezier curves. When the vertices of a face are moved, the position of nodes (intersections between Bezier curves) on the face can be calculated from the Bezier curves on which they lie. Then by tessellating the nodes and vertices, a deformed face is created and this can be saved in .stl format. Although the computing time increases as the number of Bezier curves increases, especially for the fine porous structure, it does not have a significant effect if low order Bezier curves such as a cubic Bezier curve are used.

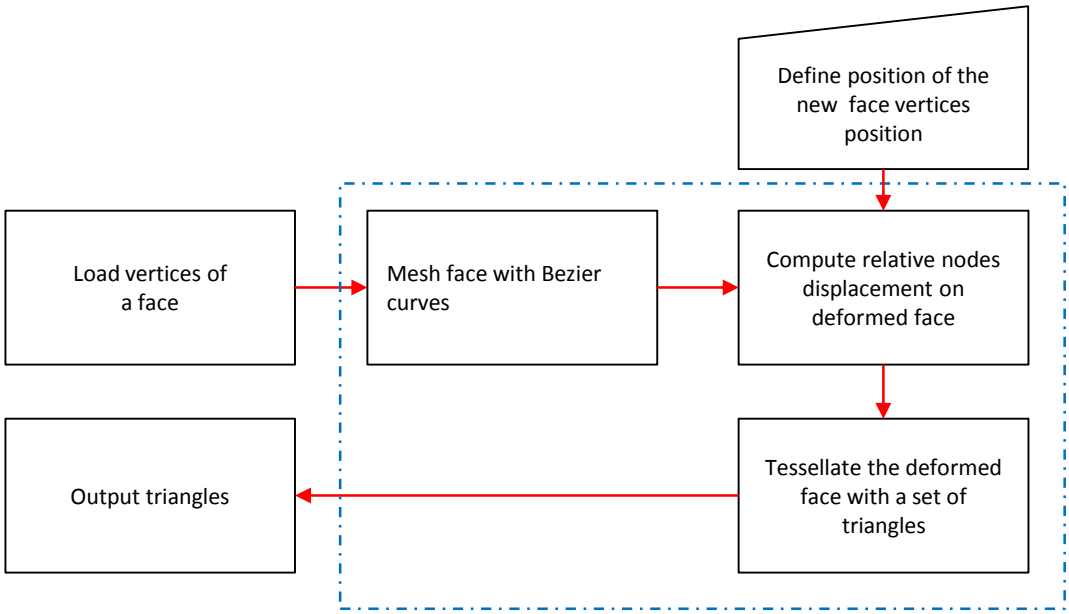

Figure 4-12 Generic step of deforming a face of unit cell in VS.

4.3.2. Randomising Mechanism

The randomised deformation of a platelet is controlled by the random motion of its vertices. The percentage randomisation is defined by the following equations to indicate the movement of the vertices.

$$percentage\ of\ randomisation\ in\ x\ direciton = \frac{movement\ in\ x\ direction}{L}$$

$$percentage\ of\ randomisation\ in\ y\ direciton = \frac{movement\ in\ y\ direction}{W}$$

$$percentage\ of\ randomisation\ in\ z\ direciton = \frac{movement\ in\ z\ direction}{H}$$

L: the length of a unit cell, W :the width of a unit cell, H: the height of a unit cell

By moving a vertex in a random manner within a specific range of distances, the vertex is transferred to a new position which is defined by its coordinates. This process is shown in detail and can be explained fully by considering the following python code:

$def\ RandomisedVertex(vertex, minx, maxx, miny, maxy, minz, maxz)$
$\#minx: the\ minimum\ percentage\ of\ movement\ in\ x\ direction$
$\#maxx: the\ maximum\ percentage\ of\ movement\ in\ x\ direction$
$\#miny: the\ minimum\ percentage\ of\ movement\ in\ y\ direction$
$\#maxy: the\ maximum\ percentage\ of\ movement\ in\ y\ direction$
$\#minz: the\ minimum\ percentage\ of\ movement\ in\ z\ direction$
$\#maxz: the\ maximum\ percentage\ of\ movement\ in\ x\ direction$

$Import\ random$
$\#\ import\ random\ funciton$

$[x, y, z] = vertex$
$\#\ a\ vertex\ is\ defined\ by\ its\ coordinates$
$direciton = [-1,1],$
$a = [0,1]$
$random\ number = random.\ choice\ (a)$
$\#\ choose\ a\ number\ between\ 0\ and\ 1\ randomly$

$\#\ random.choice\ (direction)$:
$\#choose\ a\ number - 1\ or\ 1\ randomly$

$move\ direciton\ in\ x\ direction\ = random.choice(direction)$
$move\ direciton\ in\ y\ direction\ = random.choice(direction)$
$move\ direciton\ in\ z\ direction\ = random.choice(direction)$
$movement\ in\ x\ direciton = maxx - (maxx - minx) \times random\ number$
$movement\ in\ y\ direciton = maxy - (maxy - miny) \times random\ number$
$movement\ in\ z\ direciton = maxz - (maxz - minz) \times random\ number$

$x = x + movement\ in\ x\ direction \times move\ direciton\ in\ x\ direciton$
$\times\ length\ of\ cell$
$y = y + movement\ in\ y\ direction \times move\ direciton\ in\ y\ direciton$
$\times\ width\ of\ cell$
$z = z + movement\ in\ z\ direction \times move\ direciton\ in\ z\ direciton$
$\times\ heigth\ of\ cell$

$return\ [x, y, z]$
$\#\ new\ position\ of\ a\ vertex$

In the above description, the random number is generated by the Mersenne Twister algorithm. This algorithm is either initialised by assigning a value which results in similar number sequence or using the system time as a default that will result in a different number sequence. Thus the random function must be seeded with an initial value that is fixed, otherwise a RVS created with the same parameters will still differ each time. To demonstrate this effect, a RVS was created six times with the same parameters and six different VSs (Figure 4-13) were generated.

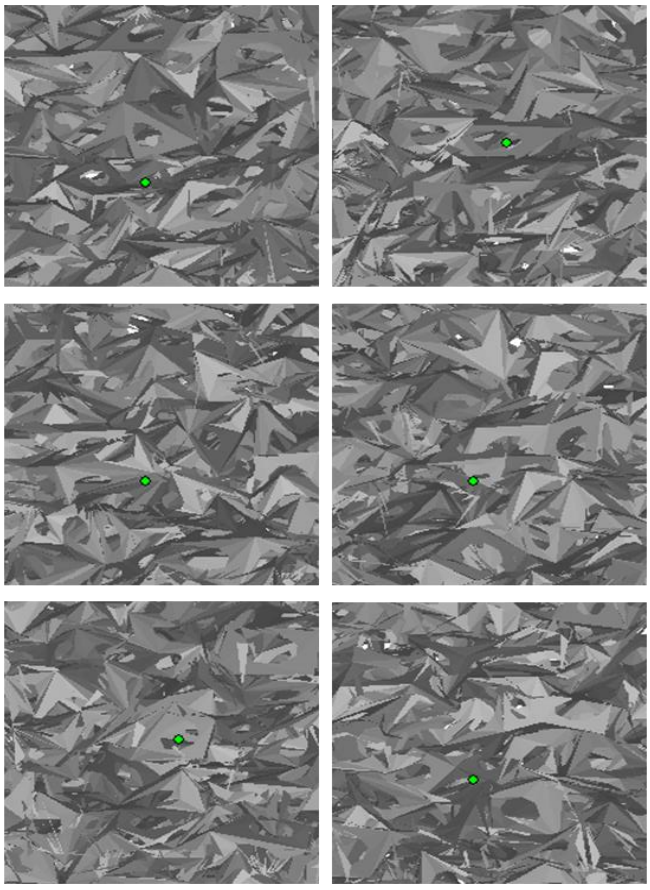

Figure 4-13 Illustration of RVSs generated 6 times without seeded pseudo random function and gives different structures.

Using the developed randomised deforming mechanism, the VSs were deformed with the structure varying with the percentage of movement in various directions (from 0% to 100% of the cell size in x, y and z direction) as shown in Figure 4-14. It also shows that both the holes and the faces are deformed in the x, y and z directions. When the randomisation is above 30%, the amount of the vertex movement is such that considerable deformation can occur. This level of deformation results in a large deformation of holes and faces. Furthermore when the percentage of randomisation is more than 60%, it is difficult to see the effect of the increased randomisation.

Randomisation 0%

Randomisation 10%

Randomisation 20%

Randomisation 30%

Randomisation 40%

Randomisation 50%

Randomisation 60%

Randomisation 70%

Randomisation 80%

Randomisation 90%

Randomisation 100%

Figure 4-14 RVSs with various percentage of randomisation in x, y and z directions.

The randomising mechanism further increases the capability of the structure to mimic the appearance of cancellous bone. Figure 4-15 shows a cancellous bone structure which can be compared with the RVS (constructed using deformed platelets with holes) and the randomised unit cell structure (constructed of struts with random distribution). The cancellous bone has a similar appearance to both the deformed platelet structure and the rod like structure. Both structures can be found in the RVS but the platelet structure is never present in the randomised unit cell structures.

A Micro CT of a cylindrical cancellous bone specimen (height 20mm,diameter 10mm, 19.5µm voxel size)

B RVS (cell size 2mm, random percentage 0 to 60%, hole size 80%, four platelets in each unit cell

C Randomised unit cell structure (cell size 2mm, random percentage -30% to 30%

Figure 4-15 The difference between the appearance of cancellous bone [180], RVS and randomised unit cell structure.

Further work was carried out to investigate the appearance of the RVS (Four platelets in each cell) by fabricating them using the SLM 100. Various randomisation percentages (0% to 100%) were at a set hole size of 80% of the maximum diameter of the inscribed circle of the platelet. This was chosen so that struts similar to those of cancellous bone would be formed. A set of RVS samples varying in the percentage of randomisation were fabricated as seen in Figure 4-16, Figure 4-17, Figure 4-18 and Figure 4-19 using the optimised parameters. The results show that the surfaces of the VSs were deformed randomly by the use of the randomised deforming mechanism; however, as the percentage of randomisation increases, the deformation of surface increases as well. When the percentage of randomisation is less than 60%, the appearance in the z direction are closer to that in the x and y directions.

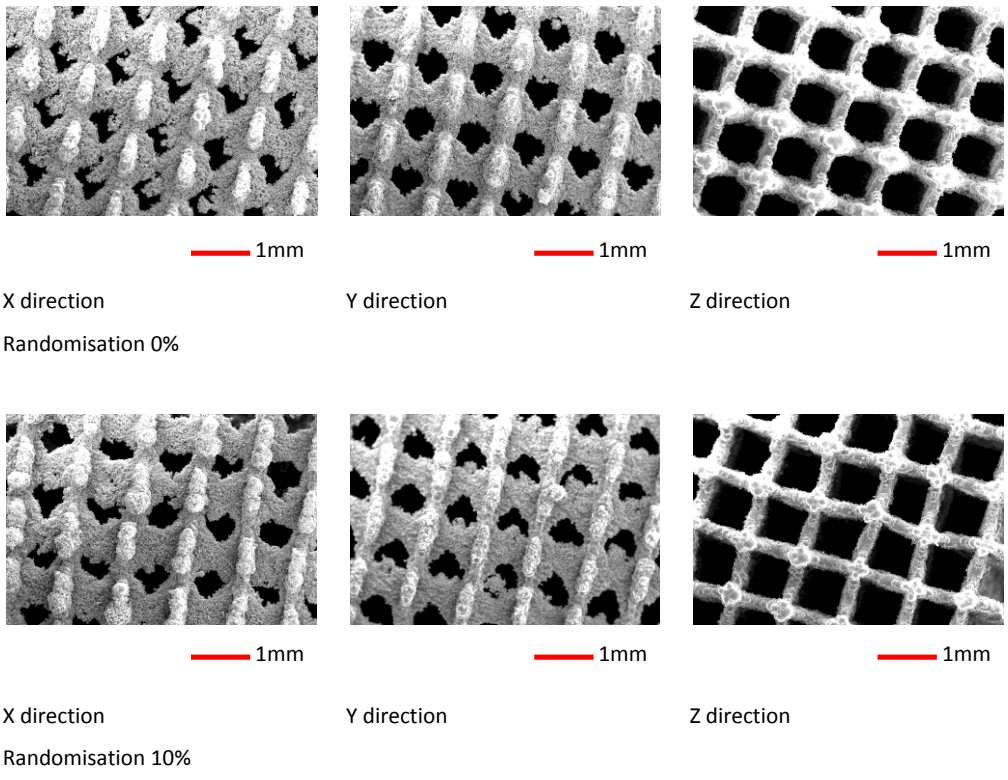

Figure 4-16 SEM images of RVSs varying in percentage of randomisation.

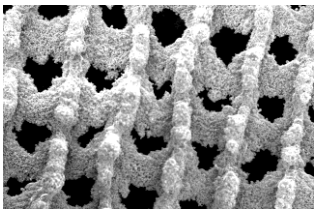

X direction

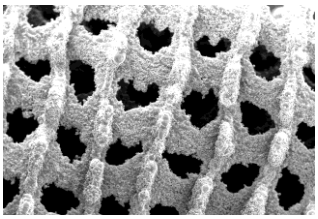

Y direction

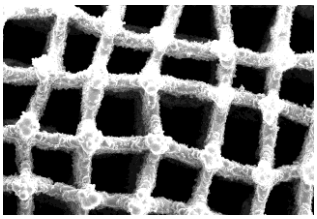

Z direction

Randomisation 20%

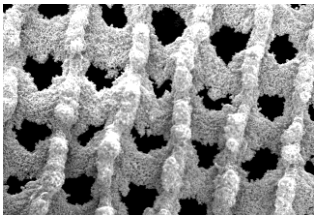

X direction

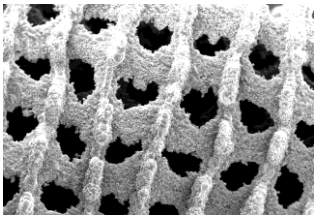

Y direction

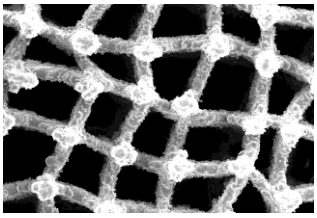

Z direction

Randomisation 30%

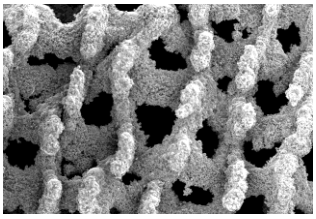

X direction

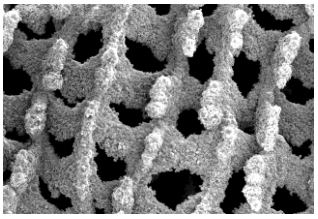

Y direction

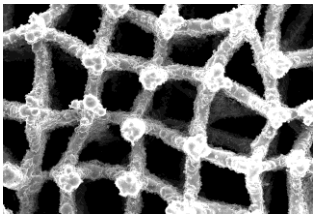

Z direction

Randomisation 40%

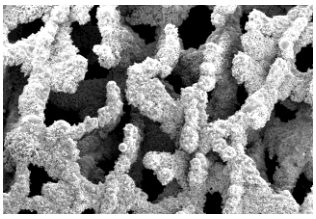

X direction

Y direction

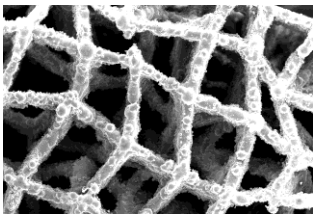

Z direction

Randomisation 50%

Figure 4-17 SEM images of RVSs varying in percentage of randomisation.

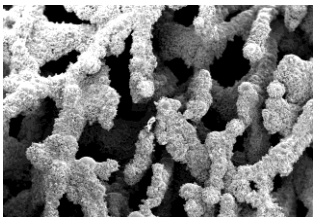

1mm

X direction

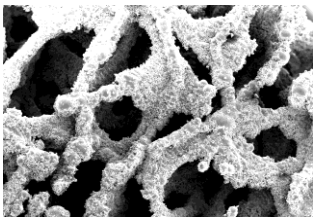

1mm

Y direction

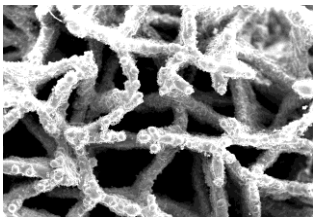

1mm

Z direction

Randomisation 60%

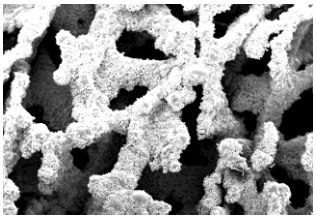

1mm

X direction

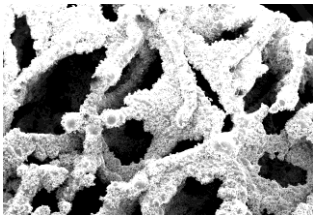

1mm

Y direction

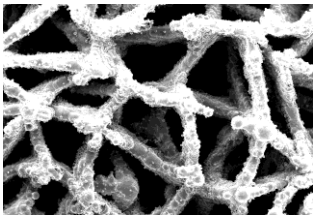

1mm

Z direction

Randomisation 70%

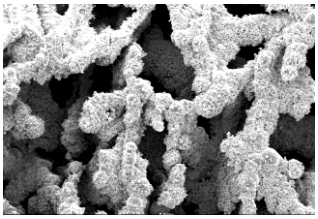

1mm

X direction

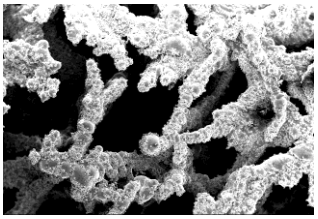

1mm

Y direction

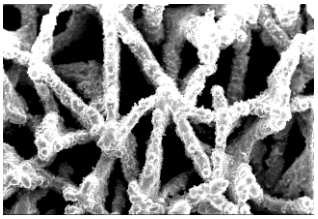

1mm

Z direction

Randomisation 80%

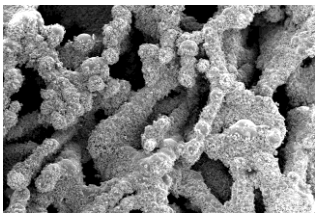

1mm

X direction

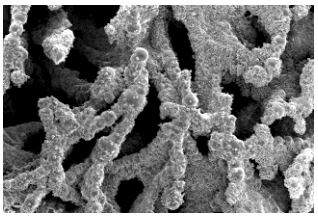

1mm

Y direction

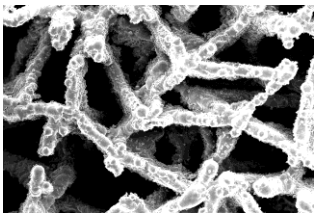

1mm

Z direction

Randomisation 90%

Figure 4-18 SEM images of RVSs varying in percentage of randomisation.

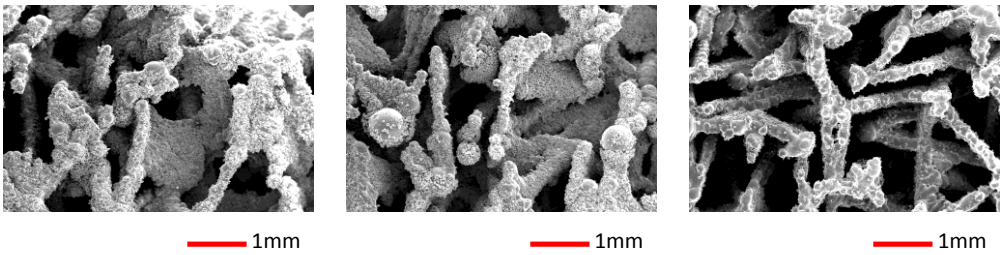

Figure 4-19 SEM images of RVSs in 100% of randomisation.

When the percentage of randomisation is larger than 60%, large deformation occurs and this gives a different appearance with well interconnected open pores. It is believed that this (percentage of randomisation >60%) randomised deformed VS can be used to create materials that resemble cancellous bone. Thus in the following section, high resolution images of cancellous bone are compared to the appearance of the RVS.

Whitehouse [181] studied the human femur and showed that the structure of the cancellous bone is affected by the magnitude of the loads it experiences. His research also shows that where the stress is low, the structure of the bone is an open and rod like structure, while the denser and platelet-like structure was found where the stress was high. Furthermore ageing has been associated with changes in bone structure especially a decrease in density (The density decreases 0.51% each year) [96]. Therefore two images of cancellous bone from both a young patient and an old patient are used to demonstrate that the RVS can resemble both of them. Figure 4-20 shows a computed-tomography image of a 4mm cube of cancellous bone sample from a 63-year-old male. It consists of large deformed platelets which are connected with each other by struts (rods). All the features in the cancellous bone such as deformed platelets and struts can be founded in the SEM images of the RVS and shows that the structure closely resembles this form of cancellous bone.

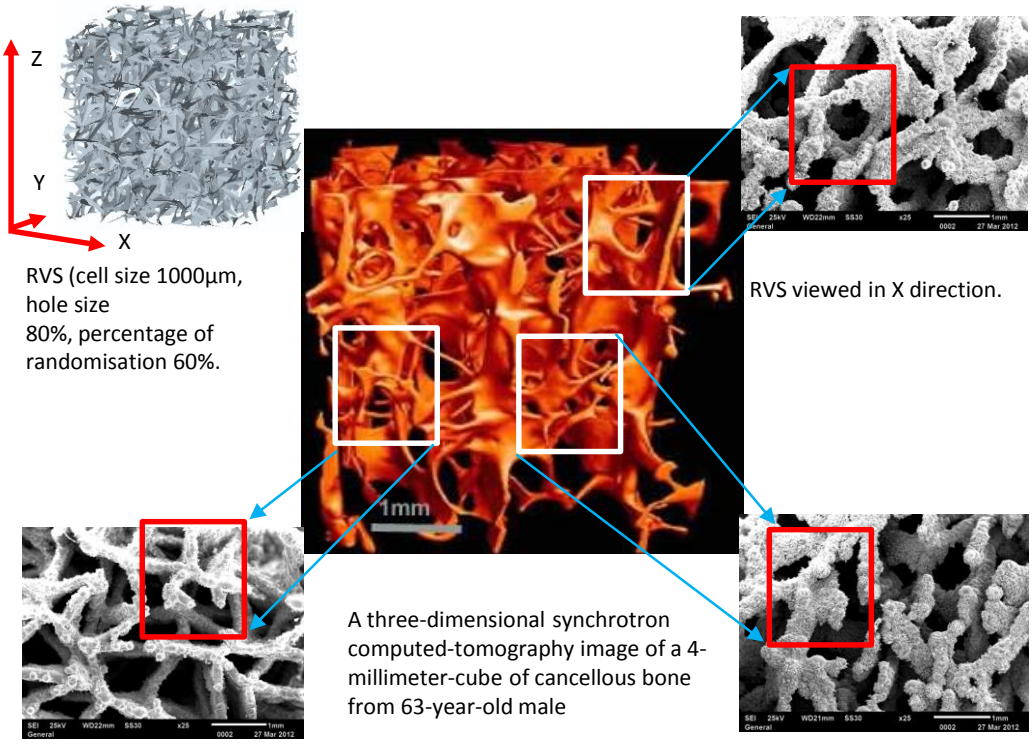

Figure 4-20 The features (in the white box) of cancellous bone from a 63-year-old male [182] are similar to the features (in the red box) of the RVS (cell size 1000µm, hole size 60%, percentage of random 0-60%) viewed in x, y and z directions.

As seen in Figure 4-21, all the features (deformed struts and platelets with hole) in the cancellous bone from a young patient can also be founded in the SEM images of the RVS. However, the sample of the 63-year-old male's bone is very different from that of a 30-year-old male (Figure 4-21). It can be seen that the cancellous bone from younger patient is more dense and has a thicker surface with smaller holes which are consistent with the descriptions given by Moskilde [183] and Partfitt [184].

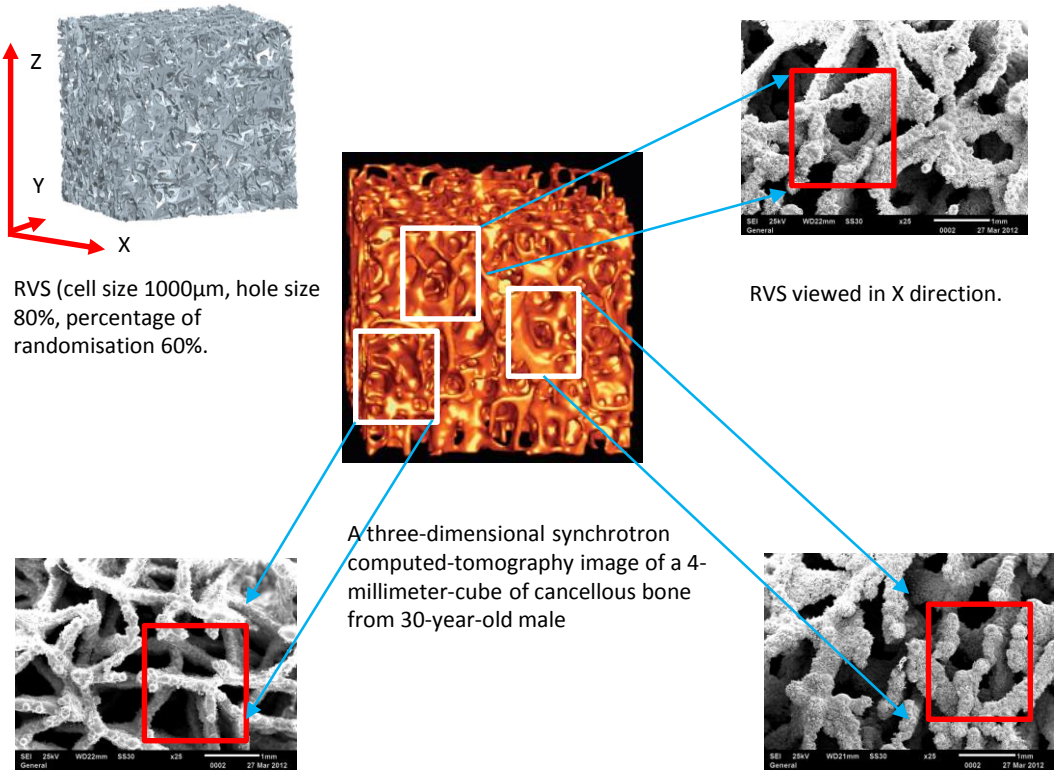

Figure 4-21 The features (in the white box) of cancellous bone from a 30-year-old male [182] are similar to the features (in the red box) of the RVS (cell size 1000µm, hole size 60%, percentage of random 0-60%) viewed in x, y and z directions.

In order to mimic the appearance of cancellous bone from a 30-year-old male, a RVS with smaller holes (60%) and cell size (600µm) are needed to give this dense appearance. In Figure 4-22, a comparison of the appearance of the cancellous bone from a 30-year-old male with this RVS shows that all the features observed in the bone are present; including the deformed surface with holes and struts.

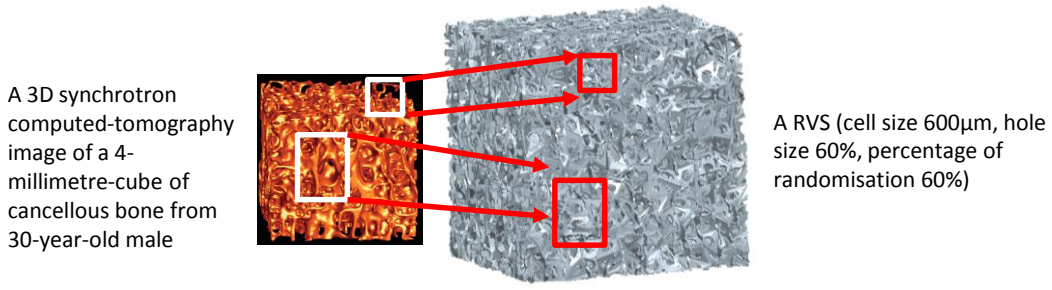

Figure 4-22 The features (in the white box) of cancellous bone from a 30-year-old male [182] are similar to those found in the RVS.

4.4. Re-Constructing the Vaulted Structure

With the non-randomised structures, if the unit cells are located outside the solid model, their surfaces are not used for constructing the shaped VS and so are ignored during processing. However with the use of the randomised deformation mechanism, these unit cells may move into the solid model and their surface will then be used for constructing the shaped structure. If these unit cells are not considered, it can lead to an open appearance as shown in Figure 4-23.

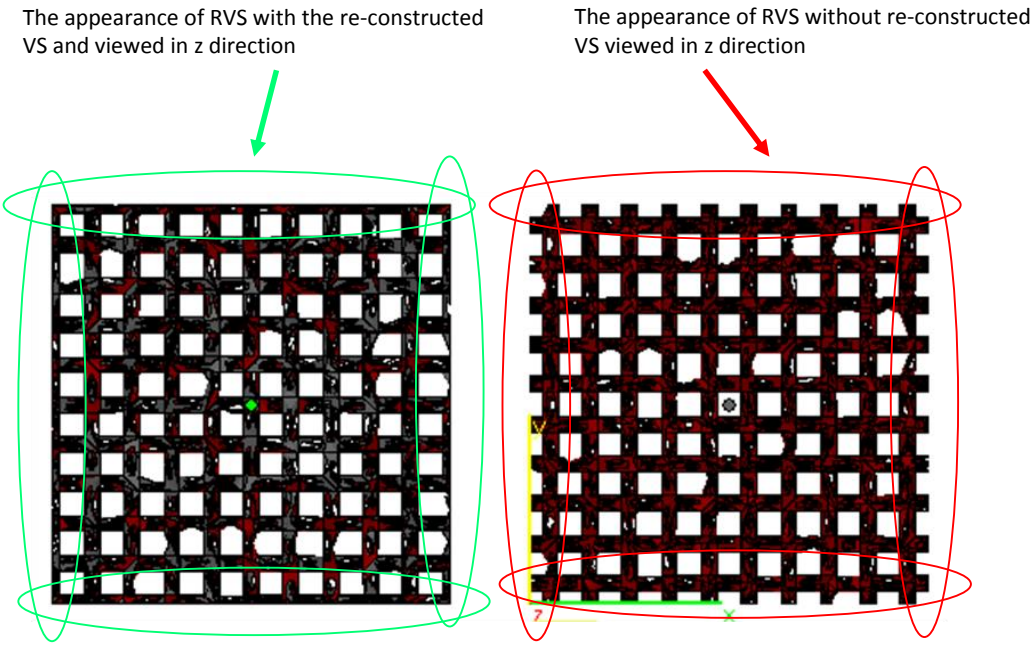

Figure 4-23 RVS generated by new custom software with re-constructed function (left) and without re-constructed function (right), they are viewed in z direction.

In order to avoid this problem, the VS block is enlarged to contain all the unit cells whose surface may fall into the solid model. This enlargement can be carried out by computing the number of extra unit cells in each direction that may form part of the structure on randomisation and the number of unit cells can be found by equation (4-26) to (4-28). The number of unit cells must be rounded to the upper integer. Then by repeating the processes in section 4.2, the enlarged VS block is used to construct the deformed structure.

$$Nx = Nx + \frac{Maximum\ move\ in\ x\ direciton}{length\ of\ cell} \quad (4\text{-}26)$$

$$Ny = Ny + \frac{Maximum\ move\ in\ y\ direciton}{width\ of\ cell} \quad (4\text{-}27)$$

$$Nz = Nz + \frac{Maximum\ move\ in\ z\ direciton}{height\ of\ cell} \quad (4\text{-}28)$$

4.5. Trimming the Vaulted Structure

In this section the trimming of the structure to a more complex shape will be considered. The tessellated surface of the solid model partitions space into a bounded inside region and an unbounded outside region. In order to simplify the computing process, the surfaces of a VS block were tessellated and then any triangle in the inner region was kept while any triangle located in the outer region was deleted. Any triangle intersected by the surface was trimmed and the section inside of the surface kept. Finally a VS block was trimmed to the desired shape. The above process involves a large amount of computing effort but the computing time can be reduced by introducing the bounding box method detailed in Chapter 2. The flowchart of the bounding box method is shown in Figure 4-24.

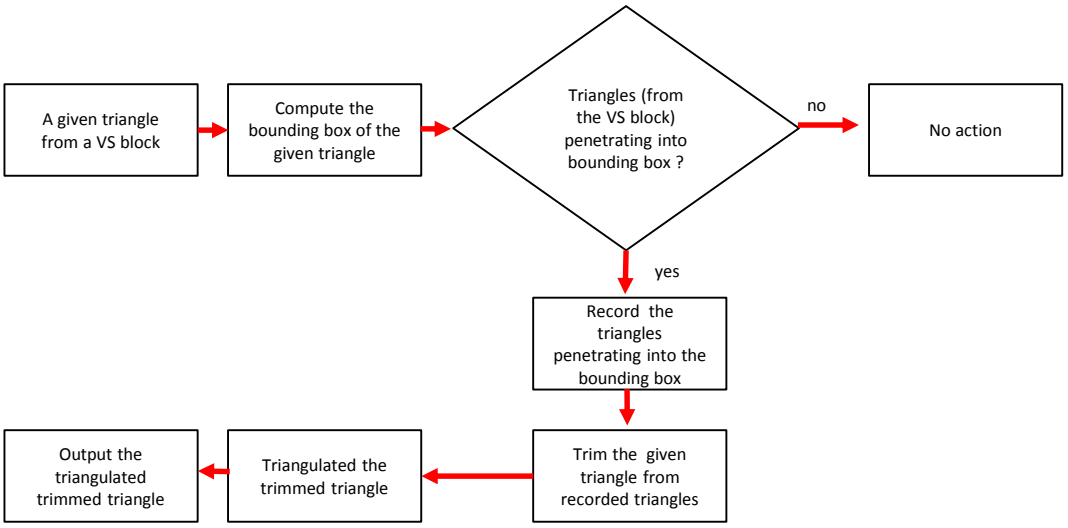

Figure 4-24 Flowchart of the bounding box method.

As discussed in the section of constructing the VS blocks, the surfaces of each unit cell were tessellated by triangles and these triangles were in one unit cell so that a unit cell can be considered as the common bounding box of triangles in the unit cell. The changes to the procedure can be seen by comparing Figure 4-24 with the flowchart for the revised method shown in Figure 4-25.

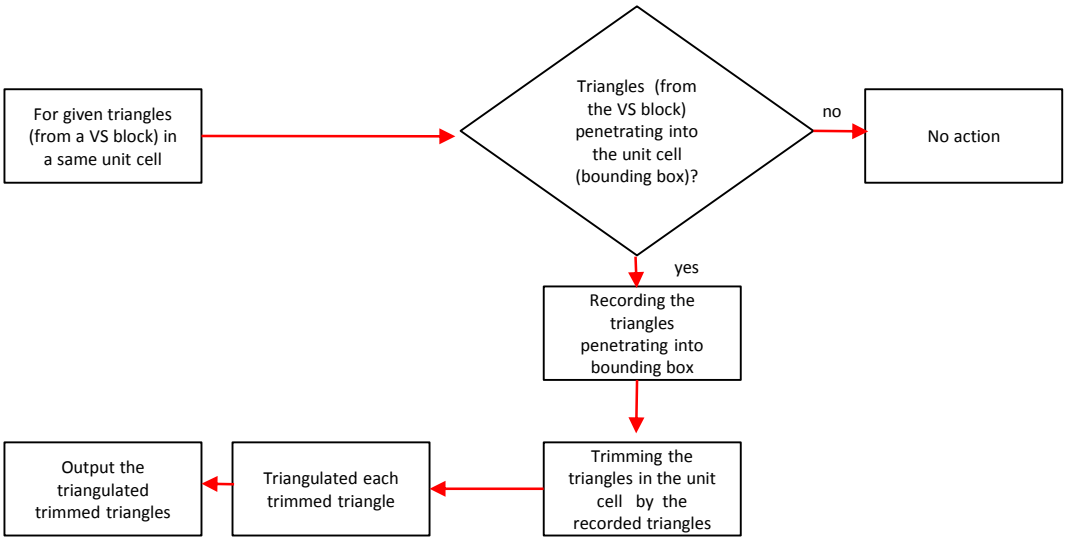

Figure 4-25 A revised method for trimming a given triangle by triangles from a tessellated surface.

Further tests were carried out to measure the computing time. Three codes were written to repeat three trimming methods while measuring the computing time. In order to eliminate the effect of other applications when measuring computing time,

the computing time of various trimming times were extracted directly by using the Psutil module discussed in Chapter 3. In these tests, a cylinder (height 32mm, diameter 15mm) with tessellated surface of 240 triangles was created by Magics. A VS block larger than the bounding box of the cylinder was created with various cell sizes which gave different numbers of structure triangles. These triangles were trimmed by the cylinder surface triangles using the three trimming methods and the various computing times were measured. Figure 4-26 shows that one of the trimming methods saves computing time especially as the number of triangles in each cell increases.

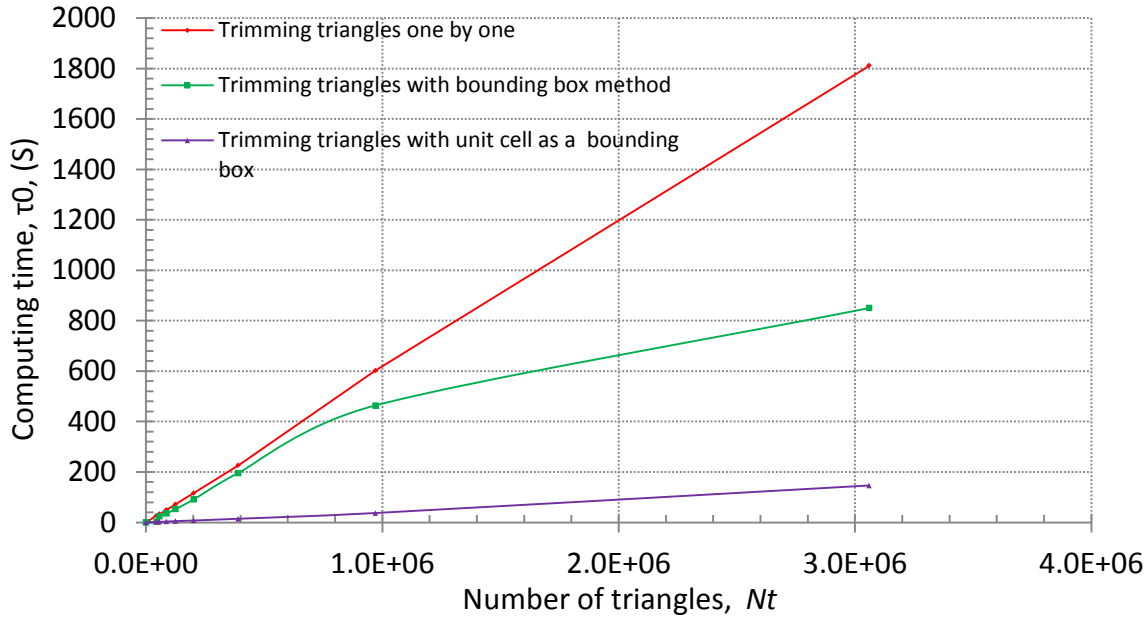

Figure 4-27 Computing time taken by three different methods to trim a VS with various numbers of triangles by a cylindrical surface (height 32mm, diameter 15mm) constructed by 240 triangles.

A problem with the commercially available software like Magics is that it can only trim a solid model that has closed surfaces. However in this research, the VS is constructed with open surfaces. Thus further work was carried out to test whether the VS with an open surface could be trimmed using commercial software. Figure 4-28 shows a VS block that was trimmed by the commercial software Magics V9.5.4.7. The trimmed result performed by the new software gives a clearer boundary. Therefore the new trimming function is necessary for trimming VS blocks with open surfaces and cannot be replaced by Magics V9.5.4.7.

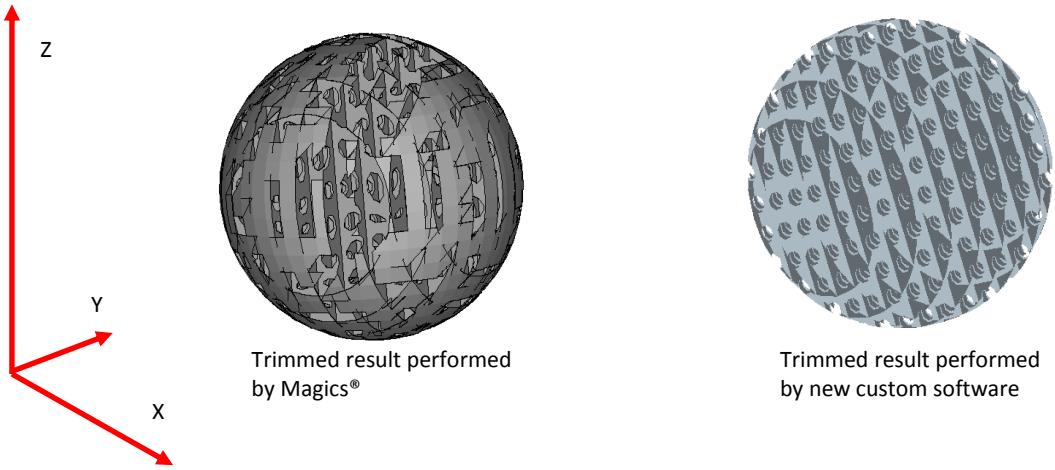

Figure 4-28 The trimming functions were performed by Magics and new custom software.

After it had been shown that a VS could be trimmed to the desired shape it was necessary to fabricate the part using the SLM. A solid model of an acetabular cup was filled with the RVS as shown in Figure 4-29. The total acetabular cup including the porous structure part and the solid part were fabricated by using the SLM 100 as shown in Figure 4-30. The smooth surface indicates that the trimming function works properly for open surfaces.

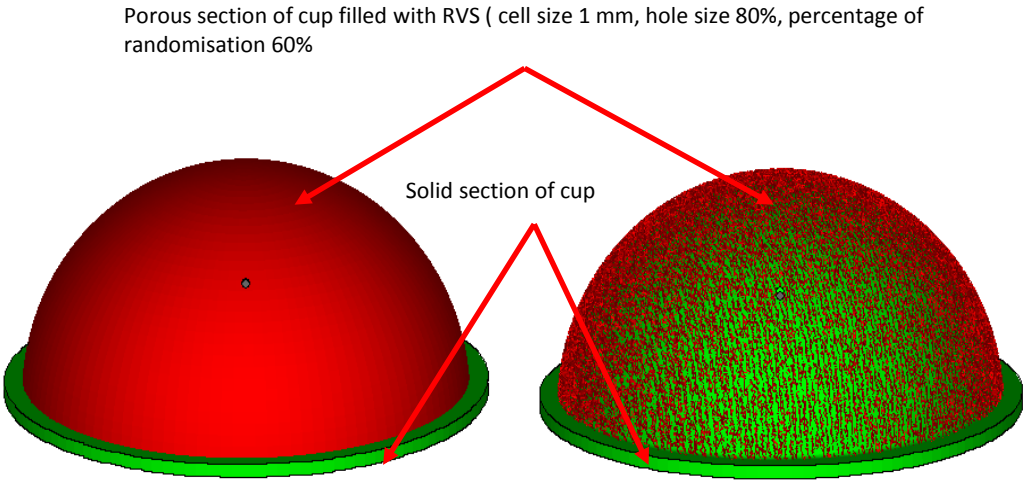

Figure 4-29 Illustration of an acetabular cup filled with VS in .stl format.

Figure 4-30 Fabricated the trimmed result by SLM Realizer 100.

When trimming the VS block, the dimensions of it were controlled to match the original shape of the solid model. The example in Figure 4-31 shows a VS created and trimmed to a cylindrical shape. The model of the cylinder (height 32mm, diameter 15mm) was created by Magics V9.5.4.7 and two VSs with the same parameters were created and trimmed by FreeSteel® and the new custom software. The overall size of a trimmed VS was measured using Magics. As can be seen (Figure 4-31), the size of the cylindrical VS block was the same as that of the original cylinder. While the size of the cylindrical VS (height 36mm and diameter 18.891mm) trimmed by Plateletqt is very different from that of the original cylinder. These results, considering the trimming of the part, indicate that the new trimming method is better at retaining the overall shape and size of the component avoiding further machining which would result in increased cost.

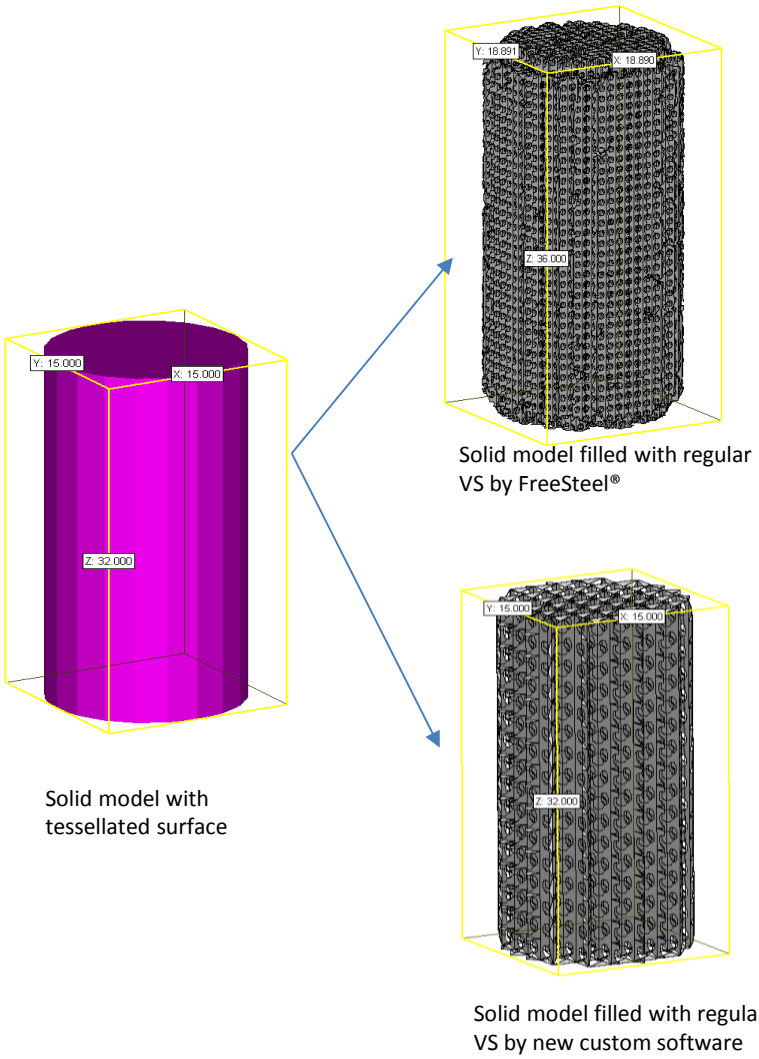

Figure 4-31 Illustration of the tolerance control in the trimming procedures done by different software.

4.6. Slicing the Vaulted Structure with a Desirable Shape

It is necessary for a structure block with the desired shape to be sliced for AM fabrication. As discussed in Chapter 2, when slicing the bone ingrowth structure with struts, some of the sliced points are too close to each other or duplicated and this results in excessive material particles being melted [152]. Similar problems can be found when slicing a VS. Figure 4-32 shows a VS that was sliced by a slicing plane. The slicing plane intersects the VS on lines which are used to direct the laser scanning. The intersections on these lines are scanned more than once by the laser and this leads to excessive melting as shown in Figure 4-34 A.

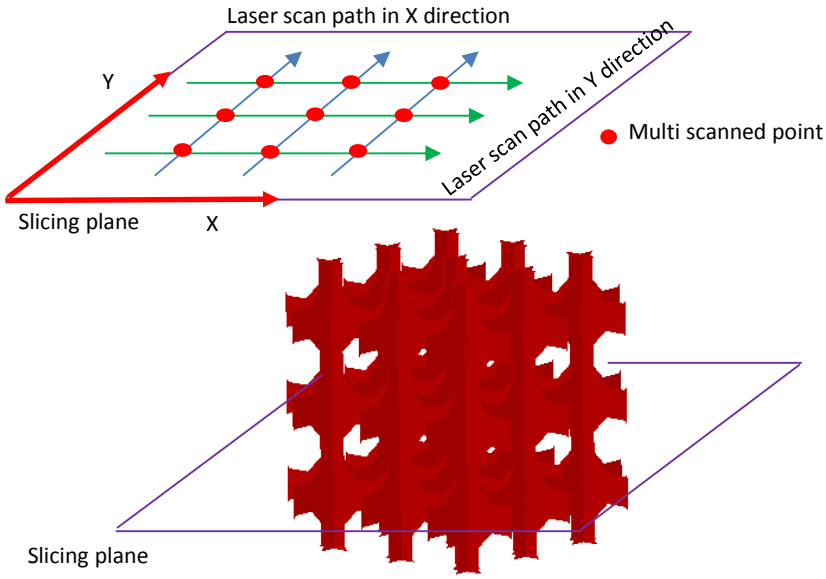

Figure 4-32 Illustration of Magics slice mechanism.

4.6.1. Slicing Mechanism

To overcome the issues raised above with the previous slicing mechanism the laser scan path was modified to remove any duplicated points so that the laser did not scan the same point twice. This is illustrated in Figure 4-33 where the laser scan path EF and HN intersects at point C which leads to a multi-scan. For Realizer SLM 100 the laser scan path is made up of many individual points and therefore the path EF can be replaced by laser scan paths EP, GF and point C with the gap between them being set to one point distance as determined by equation (4-29). This ensures complete melting between the points resulting in a full formed platelet, but not overheating one point [171].

$$point\ distance = \sqrt{2}\, r_p \qquad (4\text{-}29)$$

Where r_p is the diameter of the smallest pillar

The pillar size used was chosen from a set of single pillars that was built using a single laser spot. The single laser spot melts the powder particles to form a melt pool which is directly related to the pillar size. For a focused laser beam, the melt pool sizes can be altered by a combination of a range of laser powers and exposure

times and this gives a set of pillar sizes. With the low values of the parameters insufficient energy is provided for building a fully formed pillar and these were rejected. Then the parameters for building a full formed pillar with the smallest diameter were achieved to avoid excessive powder particles melting. Finally similar processes were carried out on the laser scan path HG and then extended to all laser scan paths on each layer.

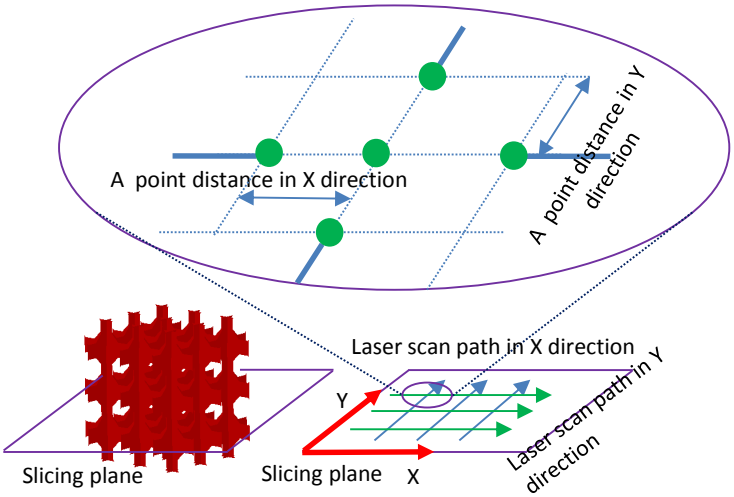

Figure 4-33 Illustration of the new slice method for eliminating the multi-scanning issue.

4.6.2. Verification of the Slice Processing Methodology

A cubic VS block was sliced using Magics V9.5.4.7 and the new software and fabricated using the SLM 100 with the fabrication parameters listed in Chapter 3. The comparison between the different slice methods was carried out by considering the SEM images and size of holes or nodes. The sizes were measured by ImageJ which is convenient for analysis as it can process a large number of size measurements. Therefore ImageJ is used here to measure the size of hole or node based on the SEM image and calibrated with reference to the SEM image scale bar. Figure 4-34 clearly shows the different sizes of node which is defined by the maximum thickness of a platelet. Then the sizes of node are summarised in Table 4-1. According to the mean of the sizes, it indicates that the new method can reduce node enlargement and gives a more constant thickness of a platelet.

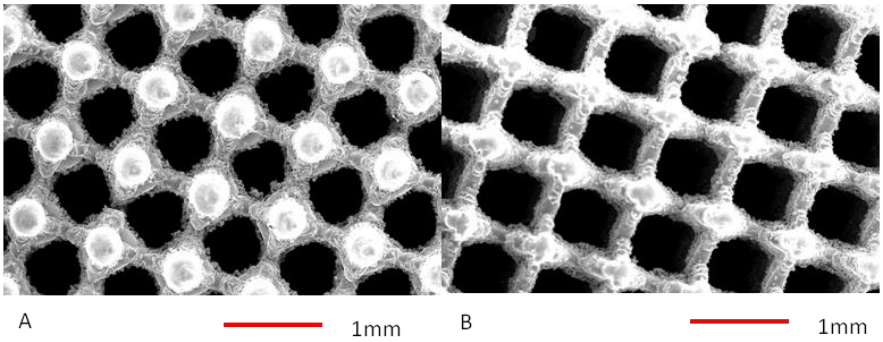

Figure 4-34 SEM images of the VS sliced by Magics (A) and by the new method (B) viewed in z direction showing reduced node enlargement.

Table 4-1 The summary of the maximum thickness of platelet varying in slicing methods

Method	Number of measurement	Mean (mm)	SD	Min (mm)	Max (mm)
Magics	10	0.66	0.05	0.58	0.72
New method	10	0.42	0.04	0.42	0.52

A comparison of the structure in the x direction, as seen in Figure 4-35, showed that by using new slicing method, the hole size was enlarged and its geometry was closer to a circle. This conclusion has been further verified by qualifying the hole size which are summarised in Table 4-2. The improvement of hole size can be identified by the larger mean of hole size and the low standard derivation.

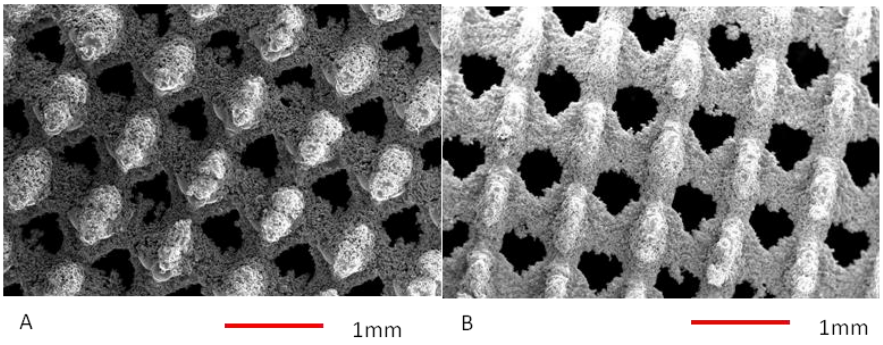

Figure 4-35 SEM images of the VS sliced by Magics (A) and by the new method (B) viewed in x direction showing improved hole resolution.

Table 4-2 The summary of the maximum hole size varying in slicing methods

Method	Number of measurement	Mean (mm)	SD	Min (mm)	Max (mm)
Magics	10	0.51	0.05	0.43	0.57
New method	10	0.57	0.03	0.53	0.62

Finally similar comparisons were carried out in y direction. As can be seen in Figure 4-36, the holes in the VS sliced by Magics are nearly closed due to the excessive sintering of the powder particles onto the hole edges. However the holes in the structure sliced by the new method is more open. Furthermore, the new method can give constant hole size and geometry. This is clarified by the summary of the maximum hole sizes for the different slicing methods in y direction in Table 4-3.

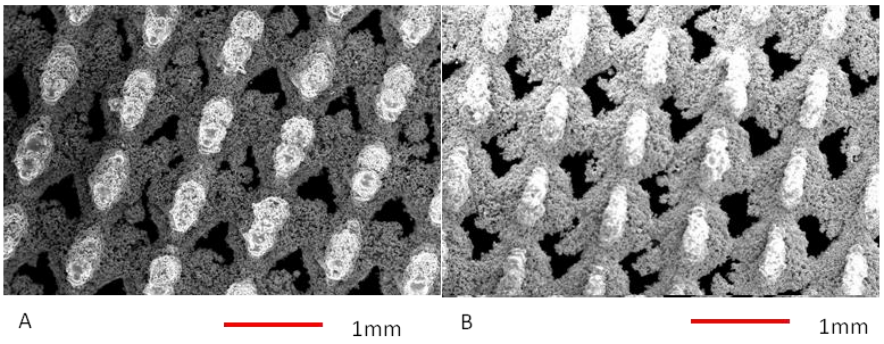

Figure 4-36 SEM images of the VS sliced by Magics (A) and by the new method (B) viewed in y direction showing more open holes.

Table 4-3 The summary of the maximum hole size varying in slicing methods

Method	Number of measurement	Mean (mm)	SD	Min (mm)	Max (mm)
Magics	10	0.47	0.05	0.36	0.57
New method	10	0.55	0.04	0.48	0.62

4.7. Determination of Part Porosity and Pore Size Distribution

In order to produce structures with the correct properties, normally a large number of samples must be fabricated and tested to determine their bone ingrowth suitability. This characterisation can be carried out on the models rather than the finished structures so the number of parts that would need to be tested is reduced. In this section, functions that allow the software to determine the porosity and pore size distribution of a VS are given and detailed.

4.7.1. Computed Porosity

The porosity of a VS sample can be computed by equation (4-30).

$$Porosity = \frac{Vol - Vol1}{Vol} \times 100\% \quad (4\text{-}30)$$

$$Vol1 = Ar \times th$$

Where $Vol1$ is the volume of triangle, Vol is the volume of a sample, Ar is the total area of triangles in VS, th is the thickness of fabricated triangles

When the random deformation mechanism is applied to the VS, the triangles in the block become extruded, rotated, transformed. This results in a change in the surface area and volume of the triangles that make up the structure, which then alters the porosity. To observe this effect, a set of cylinders filled with the randomised structure of varying levels of randomisation were created using the SLM fabrication parameters listed in Chapter 3. A model of the same structures with a platelet thickness of 310µm was also created. The effect of randomisation on the porosity was predicted by the mode and was plotted in Figure 4-37 which shows that as the percentage of randomisation increases, the porosity decreases because the volume that makes up the triangles increases.

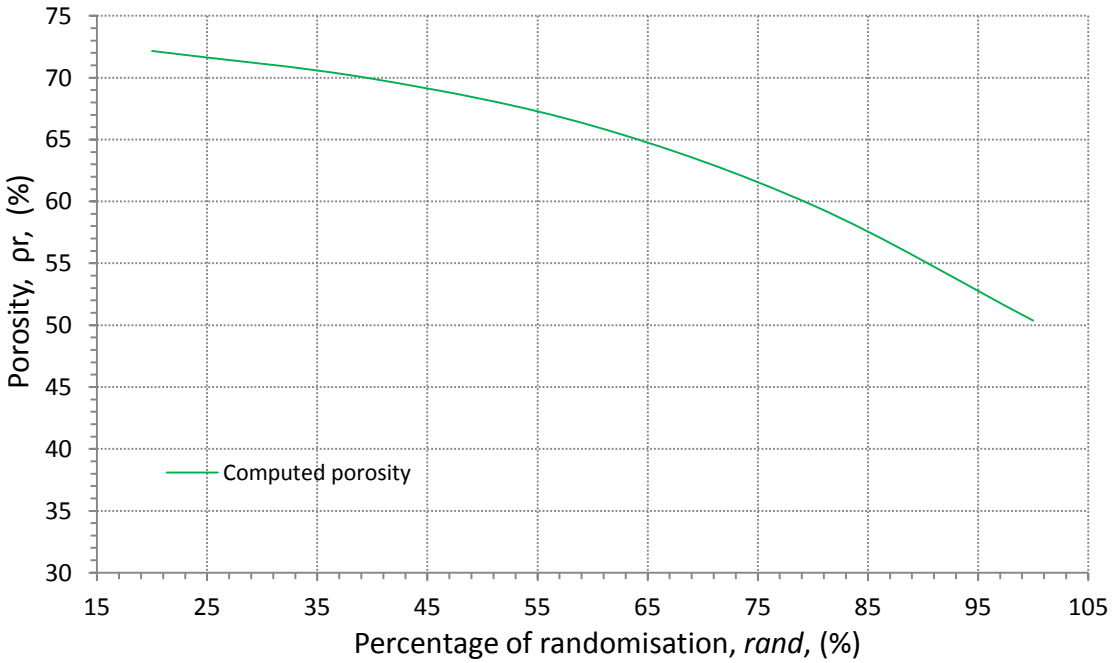

Figure 4-37 The computed porosity varying in percentage of randomisation.

It can be seen in Figure 4-38 that the SLM fabricated samples show a different trend to the model and the porosity was significantly higher than that predicted by the model. This may occur because the plates consist of both solid and sintered particles as seen in Figure 4-39. However the method used here (detailed in Chapter3) cannot tell how much sintered powder is present, resulting in a larger measured thickness of platelet. When this larger measured thickness (310µm) is used and assuming a uniform thickness, the computing porosity can be obtained and be lower than the measured porosity.

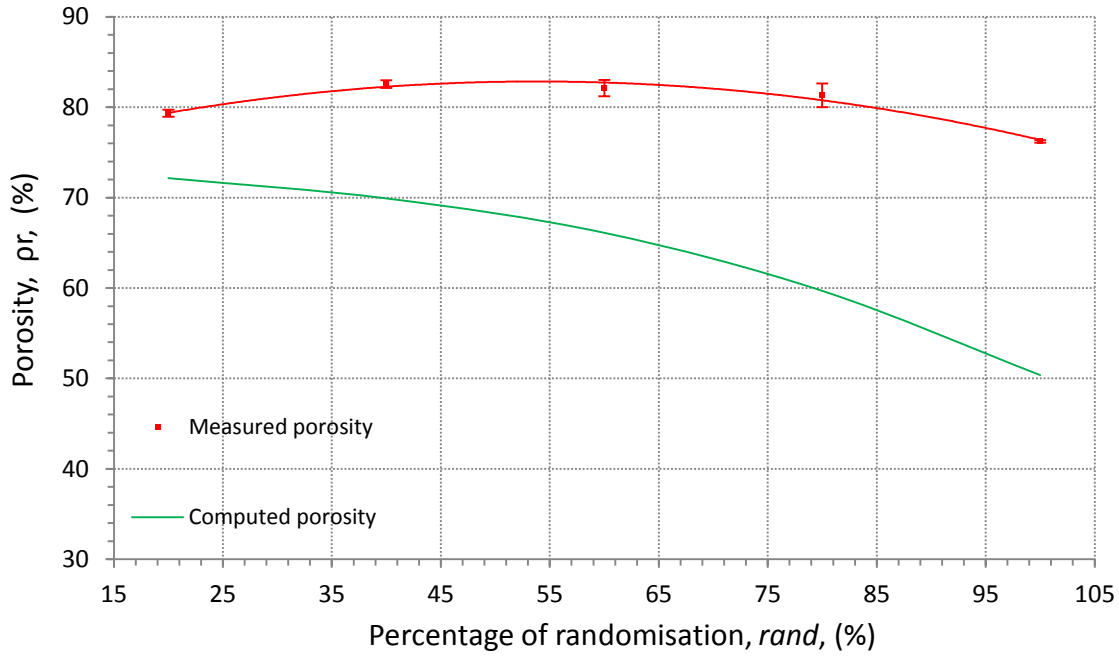

Figure 4-38 The computed porosity vs measured porosity varying in percentage of randomisation.

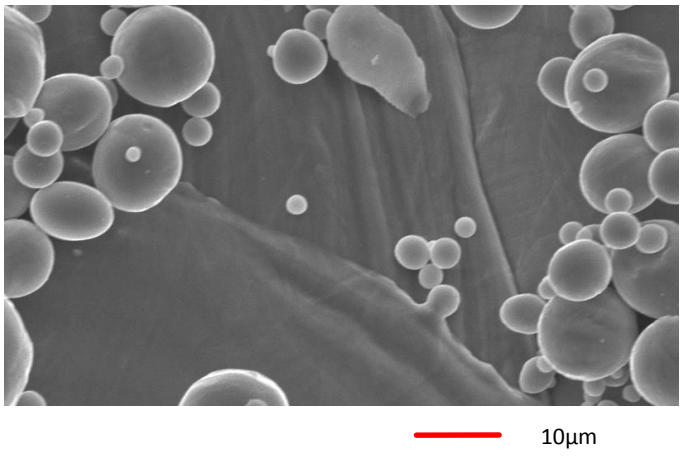

Figure 4-39 The sintered powder particles onto the platelet surface.

The other feature seen in Figure 4-38 is that the change in measured porosity is gentler in the actual samples, while the change in the model is much greater as the percentage of randomisation increases. This probably occurs because although the total area of triangles is increased with the increase in the randomisation percentage, some of triangles at low triangles cannot be built and there may also be the metal flow and bridging between the plates. The difficulty observed when fabricating at low angles to the horizontal can be seen by observing the sliced triangle in Figure 4-40 and the distance between sliced lines (AC), which is determined by equation (4-31):

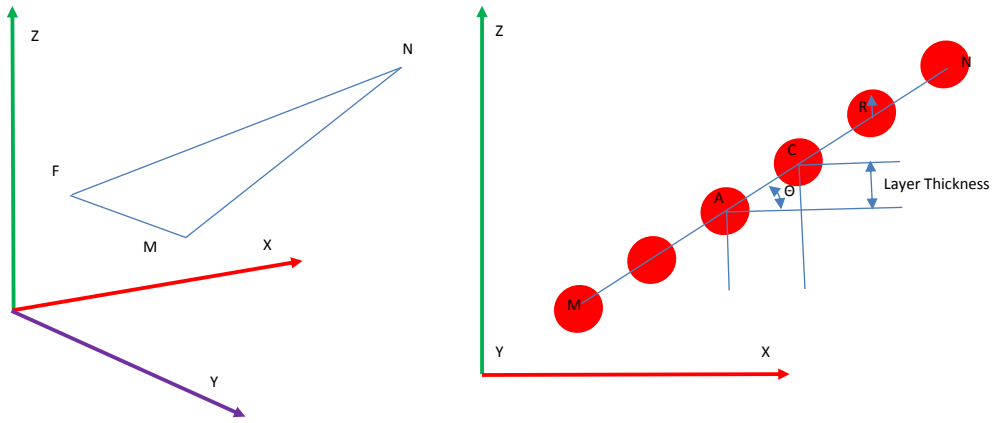

Figure 4-40 A view along the y direction of a sliced triangle FMN.

$$AC = \frac{LayerThickness}{sin(\varepsilon 0)} \qquad (4\text{-}31)$$

Where is $\varepsilon 0$ the angle between a triangle and Z plane

In order to ensure the adjacent sliced lines (scan vectors) can be melted together, the diameter (v) of fabricated sliced lines must be:

$$v \geq AC \qquad (4\text{-}32)$$

For given fabrication parameters, the angle can be determined by the diameter (v) and layer thickness.

$$\alpha = \arcsin\left(\frac{LayerThickness}{v}\right) \quad (4\text{-}33)$$

When the angle of a triangle is less than α, it is likely that the triangle will not build because the individual melt pools do not overlap. For the fabrication parameters (Table 3-3) listed in Chapter 3, any triangle at an angle of less than 21° is defined as a low angle triangle and is very unlikely to build. However, the number of low angle triangles is increased by the randomisation process. The increase in the number of low angle triangles with increased randomisation can be seen in Figure 4-41.

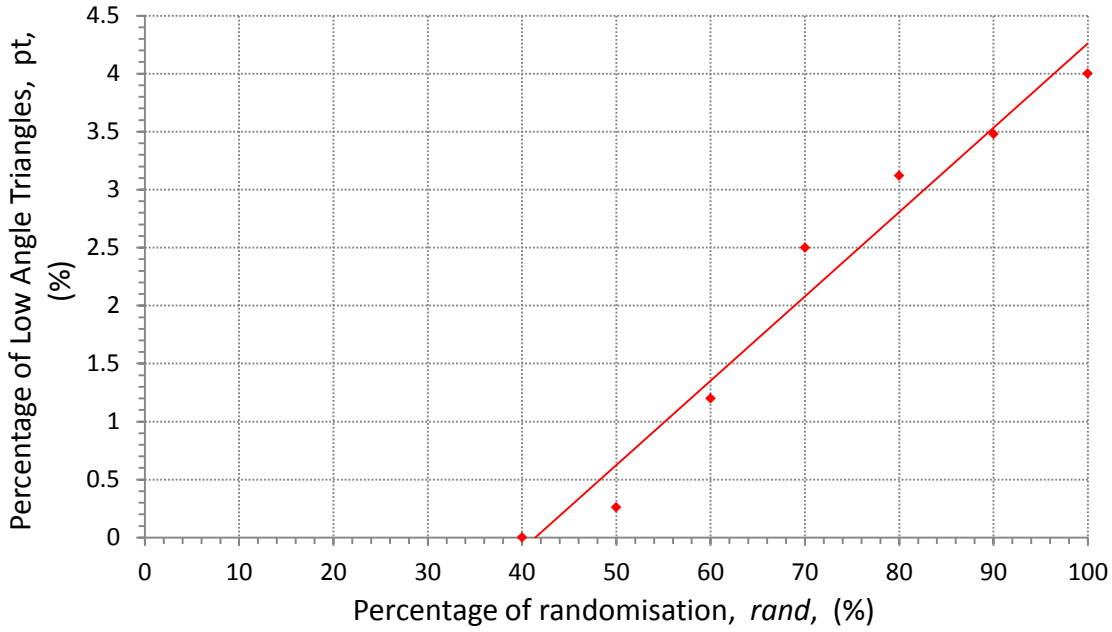

Figure 4-41 The effect of randomisation on percentage of low angle triangle.

In order to minimise the discrepancy between the model and reality the effect of low angle triangles was taken into account when computing porosity in the model. This can be seen in the revised equation for computing the porosity (4-34). Figure 4-42 shows that the revised equation can reduce the difference between the computed porosity and measured porosity.

$$Porosity = \frac{Vol - Vol1 - Vol2}{Vol} \times 100\% \quad (4\text{-}34)$$

$$Vol1 = Ar \times th$$

$$Vol2 = Ar1 \times th$$

Where $Vol1$ is the volume of triangles, Vol is the volume of a sample

$Vol2$ is the volume of low angle triangles, Ar is the total area of triangles

$Ar1$ is the total area of low angle triangles, th is the thickness of fabricated triangles

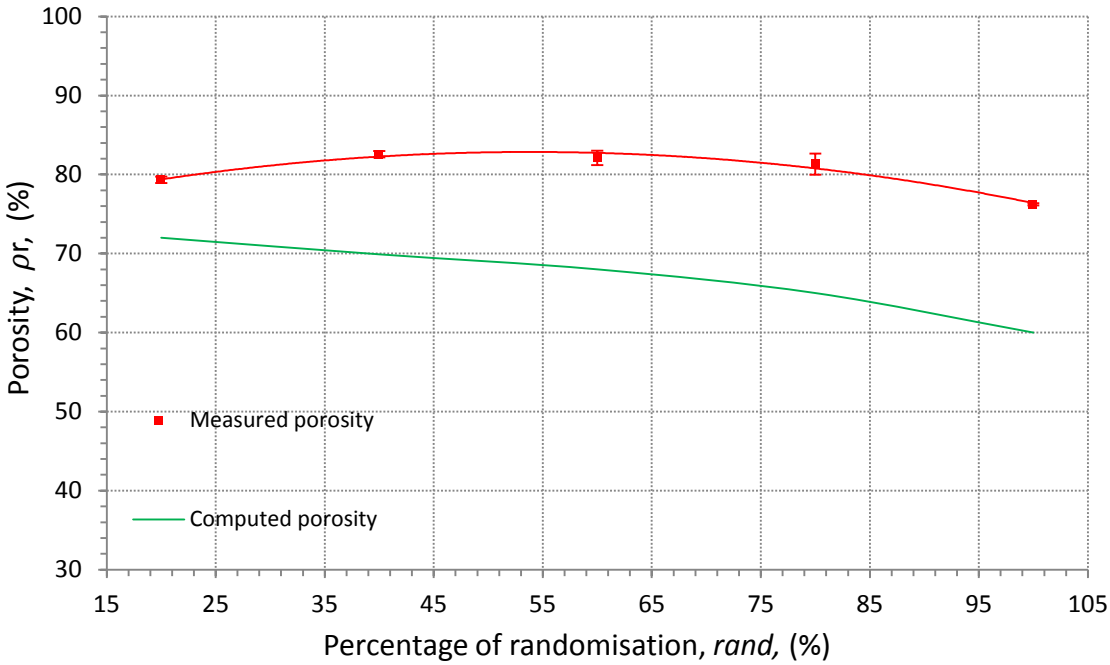

Figure 4-42 The relationship between randomisation and porosity with respect to the percentage of low angle triangles

4.7.2. Computed Pore Size Distribution

As discussed in Chapter 3, the pore size distribution can be computed by simulating mercury porosimetry and the accuracy can be up to 99.9% [173], but to do this the model needs to be represented by a set of cubic or spherical volumes in a process referred to as voxelisation [173,185]. The voxelisation of a model can lead to a large memory requirement to store the diameter and coordinates of sphere centres which limit its application. For example, a cell (10mm × 10mm × 10mm) in a VS was voxelised by the code provided by Yue [185] and the file for the voxelised cell was 1.01GB. Following trials, the voxelisation methodology proposed by Yue was difficult to implement because of computer memory usage. It proved impossible to voxelise this sample using a standard specification desktop (Intel core ™2 Duo CPU E8400@3.00GHZ with 4GB memory) and therefore the code was redeveloped as described below.

The bounding box of this porous structure was determined using equations (4-1) to (4-6). As seen in Figure 4-43, this bounding box was meshed with a specified gap termed 'resolution' defined by equation (4-35). The intersections between the grid lines are nodes which are located either in the inside region or the outside region which is partitioned by the tessellated wall of the pore.

$$resolution = \frac{minimum\ (L0, H0, W0)}{total\ number\ of\ grid\ lines} \qquad (4\text{-}35)$$

$L0$ is the length of a bounding box

$W0$ is the width of a bounding box

$H0$ Is the height of a bounding box

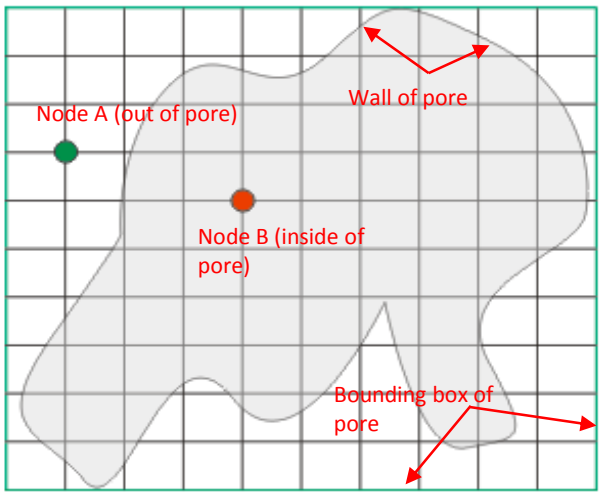

Figure 4-43 A gridded bounding box of a pore and illustrated nodes located in or out of pore.

The porosity of a single pore is measured by using a number of spheres. Taking a single pore as an example, a sphere, whose centre is located at an inside node, is grown with a specified step size, until it touches the wall (represented by triangles) of the pore using the faster intersection test method for a sphere with a triangle detailed in Chapter 2. This is principally different from the previous method which is based on the intersection test method for a sphere and sphere. It results in an intensive computing time for a large number of sphere and sphere intersection test.

As shown in Figure 4-44, once this is the case, it stops growing. The maximum sphere diameter at this node is recorded with the node coordinates. By repeating this process, a set of spheres with their centre coordinates is obtained. The total volume of the spheres, not including any overlap can be determined by using the VTK volume function (Chapter 3). This volume is the measured void space of the porous structure and the porosity can be obtained based on the definition of porosity. By decreasing the mesh size, the computed porosity is closer to the actual porosity of pore and the process is repeated. The process is a similar way to the mercury porosimetry (detailed in Chapter3) which approaches the actual porosity by increasing the pressure forcing the mercury to intrude into the smaller pores. As the pressure increases, the more mercury intrudes into void space and the measured volume of mercury is closer to the actual void space. However decreasing the mesh gap results in an increase in computing time and computer memory usage. Therefore, in the next stage, an equation (4-36) is given to stop the computing procedure when the difference between the current compute porosity and previous porosity is limited to a pre-defined value, termed stop value.

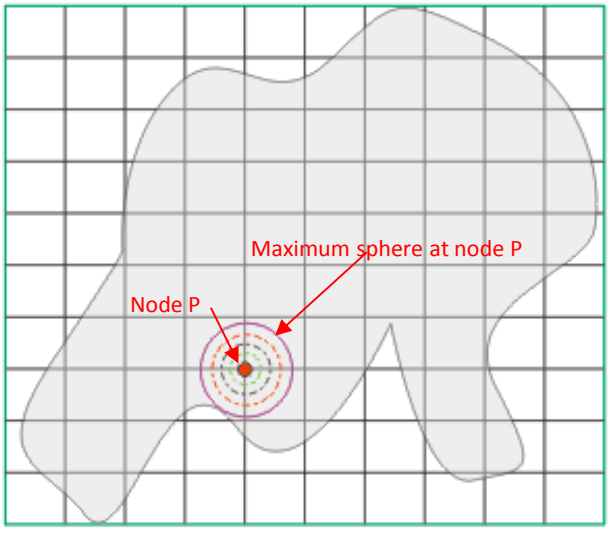

Figure 4-44 Schematic of the maximum sphere at the node P.

$$stop\ value\ = \frac{Previous\ porosity - Current\ porosity}{Current\ porosity} \times 100\% \qquad (4\text{-}36)$$

$stop\ value$ is set prior to computing procedure

Then a set of porosities was obtained as well as their corresponding smallest sphere diameters. A cumulative histogram $H(D)$ is then constructed, where $H(D)$ represents the probability of finding a point in the model space with a pore size greater than or equal to D. The pore size distribution $P(D)$ is the negative of the differential coefficient of $H(D)$ with respect to D:

$$P(D) = -\frac{dH(D)}{dD} \qquad (4\text{-}37)$$

In order to verify this method, an arbitrary porous structure (cube 10mm × 10mm × 10mm) with specified pore size distribution was generated as shown in Figure 4-45 and its file size was only 1MB. By using the revised method, the computed pore size distribution was achieved as shown in Figure 4-46 by the use of standard personal computer.

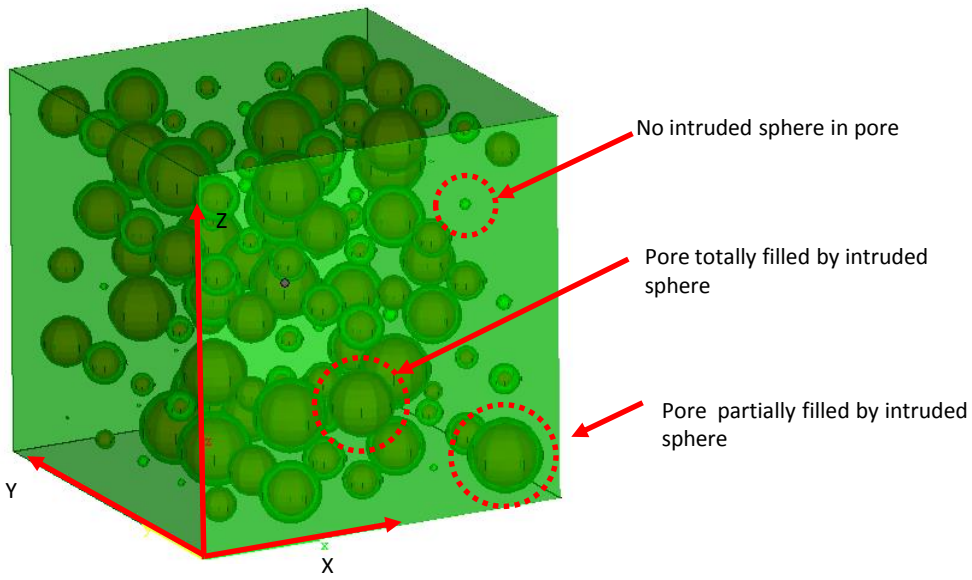

Figure 4-45 Illustration of a cube with specified pore size distribution.

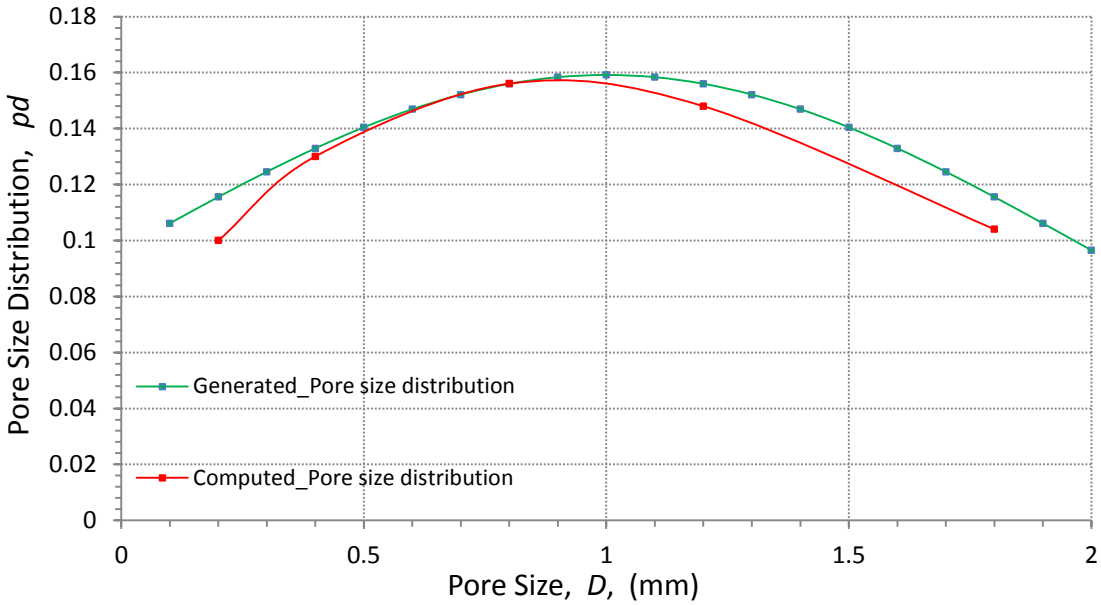

Figure 4-46 Comparison of the generated pore size distribution and computed pore size distribution.

Further work was carried out to fully understand the above results. The computed pores and arbitrary porous structure are visualised in Figure 4-47. This shows that the small pores are not intruded by the spheres and large pores are not totally filled with intruded spheres and this results in a reduced accuracy when the pore size is too small or big as in Figure 4-46. In order to solve the above issue, a higher resolution is required to ensure the smaller pores are intruded and the large pores are fully filled with spheres.

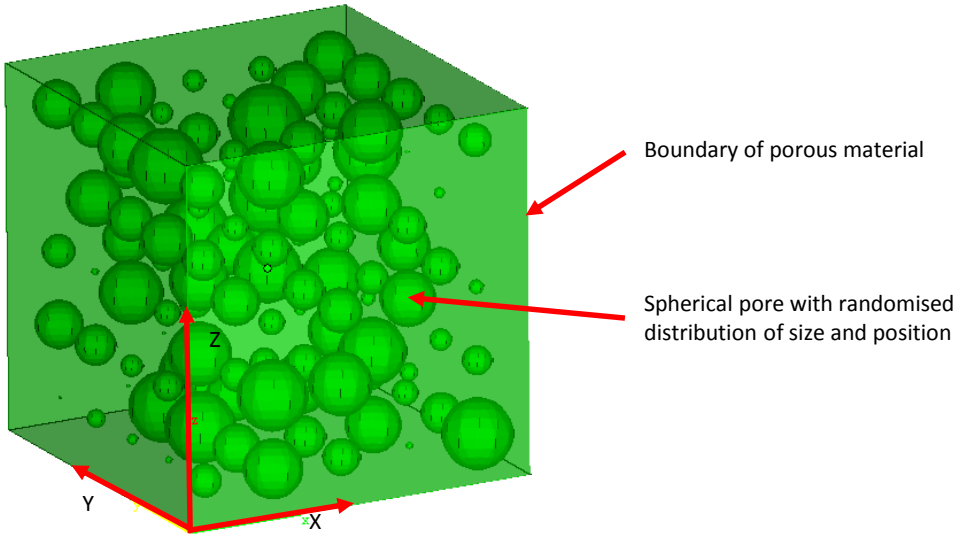

Figure 4-47 Visualisation of pores in cube and intruded spheres.

The computing error is expressed by an equation (4-38) and when it is smaller than the defined error, the process is stopped.

$$error = \frac{Previous\ PSD - Current\ PSD}{Current\ PSD} \times 100\% \qquad (4\text{-}38)$$

PSD is the pore size distribution

Alternatively, the error can be expressed by (4-39) and the porosity of a porous model can be measured by some commercial software such as Magics. The computed porosity is related to the resolution. For a given resolution, when the error is equal to zero which indicates that all the void space is intruded and further processing is not needed.

$$error = \frac{Computed\ porosity - \ Measured\ porosity}{Computed\ porosity} \times 100 \qquad (4\text{-}39)$$

4.8. Additional Function

As discussed, a VS is constructed from open surfaces (triangles). However a closed surface is required by the majority of AM technologies to produce builds. In this section, a method is introduced for creating VSs with a closed surface as described below. As can be seen in Figure 4-48, a triangle ($V_0V_1V_2$) in the VS is covered with a closed surface defined by 6 new vertices ($V_{01}V_{11}V_{21}$ and $V_{02}V_{21}V_{12}$). These vertices are obtained by offsetting the vertices ($V_0V_1V_2$) of the original triangle along the vector by half the specified thickness in position and negative direction and then tessellated to form a closed surface. Using this method, a VS with closed surfaces is obtained and trimmed to get a desired shape as discussed previously.

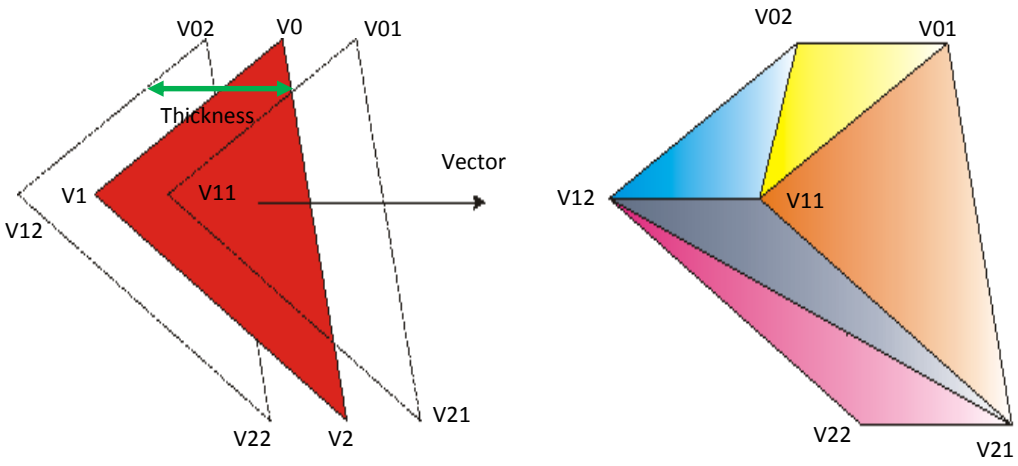

Figure 4-48 Illustration of principle of creating a closed surface for a VS with an open surface.

For clarity, closed surfaces are created for regular and RVSs and then fabricated using a 3D printer as shown in Figure 4-49 and Figure 4-50. In some cases a smooth closed and continuous surface is required. The surface can be created following the above method and the only difference is more triangles are required to construct the more complex surfaces.

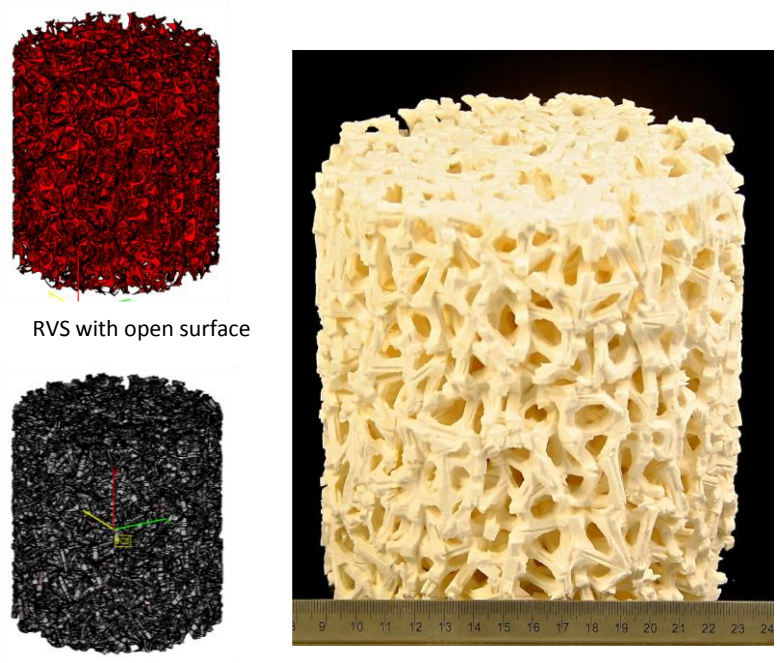

RVS with open surface

RVS with closed surface

RVS with closed surface fabricated by 3D printer

Figure 4-49 A RVS with open surface is constructed with closed surface and fabricated by a 3D Printer.

Regular VS with open surface

Regular VS with closed surface

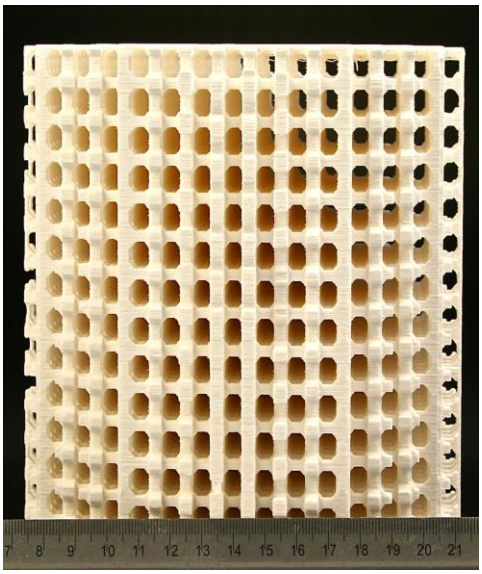

Regular VS with closed surface fabricated by 3D printer

Figure 4-50 A regular VS cylinder with open surface is constructed with closed surface and fabricated by a 3D Printer.

4.9. Summary

In this chapter, the development of a software solution for representation of VS was described and detailed. By using this software, a VS can be created and trimmed with a desired shape and then sliced for AM fabrication. This VS can mimic the appearance of cancellous bone both for young and old patients. Furthermore, it provides functions for computing the porosity and pore size distribution of a digital model rather than the finished structure reducing the number of test samples required for verification. Additionally, in order to fabricate the VS by other AM technologies such as 3D printing, a function was designed to create closed surfaces for the VS. Finally all the source codes and software involved in this research project have been submitted on the attached optical disk.

CHAPTER 5

REGULAR VAULTED STRUCTURES

As discussed in Chapter 4, the new custom software can create shaped vaulted structures with random deformed surfaces. However by introducing the random deforming mechanism, the randomised VS becomes quite complex. This complexity makes it difficult to investigate the range of available mechanical properties of the structure directly. In this section of the research, we investigate how to control both the porosity and the mechanical behaviour of the regular vaulted structures. This experience and methods are then extended to investigate randomised vaulted structures.

This work is based on the vaulted structures with four platelets in each cell. The effect of design parameters including hole size, platelet thickness and cell size are investigated. The results indicate that a wider range of properties is possible compared with the unit cell structure with struts described in Chapter 2. However even though there were improvements it was not possible to completely remove the anisotropic behaviour of the structure.

5.1. Candidates for the Regular Vaulted Structure

As discussed in Chapter 4, if the cells in the vaulted structures are continuous and well connected to each other by sharing platelets or edges there are many ways to create different vaulted structures with various distributions of platelets in each unit cell. Hexagonal, quadrilateral and triangular distributions of platelets are possible. Platelets with these distributions can be used as models to investigate porous structures that mimic wood, foam and bone [174].

For a quadrilateral distribution as shown in Chapter 4, there are four combinations of platelets in each unit cell. For the six platelets in each unit cell, it is difficult for SLM machine to build the platelets that are perpendicular to the fabrication direction and so these are left out of the structure. For the two platelets in each

unit cell, they can be arranged vertical to each other (Figure 5-1) and the overlap can be defined by equation (5-1).

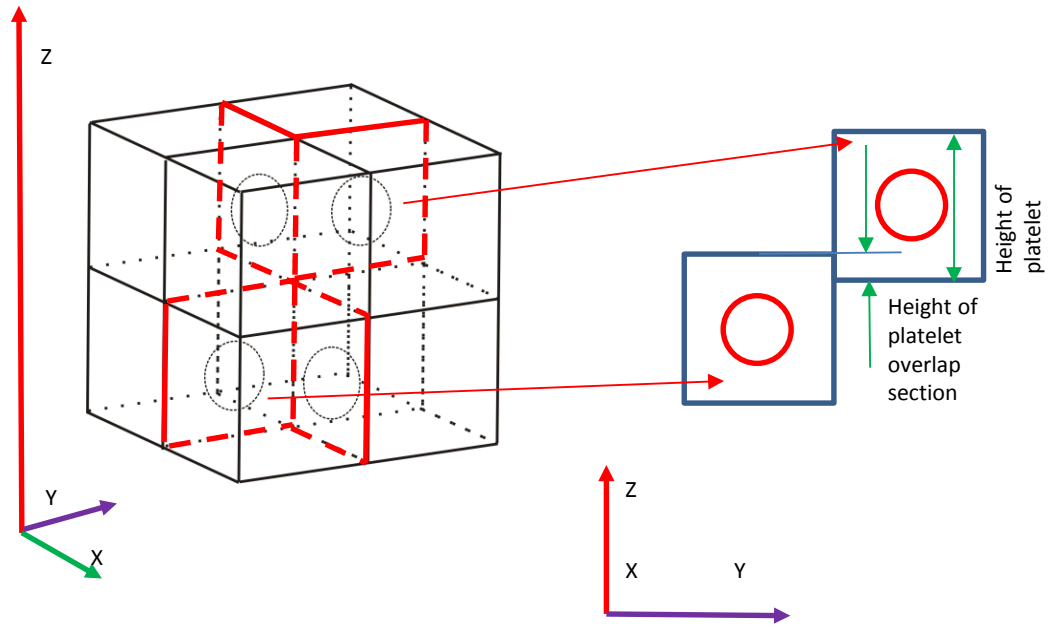

Figure 5-1 A VS (two vertical platelets with right angle in each unit cell) viewed in the X direction.

$$overlap = \frac{Height\ of\ platelet\ overlap\ section}{Height\ of\ platelet} \times 100 \qquad (5\text{-}1)$$

In order to investigate the effect of the overlap on the compressive strength and porosity of the structures, an experiment was arranged. In this experiment, a group of VS samples (cell size 900µm, hole size 60% and two platelets vertical to each other in each unit cell) were created and fabricated using SLM with the parameters listed in Table 3-3. The experimental results presented in Figure 5-2 show the structure to be very weak, the platelets in adjacent cells only being connected together by the melting of the overlap section. This section represents the weak point of the structure [95]. When loaded in compression parallel to this overlap

section, shear failure occurs at [95] very low loads. However, if the overlap is increased the fused section is greater and the structure is stronger.

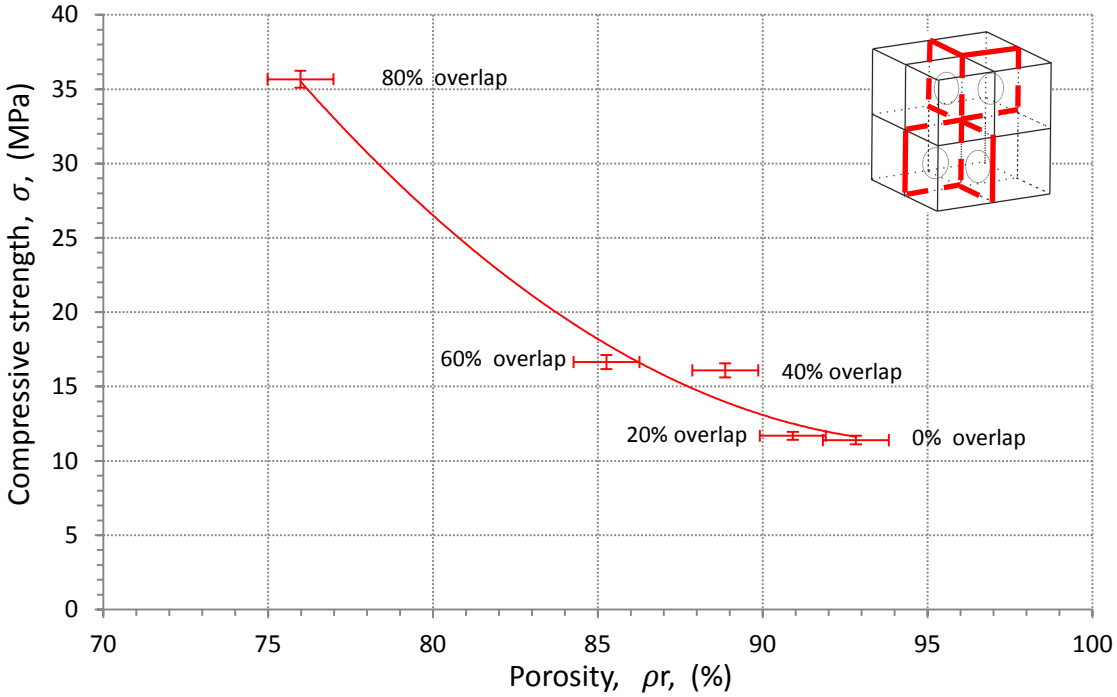

Figure 5-2 Overlap effect on porosity and compressive strength of the regular VS (two vertical plates in each cell, cell size 900µm, hole size 60%).

A similar experiment was conducted on the VS with two parallel platelets in each cell (Figure 5-3) and using an overlap defined by equation (5-1). The platelet in one cell is perpendicular to and sits on top of the platelet from its adjacent cells. Therefore, when loaded in compression the load is perpendicular to the plane (x, y plane) of the welded section and the failure mechanism is compressive yield rather than shear failure [95]. Shear failure typically occurs at lower loads than compressive yield [95], therefore a stronger structure can be seen in Figure 5-4. The increased strength is also due to the laser multi-scan on the overlap section, as the increased thickness gives more resistance to platelet deformation. Therefore, the increased overlap can improve the compressive strength of this structure; however the increased thickness only occurs in certain parts of the platelets in a non-uniform thickness.

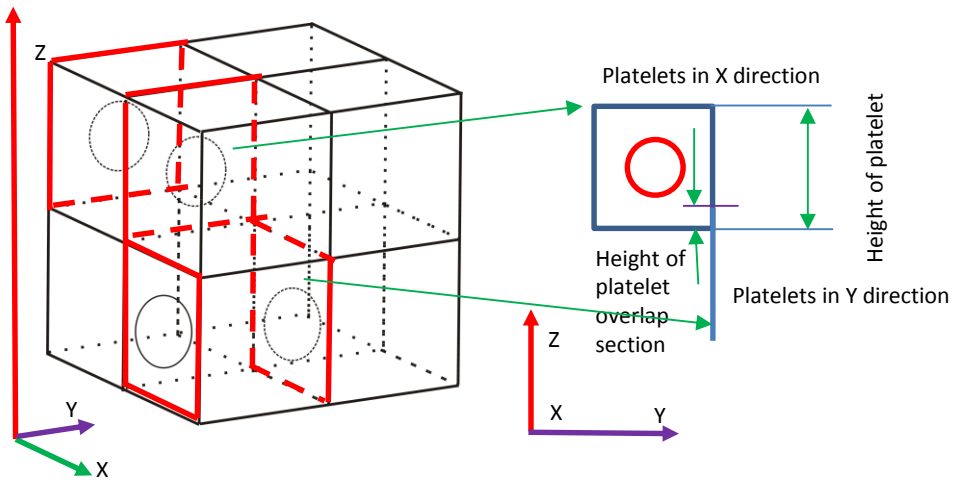

Figure 5-3 A VS (two parallel platelets in each unit cell) viewed in y direction.

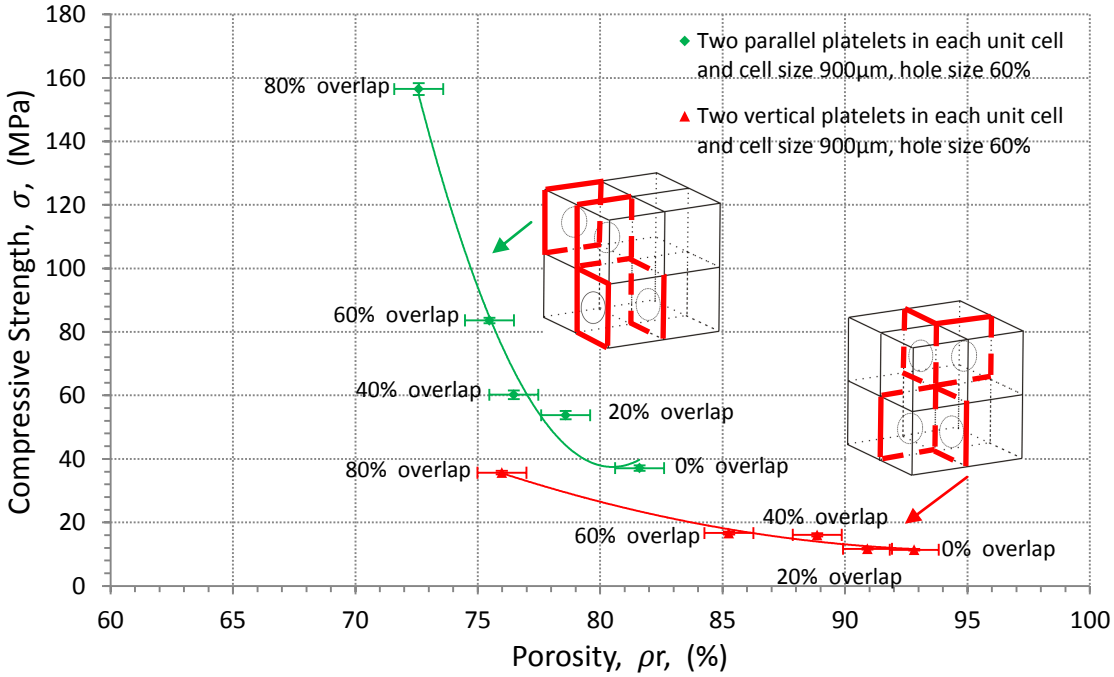

Figure 5-4 Overlap effect on porosity and compressive strength of the regular VS (two parallel platelets in each unit cell and two vertical plates in each cell)

Based on this knowledge, it appears that the strength can be improved by orientating the structure so the weld section (plane) is perpendicular to the loading direction and that it is important to avoid overlaps between platelets so that the platelets have a uniform thickness. Hence the VS with four platelets in each cell (Figure 5-5) was produced and this was subjected to further study and investigated in the following section.

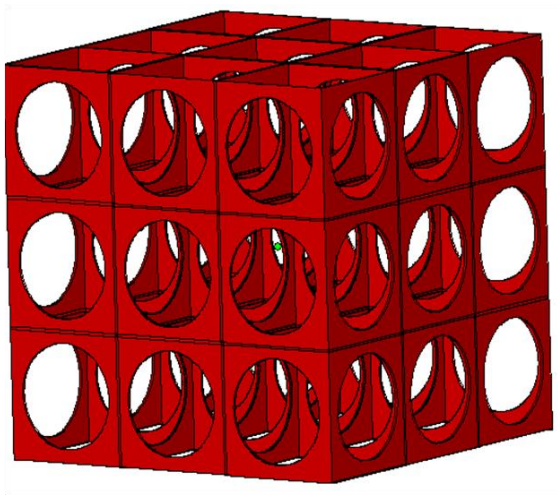

Figure 5-5 VS with four platelets in each unit cell.

5.2. Model of the Vaulted Structure with Four Platelets in Each Cell

The compressive strength of a VS (four platelets in each unit cell) is governed by the ratio of $T/L,\ T/W,\ T/H$ [174] and $R/H,\ R/W$ and $R/\ L$ [186] with reference to Figure 5-6. The porosity (ρr) of a VS can be expressed by (5-2).

$$Porosity = \frac{Vol - Vol1}{Vol} \times 100\% \qquad (5\text{-}2)$$

$$Vol1 = Ar\ \times th$$

Where $Vol1$ is the volume of the triangles, Vol is the volume of a sample Ar is the total area of triangles in the vaulted structure, is the thickness of fabricated triangles

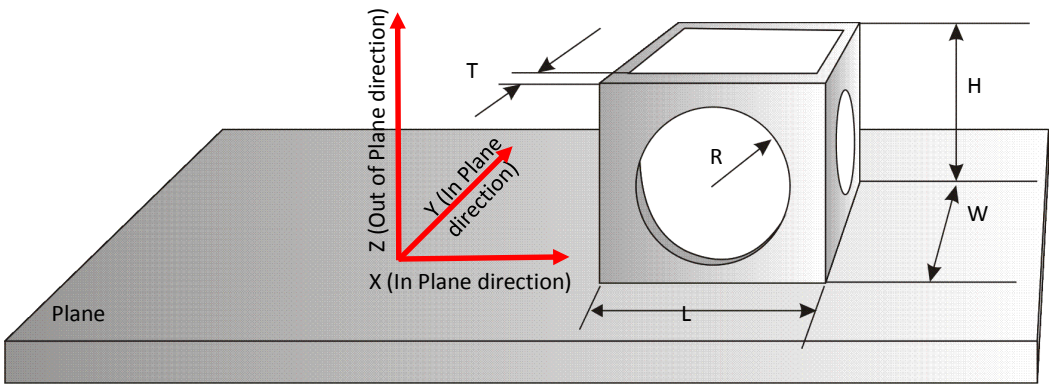

Figure 5-6 Notation used in a VS model

5.3. Enlarging the Range of Possible Mechanical Properties

According to the descriptions above, the compressive strength can be altered by changing the ratio of T/L, T/W, T/H, R/H, R/W and R/L which can be classified into two groups. In the first group (ratio of T/L, T/W, T/H), the compressive strength can be improved by increasing the thickness of the platelets, this results in an improvement of the compressive strength both out of and in the plane directions. In the second group (ratios of R/H, R/W and R/L), the compressive strength can be modified by a change in the radius of the hole (R), this results in a change in the compressive strength both out and in the plane directions. The change of T and R can also lead to changes in porosity. If the change of compressive strength is greater than the change of porosity, the range of available properties can be enlarged which allows more options for making the porous structure suitable for use with a wider range of patients. Furthermore, the change of L, W and H can give various compressive strengths in each direction and may lead to the design of specific structures with anisotropic behaviour. In order to verify these hypotheses, in the following section, a series of experiments was under taken.

5.3.1 The Effect of Hole Size

As mentioned in Chapter 4, the hole size is defined by the ratio of the radius of the hole to the radius of the maximum possible hole in a platelet. Therefore the hole size is directly related to the ratio of R/H, R/W and R/L. Thus vaulted structures with various hole sizes should exhibit different compressive strengths and porosities. In order to test this hypothesis, the following experiments were carried out.

Experimental Arrangement

Cylindrical samples (Ø15mm × 30mm) of vaulted structures with four platelets in each unit cell were designed. The aspect ratio of the cell was set to 1: 1: 1 (x: y: z) to ensure that the hole size was equal to the ratio of R/H, R/W and R/L. A range of hole sizes were used in the range of 0% to 80% in steps of 20% to create vaulted structures with different compressive strengths and porosities. The cell size was set to 900μm to ensure at least seven cells were present in each direction of the

sample so that any edge effects were minimised for the compressive strength test compliant with the protocol devised by Ashby [174]. The samples were fabricated using the SLM machine based on the parameters listed in Table 3-3. Finally the compressive strength of the samples was measured using the Instron 4505 based on ASTM-E9 with the porosity being measured gravimetrically.

Results

Figure 5-7 shows that the compressive strength of the regular vaulted structures decreases as hole size increases from 0% to 80%. The compressive strength drops from 184.80MPa to 41.39MPa. The compressive strength decreases from 184.8MPa to 41.3MPa when the hole size increases from 0% to 80%. The decrease of compressive strength was up to 77%.

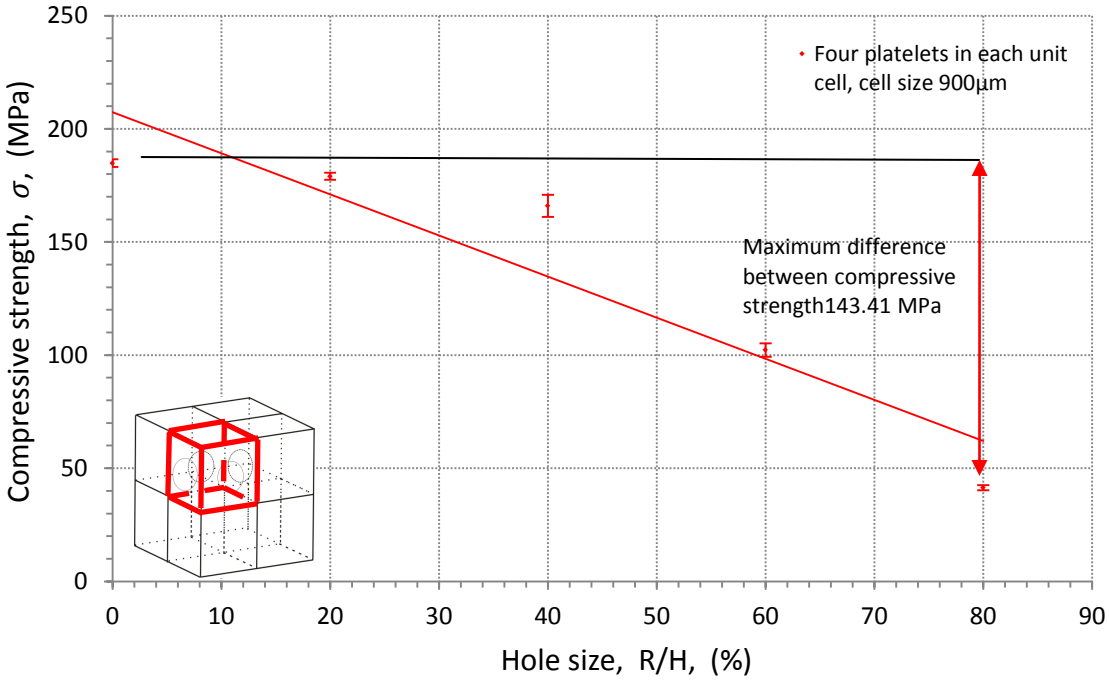

Figure 5-7 The change of compressive strength of regular VS at various hole sizes.

In Figure 5-8, the graph shows the porosity increase as the hole size increases and this effect is not linear. This trend however slightly changed when the hole size lies in the range of 0% to 20%. In this range, the porosity decreases as hole size increases.

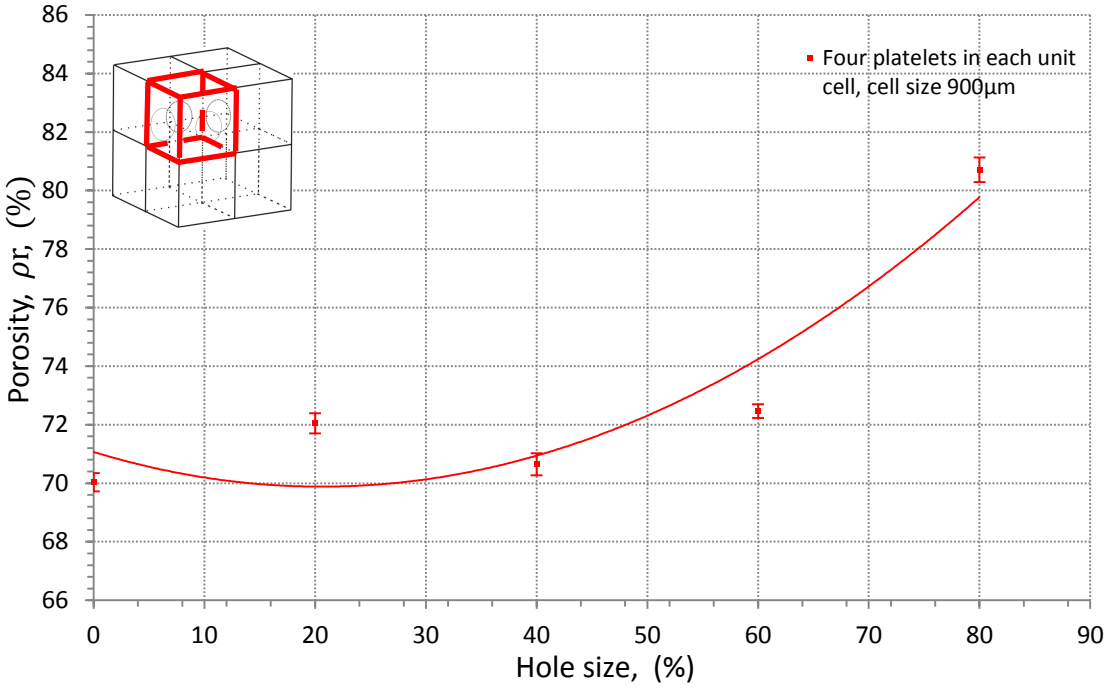

Figure 5-8 The change of porosity of regular VS at various hole sizes.

Discussion

The hole in the platelet not only causes the decrease of cross section area but also generates a concentration effect further decreasing that the load the plate can withstand. Based on the stress distribution on a platelet, the stress concentration effect is described by a stress concentration factor in equation (5-3).

$$K_{tg} = \frac{\sigma_{max}}{\sigma 0} \times 100 \qquad (5\text{-}3)$$

K_{tg} is the stress concentration factor based on the gross stress

σ_{max} is the maximum stress at the edge of the hole

$\sigma 0$ is the stress on the cross section far from the hole

The stress concentration factor is determined by the geometry of the hole. As discussed in Chapter 4, the hole in a platelet is approximated by a polygon with a specified number of edges. This results in a complex geometry hole rather than an ideal circle. This complex geometry is related to the stress concentration factor which leads to a non-linear change of compressive strength as the hole size increases.

For the SLM fabrication, the structure is sliced into layers and so the edge of the part consists of a set of laser scan ends as seen in Figure 5-9. While processing these ends there can be an increase in the local energy density and the excess energy can over melt the region or sinter powder particles to the hole so as to close the hole. Therefore no holes can be seen in Figure 5-10, (when the pre-defined hole size was less than 20%), because the excess energy still partly melts the particles so that they are attached to the platelets and this decreases the porosity.

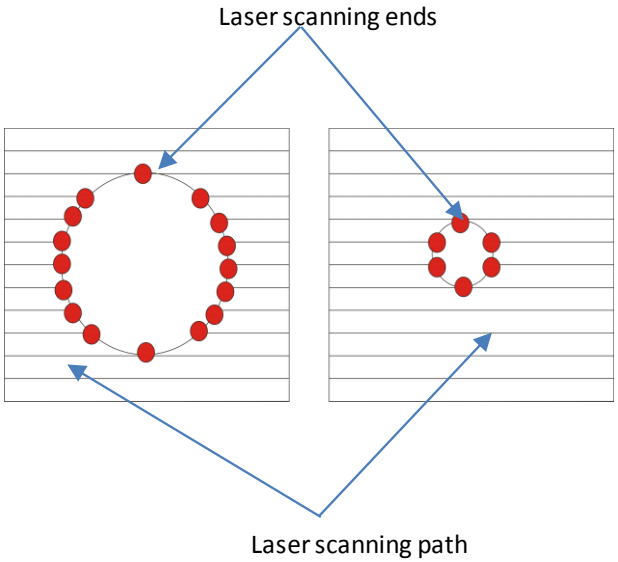

Figure 5-9 Platelets with different hole size sliced by same layer thickness.

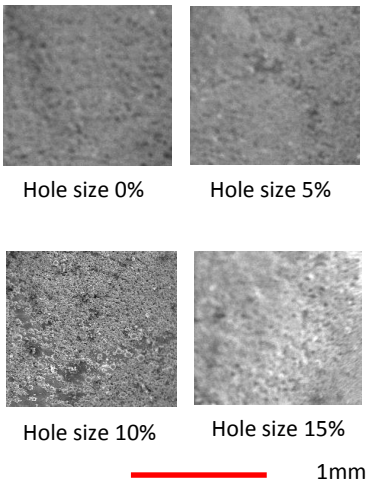

Figure 5-10 The fabricated hole sizes when the pre-defined hole size is less than 20%

When the pre-defined hole size is more than 20% (180µm), the hole emerges as seen in Figure 5-11. The geometry of the hole is not a circle and its size is defined by the maximum diameter of a circle in the hole. It clearly shows that the pre-defined hole size is larger than fabricated hole size (101µm). As the pre-defined hole size increases, although the excess energy still partly melts the particles and attaches them to the platelets, the fabricated hole size still increases. The increase in the fabricated hole size creates more void space and increases the porosity. This is consistent with the experiment result in Figure 5-8.

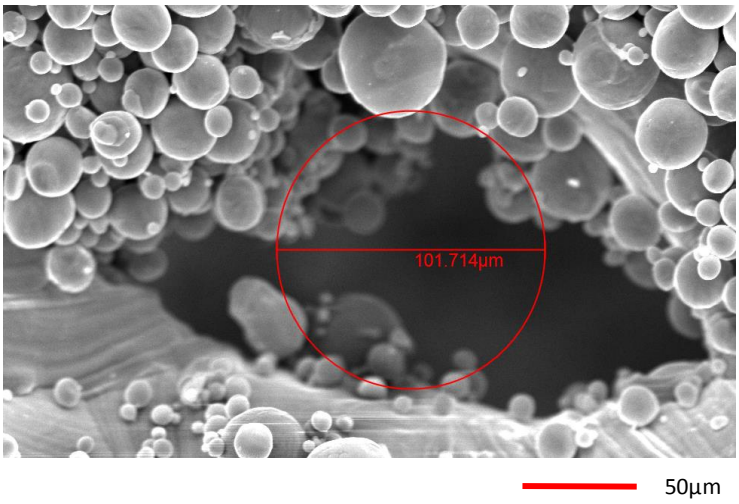

Figure 5-11 The fabricated hole size when the pre-defined hole size is 20%

Although the increase in the pre-defined hole size leads to an increase in the fabricated hole size and results in an increase in porosity, the sintered powder particles on the edge hole can reduce this increase. Therefore a smaller change of porosity (10.6%) can be seen. The increase in the fabricated hole size reduces the cross section area and introduces a stress concentration effect, resulting in a larger change of compressive strength (77.5%). This difference between the change of porosity and compressive strength indicates that altering the hole size in a VS is an effective way to enlarge the range of available properties.

5.3.2 The Effect of Platelet Thickness

The thickness of the platelets can be modified by changing the laser power and/or exposure time. By increasing the thickness of the platelets, the compressive strength of a VS should be increased but at the expense of a decrease in porosity. When the increase in compressive strength is greater than the decrease of porosity, the specific strength is increased allowing a greater range of possible properties. In order to test this hypothesis, the following experiments were carried out.

Experimental Arrangement

In order to investigate the platelet thickness effect on the change of porosity and the compressive strength of the vaulted structures, samples were created with the same parameters as above but with a higher laser power (100W) as compared with 80W so as to give thicker platelets. The compressive strength and porosity of these samples were measured following the same protocol as the above set. By comparing the experimental results for the two wall thickness for each hole size, the effect of increased platelet thickness can be observed.

Results

As shown in Figure 5-12, although the higher laser power (100W) causes a decrease in porosity, the trend is still consistent with the conclusion from the hole size effect on porosity. Similarly, as shown in Figure 5-13, the higher laser power (100W) increase the compressive strength and hole size effect still can be seen in this case. In order to fully understand the platelet thickness effect on porosity and compressive strength, SEM images of fabricated holes with higher power and the CAD porosity technology detailed in Chapter 4 are used in following section.

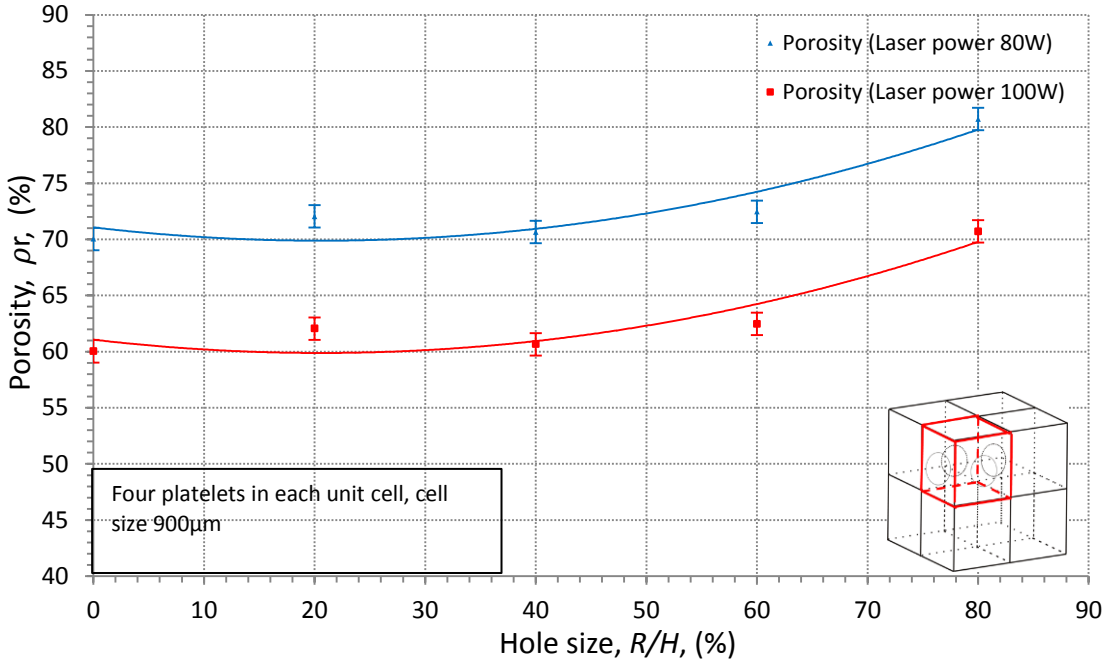

Figure 5-12 The porosities of vaulted structures varying with laser input current which can give different platelet thickness.

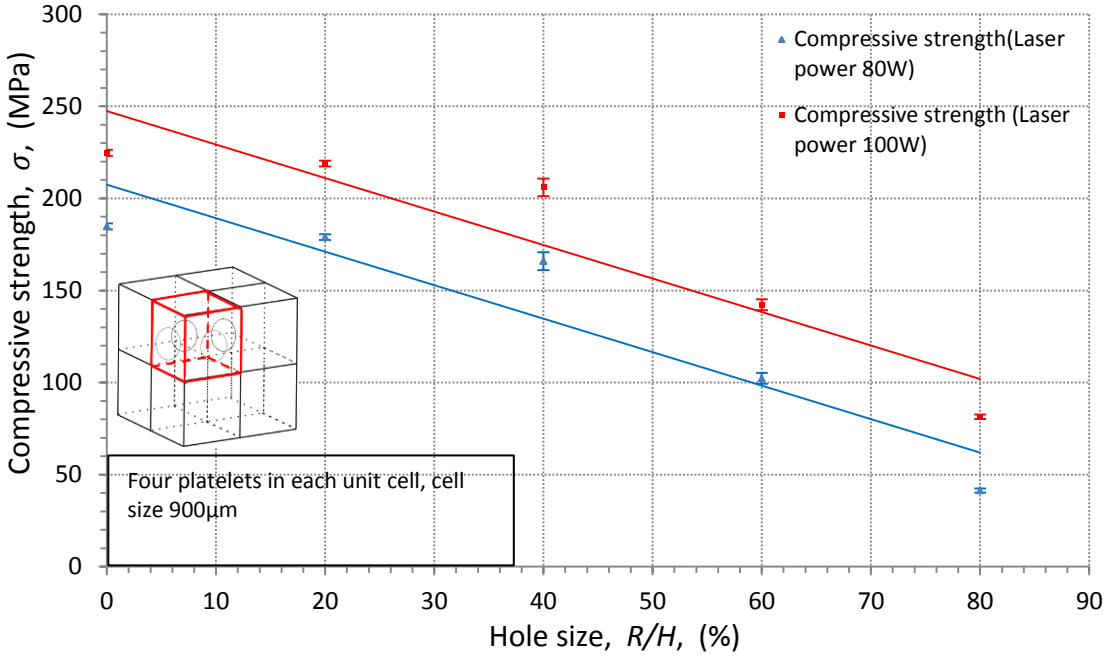

Figure 5-13 The compressive strength of vaulted structures varying with laser input current which can give different platelet thickness.

Discussion

As discussed earlier when considering the effect of hole size effect, the increase in porosity is related to the increased size of the fabricated hole, which give more void space. By using a higher laser power (100W), there are more powder particles

melted and this gives a smaller fabricated hole size. For example, the same structure (hole size 20%) fabricated by different laser powers and gives different fabricated hole sizes as seen in Figure 5-14. The decrease of fabricated hole size also give less void space and results in the decrease of porosity as seen in Figure 5-12.

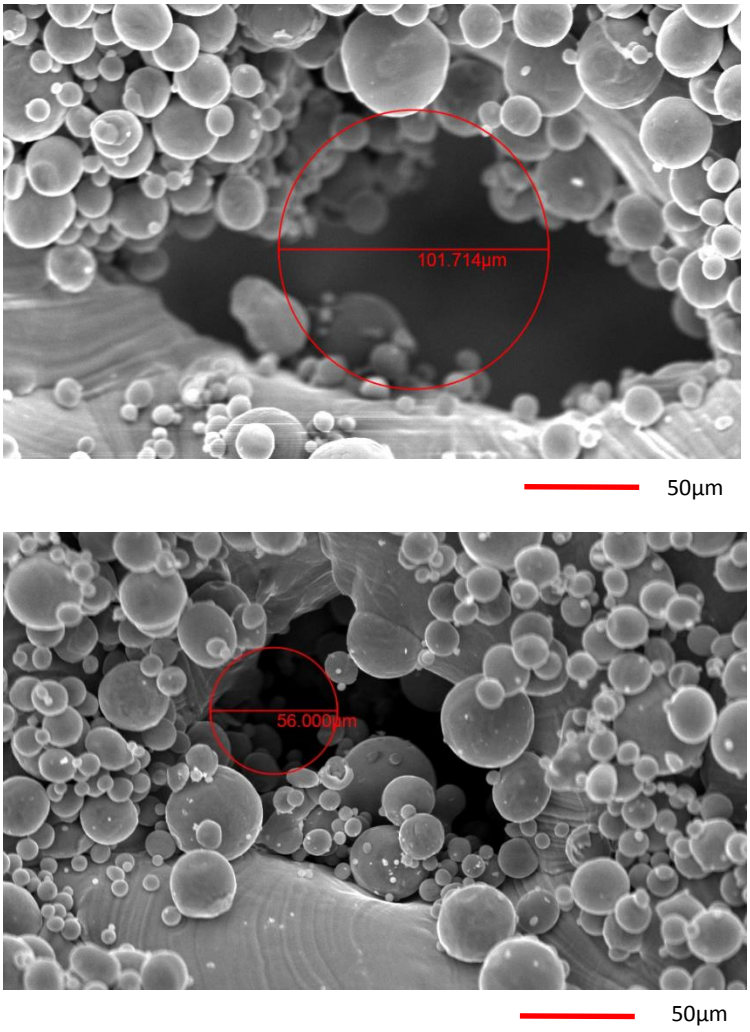

Figure 5-14 The different fabricated holes caused by the various laser power (Up 80W,Down 100W)

The porosity of the fabricated structures also can be predicted from the CAD model developed in this research described in section 4.7.1. As seen in Figure 5-15, although the trend of porosities can be clearly seen and is consistent with the trend in Figure 5-12, the computer model still needs to be further developed with considering the hole geometry and size created by the higher laser power. These

complex fabricated hole geometries result in the difference between the measured curve and computed curve.

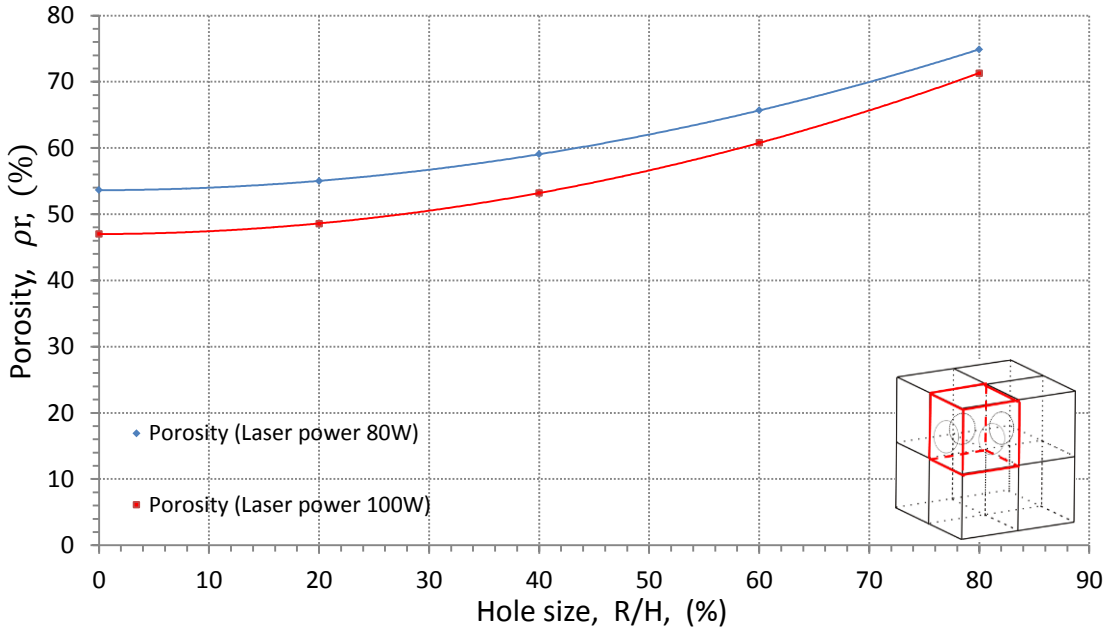

Figure 5-15 The porosity of the fabricated structures predicated by CAD model

The structure fabricated by SLM could exhibit a fine microstructure as a consequence of the rapid cooling rate [187]. This fine microstructure could improve certain mechanical properties [9] and may be changed by altering laser parameters. However in this research, the laser parameters are constant. Based on the equation (5-4), it clearly shows that the porosity has a greater influence on the mechanical properties.

$$\sigma_P = C\sigma_0 D^m \qquad (5\text{-}4)$$

Where σ_0 is the strength of fully dense material, D is the porosity, C is an empirical constant and m being a constant that varies between 3 and 6 for metallic materials [188]

Therefore in this section, the research focussed on the relationship between the mechanical properties and porosities. By using a higher laser power (100W), more particles were melted together to form a larger cross sectional area perpendicular

to the z direction and this produces a thicker platelet (340µm). When loaded in compression along the z direction, the thicker platelets exhibit more resistance to platelet deformation which is related to T/L, T/W, and T/H [174]. However, when comparing the improvement in compressive strength with the decrease of porosity it can be seen that the effect is quite small and that increasing the thickness of the platelets is not an effective way to enlarge the range of available properties.

5.3.3 The Effect of Cell Size

As discussed earlier when considering the hole size effect and platelet thickness effect, the cell size was set to 900µm to ensure that at least seven cells were present in each direction of the sample to try and avoid edge effects when performing the compressive strength test. However a change of cell size can lead to the change of ratios (T/H, T/W and T/L) which can give various compressive strengths and porosities. Thus in the following section, a set of experiments are presented that show the effect of altering the cell size.

Experimental Arrangement

Cylindrical samples (Ø 15mm × 30mm) of the four platelet VS were created. The aspect ratio of the cell was set to 1: 1: 1 (x: y: z) to ensure that the hole size and ratio of T/H, T/W and T/L were equal to each other. The hole sizes created were in the range 0% to 80% in steps of 20% to create vaulted structures with different compressive strengths and porosities. The cell size was set to 1200µm giving a different experimental result. All other experimental parameters were the same as previous experiments. By comparing the experiential result from the hole size effect test, the effect of cell size on the properties of the structure can be seen.

Results

As shown in Figure 5-16 the compressive strength of the regular VS with a smaller cell size (900µm) has a significantly higher compressive strength for all hole sizes. However in Figure 5-17, the porosity of the regular VS with a larger cell size (1200µm) has a slightly higher porosity for all hole sizes.

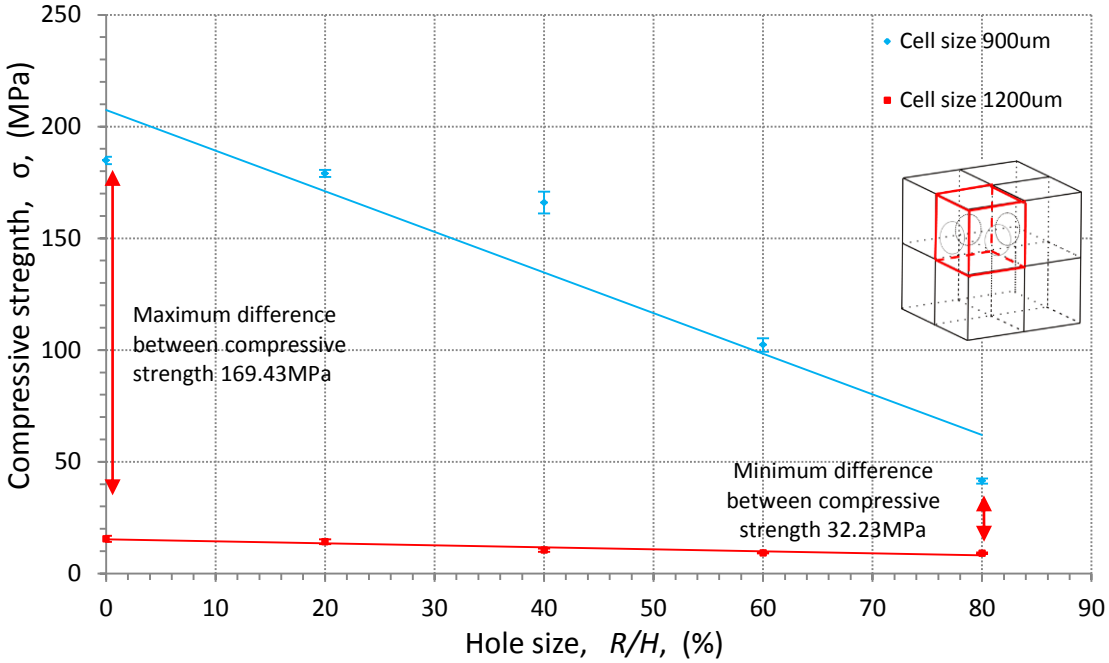

Figure 5-16 Compressive strength of regular VS at various cell size.

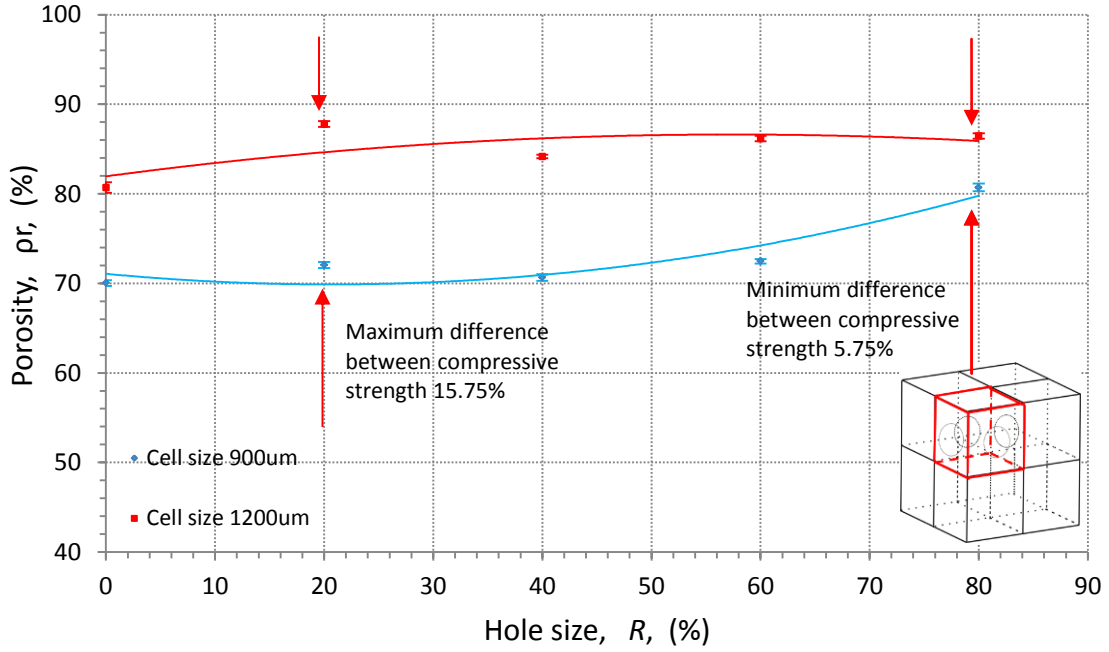

Figure 5-17 Porosity of regular VS at various cell sizes.

Discussion

Based on the definition of porosity in Chapter 3, it indicates that the smaller cell size can result in more void space being filled and gives a lower porosity. However, the slight change of porosity caused the significant change of compressive strength

since the different failure modes occur due to the change of cell size and these modes can be seen in Figure 5-18.

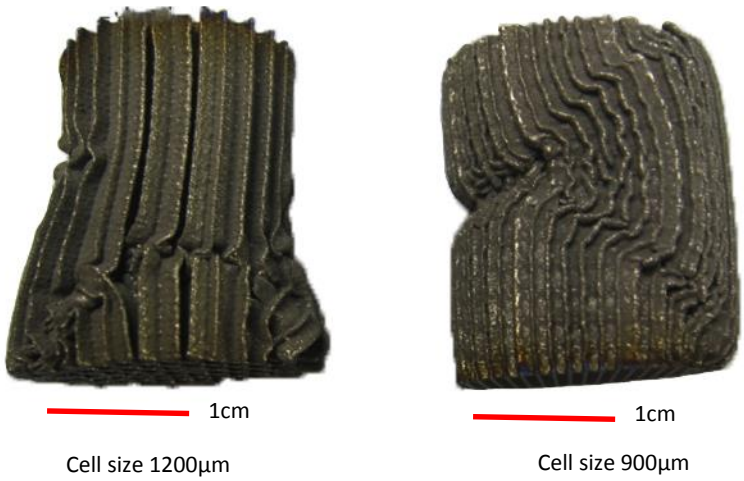

Figure 5-18 Different failure mode of compression samples with different cell sizes.

The collapse of the regular VS (cell size 1200μm) is caused by plastic buckling [174]. For the platelets in the cells of platelet structure, they fold progressively with a wavelength which is often roughly equal to the cell side length [174]. Figure 5-19 shows deformation of platelets in a layer. As the test progresses, the plastic hinges may be moved to interact with each other giving a compression sample as shown in Figure 5-19.

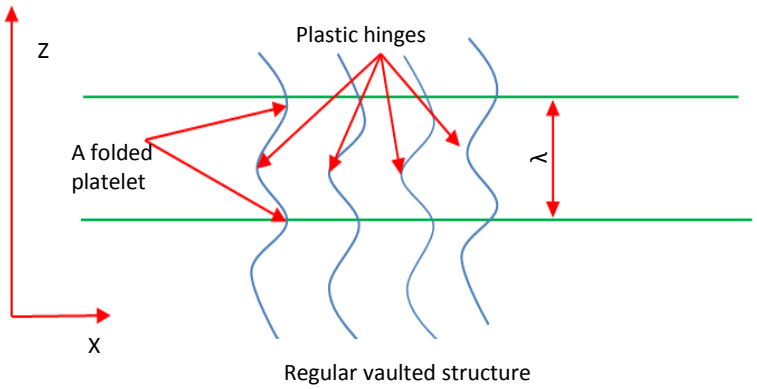

Figure 5-19 The two-dimensional schematic of buckling in a regular VS viewed in the y direction.

When the regular VS has a higher density, for example the cell size was set to 900μm, the deformation mechanism is different, the platelets in the cells undergo local plastic buckling and form creases due to the yielding of the platelets [174].

5.4. Regular Vaulted Structure Isotropy

The isotropy of a porous structure arises from its structure [189]. For example, in Chapter 4, the regular VS shows a significantly different structure in the plane and out plane directions. The anisotropy of a porous structure can also arise from material anisotropy within it [189]. Furthermore anisotropy is very sensitive to the changes of cell shape [189]. The anisotropy of cell shape can be measured by the ratio of the largest cell dimension to the smallest being termed the shape anisotropy ratio [189]. For the regular vaulted structure, the shape anisotropy ratio is represented by H/L *or* H/W. Thus by alerting the shape anisotropy ratio, the regular VS anisotropy can be changed. In the following section, a set of experiments are undertaken to test this theory.

Experimental Arrangement

This starts by creating cylindrical samples (Ø15mm × 30mm) with various orientations. In order to measure the anisotropy of the regular vaulted structure, the shape anisotropy ratio was set to 1:1, 1:2 and 2:1 (H/L *or* H/W and smallest cell dimension 900μm). Considering the stress concentration effect, the hole sizes were in the range of 0% to 80% (step 20%). These samples were fabricated using the SLM Realizer 100 based on the parameters listed in Chapter 3. Finally the compressive strength of the samples were measured based on ASTM E9 and their porosities were measured by gravimetric analysis.

Results

As shown in Figure 5-20 and Figure 5-21, when the shape anisotropy ratio was equal to 1:1:2 or 2:2:1, the compressive strengths in and out of the plane direction are very different. However in Figure 5-22, when the shape anisotropy ratio was equal to 1:1:1, although the compressive strengths in plane direction and out plane

direction are located in the different section, as the hole size increases, the difference of compressive strength is reduced. When the hole size is equal to 80%, the regular VS still exhibits anisotropic behaviour.

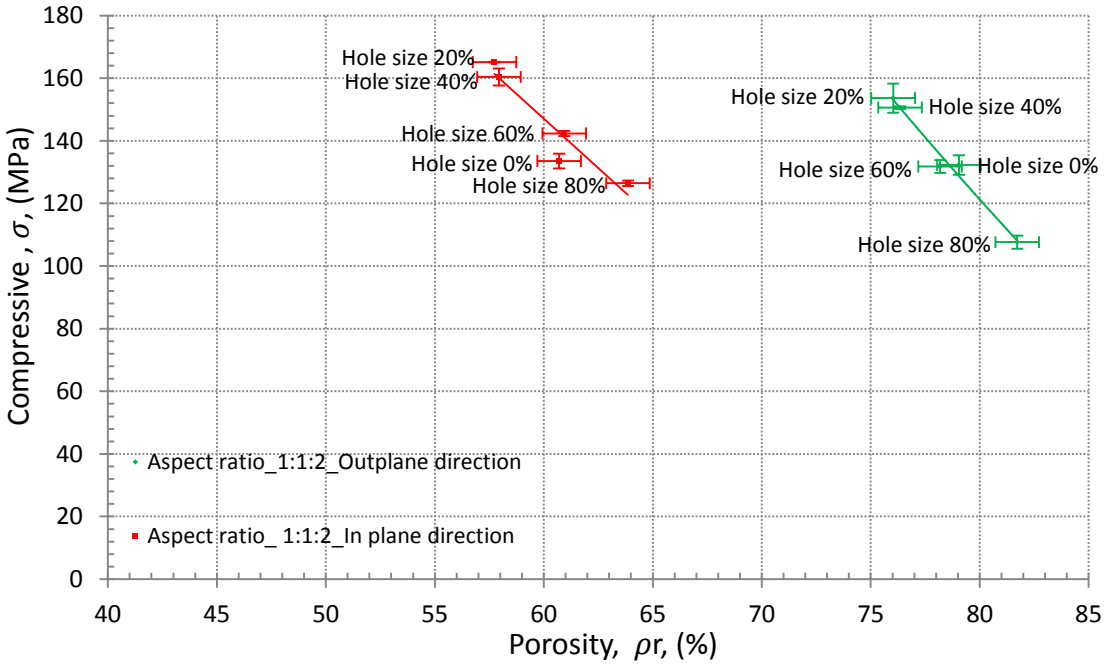

Figure 5-20 The compressive strength of VS in plane and out plane direction varying in porosity when shape anisotropy ratio is 1:1:2.

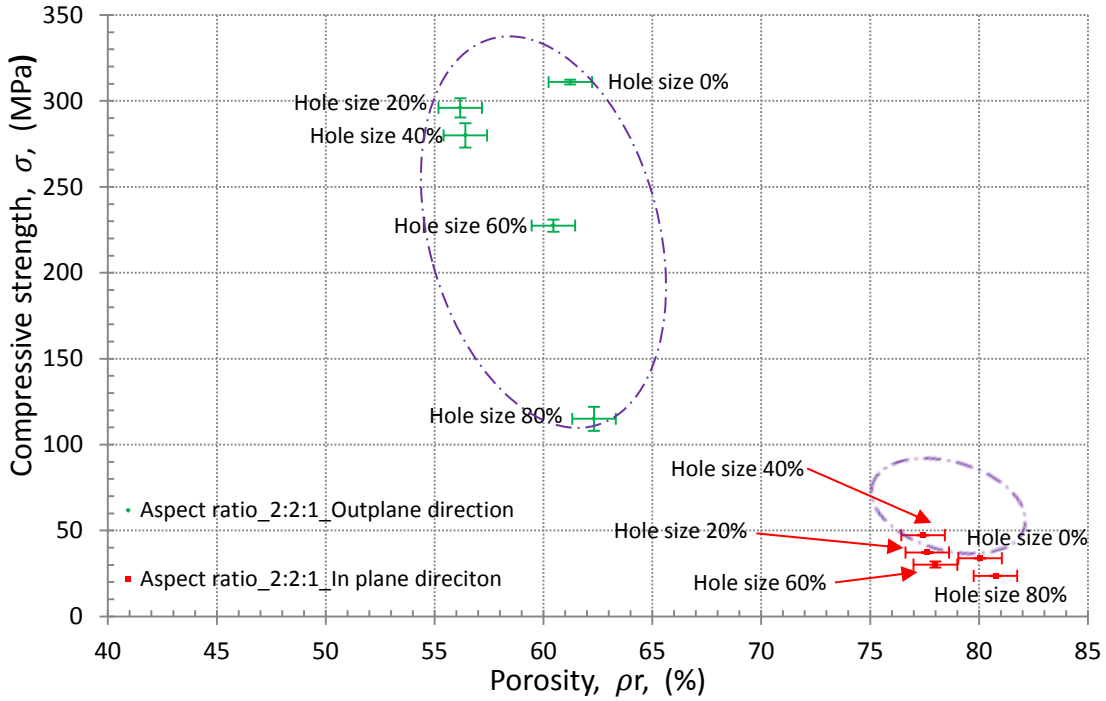

Figure 5-21 The compressive strength of VS in plane and out plane direction varying in porosity when shape anisotropy ratio is 2:2:1.

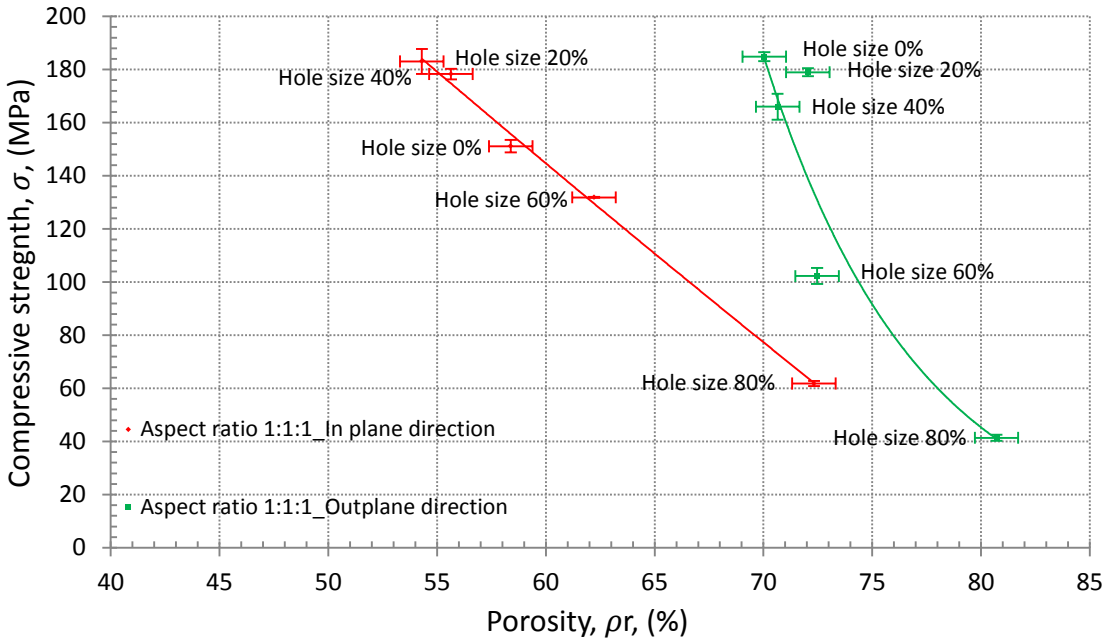

Figure 5-22 The compressive strength of VS in plane and out plane direction varying in porosity when shape anisotropy ratio is 1:1:1.

Discussion

The mechanical properties of structures fabricated by SLM are related to their final microstructures [9]. However in this case, all the samples were fabricated by the same SLM machine with same parameters. Therefore it is believed that the principle factor that affects the mechanical properties derives from the sample creation and fabrication detailed in following section.

Due to the requirement of the compressive strength test standard (ASTM E9), cylindrical samples were needed. In order to investigate the different compressive strengths in and out of the plane direction, these samples were created, fabricated and tested as shown in Figure 5-23. As discussed in Chapter 4, the sections of the triangles located inside the sample are kept to form a desired shape and these define the porosity. In this case, the different builds change in relative direction and the different z direction leads to a different selection of triangles being located inside the sample, resulting in different porosities of samples that depend on plane test direction.

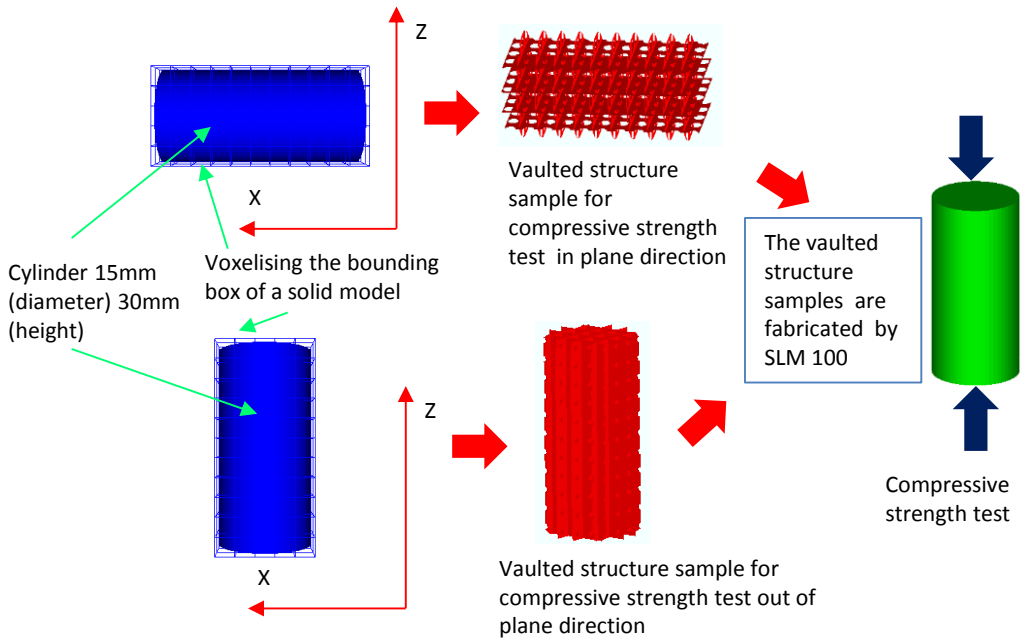

Figure 5-23 The orientations of samples involved in creating, fabricating and testing.

By altering the aspect ratio from 1:1:1 to 1:1:2 and then to 2:2:1, the failure mechanism for the failed samples (in plane direction) changes as can be seen in Figure 5-24. When the aspect ratio was set to 2:2:1, a larger cell size was observed in Figure 5-24, and this triggers the cell size effect as discussed and therefore this structure is quite weak.

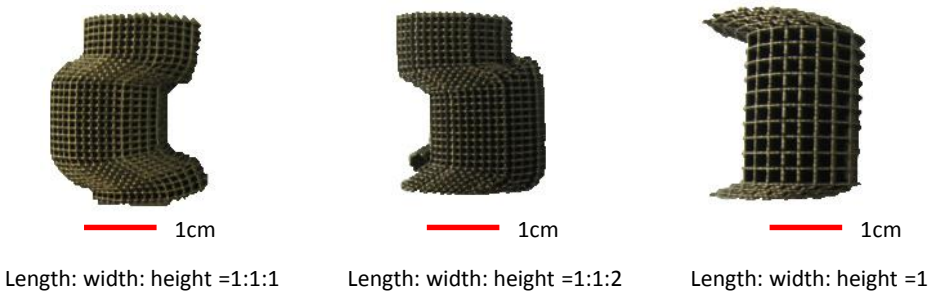

Figure 5-24 The different failure mode of compression sample out plane varying in aspect ratio.

The failed in plane samples are shown in Figure 5-24. They exhibit a failed mechanism which causes the platelets to collapse layer by layer and the collapsed section moves towards the middle section with increased deformation. To explain this mechanism, a sequence of collapse configurations is shown in Figure 5-25.

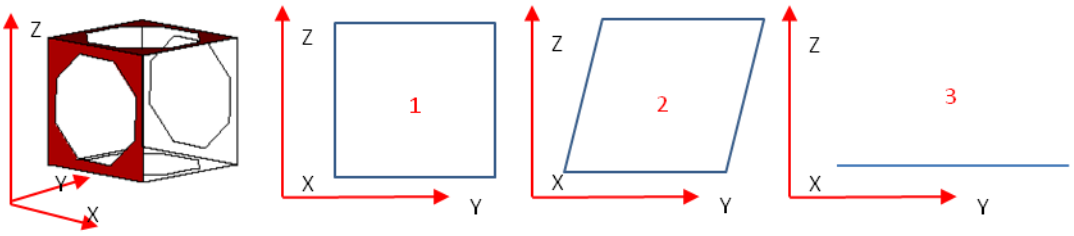

Figure 5-25 Sequence of collapsed configurations of a cell in a vaulted structure.

Similar reasoning can be used to explain the difference in the compressive strength and failure mode in the out of plane direction. Therefore, the different failure modes and porosities vary with orientations which make it difficult to achieve a VS with truly isotropic behaviour by just alerting the aspect ratio of the cell size.

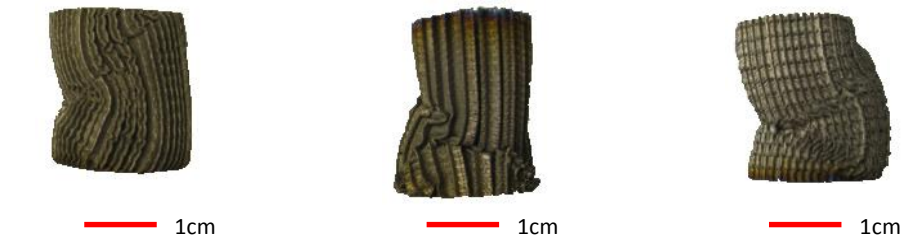

Length: width: height =1:1:1 Length: width: height =1:1:2 Length: width: height =1:1:2

Figure 5-26 The different failure mode of compression sample out of plane direction varying in aspect ratio.

5.5. Summary

The range of available properties of a regular VS can be enlarged by altering the cell size and hole size rather than increasing the thickness of platelets. As a summary (Figure 5-27**Error! Reference source not found.**), the range of available properties that can be produced is much greater for regular VS than that for a unit cell structure with struts. Although the theory indicates that there is a possibility to create a regular structure exhibiting isotropic behaviour, the experimental results show that the regular VS demonstrates anisotropic behaviour even when the cell size aspect ratio was set to 1:1:1.

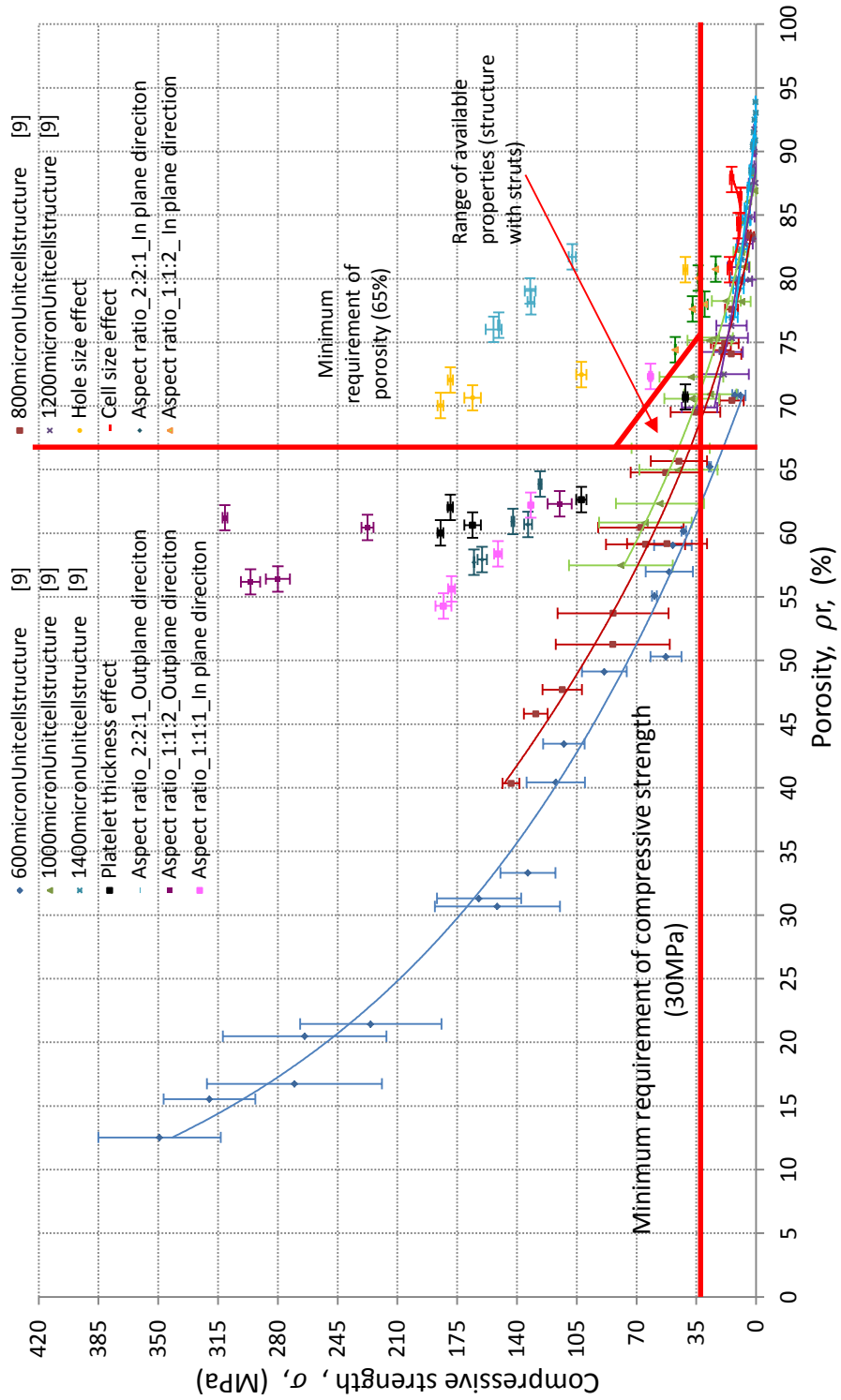

Figure 5-27 The range of available properties of unit cell structure with struts and VS (experiment data listed in Appendix E).

CHAPTER 6

RANDOMISED VAULTED STRUCTURES

As discussed in Chapter 4, a RVS can be made that resembles cancellous bone. The randomisation effect on the pore size distribution and mechanical properties will be discussed in the first section of this chapter. This chapter then considers the possible methods to enlarge the range of available properties and these methods include decreasing the hole size, increasing the thickness of the platelets and decreasing the cell size. As discussed in Chapter 5, the regular VS exhibits heavily anisotropic behaviour and therefore in this chapter, a set of experiments are reported that consider a RVS with reasonable isotropic behaviour by altering the cell aspect ratio and percentage of randomisation.

6.1. Randomisation Effect

The pores in the VS were created by the building of the platelets. The uniform distribution of the platelets in the regular structure (0% of randomisation) leads to a pore size distribution as seen in Figure 6-1. It shows clearly that most pore sizes are located in the range 200µm to 700µm and very few pore sizes are observed with sizes in the range 0µm to 100µm. With reference to the optimum pore size discussed in Chapter 2, a pore size less than 100µm should be avoided if bone is to grow into the structure. By introducing the random deformation mechanism; the platelets are deformed, changing the distribution of pores as seen in Figure 6-1. This shows that more pore size lies in the range of 0µm to 100µm at higher randomisation and when the percentage of randomisation increases to 100%, the platelets are significantly deformed and the number of pores with sizes less than 100µm increases. Therefore it is recommended that the percentage randomisation should be limited to avoid the increase in the number of pore in the size range 0µm to 100µm, which can inhibit the bone generation as discussed in Chapter 2.

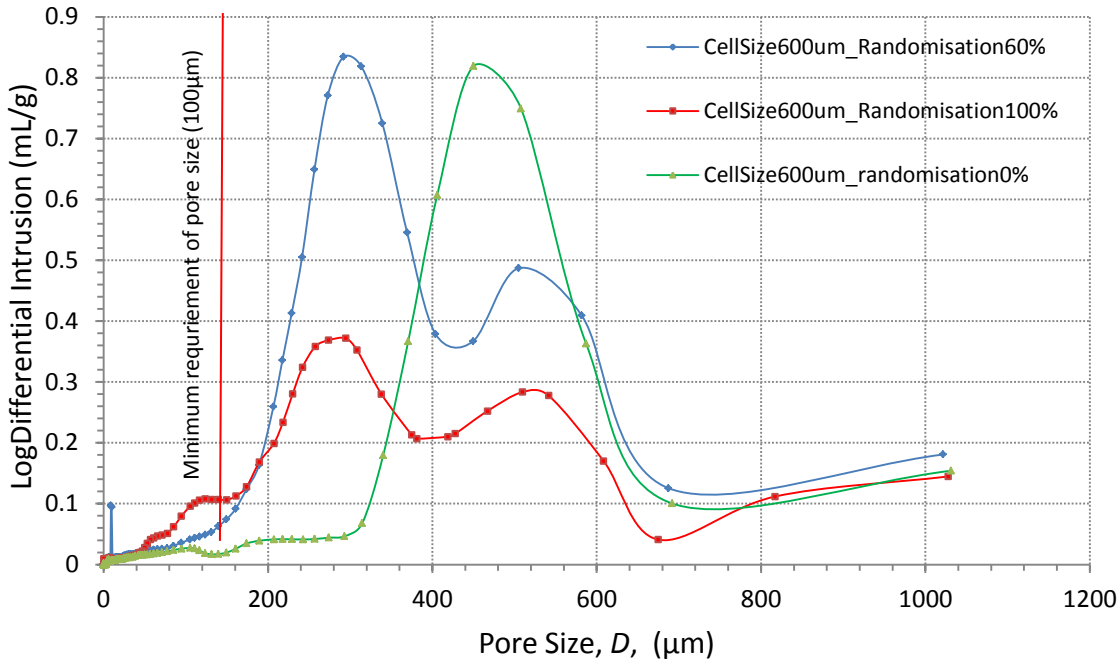

Figure 6-1 Effect of randomisation on pore size distribution

Randomisation mechanism may also affect the mechanical properties and is therefore studied. When randomised structures were mechanically tested, this had improved properties as seen in Figure 6-2 and it was observed that the failure modes of regular VS and RVS were different and exhibited various mechanical behaviours.

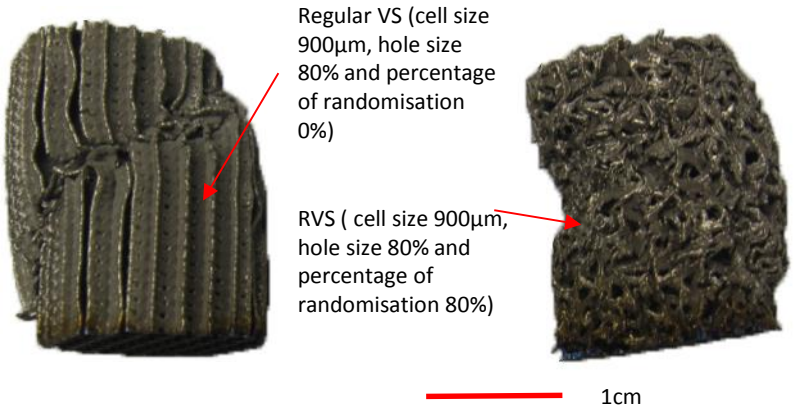

Figure 6-2 The different failure mode of the compression samples (regular and randomised vaulted structure, CpTi, MCP Realizer 100, fabrication parameters listed in Chapter 3).

Further information can be found by considering the stress-strain curves of the regular vaulted structures as seen in (Figure 6-3). It begins with linear-elasticity and then progressive crushing layer by layer leads to a plateau formation which continues until the structure is completely crushed. This mechanical behaviour of regular VS resembles that of brittle foams such as wood (stress-strain curves of sample loaded in the axial directions) [174].

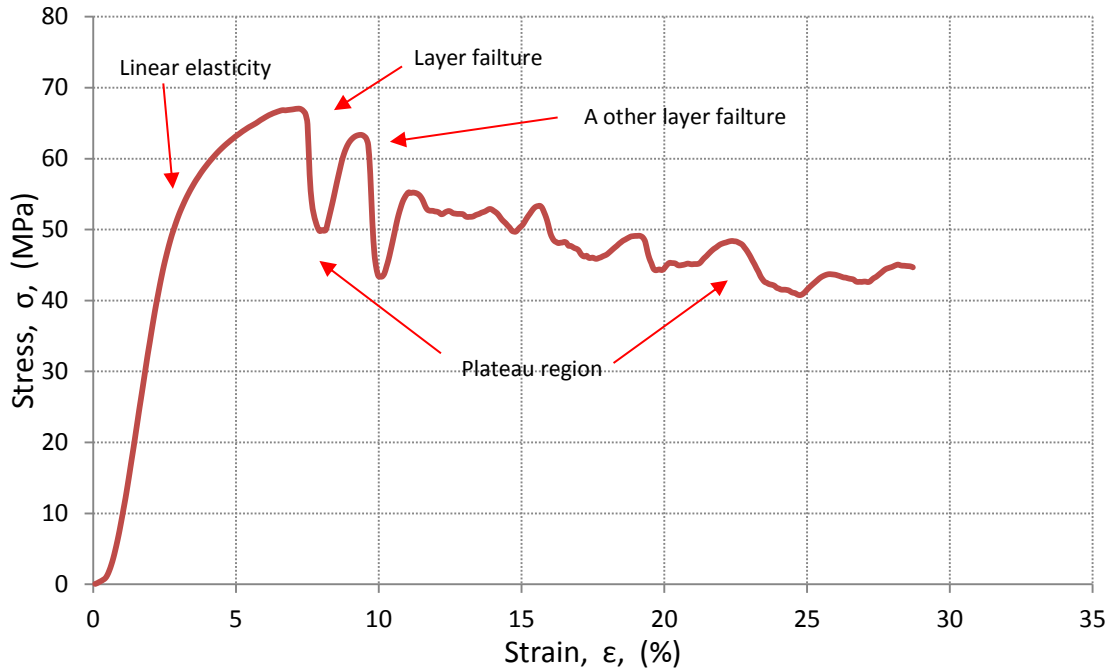

Figure 6-3 The stress-strain curves of a regular VS (cell size 900µm, hole size 80%).

However by introducing randomisation mechanism, the RVS exhibits a distinguished stress-strain curve as seen in Figure 6-4. The curve starts with linear-elasticity, followed by progressive compressive collapse, which creates the long horizontal plateau to the curve. This curve continues until opposing platelets meet and touch causing the stress to rise steeply (densification). This mechanical behaviour of the RVS mimics that of wet cancellous bone (stress-strain curves of sample loaded in the axial directions) [174]. By examining these stress-strain curves, it can be seen that the mechanical properties are improved by randomisation and further the capability of the structures to resemble the mechanical properties of cancellous bone.

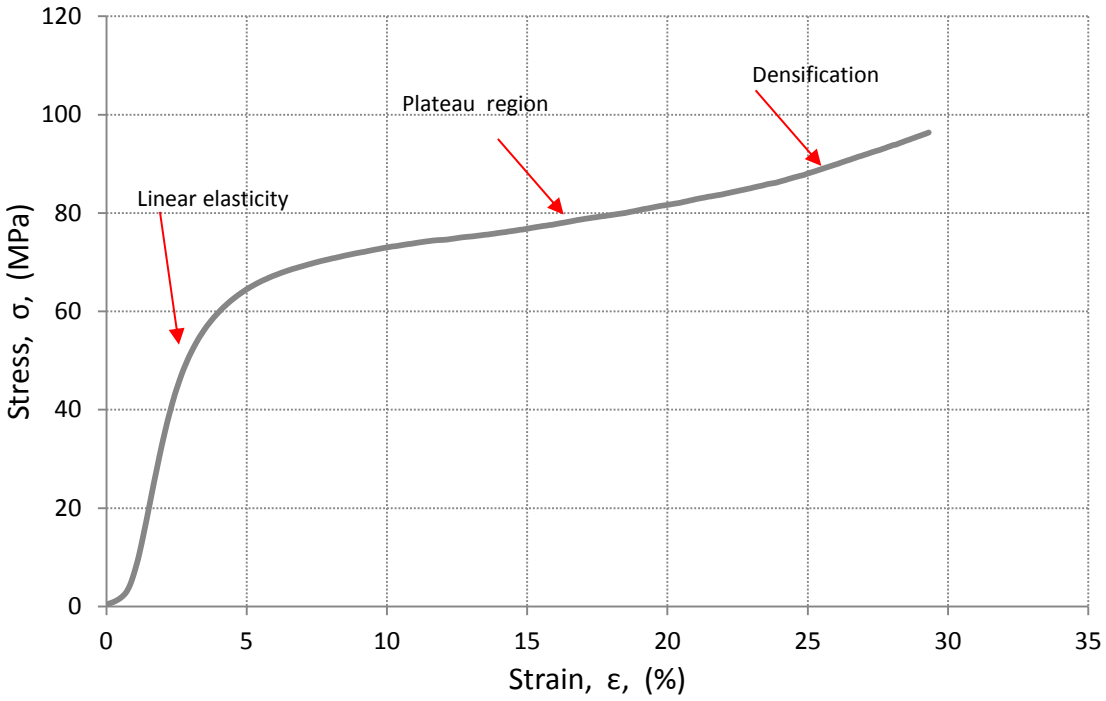

Figure 6-4 The stress-strain curves of a RVS (cell size 900µm, hole size 80%, 80% of randomisation).

6.2. Enlarging the Range of Available Properties

In Chapter 5, a method was used to improve the compressive strength by decreasing the cell size and reducing the hole size. However, in a randomised vaulted structure, the hole size and cell size are not homogeneous and therefore the hole size and cell size are referenced to the defined hole size and cell size when creating a structure. These variously randomised structures exhibit different compressive strengths. Methods similar to those used in Chapter 5 were used to investigate how to enlarge the range of available properties of the structure. Although increasing the thickness of the platelets can enlarge the range of available properties of a regular vaulted structure, it is not known what effect this will have on a random structure.

6.2.1. The Effect of Hole Size

By introducing the random deformation mechanism, the hole is deformed randomly and therefore develops a more complex shape. Stress concentration theory

suggests that the development of stress concentration points should decrease the compressive strengths of the RVS [190,191] compared to the ordered structure. Consequently whether the range of available properties can be enlarged needs to be shown by a series of experiments.

Experiment Arrangement

Two groups of RVS samples (Cylinder Ø 15mm × 30mm) were generated. The hole sizes were set to 40% and 80% respectively, to show the effect of hole size on mechanical behaviour. The cell size was set to 900µm to ensure at least seven cells were present in each direction of the RVS in order to avoid edge effects when performing the compressive strength tests [175]. The number of cells in each direction was checked by considering the pre-sliced layer image. For example in Figure 6-5, a RVS sample in STL format has been pre sliced by Magics and the number of cells in the z direction can be seen based on the contour of the sliced platelets. Similarly the number of cells in x and y direction can also be checked. The percentage of randomisation studied in a range of 20% to 100% to ensure the change of porosity and compressive strength can be seen for all percentage of randomisation. Samples were fabricated by the SLM Realizer 100 based on the parameters listed in Chapter 3.

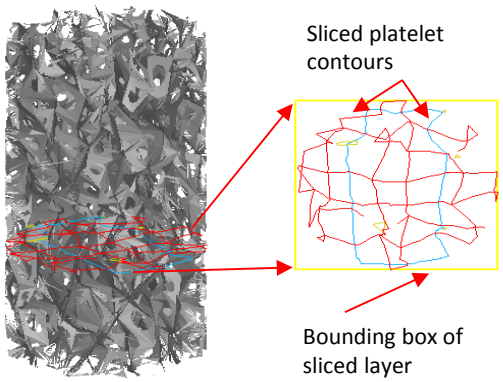

Figure 6-5 A RVS was pre sliced by Magic.

Results

The presence of the larger holes (80%) leads to a higher porosity and this can be seen for all percentages of randomisation (Figure 6-6). The difference in porosities

lies in a range of 21% to 31% when the hole sizes were set to 40% and 80%. However, the compressive strength dropped significantly as hole size increases. As shown in Figure 6-7, the maximum difference of compressive strength was 197MPa and the minimum difference of compressive strength was 154MPa.

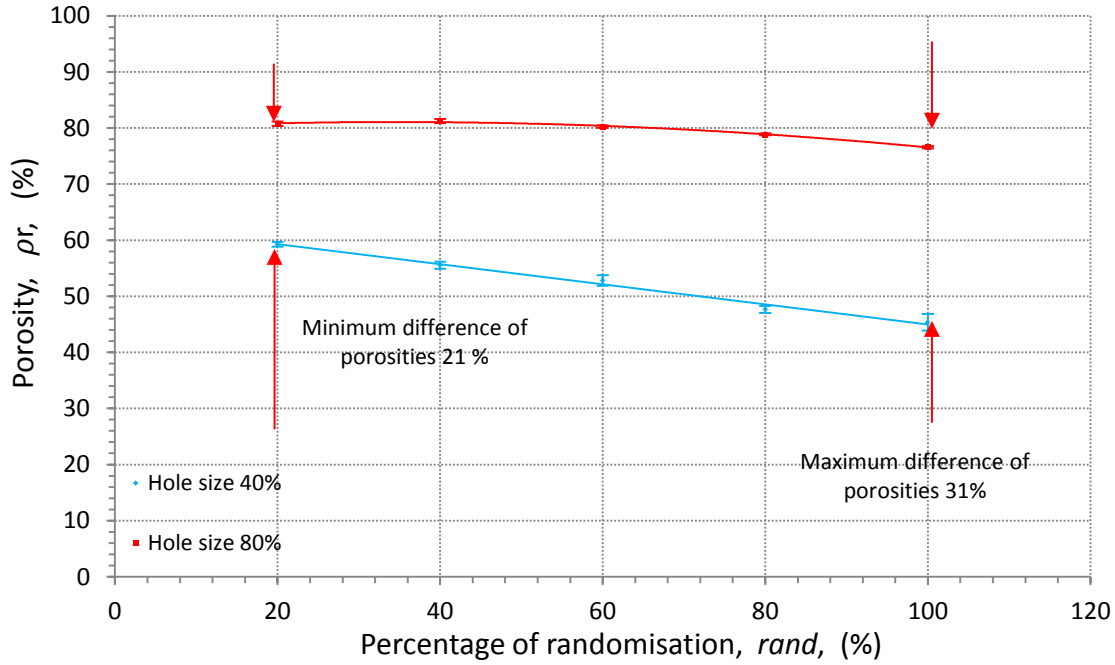

Figure 6-6 The porosity varying percentage of randomisation at different given hole size.

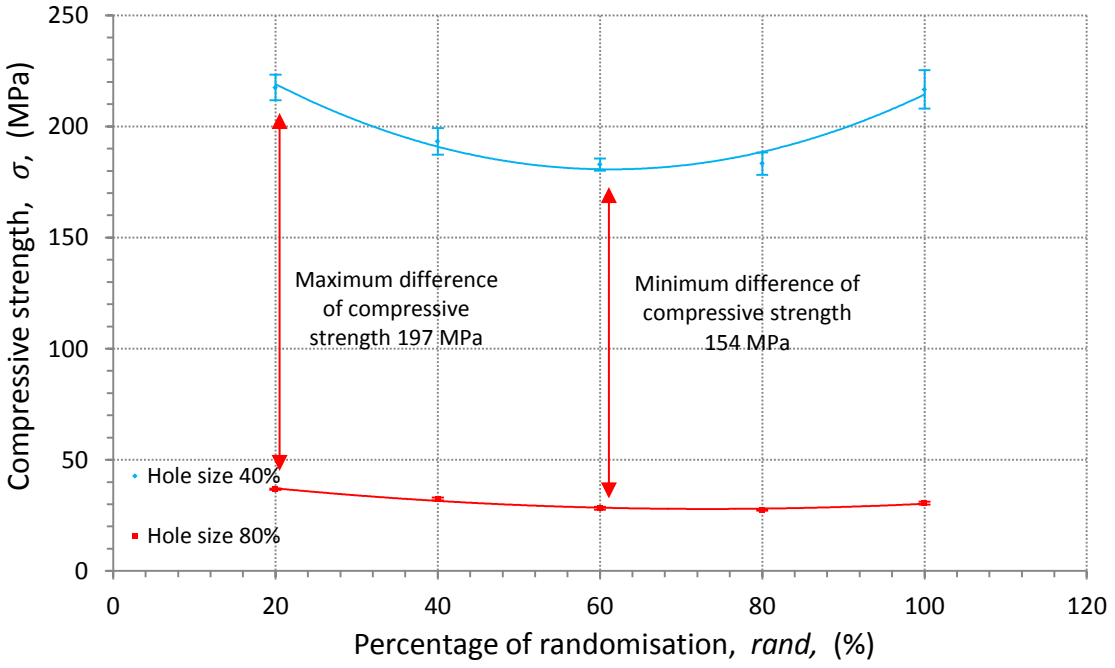

Figure 6-7 The compressive strength varying in percentage of randomisation at different given hole size.

Discussion

As discussed in Chapter 4, a larger hole size creates a structure with elements similar to struts (wire frames) while with a smaller hole size the elements are more platelet-like. The difference in compressive strength with porosity arises from this change in the nature of the vaulted structure. The failure in compression of this foam-like RVS is dictated by the cell wall bending. The rod-like elements possess a lower second moment of area which exhibits lower resistance to the bending moment acting on them and contributes to higher porosity. However the platelet-like elements possess a higher second moment of area but exhibits lower porosity. In Chapter 2, the literature review on various porous structures also shows that the platelet based structure can provide higher compressive strength with higher porosity.

Furthermore the change of porosity and compressive strength also can be found in cancellous bone. The porosity of cancellous bone is decreased by enlargement of circular perforation within the cell wall [184] to form a rod-like structure which shows lower strength [181]. Therefore these changes of porosity and compressive strength can be resembled by increasing the hole size within the platelets of a randomised vaulted structure.

6.2.2. The Effect of Platelet Thickness

As discussed in Chapter 5, increasing the thickness of the platelets is not an effective way to increase the range of available properties for the non-random structures, because it does not lead to a change in specific properties. However, in this section, these experiments were repeated to see if the same effect was seen in the randomised structure.

Experiment Arrangement

Samples with the same structures as above were used and they were fabricated with the sample parameters listed in Table 3-3, however a higher laser power (130W) was used in order to produce thicker platelets. Similarly the compressive strength of the samples were measured using an Instron 4505 using test procedures

based on ASTM-E9 and the porosity was measured by gravimetric analysis. By comparing the experimental results for each hole size, the effect of increased platelet thickness was observed.

Results

As shown in Figure 6-8, the porosity decreases with increased laser input current. The maximum difference in the porosity was 32% and the minimum difference in porosity was 26%. As shown in Figure 6-9, the higher laser input current leads to a higher compressive strength and the maximum difference in compressive strength being 169MPa while the minimum difference of compressive strength being 123MPa.

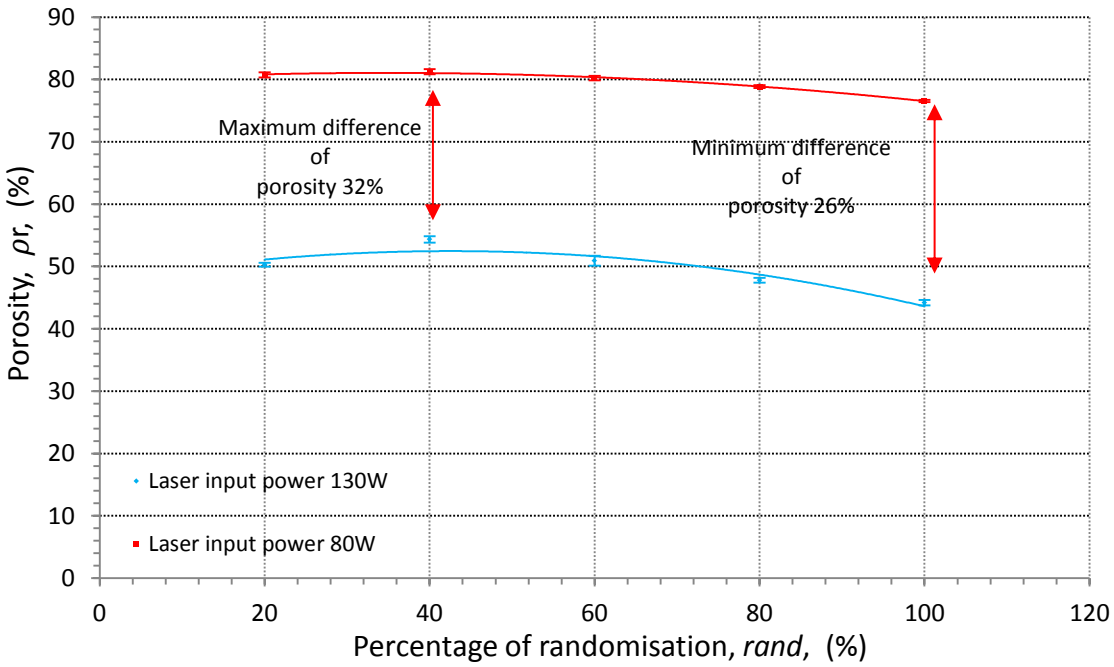

Figure 6-8 The change of porosity of a RVS at various percentage of randomisation, fabricated by different laser input current (CpTi).

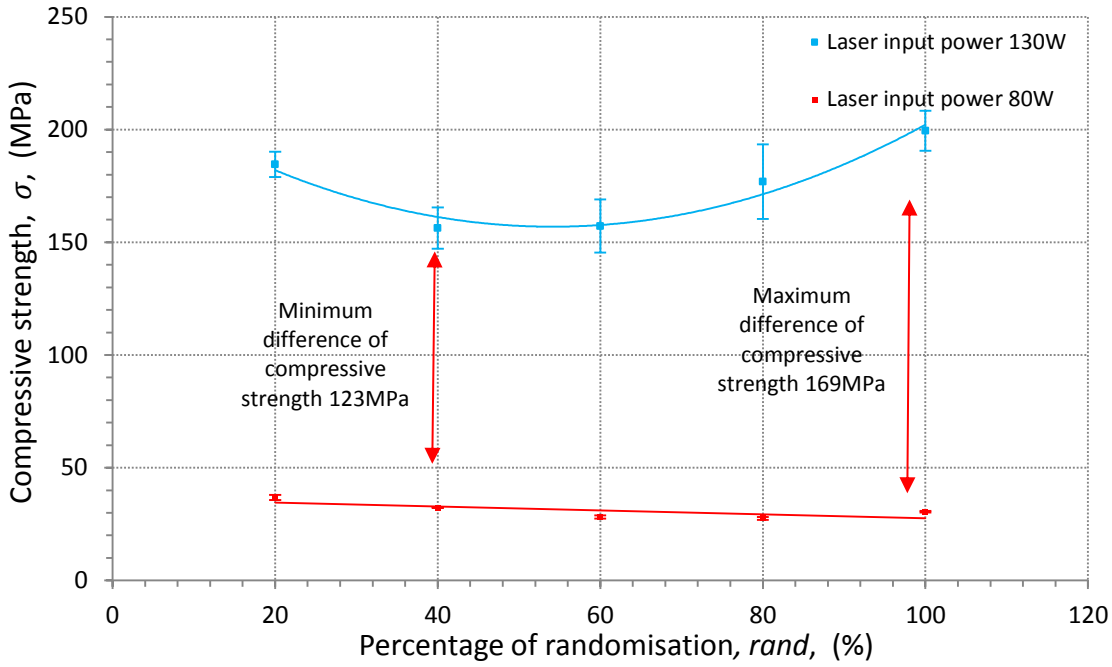

Figure 6-9 The compressive strength of a RVS varying in various percentage of randomisation and fabricated by different laser input current (CpTi).

Discussion

The surfaces of the randomised vaulted structures were deformed to form curved surfaces and this foam-like structure and mechanical behaviour was dictated by the cell wall bending rather than stretching and compressing [111]. As the laser power increases, the cross-section area of each platelet is increased leading to a higher second moment of area which is represented by equation (6-1)

$$J_{qq} = \int_A LL^2 dA \qquad (6\text{-}1)$$

J_{qq} Is the second moment of area about line q , dA is an element area LL is the perpendicular distance from line q to element dA

While the higher laser power increases the thickness of the platelet, it also leads to a lower porosity which increases the strength. If the change in porosity and compressive strength are considered, it is apparent that the increase in thickness of the platelets can enlarge the range of available properties.

As seen in Figure 6-10, the dark spot in the circle was formed by a number of scanning points assembled in a small area. When the laser scanned these points, it leads to the increase of the local energy density and this resulted in solid blocks which can be found in fabricated RVS samples. The geometries of these solid blocks vary with each fabrication and it is this that leads to the variability in behaviour of different samples and thus the larger error bar (Figure 6-9) in porosity and compressive strength.

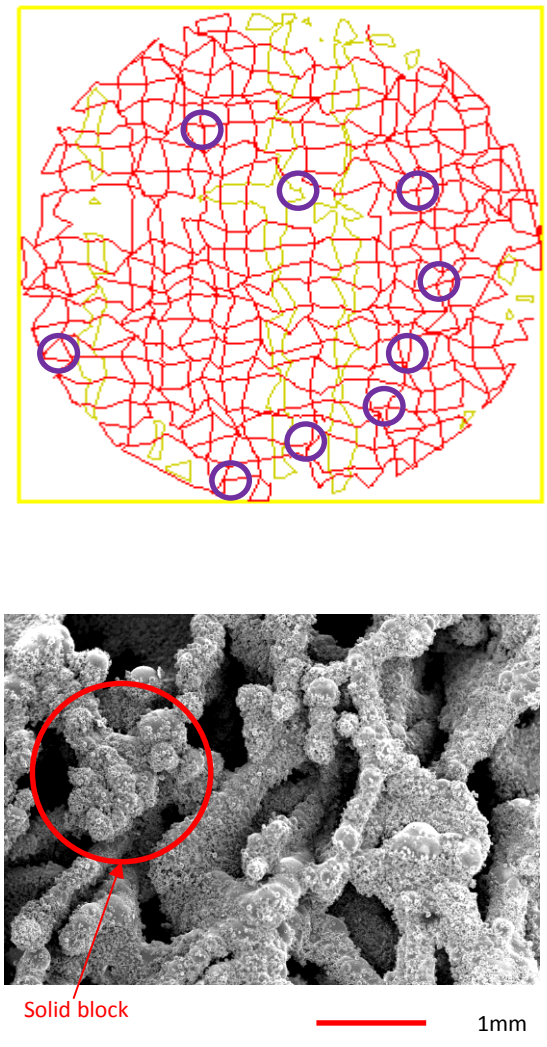

Figure 6-10 Sliced layer of a RVS and a solid block caused by local higher energy density.

Furthermore the cancellous bone mass reduces over time with aging to give high porosity structure. This reduction is due to the thinning of the cell walls and

decreases the compressive strength of cancellous bone. This result is consistent with the experimental result.

6.2.3. The Effect of Cell Size

As discussed in Chapter 5, it has been seen that the cell size can cause a change in porosity and compressive strength in the regular vaulted structures. In this section, the cell size effect is investigated for the randomised structures by the following experiments.

Experiment Arrangement

Two groups of RVS samples (Cylinder Ø 15mm × 30mm) were generated by using the new software and fabricated by using the SLM Realizer 100 based on the parameters listed in Chapter 3. The cell size was set to 900µm or 1200µm which will alter the porosity and compressive strength of the randomised vaulted structure. The VS with 1200µm cell size was predicated to give a lower compressive strength by the Ashby's equation (5-4), and therefore the hole size was set at 40% so as to ensure the compressive strength test could be performed using the Instron 4515 with the same load cell.

$$\sigma_P = C\sigma_0 D^m \qquad (6\text{-}2)$$

Where σ_0 is the strength of fully dense material, D is the porosity, C contains all the constant of proportionality varying between 1 and 3/2 for open porous structure [174]

Results

As shown in Figure 6-11, when the cell size was reduced from 1200µm to 900µm, the porosity was reduced. The maximum difference in porosities is 26% and the minimum difference is 25%. As shown in Figure 6-12, when the cell size was set to 900µm, it provides a higher compressive strength. The lower limit of difference in compressive strength is 145MPa and the upper limit of difference in compressive strength is 175MPa.

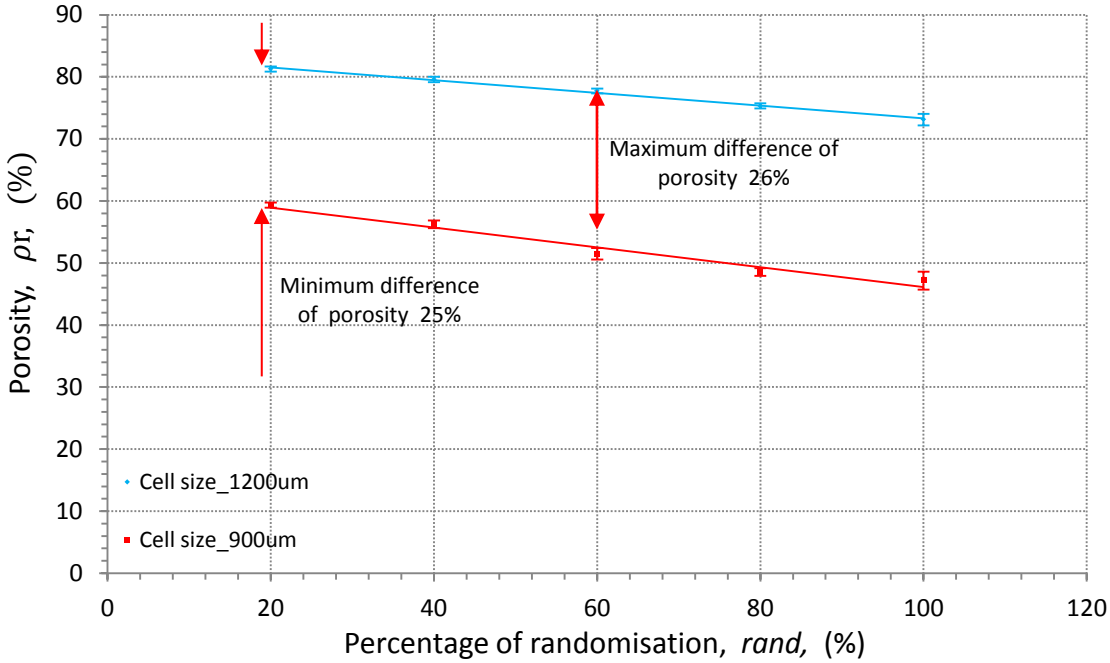

Figure 6-11 The change of porosity versus percentage randomisation at different zero percentage of randomisation (CpTi).

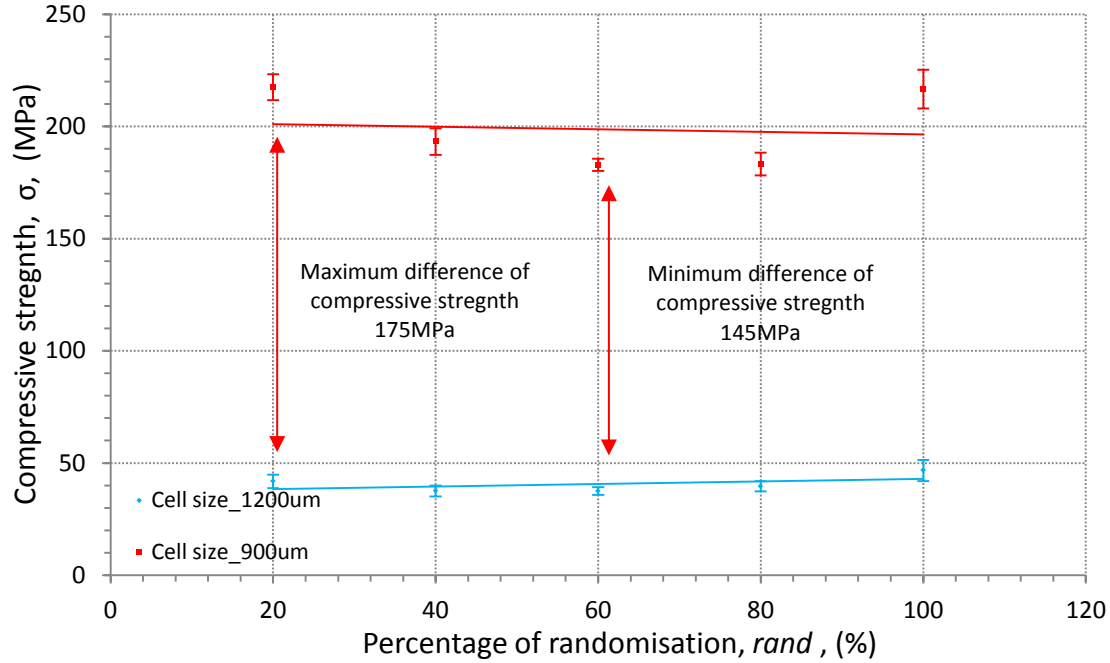

Figure 6-12 The change of compressive strength versus percentage randomisation at different zero percentage of randomisation (CpTi).

Discussion

As discussed in Chapter 4, the deformation of a platelet was controlled by its vertex coordinates which are defined by following equation (6-3) to (6-8):

$$x = x0 + percentage\ of\ randomisation\ in\ x\ axis \times move\ direciton\ in\ x\ axis \times length\ of\ cell \quad (6\text{-}3)$$

$$y = y0 + percentage\ randomisation\ in\ y\ axis \times move\ direciton\ in\ y\ axis \times width\ of\ cell \quad (6\text{-}4)$$

$$z = z0 + percentage\ of\ randomisation\ in\ z\ axis \times move\ direciton\ in\ z\ axis \times heigth\ of\ cell \quad (6\text{-}5)$$

Where $x0, y0, z0$ is the original coordinates of a vertex and x, y, z is the current coordinates of a vertex.

$$percentage\ of\ randomisation\ in\ x\ axis = \frac{movement\ in\ x\ axis}{length\ of\ cell} \times 100 \quad (6\text{-}6)$$

$$percentage\ of\ randomisation\ in\ y\ axis = \frac{movement\ in\ y\ axis}{width\ of\ cell} \times 100 \quad (6\text{-}7)$$

$$percentage\ of\ randomisation\ in\ z\ axis = \frac{movement\ in\ z\ axis}{heigth\ of\ cell} \times 100 \quad (6\text{-}8)$$

The equations (6-3) to (6-8) are used to define the movement of the coordinates, which in turn control the randomisation and the amount of distortion in the platelet. More importantly they also control the alignment of the plates relative to the principal load direction in the compression test. In the non-random structure the vertical platelets align directly with the applied load, like the walls in a building. As randomisation initially increases the strength of the structure decreases due to misalignment of these walls with the load. However as the randomisation increases further the original strength is regained as at higher levels of randomisation creates cross bracing in the cells of the structure. This has the main advantage of stopping the layer by layer collapse seen in the regular structures, and in buildings. This effect is only true when the cell size is small. For a small cell size, when the percentage of randomisation is more than 60%, a vertex may move into a neighbouring cell, resulting in the platelets intersecting. These intersections can be seen in Figure 6-13 (the sliced digital model of the structure), the layer image showing that the intersection starts to occur at about 60% randomisation and increase with the percentage of randomisation, in the range of 60% to 100%. The

thickness the platelets in the intersection are increased by the laser scanning the region more than once.

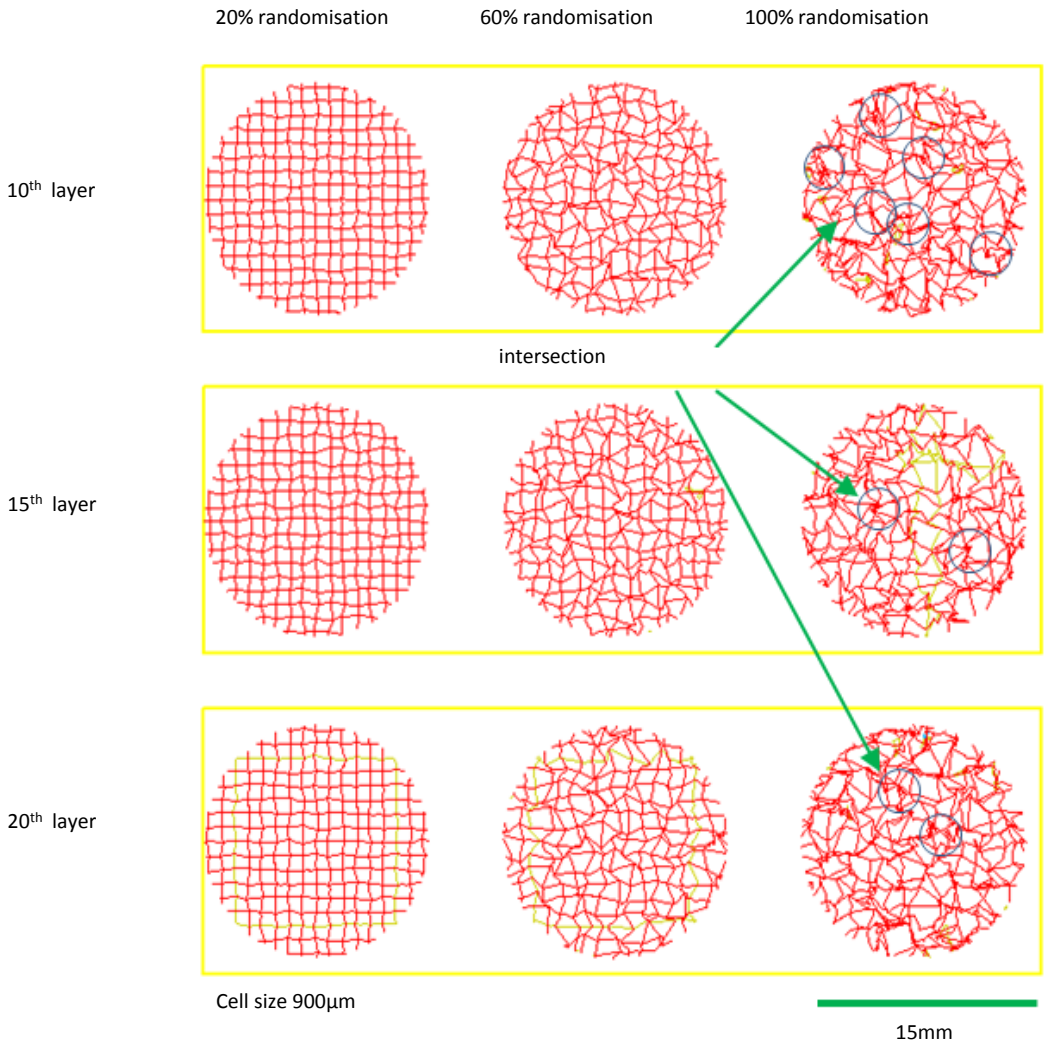

Figure 6-13 Layer image varying in layer number and percentage of randomisation

However, when the cell size is larger different effects are observed with a much lower strength that is less affected by randomisation, although there is still some increase in strength at very high randomisations. The effect of randomisation on the structure can be seen in Figure 6-14, and in this case the deformed platelet size is larger and gives less intersections and therefore less triangulation of the structure, while also developing some fairly large regions which are devoid of platelets. Therefore when loaded in compression, the larger platelet exhibited lower resistance to platelet bending and collapse of the structure.

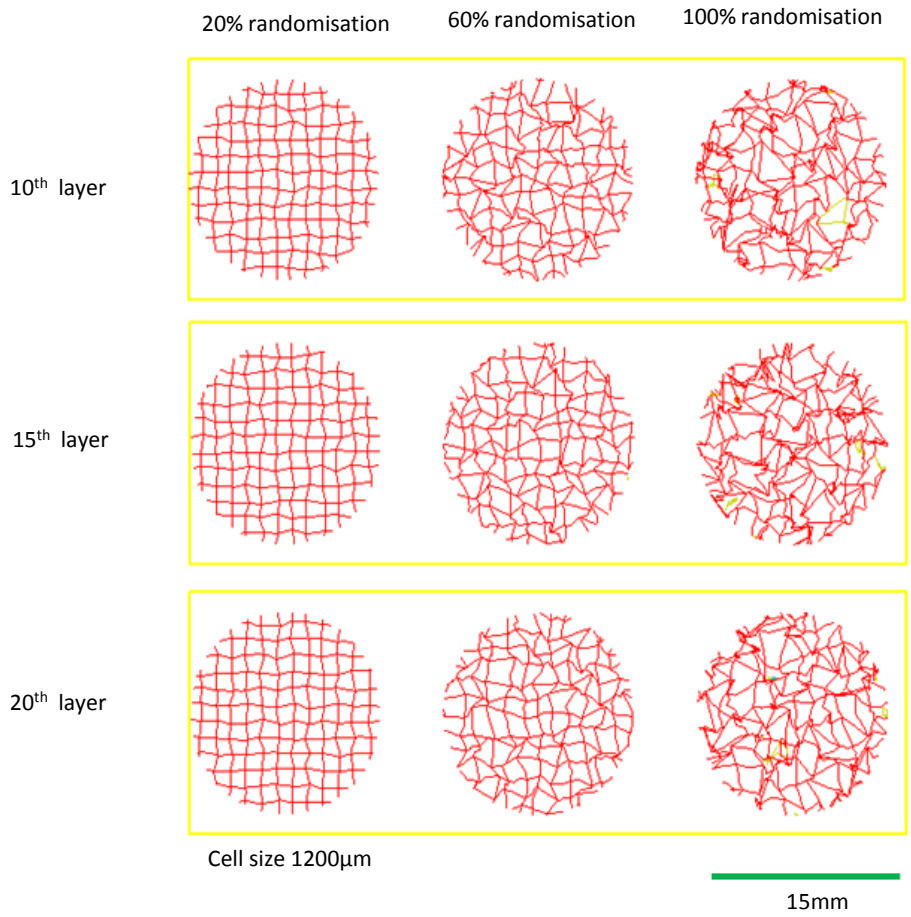

Figure 6-14 Layer image varying in layer number and percentage of randomisation

By comparing the change in porosities (44% to 51%) with the change of compressive strength (387% to 419%), it indicates that changing the cell size is an effective way of enlarging the range of available properties for a randomised vaulted structure.

6.2.4. Randomised Vaulted Structure Isotropy

As discussed in Chapter 5, the regular vaulted structures do not behave in an isotropic manner regardless of which cell aspect ratio is used. In this section, a set of experiments was arranged to investigate if it is possible to get isotropic behaviour within the RVS by altering the cell aspect ratio as well as the random deformation mechanism.

Experiment Arrangement

Three groups of samples (Cylinders Ø 15mm × 30mm) varying with cell size and aspect ratio (1:1:1, 2:2:1 and 1:1:2) were created. In each group, the hole size was

set to 80% to ensure the compressive strength test was suitable for testing using the Instron 4515 and the cell size was set to 900µm to ensure the number of cells in each direction was more than seven. In order to measure the compressive strength in each direction, the process for creating, fabricating and testing sample followed that detailed in Figure 5-23.

Results

Figure 6-15 shows the compressive strength and porosity when the aspect ratio of the cell was set to 1:1:1. The compressive strength with its corresponding porosity varies in different directions and percentage of randomisation. The results were clustered in different areas of the graph with no overlap between them. Similar results are observed in Figure 6-16 when the aspect ratio was set to 2:2:1. The result was approximated by two trend lines, the trend lines appear parallel and there is no intersection between them. Although a similar result is observed in Figure 6-17 (cell aspect ratio 1:1:2) as well, the differences of compressive strength and porosity in the plane direction and out of the plane direction are quite close to each other when the percentage of randomisation is more than 60%.

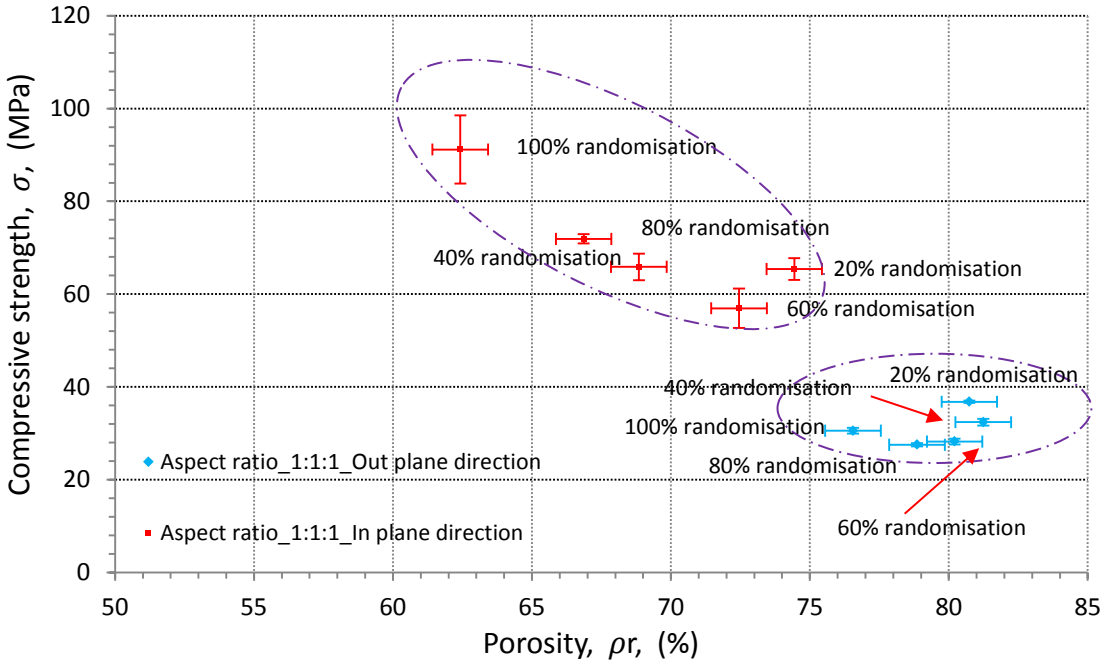

Figure 6-15 When the aspect ratio is set to 1:1:1, the compressive strength of RVS with its corresponding porosity varying in direction and percentage of randomisation (CpTi).

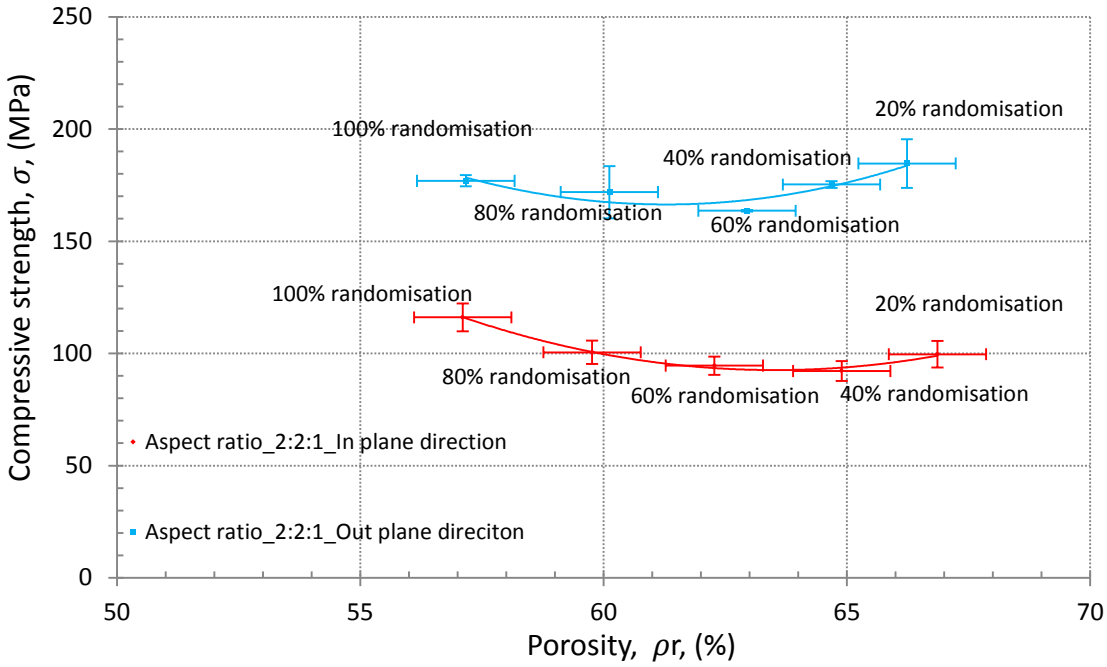

Figure 6-16 When the aspect ratio is set to 2:2:1, the compressive strength of RVS with its corresponding porosity varying in direction and percentage of randomisation (CpTi).

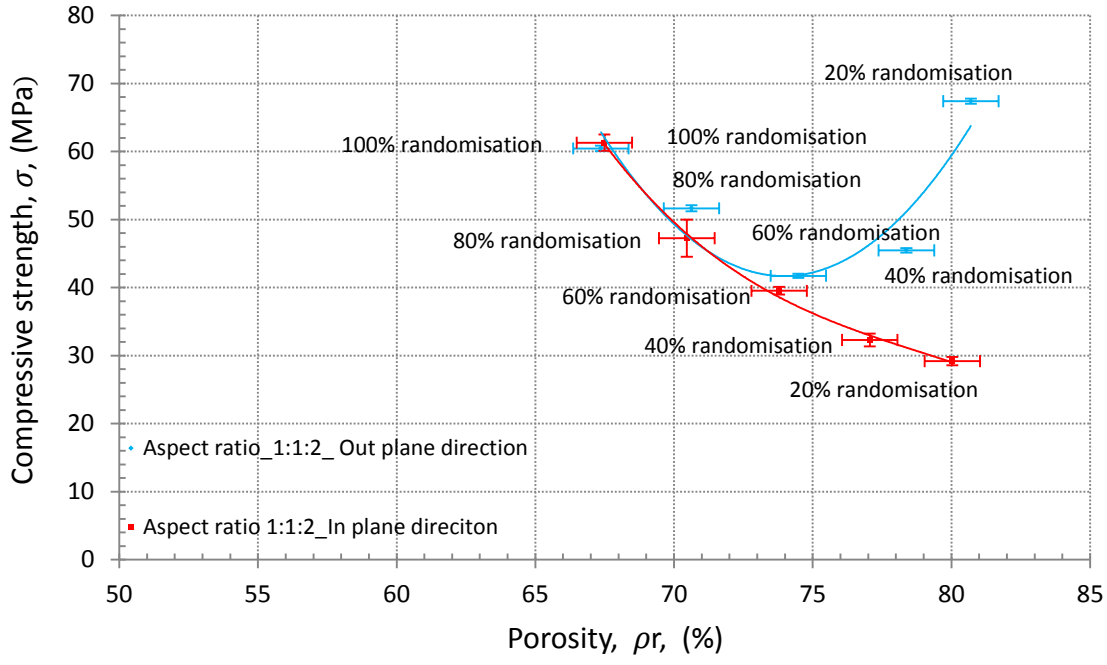

Figure 6-17 When the aspect ratio is set to 1:1:2, the compressive strength of RVS with its corresponding porosity varying in direction and percentage of randomisation (CpTi).

Discussion

Consideration of these results requires a discussion of the RVS appearance. In Chapter 4, the hole size is defined as the percentage of the possible maximum hole in a platelet and the various aspect ratio of cell (platelet) can allow the structure to exhibit different appearances. As seen in Figure 6-18, when the aspect ratio of the platelets was set to 1:1, the appearance in the X direction and Z direction gives same appearance (rod like structure or platelet like structure). However when the aspect ratio was 1:2, the appearance (platelet like structure) in the X direction was different to that in the Z direction (rod like structure). When the aspect ratio was 2:1, a rod like structure was exhibited in the X direction and a platelet like structure was seen in the Z direction. These structures varied with aspect ratio and can exhibit either anisotropic or isotropic behaviour.

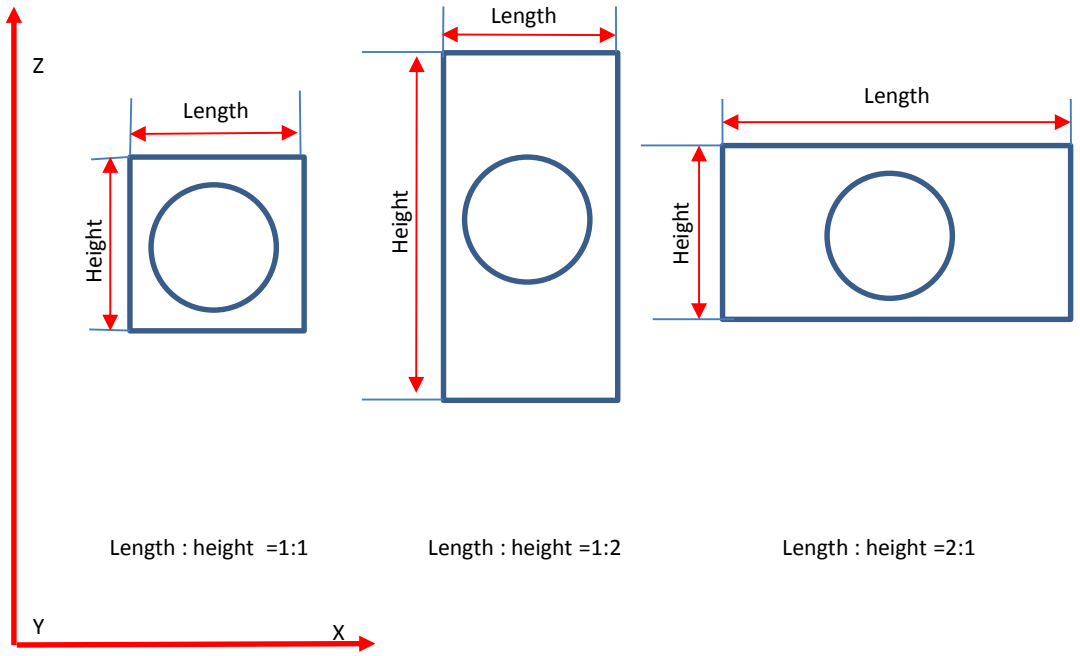

Figure 6-18 The net cross section area varying in the platelet aspect ratio.

Figure 6-19 shows the structure of a specimen from the human femoral condyle which shows a structure with rods normal to the platelets. This structure gives stress-oriented mechanical properties and the compressive strength parallel to the platelets is higher than that vertical to the platelets [174]. However a specimen (Figure 6-19) from the human femoral head shows a lower density and rod like

structure and the principal stresses are roughly equal to each other [174]. Therefore the compressive strength of a structure is dictated by the elements (rod or platelet) ability to resist the bending moment acting on itself.

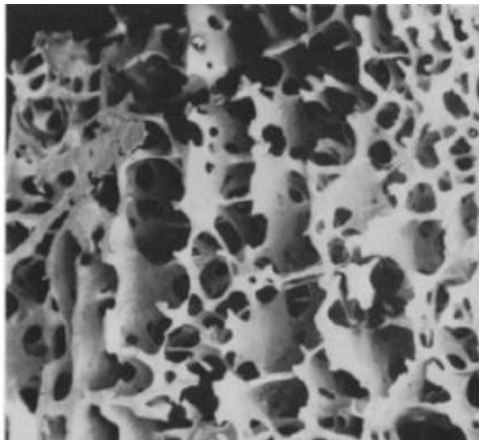

A specimen from the femoral condyle

A specimen from the femoral head

Figure 6-19 SEM image of specimens from the femoral condyle and femoral head [174].

By comparing the compressive strength in the various directions (Figure 6-15, Figure 6-16 and Figure 6-17) for various aspect ratios, it is apparent that when the aspect ratio was set to 1:1:2, the behaviour was fairly tending forwards isotropic behaviour if the percentage of randomisation was more than 60%.

6.3. Application

As discussed in Chapter 2, this RVS was designed for use as a surface coating in THRs to promote bone ingrowth and for other orthopaedics applications. In order to compare the appearance of a RVS to that of a randomised unit cell structure, a RVS (cell size 600µm) was created by the software and fabricated based on the parameters listed in Chapter 3. Figure 6-20 shows that the appearance of the RVS is close to that of randomised unit cell structure (Figure 6-21).

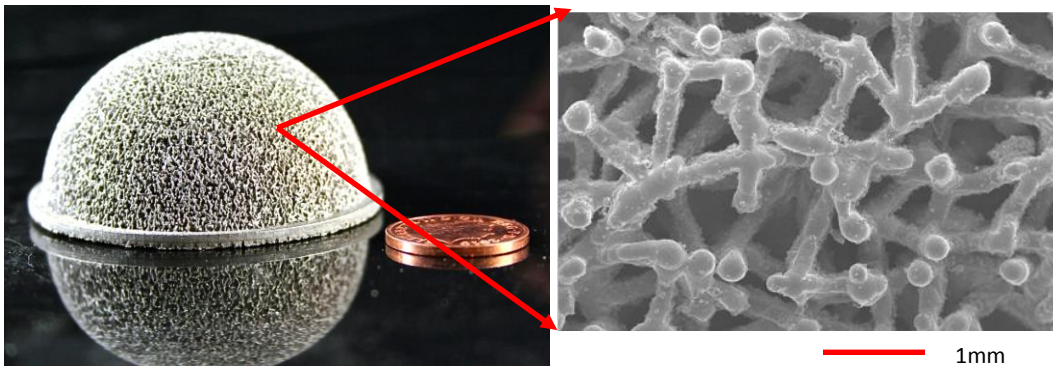

Randomised vaulted structure, cell size600µm, cell size aspect ratio 1:1:1,percentage of random (60%), CpTi, fabricated by MCP Realizer.

Figure 6-20 RVS (fabrication parameters listed in Appendix A).

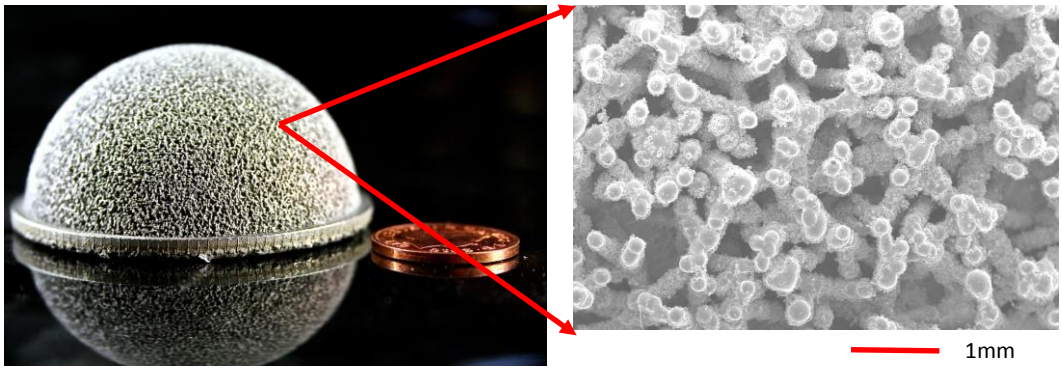

Randomised unit cell structure, cell size600µm, cell size aspect ratio 1:1:1,percentage of random (-30% to 30%), CpTi, fabricated by MCP Realizer.

Figure 6-21 Randomised unit cell structure (fabrication parameters listed in Appendix A).

The pore size distribution of this structure has been measured by mercury porosimetry as can be seen in Figure 6-22. Limited number of pore sizes less than 100µm and most of them lie in the range of 100 to 600µm which is the optimum

size for promoting bone ingrowth. Furthermore this RVS possesses a higher compressive strength 155MPa (minimum required compressive strength 30MPa) at the porosity of 65%, while still meeting the bone ingrowth requirements set out in Chapter 2. This new structure ensures sufficient space for bone ingrowth under loading condition along with sufficient strength.

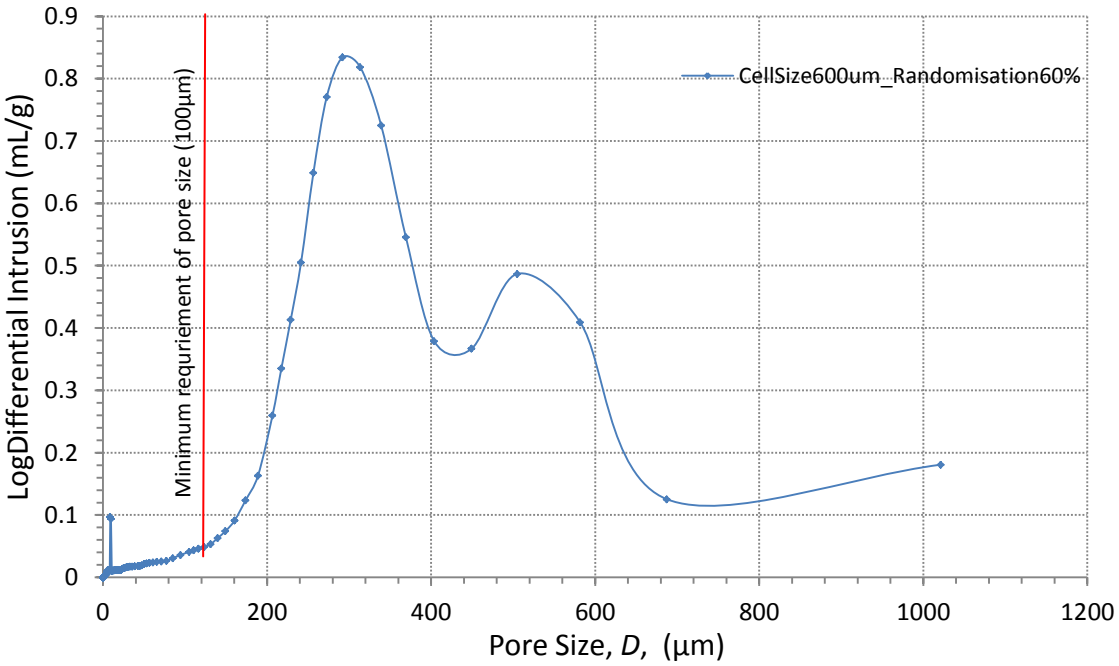

Figure 6-22 Pore size distribution of 60% of RVS

6.4. Summary

As discussed in Chapter 4, a RVS that resembles cancellous bone has successfully been created in Chapter 5, further work has been presented to show that its behaviour mimics the mechanical properties of cancellous bone. By using the random deformation mechanism, the mechanical properties of the structures was highly improved and their stress-strain curve is seen to resemble that of a cancellous bone. Furthermore, the range of available properties (Figure 5-27) has been enlarged by modifying the cell size, hole size and thickness of platelets. The enlarged range of properties can give more choices for patients of all age groups or extended to different application.

Previous studies showed that the anisotropic or isotropic behaviour of cancellous bone varies with its location, for example, the femoral condyle exhibits anisotropic behaviour while the femoral head shows approximately isotropic behaviour and also the appearance of cancellous bone structure varies with orientation and this dictates the anisotropic or isotropic behaviour. By extending these studies, a RVS with near isotropic behaviour has been achieved. This method for altering the anisotropic or isotropic behaviour increases the capability of the structure to resemble the mechanical properties of cancellous bone varying with location.

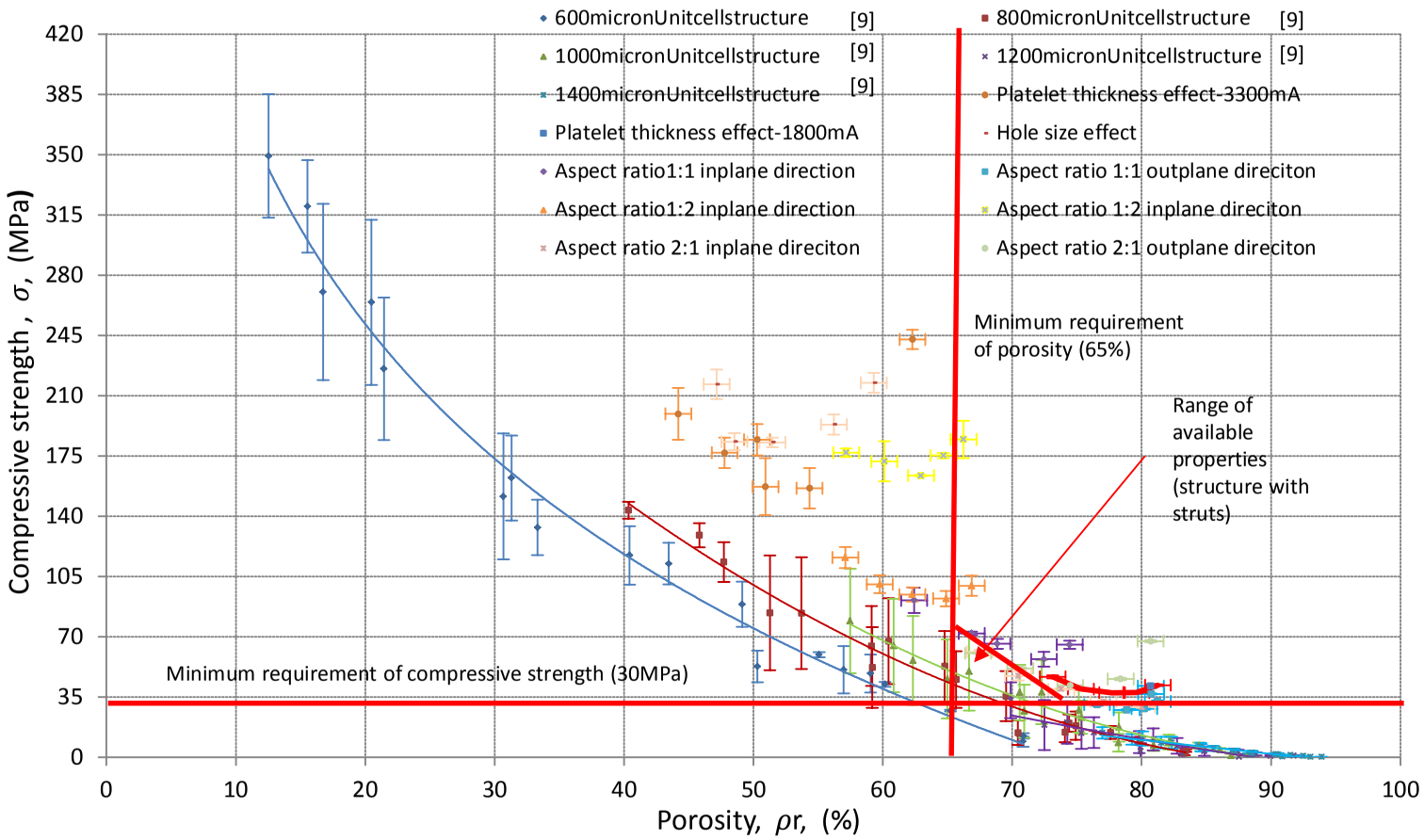

Figure 6-23 The range of available properties of unit cell structure with struts and RVS (experiment data listed in Appendix E).

CHAPTER 7

CONCLUSION AND FUTURE WORK

The aim of this research was to create a platelet based structure, fabricated by SLM for use in surface coatings for promoting bone ingrowth. This chapter collates the conclusions drawn from this research. In order to further the use of these structures as bone ingrowth structures in orthopaedic components, this chapter also outlines future work.

7.1. Conclusions

In this research, platelet-based structures produced by SLM were designed, fabricated and tested to determine whether they were suitable to be considered for orthopaedic implants. In order to run this newly developed software, a user interface was designed, with particular attention being played to its role in device history record keeping. Through the interface, the user is able to manipulate the functions to produce all porous or integrally solid and porous based upon unit geometries, whose features are capable of being accurately and consistently modified to change the part property. The inclusion of diagnostics which are able of estimating some physical attributes is also included, together with the capability of data visualisation. The inter-relationships between various structures and variables are determined with respect to part compressive strength and porosity with the objective of proving that the optimally designed structures have useful mechanical properties with the capability of producing functional medical device components. The conclusion of this work are summarised in 4 sections namely: software development, process parameter development, mechanical properties testing and part production

7.1.1. Software Development

The software has been developed to operate with a range of basic geometries which include hexagonal prism and cubes which are stacked together in part shape.

The features of the geometries can be changed in many ways, for example by omitting portions of the surface such as a connecting wall and/or a parallel wall in a cube, the inclusion of holes in walls and changing the thickness of the plates. The software has been developed on 4-walled cubes, but the capability is embedded into the software to changes the shape of the basic geometry. Finally this software full fills the following tasks:

a) Create a bone ingrowth structure with tessellated surface to reduce the requirement of PC memory, which is the bottle neck for current method limited in constructing more than 2000 continuous surfaces.
b) Randomly deform the surface of the bone ingrowth structure to mimic the appearance of cancellous bone both from young and old patients.
c) Efficiently trim a bone ingrowth structure block to the desired shape using a revised bounding box method.
d) Slice the bone ingrowth structure for SLM fabrication and overcome the laser multi-scanning issue by offsetting intersections by one point distance.
e) Outputting the files in the required format.

The output can be diagnosed such as computing the porosity and pore size distribution to reduce the number of samples that has been manufactured for testing. Comparing the computed porosity and measured porosity, the difference between them is limited in 15% by considering the low angle triangles. A revised method has been programmed and run in a standard PC (Intel core™ 2 Due CPU E8400@3.00GHZ with 4GB memory) to compute the pore size distribution of porous sample. The required memory can be reduced by representing porous sample by a set of triangles rather than voxels and the computing time can be saved by introducing fast intersection test between sphere and triangle. This method has been validated by comparing the generated pore size distribution of an arbitrary porous structure to computed pore size distribution and visualising them.

7.1.2. Process Parameter Development

The process parameters for fabricating unit cells structure, solid part and vaulted structure are fully developed with reference to the SLM 100 manual. These process parameters are embedded into a material file (.dat). By using these parameters, a set of orthopaedic implants for demonstration and porous samples have been successfully fabricated for investigating the mechanical properties of these structures.

7.1.3. Mechanical Properties Testing

The range of available mechanical properties of the regular vaulted structure can be significantly enlarged by modifying the cell size and/or the hole size but not the platelet thickness. By using a randomisation mechanism, a RVS was created and its range of available mechanical properties can be enlarged by altering the cell size, hole size and thickness of platelet. The range of available mechanical properties is larger than that of unit cell structures and the larger range can provide more option for all age patients. A summary of this enlarged range of available properties is presented in Figure 7-1, in graphical form, and it shows how these structures compare with other porous structures (data compiled from Cambridge Materials Selector database (University Edition)).

By using the randomisation mechanism, the mechanical properties of the vaulted structures were improved and exhibited stress versus strain behaviour very similar to cancellous bone. Furthermore, the anisotropic or isotropic behaviour can be controlled by changing the cell size aspect ratio and percentage of randomisation. When the cell size aspect ratio was set to 1:1:2 and the percentage of randomisation was more than 60%, the structure exhibited isotropic behaviour that can mimic that of human cancellous bone in varying with location.

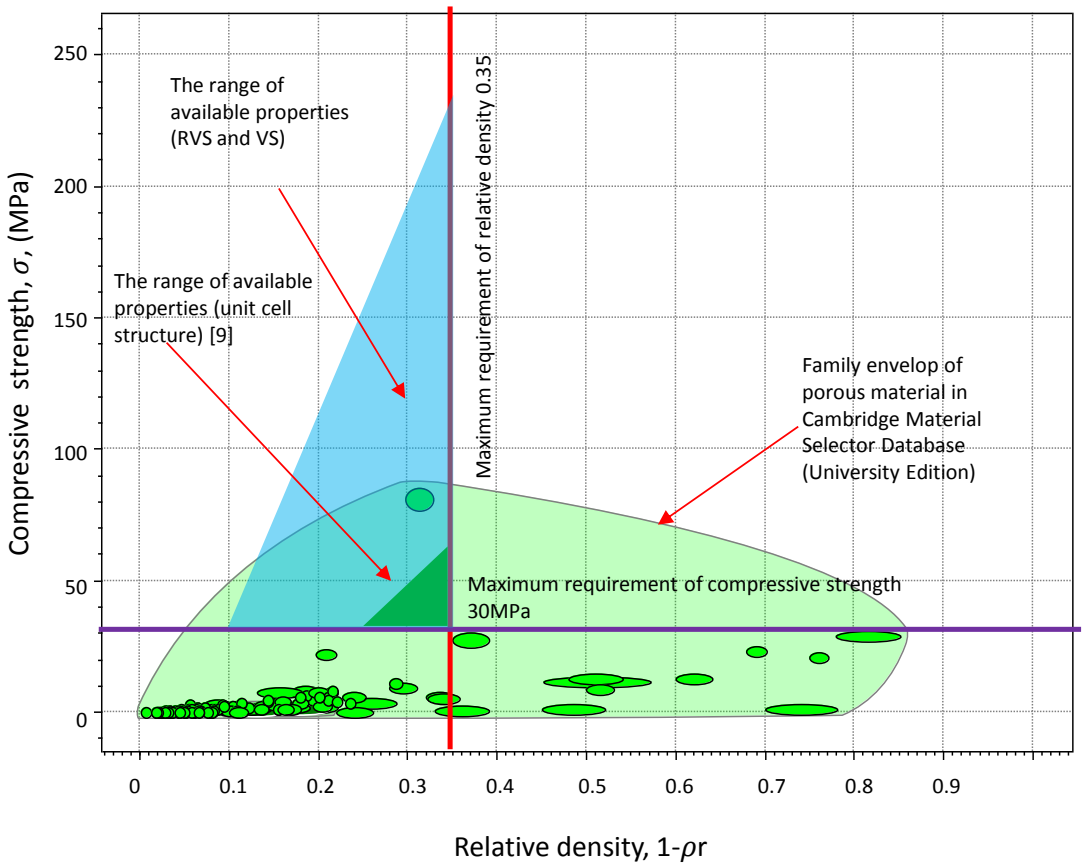

Figure 7-1 The variation of compressive strength with relative density for different porous materials.

7.1.4. Part Production

The software has been tested by creating a range of typical implants with different geometries such as solid part and porous parts that include regular and RVSs. The structures can be produced to have the appearance requested by orthopaedic surgeons, and mechanical test results on standard test geometries would indicate that implants can be produced with improved mechanical properties.

7.2. Future Work

As discussed, a bone ingrowth structure should meet the requirements listed in Chapter 2 to promote the bone ingrowth and therefore one of the future works will carry out a biological study to measure the bone ingrowth rates. Furthermore, the mechanical properties of a bone ingrowth structure also need to meet the following requirements[95].

Table 7-1 The bone ingrowth structure requirements for mechanical properties with appropriate test standard

Test type	Required value	ASTM standard number
Tensile	20MPa	ASTM F 1147-05
Shear	20MPa	ASTM F 1044-05
Shear and bending fatigue	10^7 Cycles	ASTM F 1160-05

A previous study indicated that the structure of cancellous bone changes over time due to the reduction in bone mass with ageing [183] and leads to the increase in porosity. This increase may be due to the complete loss of some cell wall [184]. Thus future work is needed to investigate the structure with 2 platelets (Figure 7-2) in each cell which also can be created by the new software.

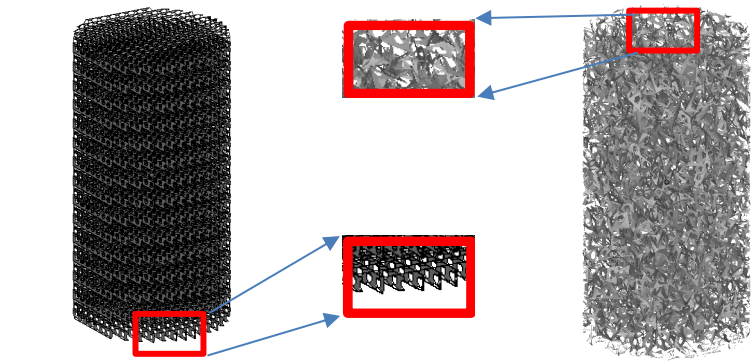

Two parallel platelets in each cell and percentage of randomisation:0%

Two parallel platelets in each cell and percentage of randomisation:60%

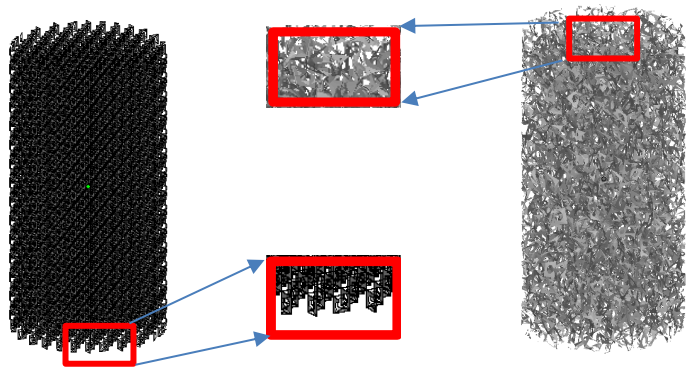

Two vertical platelets with right angle in each cell and percentage of randomisation:0%

Two vertical platelets with right angle in each cell and percentage of randomisation:60%

Figure 7-2 Regular and RVS with two platelets in each cell.

Furthermore, in this research, the structure was created based on the quadrilateral distribution of platelets in each cell, however the hexagonal and triangular

distribution of platelets in each cell have been shown to mimic the mechanical properties of cellar material [189]. Potentially, more novel platelet based structures may be found to exhibit larger range of available properties. These structures (Figure 7-3) also can be created using these techniques discussed here.

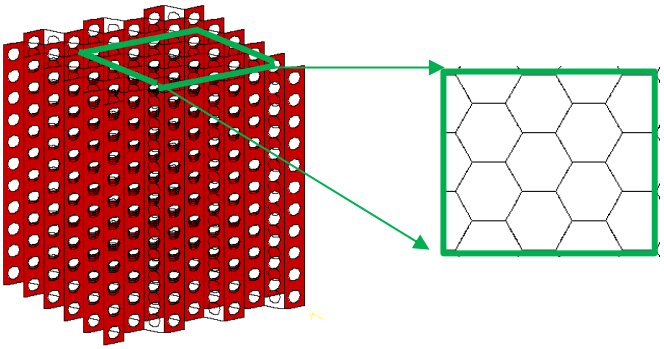

Hexagonal distribution of platelets in each cell

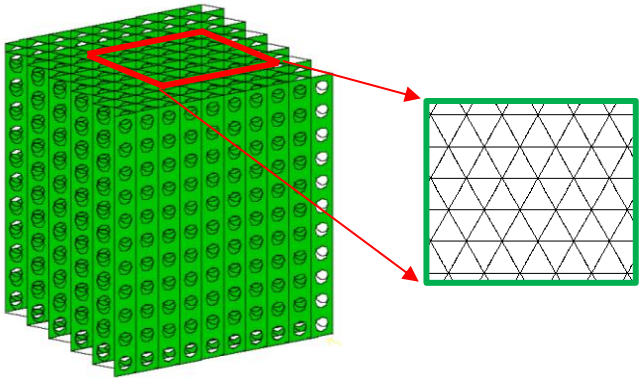

Triangular distribution of platelets in each cell

Figure 7-3 Hexagonal and triangular distribution of platelets in each cell of vaulted structure.

7.3. Publications and Patents

The highly novel technique developed for creating and fabricating the vaulted structure have been reviewed for potential publications as patents. Following approval of release from this research, the studies in this project will be published under following publication headings:

- Platelet based structure for orthopaedic applications.
- Isotropy in platelet based structure fabricated by selective laser melting.
- A methodology for computing pore size distribution.

CHAPTER 8

REFERENCES

1. Yamada H, Yoshihara Y, Henmi O, Morita M, Shiromoto Y, Kawano T, et al. Cementless total hip replacement: past, present, and future. Journal of Orthopaedic Science. 2009 Mar;228–41.

2. Huiskes R, Stolk J. Biomechanics and preclinical testing of artificial joints: the hip basic. In: Van CM, Huiskes R, editors. Basic Orthopaedic Biomechanics and Bechano-Biology. Lippincott Williams & Wilkins.; 2005.

3. Knee replacement revision surgery [Internet]. 2013. Available from: http://www.drugwatch.com/knee-replacement/revision-surgery/

4. Hip Implants - OrthoInfo - AAOS [Internet]. [cited 2012 Oct 22]. Available from: http://orthoinfo.aaos.org/topic.cfm?topic=A00355

5. Corten K, Bourne RB, Charron KD, Au K, Rorabeck CH. Comparison of total hip arthroplasty performed with and without cement: a randomized trial: a concise follow-up, at twenty years, of previous reports. Journal of Bone and Joint Surgery. American volume. 2011 Jul 20;1335–8.

6. Corten K, Bourne RB, Charron KD, Au K, Rorabeck CH. What works best, a cemented or cementless primary total hip arthroplasty?: minimum 17-year followup of a randomized controlled trial. Journal of Clinical Orthopaedics and Related Research. 2011 Jan;209–17.

7. Hooper GJ, Rothwell AG, Stringer M, Frampton C. Revision following cemented and uncemented primary total hip replacement: a seven-year analysis from the New Zealand Joint Registry. Journal of Bone and Joint Surgery. British volume. 2009 Apr;451–8.

8. Stamp R, Fox P, O'Neill W, Jones E, Sutcliffe CJ. The development of a scanning strategy for the manufacture of porous biomaterials by selective laser melting. Journal of Materials Science. Materials in Medicine. 2009 Sep;1839–48.

9. Mullen L. The characterisation and structural optimisation of additively fabricated porous components specifically for use in orthopaedic applications. University of Liverpool; 2010. p. 195.

10. Stucker IG l DWR l B. Additive Manufacturing Technologies. Springer; 2010. p. 298.

11. Grace PA. Doctors differ over the German crown prince. British Medical Journal. 1992;1536–8.

12. Charnley J. Anchorage of the femoral prosthesis. Journal of Bone and Joint Surgery. 1960;28–30.

13. Hailer NP, Garellick G, Kärrholm J. Uncemented and cemented primary total hip arthroplasty in the Swedish Hip Arthroplasty Register. Journal of Acta Orthopaedica. 2010 Feb;34–41.

14. Engh CA, Bobyn JD, Glassman AH. Porous-coated hip replacement. The factors governing bone ingrowth, stress shielding, and clinical results. Journal of Bone and Joint Surgery. 1987;45–55.

15. American Academic Orthopaedic Surgeons [Internet]. [cited 2012 Feb 7]. Available from: http://orthoinfo.aaos.org/

16. Iorio R, Puskas B, Healy WL, Tilzey JF, Specht LM, Thompson MS. Cementless acetabular fixation with and without screws: analysis of stability and migration. Journal of Arthroplasty. 2009;309–13.

17. Hopper RH, Engh CA. Long-term porous-coated cup survivorship using spikes, screws and press-fitting for initial fixation. Journal of Arthroplasty. 2004;54–60.

18. Ihle M, Mai S, Pfluger D, Siebert W. The results of the titanium-coated RM acetabular component at 20 years: a long-term follow-up of an uncemented primary total hip replacement. Journal of Bone and Joint Surgery. British volume. 2008 Oct;1284–90.

19. Lee K, Goodman SB. Current state and future of joint replacements in the hip and knee review. Journal of Expert Rev Med Devices. 2008;383–93.

20. Russell RC, Ghassemi A, Dorrell JH, Powles DP. The Bimetric cementless total hip replacement: 7-18 year follow-up assessing the influence of acetabular design on survivorship. Journal of International Orthopaedics. 2009 Aug;933–7.

21. Le D, Smith K, Tanzer D, Tanzer M. Modular femoral sleeve and stem implant provides long-term total hip survivorship. Journal of Clinical Orthopaedics and Related Research. 2011 Feb;508–13.

22. McLaughlin JR, Lee KR. Total hip arthroplasty with an uncemented tapered femoral component. Journal of Bone and Joint Surgery. 2008 Jun;1290–6.

23. Total hip replacement for young patient [Internet]. [cited 2011 Feb 3]. Available from: http://evertsmith.com/innovations/

24. Learmonth ID, Young C, Rorabeck C. The operation of the century: total hip replacement. Journal of Lancet. 2007 Oct 27;1508–19.

25. Krause WR, Krug W, Miller J. Strength of the cement-bone interface. Journal of Clinical Orthopaedics and Related Research. 1982 Mar;290–9.

26. Dorr LD, Bloebaum R, Emmanual J, Meldrum R. Histologic, biochemical, and ion analysis of tissue and fluids retrieved during total hip arthroplasty. Journal of Clinical Orthopaedics and Related Research. 1990 Dec;82–95.

27. Shanbhag AS, Jacobs JJ, Black J, Galante JO, Glant TT. Cellular mediators secreted by interfacial membranes obtained at revision total hip arthroplasty. Journal of Arthroplasty. 1995 Aug;498–506.

28. Willert HG, Semlitsch M. Tissue reactions to plastic and metallic wear products of joint endoprostheses. Journal of Clinical Orthopaedics and Related Research. 1996 Dec;4–14.

29. Willert HG, Semlitsch M. Reactions of the articular capsule to wear products of artificial joint prostheses. Journal of Biomedical Materials Research. 1977 Mar;157–64.

30. Goldring SR, Jasty M, Roelke MS, Rourke CM, Bringhurst FR, Harris WH. Formation of a synovial-like membrane at the bone-cement interface. Its role in bone resorption and implant loosening after total hip replacement. Journal of Arthritis and Rheumatism. 1986 Jul;836–42.

31. Charnley J. Arthroplasty of the hip. A new operation. Journal of Lancet. 1961 May 27;1129–32.

32. Charnley J, Follacci FM, Hammond BT. The long-term reaction of bone to self-curing acrylic cement. Journal of Bone and Joint Surgery. British volume. 1968 Nov;822–9.

33. Dennis K. Collis M. Hip replacement: current trends and controversies. Journal of Bone and Joint Surgery. 2003 Mar 1;587–8.

34. Bjørgul K, Novicoff WM, Andersen ST, Brevig K, Thu F, Wiig M, et al. No differences in outcomes between cemented and uncemented acetabular components after 12-14 years: results from a randomized controlled trial comparing Duraloc with Charnley cups. Journal of Orthopaedics and Traumatology. 2010 Mar;37–45.

35. Kim Y-H, Kim J-S, Park J-W, Joo J-H. Total hip replacement with a short metaphyseal-fitting anatomical cementless femoral component in patients aged 70 years or older. Journal of Bone and Joint Surgery. British volume. 2011 May;587–92.

36. Mäkelä KT, Eskelinen A, Paavolainen P, Pulkkinen P, Remes V. Cementless total hip arthroplasty for primary osteoarthritis in patients aged 55 years and older. Journal of Acta Orthopaedica. 2010 Feb;42–52.

37. Gross TP, Liu F. The first 100 fully porous-coated femoral components in hip resurfacing. Bulletin of the NYU Hospital for Joint Diseases. 2011;30–5.

38. Jamieson ML, Russell RD, Incavo SJ, Noble PC. Does an enhanced surface finish improve acetabular fixation in revision total hip arthroplasty? Journal of Arthroplasty. Elsevier Inc.; 2011 Jun;644–8.

39. Black J. Orthopaedic Biomaterials in Research and Practice. Churchill Livingstone; 1988.

40. Harris WH, White RE, McCarthy JC, Walker PS, Weinberg EH. Bony ingrowth fixation of the acetabular component in canine hip joint arthroplasty. Journal of Clinical Orthopaedics and Related Research. 1983 Jun;7–11.

41. Alexander H, Brunski JB. Biomaterials Science: an Introduction to Materials in Medicine. Academic Press; 2004.

42. Sandborn PM, Cook SD, Spires WP, Kester MA. Tissue response to porous-coated implants lacking initial bone apposition. Journal of Arthroplasty. 1988 Jan;337–46.

43. Søballe K, Hansen ES, B-Rasmussen H, Jørgensen PH, Bünger C. Tissue ingrowth into titanium and hydroxyapatite-coated implants during stable and unstable mechanical conditions. Journal of Orthopaedic Research. 1992 Mar;285–99.

44. Engh CA, Massin P. Cementless total hip arthroplasty using the anatomic medullary locking stem. Results using a survivorship analysis. Journal of Clinical Orthopaedics and Related Research. 1989 Dec;141–58.

45. Hip Replacement Recovery Time [Internet]. [cited 2012 Feb 6]. Available from: http://www.buzzle.com/articles/hip-replacement-recovery-time.html

46. Meneghini RM, Meyer C, Buckley CA, Hanssen AD, Lewallen DG. Mechanical stability of novel highly porous metal acetabular components in revision total hip arthroplasty. Journal of Arthroplasty. Elsevier Inc.; 2010 Apr;337–41.

47. Roth A, Winzer T, Sander K, Anders JO, Venbrocks RA. Press fit fixation of cementless cups: how much stability do we need indeed? Journal of Archives of Orthopaedic and Trauma Surgery. 2006 Mar;77–81.

48. Williams DF. The Williams Dictionary of Biomaterials. University press. 1999. p. 40.

49. Wapner KL. Implications of metallic corrosion in total knee arthroplasty. Journal of Clinical Orthopaedics and Related Research. 1991 Oct;12–20.

50. Geetha M, Singh AK, Asokamani R, Gogia AK. Ti based biomaterials, the ultimate choice for orthopaedic implants – a review. Journal of Progress in Materials Science. Elsevier Ltd; 2009 May;397–425.

51. Kato H, Nakamura T, Nishiguchi S, Matsusue Y, Kobayashi M, Miyazaki T, et al. Bonding of alkali and heat-treated tantalum implants to bone. Journal of Biomedical Materials Research. 2000 Jan;28–35.

52. Bermudez MD, Carrion FJ, Martinez Nicolas G, Lopez R. Erosion-corrosion of stainless steels, titanium, tantalum and zirconium. Journal of Wear. Elsevier; 2005;693–700.

53. Bobyn JD, Toh KK, Hacking SA, Tanzer M, Krygier JJ. Tissue response to porous tantalum acetabular cups: a canine model. Journal of Arthroplasty. 1999/04/29 ed. 1999;347–54.

54. Jasty M, Bragdon CR, Haire T, Mulroy RD, Harris WH. Comparison of bone ingrowth into cobalt chrome sphere and titanium fiber mesh porous coated cementless canine acetabular components. Journal of Biomedical Materials Research. 1993;639–44.

55. Black J. Biological performance of tantalum. Journal of Clinical Materials. 1994 Jan;167–73.

56. Blokhuis TJ, Termaat MF, den Boer FC, Patka P, Bakker FC, Haarman HJ. Properties of calcium phosphate ceramics in relation to their in vivo behavior. Journal of Trauma. 2000 Jan;179–86.

57. Bobyn JD, Pilliar RM, Cameron HU, Weatherly GC. The optimum pore size for the fixation of porous-surfaced metal implants by the ingrowth of bone. Journal of Clinical Orthopaedics and Related Research. 263–70.

58. Osborn JF, Newesely H. The material science of calcium phosphate ceramics. Journal of Biomaterials. 1980 Apr;108–11.

59. Levine BR, Sporer S, Poggie RA, Della Valle CJ, Jacobs JJ. Experimental and clinical performance of porous tantalum in orthopaedic surgery. Journal of Biomaterials. 2006 Sep;4671–81.

60. Lemons JE. Ceramics: past, present, and future. Journal of Bone. 1996 Jul;121S–128S.

61. Jones JR, Poologasundarampillai G, Atwood RC, Bernard D, Lee PD. Non-destructive quantitative 3D analysis for the optimisation of tissue scaffolds. Journal of Biomaterials. 2007 Mar;1404–13.

62. Itälä a I, Ylänen HO, Ekholm C, Karlsson KH, Aro HT. Pore diameter of more than 100 microm is not requisite for bone ingrowth in rabbits. Journal of Biomedical Materials Research. 2001 Jan;679–83.

63. Tsuruga E, Takita H, Itoh H, Wakisaka Y, Kuboki Y. Pore size of porous hydroxyapatite as the cell-substratum controls BMP-induced osteogenesis. Journal of Biochemistry. 1997 Mar;317–24.

64. Hulbert SF Mathews RS, Klawitter JJ, Talbert CD, Stelling FH. YFA. Potential of ceramic materials as permanently implantable skeletal prostheses. Journal of Biomedical Materials Research. 1970;433–56.

65. Hannink G, Arts JJ. Bioresorbability, porosity and mechanical strength of bone substitutes: what is optimal for bone regeneration? Journal of Injury. 2011 Jun 27;22–5.

66. Kuhne JH, Bartl R, Frisch B, Hammer C, Jansson V, Zimmer M. Bone-formation in coralline hydroxyapatite - effects of pore-size studied in rabbits. Journal of Acta Orthopaedica Scandinavica. 1994;246–52.

67. Harris W, Jasty M. Bone ingrowth into porous coated canine acetabular replacements: the effect of pore size, apposition, and dislocation. Journal of Hip. 1985;214–34.

68. Shimazaki K, Mooney V. Comparative-study of porous hydroxyapatite and tricalcium phosphate as bone substitute. Journal of Orthopaedic Research. 1985;301–10.

69. Holmes RE, Bucholz RW, Mooney V. Porous hydroxyapatite as a bone-graft substitute in diaphyseal defects - a histometric study. Journal of Orthopaedic Research. 1987;114–21.

70. Salvatore JE, Kashgarian M, Barbee WR, Gilmer WS. An experimental study of the influence of pore size of implanted polyurethane sponges upon subsequent tissue formation. Journal of Surg Forum. 1961;463–8.

71. Chvapi l M, Kliment K, Stoll M, Holusa R. Some chemical and biological characteristics of a new collagen-polymer compound material. Journal of Biomedical Materials Research. 1969;315–32.

72. Hulbert SF, Klawitte JJ, Talbert CD, Fitts CT. Materials of construction for artificial bone segments. Korostoff B, editor. Research in Dental and Medical Materials. New York: Plenum Press; 1966. p. 19–67.

73. Uchida A, Nade SML, Mccartney ER, Ching W. The use of ceramics for bone-replacement - a comparative-study of 3 different porous ceramics. Journal of Bone and Joint Surgery British volume. 1984;269–75.

74. Eggli PS, Muller W, Schenk RK. Porous hydroxyapatite and tricalcium phosphate cylinders with two different pore size ranges implanted in the cancellous bone of rabbits. A comparative histomorphometric and histologic study of bony ingrowth and implant substitution. Journal of Clinical Orthopaedics and Related Research. 1988/07/01 ed. 1988;127–38.

75. Taylor DF, Smith FB. Porous methyl methacrylate as an implant material. Journal of Biomedical Materials Research. 1972;467–79.

76. Predecki P, Kirkland K, Mooney VL, Auslaend.Ba, Stephan JE. Kinetics of bone growth into cylindrical channels in aluminum-oxide and titanium. Journal of Biomedical Materials Research. 1972;375–400.

77. Mour M, Das D, Winkler T, Hoenig E, Mielke G, Morlock MM, et al. Advances in porous biomaterials for dental and orthopaedic applications. Journal of Materials. 2010 Apr 28;2947–74.

78. Koegler WS, Griffith LG. Osteoblast response to PLGA tissue engineering scaffolds with PEO modified surface chemistries and demonstration of patterned cell response. Journal of Biomaterials. 2004 Jun;2819–30.

79. Stryker. Technical Report NC S03-001. Mahwah,NJ;

80. Bobyn JD, Stackpool GJ, Hacking SA, Tanzer M, Krygier JJ. Characteristics of bone ingrowth and interface mechanics of a new porous tantalum biomaterial. Journal of Bone and Joint Surgery. British volume. 1999 Sep;907–14.

81. Karageorgiou V, Kaplan D. Porosity of 3D biomaterial scaffolds and osteogenesis. Journal of Biomaterials. 2005 Sep;5474–91.

82. Hu Y, Grainger DW, Winn SR, Hollinger JO. Fabrication of poly (alpha-hydroxy acid) foam scaffolds using multiple solvent systems. Journal of Biomedical Materials Research. 2002;563–72.

83. Maspero FA, Ruffieux K, Müller B, Wintermantel E. Resorbable defect analog PLGA scaffolds using CO2 as solvent: structural characterization. Journal of Biomedical Materials Research. 2002 Oct;89–98.

84. Fini M, Giavaresi G, Torricelli P, Borsari V, Giardino R, Nicolini A, et al. Osteoporosis and biomaterial osteointegration. Journal of Biomedicine and Pharmacotherapy. 2004 Nov;487–93.

85. Thomas KA, Cook SD. An evaluation of variables influencing implant fixation by direct bone apposition. Journal of Biomedical Materials Research. 1985 Oct;875–901.

86. Bowers KT, Keller JC, Randolph BA, Wick DG, Michaels CM. Optimization of surface micromorphology for enhanced osteoblast responses in vitro. International Journal of Oral and Maxillofacial Implants. 1992 Jan;302–10.

87. Goldberg VM, Stevenson S, Feighan J, Davy D. Biology of grit-blasted titanium alloy implants. Journal of Clinical Orthopaedics and Related Research. 1995 Oct;122–9.

88. Könönen M, Hormia M, Kivilahti J, Hautaniemi J, Thesleff I. Effect of surface processing on the attachment, orientation, and proliferation of human gingival

fibroblasts on titanium. Journal of Biomedical Materials Research. 1992 Oct;1325–41.

89. Curtis A, Wilkinson C. New depths in cell behaviour: reactions of cells to nanotopography. Journal of Biochemical Society Symposium. 1999;15–26.

90. Keller JC, Schneider GB, Stanford CM, Kellogg B. Effects of implant microtopography on osteoblast cell attachment. Journal of Implant Dentistry. 2003 Jan;175–81.

91. LeGeros RZ, Lin S, Rohanizadeh R, Mijares D, LeGeros JP. Biphasic calcium phosphate bioceramics: preparation, properties and applications. Journal of Materials Science: Materials in Medicine. Springer Netherlands; 2003 Mar 1;201–9.

92. Zhu X, Chen J, Scheideler L, Reichl R, Geis-Gerstorfer J. Effects of topography and composition of titanium surface oxides on osteoblast responses. Journal of Biomaterials. 2004 Aug;4087–103.

93. Anselme K, Bigerelle M. Topography effects of pure titanium substrates on human osteoblast long-term adhesion. Journal of Acta Biomaterialia. 2005 Mar;211–22.

94. Taché A, Gan L, Deporter D, Pilliar RM. Effect of surface chemistry on the rate of osseointegration of sintered porous-surfaced Ti-6Al-4V implants. International Journal of Oral and Maxillofacial Implants. 2004;19–29.

95. Stamp R. The rapid manufacture of hierarchical structures for orthopaedic applications. University of Liverpool; 2007.

96. McCalden RW, McGeough JA, Court-Brown CM. Age-related changes in the compressive strength of cancellous bone. The relative importance of changes in density and trabecular architecture. Journal of Bone and Joint Surgery. American volume. 1997 Mar;421–7.

97. Zardiackas LD, Parsell DE, Dillon LD, Mitchell DW, Nunnery LA, Poggie R. Structure, metallurgy, and mechanical properties of a porous tantalum foam. Journal of Biomedical Materials Research. 2001;180–7.

98. Apatsidis DP, Ryan G, Pandit A. Fabrication methods of porous metals for use in orthopaedic applications. Journal of Biomaterials. 2006;2651–70.

99. Levine BR, Fabi DW. Porous metals in orthopedic applications - A review. Poröse Metalle in orthopädischen Anwendungen - Eine Übersicht. Journal of Materialwissenschaft und Werkstofftechnik. 2010 Dec 4;1001–10.

100. Frenkel SR, Jaffe WL, Dimaano F, Iesaka K, Hua T. Bone response to a novel highly porous surface in a canine implantable chamber. Journal Of Biomedical Materials Research. Part B, Applied Biomaterials. 2004 Nov 15;387–91.

101. Davis JR. Handbook of Materials for Medical Devices. ASM International; 2003.

102. Fiber mesh [Internet]. [cited 2013 Feb 1]. Available from: http://www.zimmer.com

103. Thieme MP, Wieters K, Bergner F, Scharnweber D, Worch H, Ndop J. Titanium powder sintering for preparation of a porous functionally graded material destined for orthopaedic implants. Journal of Materials Science. 2001;225–31.

104. Yang YZ, Tian JM, Tian JT, Chen ZQ, Deng XJ, Zhang DH. Preparation of graded porous titanium coatings on titanium implant materials by plasma spraying. Journal of Biomedical Materials Research. 2000 Nov;333–7.

105. Van Der Loos CM. A focus on fixation. Journal of Biotechnic and Histochemistry. 2007 Jun;141–54.

106. Plasma spraying [Internet]. [cited 2013 Feb 1]. Available from: http://www.eurocoating.it

107. Trabecular metal [Internet]. [cited 2012 Feb 8]. Available from: http://www.zimmer.com

108. Vigorita V, Minkowitz B, Dichiara JF, Higham PA. A histomorphometric and histologic analysis of the implant interface in five successful, autopsy-retrieved, noncemented porous-coated knee arthroplasties. Journal of Clinical Orthopaedics and Related Research. 1993;211–8.

109. Reticulate foam [Internet]. [cited 2012 Feb 8]. Available from: http://www.fxi.com/html/03_processes/reticulated-polyurethane-foam.php

110. Vlasea M, Basalah A. Additive manufacturing of scaffolds for tissue engineering of bone and cartilage. Journal of Design. 2011;124–47.

111. Gibson I, Rosen DW, Stucker B. Additive Manufacturing Technologies Rapid Prototyping to Direct Digital Manufacturing. New York: Springer; 2010.

112. Melchels FPW, Domingos MAN, Klein TJ, Malda J, Bartolo PJ, Hutmacher D. Additive manufacturing of tissues and organs. Journal of Progress in Polymer Science. Elsevier Ltd; 2011 Dec;1079–104.

113. Pandey PM, Reddy NV, Dhande SG. Slicing procedures in layered manufacturing: a review. Journal of Rapid Prototyping. 2003. p. 274–88.

114. ASTM. Standard terminology for additive manufacturing technologies. ASTM F2792. Available from

115. Leong KF, Chua CK, Ng YM. A study of stereolithography file errors and repair. Part 1. Generic solution. International Journal of Advanced Manufacturing Technology. Springer London; 1996 Nov 1;407–14.

116. Ma D, Lin F, Chua CK. Rapid prototyping applications in medicine. Part 2: STL file generation and case studies. International Journal of Advanced Manufacturing Technology. Springer London; 2001 Jul 1;118–27.

117. Zhao J, Xia R, Liu W, Wang H. A computing method for accurate slice contours based on an STL model. Journal of Virtual and Physical Prototyping. Taylor & Francis; 2009 Mar;29–37.

118. Yang S, Leong K-F, Du Z, Chua C-K. The design of scaffolds for use in tissue engineering. part II. rapid prototyping techniques. Journal of Tissue Engineering. 2002 Feb;1–11.

119. Liska R, Schuster M, Inführ R, Turecek C, Fritscher C, Seidl B, et al. Photopolymers for rapid prototyping. Journal of Coatings Technology and Research. 2007 Nov 2;505–10.

120. Melchels FPW, Feijen J, Grijpma DW. A review on stereolithography and its applications in biomedical engineering. Journal of Biomaterials. 2010 Aug;6121–30.

121. Gong JP, Katsuyama Y, Kurokawa T, Osada Y. Double-network hydrogels with extremely high mechanical strength. Journal of Advanced Materials. 2003 Jul 17;1155–8.

122. Hutmacher DW, Schantz T, Zein I, Ng KW, Teoh SH, Tan KC. Mechanical properties and cell cultural response of polycaprolactone scaffolds designed and fabricated via fused deposition modelling. Journal of Biomedical Materials Research. 2001 May;203–16.

123. Xiong Z. Fabrication of porous scaffolds for bone tissue engineering via low-temperature deposition. Journal of Scripta Materialia. 2002 Jun 7;771–6.

124. Greulich M, Greul M, Pintat T. Fast, functional prototypes via multiphase jet solidification. Journal of Rapid Prototyping. 1995;20–5.

125. Li JP, De Wijn JR, Van Blitterswijk CA, De Groot K. Porous Ti6Al4V scaffolds directly fabricated by 3D fibre deposition technique: effect of nozzle diameter. Journal of Materials Science. Materials in Medicine. 2005 Dec;1159–63.

126. Laminated Object Manufacture (LOM) [Internet]. [cited 2012 Feb 3]. Available from: http://www.jharper.demon.co.uk/rptc01.htm

127. Kusakabe H, Sakamaki T, Nihei K, Oyama Y, Yanagimoto S, Ichimiya M, et al. Osseointegration of a hydroxyapatite-coated multilayered mesh stem. Journal of Biomaterials. 2004 Jul;2957–69.

128. Leong KF, Cheah CM, Chua CK. Solid freeform fabrication of three-dimensional scaffolds for engineering replacement tissues and organs. Journal of Biomaterials. 2003 Jun;2363–78.

129. 3D printing [Internet]. [cited 2013 Feb 1]. Available from: http://www.custompartnet.com/wu/images/rapid-prototyping/3dp.png

130. Andreas G. Rapid prototyping. Munich; 2003.

131. Tolochko NK, Khlopkov Y V, Mozzharov SE, Ignatiev MB, Laoui T, Titov VI. Absorptance of powder materials suitable for laser sintering. Journal of Rapid Prototyping. 2000;151–60.

132. Noorani RI. Medical applications of rapid prototyping. Rapid prototyping: principles and applications. John Wiley and sons; 2006.

133. DEWIDAR MM, KHALIL KA. Processing and mechanical properties of porous 316L stainless steel for biomedical applications. Elsevier. 2007;468–73.

134. Selective laser sintering [Internet]. [cited 2012 Feb 11]. Available from: http://www.custompartnet.com/wu/images/rapid-prototyping/sls.png

135. Realizer-Rapid Laser Manufacturing [Internet]. [cited 2013 Feb 3]. Available from: http://www.realizer-gmbbh.de

136. S. Das. Physical aspects of process control in selective laser sintering of metals. Advanced Engineering Materials. 2003;701–11.

137. Mullen L, Stamp RC, Brooks WK, Jones E, Sutcliffe CJ. Selective Laser Melting: a regular unit cell approach for the manufacture of porous, titanium, bone in-growth constructs, suitable for orthopaedic applications. Journal of Biomedical Materials Research. Part B, Applied Biomaterials. 2009 May;325–34.

138. Eleftherios L. Techniques for producing high relative density aluminium alloy components with selective laser melting. University of Liverpool; 2012. p. 65.

139. Bakish R. The substance of a technology: electron-beam melting and refining. Journal of Minerals. 2007;28–30.

140. Hopkinson N, Hague R, Dickens P. Rapid manufacturing: an industrial revolution for the digital age. Chichester: John Wiley and Sons, Ltd; 2006.

141. Gaytan SM, Murr LE, Martinez E, Martinez JL, Machado BI, Ramirez DA, et al. Comparison of microstructures and mechanical properties for solid and mesh cobalt-base alloy prototypes fabricated by electron beam melting. Journal of Metallurgical and Materials Transactions. 2010 Aug 21;3216–27.

142. Parthasarathy J, Starly B, Raman S. A design for the additive manufacture of functionally graded porous structures with tailored mechanical properties for biomedical applications. Journal of Manufacturing Processes. Elsevier Ltd; 2011 Mar 1;160–70.

143. Pattanayak DK, Fukuda A, Matsushita T, Takemoto M, Fujibayashi S, Sasaki K, et al. Bioactive Ti metal analogous to human cancellous bone: Fabrication by selective laser melting and chemical treatments. Journal of Acta Biomaterialia. Acta Materialia Inc.; 2011 Mar;1398–406.

144. Starly B, Fang Z, Sun W. Three-Dimensional reconstruction for medical-CAD modelling. Journal of Computer-Aided Design. 2005;431–8.

145. Abdelaal OA, Darwish SM. Fabrication of tissue engineering scaffolds using rapid prototyping techniques. Journal of World Academy of Science, Engineering and Technology. 2011;577–85.

146. Naing MW, Chua CK, Leong KF, Wang Y. Fabrication of customised scaffolds using computer-aided design and rapid prototyping techniques. Journal of Rapid Prototyping. 2005;249–59.

147. Earths R. Design and fabrication of bone tissue engineering scaffolds via rapid prototyping and CAD. Journal of Rare Earths. 2007;379–83.

148. Heinl P, Müller L, Körner C, Singer RF, Müller FA. Cellular Ti-6Al-4V structures with interconnected macro porosity for bone implants fabricated by selective electron beam melting. Journal of Acta Biomaterialia. 2008 Sep;1536–44.

149. Heinl P, Rottmair A, Körner C, Singer RF. Cellular titanium by selective electron beam melting. Journal of Advanced Engineering Materials. 2007 May;360–4.

150. Giannatsis J, Dedoussis V. Additive fabrication technologies applied to medicine and health care: a review. International Journal of Advanced Manufacturing Technology. 2007 Dec 18;116–27.

151. Brooks WK, Todd J, Sutcliffe CJ. Rapid design and manufacture of ultralight cellular materials. 16th Proceedings of the Solid Freeform Fabrication Symposium. Austin, TX; 2005. p. 231–41.

152. Brooks WK. The creation of lattice structures using selective laser melting. University of Liverpool; 2011.

153. Crawford RH, Beaman JJ. A method to generate exact contour files for solid freeform fabrication. Proceedings of the 1992 Solid Freeform Fabrication Symposium. Austin, TX; 1992. p. 95–101.

154. Vuyyuru P, Kirschman CF, Fadel G, Bagchi A, Almonte CCJ. A NURBS – Based Approach for Rapid Product Realization. The Fifth International Conference on Rapid Prototyping. Dayton,Ohio,USA; 1994. p. 229–40.

155. Jamieson R, Hacker H. Direct slicing of CAD models for rapid prototyping. Journal of Rapid Prototyping. 1995;4–12.

156. Zhao, Z. and Laperriere L. Adaptive direct slicing of the solid model for rapid prototyping. International Journal of Production Research. 2000;89–98.

157. Schneider PJ, Eberly DH. Geometric Tools for Computer Graphics. Elsevier Inc. Elsevier Inc; 2003.

158. Georgiades P. Signed distance from point to plane. Graphics Gems III. Academic Press; 1992. p. 223–4.

159. Möller T. A fast triangle-triangle intersection test. Journal of Graphics Tools. 1997 Jan;25–30.

160. Narkhede A, Manocha D. Polygon triangulation [Internet]. [cited 2012 Feb 5]. Available from: http://www.cs.unc.edu/~dm/CODE/GEM/chapter.html

161. Haines E. Point in polygon strategies. Graphics Gems IV. Paul Heckbert, Academic Press; 1994. p. 24–46.

162. Bounding containers for polygons, polyhedra, and point Sets (2D & 3D) [Internet]. [cited 2012 Feb 6]. Available from: http://softsurfer.com/Archive/algorithm_0107/algorithm_0107.htm

163. Eberly D. A practical approach to real-time computer graphics. 3D Game Engine Design [Internet]. San Francisco: Morgan Kaufmann Publishers Inc; 2000.

164. Moller T, Eric H. Real-time rendering [Internet]. Natick, MA: AK Peters Ltd; 1999.

165. Akenine-MÄoller T. Fast 3D Triangle-Box Overlap Testing Derivation and Optimization. Journal of Graphics Tools. 2001;29–33.

166. Ericson C. Real-time Collision Detection. Morgan Kaufmann. 2005.

167. Pyside [Internet]. [cited 2011 Feb 6]. Available from: http://pypi.python.org/pypi/PySide#introduction

168. Numpy [Internet]. [cited 2011 Feb 2]. Available from: http://numpy.scipy.org/

169. Cambridge technology [Internet]. [cited 2012 Feb 8]. Available from: http://www.camtech.com/products/6200/6240.html

170. Pease, L.F. & West WG. Fundamentals of powder metallurgy. Princeton, N.J.: Metal Powder Industries Federation; 2002.

171. A Guide to Developing New Materials for the SLM Process. Stone; 2008 p. 15–33.

172. Tsopanos S. Micro heat exchangers by selective laser melting. University of Liverpool; 2008.

173. Bhattacharya S, Gubbins KE. Fast method for computing pore size distributions of model materials. The ACS journal of Surfaces and Colloids. 2006 Aug 29;7726–31.

174. Ashby MF, Gibson LJ. Cellular Solids Structure and Properties. 2th ed. Cambridge University Press; 2001.

175. ASTM. Standard test method of compression testing of metallic materials at room temperature. ASTM.E9.

176. A. Kaufman, D. Cohen and RY. Volume graphics. Journal of IEEE Computer. 1993;51–64.

177. FreeSteel [Internet]. [cited 2009 Feb 20]. Available from: http://www.freesteel.co.uk/

178. Feng J, Ma L, Peng Q. A NEW FREE-FORM DEFORMATION CONTROL OF PARAMETRIC THROUGH SURFACES. Science. 1996;531–9.

179. J. Montagnat HDNA. A Review of Deformable Surfaces: Topology, Geometry and Deformation.

180. Perilli E, Baleani M, Ohman C, Baruffaldi F, Viceconti M. Structural parameters and mechanical strength of cancellous bone in the femoral head in osteoarthritis do not depend on age. Journal of Bone. 2007 Nov;760–8.

181. Whitehouse WJ, Dyson ED. Scanning electron microscope studies of trabecular bone in the proximal end of the human femur. Journal of Anatomy. 1974 Dec;417–44.

182. Synchrotron computed tomography image of cancellous bone [Internet]. [cited 2012 Feb 8]. Available from: https://www.llnl.gov/str/Sep06/gifs/Kinney2.jpg

183. Mosekilde L. Sex differences in age-related loss of vertebral trabecular bone mass and structure--biomechanical consequences. Journal of Bone. 1989 Jan;425–32.

184. Parfitt AM. Implications of architecture for the pathogenesis and prevention of vertebral fracture. Journal of Bone. 1992 Jan;S41–7.

185. Yue S. None-destructive quantification of tissue scaffolds and augmention implants using X-ray microtomography. Imperial College London; 2010. p. 125.

186. Pilkey WD, Pilkey DF. Peterson's Stress Concentration Factors. New York: John Wiley and Sons; 2008.

187. Rehme, O. ; Emmelmann C. Reproducibility for properties of selective laser melting products. the Third International WLT-Conference on Lasers in Manufacturing. Munich, Germany; 2005.

188. Lü L, Fuh JYH, Wong Y-S. Laser-Induced Materials and Processes for Rapid Prototyping (Google eBook) [Internet]. Springer; 2001. p. 267.

189. Ashby MF, Gibson LJ. Cellular Solids Structure and Properties. Cambridge University Press; 1998.

190. Paloto JC, Santos RD. Stress concentration factors for a circular hole in curved beams under bending loads. Journal of Strain. 2003;27–30.

191. Reissner E. The effect of transverse shear deformation on the bending of elastic plates. Journal of Applied Me-chanics. 1945;A69–A77.

APPENDIX A

PART FILE (.f&s file)

Strut Structure Part File

```
#
C:\thesis_strut.f&s                                   **Strut structure part file save path
4 Version
1454586 FileLength
198 SliceCount
0.000 0.000 0.000 0.000 0.000 0.000  bounds
6.97962e-39 9.64283e-39 9.27554e-39 1.11121e-38 0 0 0 0 0 0 0 0 0 0 0 0 0 0 0 0 0 0 0 0 0 0 0 0 0 0 0 0 0 0 0 0  LightExposureBlock
HS
15 length of header text
test info text
HE
Start slice
1 TotalBlockCount in slice #0
0.0500 0.0500 9.9500 9.9500  bounds          **Boundary of layer
0.0500 zlevel                                 **Z=0.05mm
Start contour block
20 ContourType in contour #0                  **Contour type 20
4 PointCount                                  **4 points on this layer
0.050 0.050                                   **X=0.050 Y=0.050
9.950 0.050                                   **X=9.950 Y=0.050
9.950 9.950                                   **X=9.950 Y=9.950
0.050 9.950                                   **X=0.050 Y=9.950
End slice
Start slice
.....
End slice
.....
```

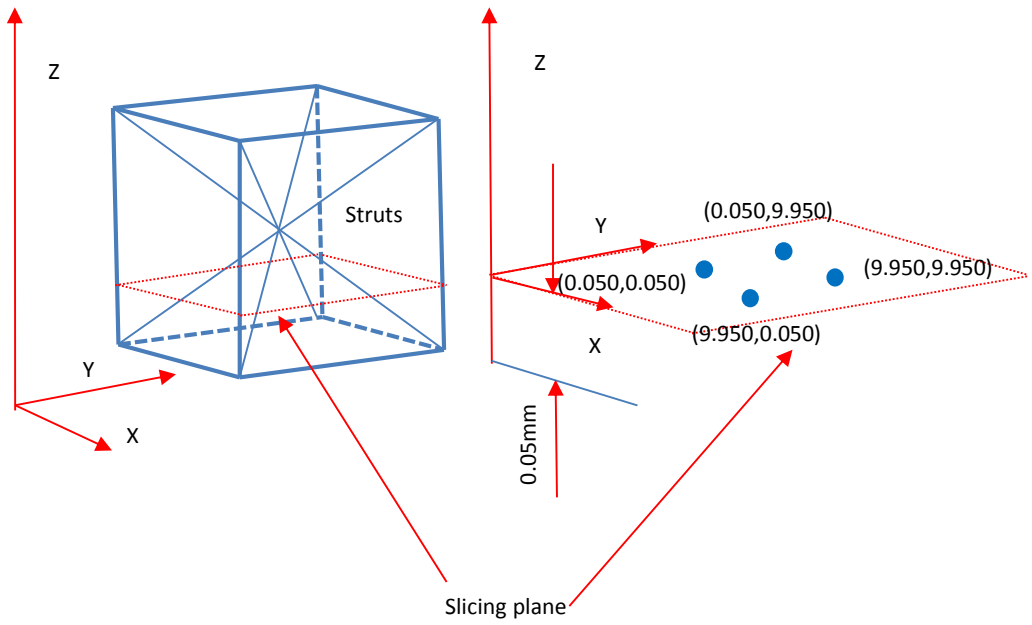

Figure A 1 Notation used in material file for strut structure part

Solid Part File

```
#
C:\thesis_solid part.f&s                                  **Solid part save path
4 Version
181656 FileLength
200 SliceCount
0.0995 9.9115 0.0995 9.9115 0.001 9.951  bounds
7.84908e-039 7.27736e-038 0 0 4.59332e-041 0 0 0 0 0 0 0 0 1.4013e-045
7.27736e-038 1.74369e-039 3.39226e+009 1.49929e-024 1.4013e-045
3.39226e+009 4.22462e-038 1.4013e-045 0 0 3.58732e-043 0 1.4013e-045 0
9.21942e-041 0  LightExposureBlock
HS
5086 length of header text
HE
Start slice
5 TotalBlockCount in slice #0                             **5 types of contours
0 1 0 0 2 1 0 0 0 0 0 0 0 0 0 0 0 1 0 0 0 0 0 0 0 0 0 0 0 0
BlockCountPerType
0 0 0 0 0 0 0 0 0 0 0 0 0 0 0 0 0 0 0 0 0 0 0 0 0 0 0 0 0 0
AnzahlPunkteAllerBloecke
0 0 10.0113 10.0113  bounds
0.001 zlevel                                              **Z=0.001mm
Start hatch block
5 HatchType in hatch block #0                             **Contour type 5 ( hatch lines)
95 HatchCount                                             **95 hatch lines
0.3 0.24949 0.3 9.76151 start end                         **Xstart =0.3,Ystart=0.24949;Xend=0.3,Yend=9.76151
.....
.....
Start contour block
17 ContourType in contour #0                              **Contour type :17 (original outer contour of cube)
5 PointCount                                              **5 points on the original outer contour of cube
10.0113  0                                                **X=10.0113 Y=0
0 0                                                       **X=0 Y=0
0 10.0113                                                 **X=0 Y=10.0013
10.0113 10.0113
10.0113 0
Start contour block
1 ContourType in contour #1                               **Contour type :1 (outer contour or boundary of cube)
5 PointCount                                              **5 points on the outer contour boundary of cube
9.9115 0.0995                                             **X=9.9115 Y=0.0995
0.0995 0.0995
0.0995 9.9115
9.9115 9.9115
9.9115 0.0995
Start contour block
4 ContourType in contour #2                               **Contour type :1 (fill  contour of cube )
5 PointCount                                              **5 points on the fill contour of cube
9.8615 0.1495                                             **X=9.8615 Y=0.1495
0.1495 0.1495
0.1495 9.8615
9.8615 9.8615
9.8615 0.1495
Start contour block
4 ContourType in contour #3
5 PointCount
9.8115 0.1995
0.1995 0.1995
0.1995 9.8115
9.8115 9.8115
9.8115 0.1995
End slice
.....
```

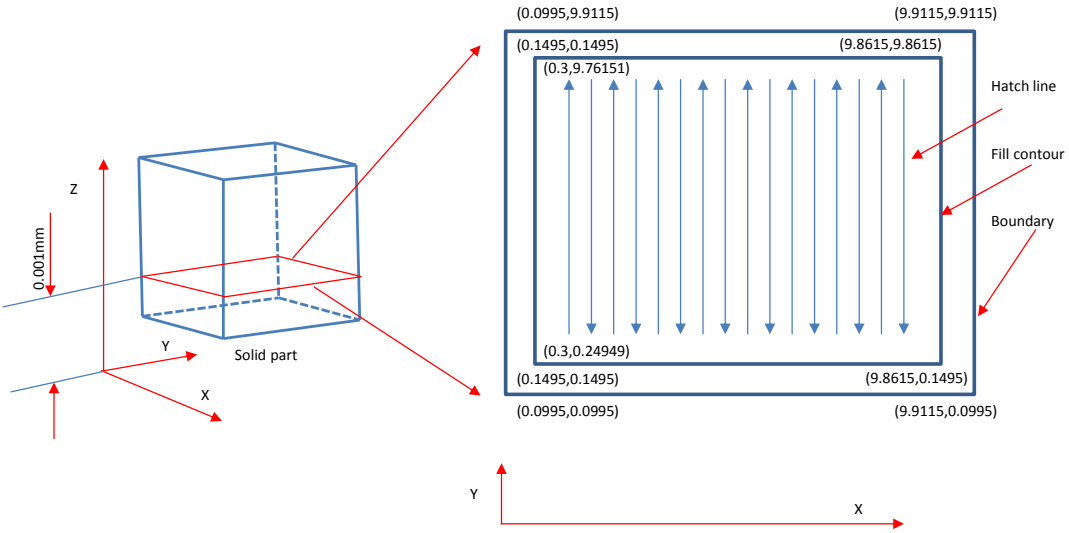

Figure A 2 Notation used in material file for a strut structure part

VS Part File

```
#
C:\thesis_vauled structure. f&s                          **VS part file save path
4 Version
1454586 FileLength
198 SliceCount
0.000 0.000 0.000 0.000 0.000 0.000  bounds
6.97962e-39 9.64283e-39 9.27554e-39 1.11121e-38 0 0 0 0 0 0 0 0 0 0 0 0 0 0 0 0 0 0 0 0 0 0 0 0 0 0 0 0 0 0 0 0  LightExposureBlock
HS
15 length of header text
test info text
HE
Start slice
1 TotalBlockCount in slice #0
0.0 0.0 10.0 10.0 bounds                                 **Boundary of layer
0.050 zlevel                                             **Z=0.05mm
Start contour block
14 ContourType in contour #0                             **Contour type 14
2 PointCount                                             **2 points on contour #0
0.00 0.00                                                **Segment start point X=0.00 Y=0.00
0.00 10.00                                               **Segment end point X=0.00 Y=10.00
14 ContourType in contour #1                             **Contour type 14
2 PointCount                                             **2 points on contour #1
0.00 10.00                                               **Segment start point X=0.00 Y=10.00
10.00 10.00                                              **Segment end point X=10.00 Y=10.00
14 ContourType in contour #2                             **Contour type 14
2 PointCount                                             **2 points on contour #2
10.00 10.00                                              **Segment start point X=10.00 Y=10.00
10.00 0.00                                               **Segment end point X=10.00 Y=0.00
14 ContourType in contour #3                             **Contour type 14
2 PointCount                                             **2 points on contour #3
10.00 0.00                                               **Segment start point X=10.00 Y=0.00
0.00 0.00                                                **Segment end point X=0.00 Y=0.00
End slice
.....
```

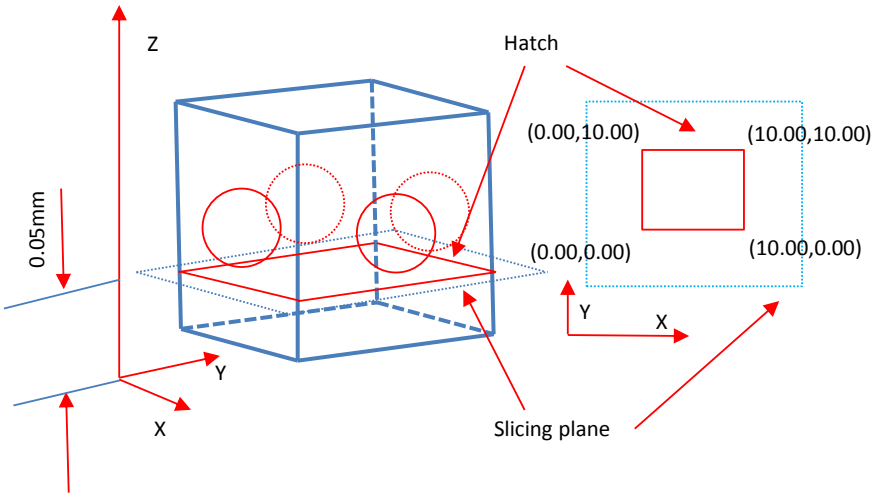

Figure A 3 Notation used in material file for a VS part

APPENDIX B

MATERIAL FILE (.dat file)

```
[SUPPORTER]
verbose=1
meander=1
defaultTipSize=0.800000
defaultPinSize=0.800000
defaultSingePinSize=1.000000
defaultGridOffset=-0.200000
defaultCX=2.0
defaultCY=2.0
defaultTolerance=0.000000
minCubeToPart=1
minSVH=3
minButterfly=12
defaultSVH=256
defaultFloor=1
defaultSocket=40
connectSupportLines=1
withBaseGrid=0
baseGridHeightInMM=1.000000
bridgeHeight=1
defaultSlimProfilesToBeBridged=3.000000
defaultGeoType=1
useSplit=0
evenNumberOfCells=1
defaultSinglePinSize=0.000000
defaultMinSliceDistance=0
minTipPinSize=0.07500000
maxCubeSize=5.000000
maxVoxelSizeAtPart=6.00000
supportPerforation=1
debugSuppo=0
crossBitSize=1.00000
sortSupport=1
extraBridgePass=1
defaultCutSuppoContourOffset=0.300000
defaultCutSuppoHatchMinLength=0.300000
[PARAMETER]
overscan=0
longDistance=1.000000
warmUpTimeFactor=1.000000
warmUpDistance=0.000000
debugWarmUp=0
[EXPOSURE]
exposure_50=50µLAYER                    **Layer thickness 50µm
[50µLAYER]
exposureSequence=1
expoBoundary=1
expoBoundarySolid=350
expoPointSequence=380
expoHatch=200
expoHatchSolid=400
expoSkinHatch=200
expoFillContour=700
expoFillContourSolid=700
expoSupport=700
expoInnerSupport=400
pdistBoundary=50
pdistBoundarySolid=30
pdistHatch=30
pdistHatchSolid=30
```

pdistSkinHatch=30
pdistFillContour=30
pdistFillContourSolid=30
pdistSupport=30
pdistInnerSupport=30
laserPowerBoundary=1800
laserPowerBoundarySolid=2350
laserPowerPointSequence=2650
laserPowerHatch=2000
laserPowerHatchSolid=4000
laserPowerSkinHatch=1600
laserPowerFillContour=4500
laserPowerFillContourSolid=4500
laserPowerSupport=4500
laserPowerInnerSupport=3000
laserFrequenceBoundary=0
laserFrequenceBoundarySolid=0
laserFrequencyPointSequence=1600
laserFrequenceHatch=0
laserFrequenceHatchSolid=0
laserFrequenceSkinHatch=0
laserFrequenceFillContour=0
laserFrequenceFillContourSolid=0
laserFrequenceSupport=0
laserFrequenceInnerSupport=0
lensPosBoundary=1515
lensPosBoundarySolid=1515
lensPosPointSequence=1515
lensPosHatch=1515
lensPosHatchSolid=1515
lensPosSkinHatch=1515
lensPosFillContour=1515
lensPosFillContourSolid=1515
lensPosSupport=1515
lensPosInnerSupport=1515
numberOfExposuresBoundary=1
[HATCH]
spotSize=0.3
default_withBeamCompensation=0
minHatchLength=0.1000
hatchStripesRightLeft=0
hatchStripesUpDown=0
hatchSortBlockSize=800
default_hatch_sortType=3
default_pointsequence_sortType=1
default_hatch_wallThickness=1.5
default_hatch_innerSupport=1
default_hatch_innerSupport_xDistance=1.5
default_hatch_innerSupport_yDistance=1.5
default_wallHatched=1
default_hatch_type=1
default_hatch_shrinkFactor=0.200000
default_hatch_weakSizeLimit=0.100000
default_hatch_contour_fill_offset=0.090000
default_hatch_contour_fill_count=0
default_hatch_offset=0.03000
default_hatch_xDistance=0.13
default_hatch_yDistance=0.13
default_hatch_withStripes=0
default_hatch_stripeSize=2.000000
default_skinHatchLimit=0.800000
default_skin_hatch_type=0
default_skin_hatch_offset=0.05000000
default_skin_hatch_xDistance=0.1000
default_skin_hatch_yDistance=0.1000
default_skin_hatch_withStripes=0
default_skin_hatch_stripeSize=2.000000
default_hatch_typeSolid=1
default_hatch_shrinkFactorSolid=0.08
default_hatch_contour_fill_offsetSolid=0.10000
default_hatch_contour_fill_countSolid=0

default_hatch_offsetSolid=0.08
default_hatch_xDistanceSolid=0.12
default_hatch_yDistanceSolid=0.12
default_hatch_withStripesSolid=0
default_hatch_stripeSizeSolid=2.000000

Table B 1 Details the names of parameters in the material file

expo	Exposure Time
pdist	Point Distance
laserPower	Laser Power
lensPos	Focus optic position
numberOfExposures	Number of times to repeat scan slice geometries

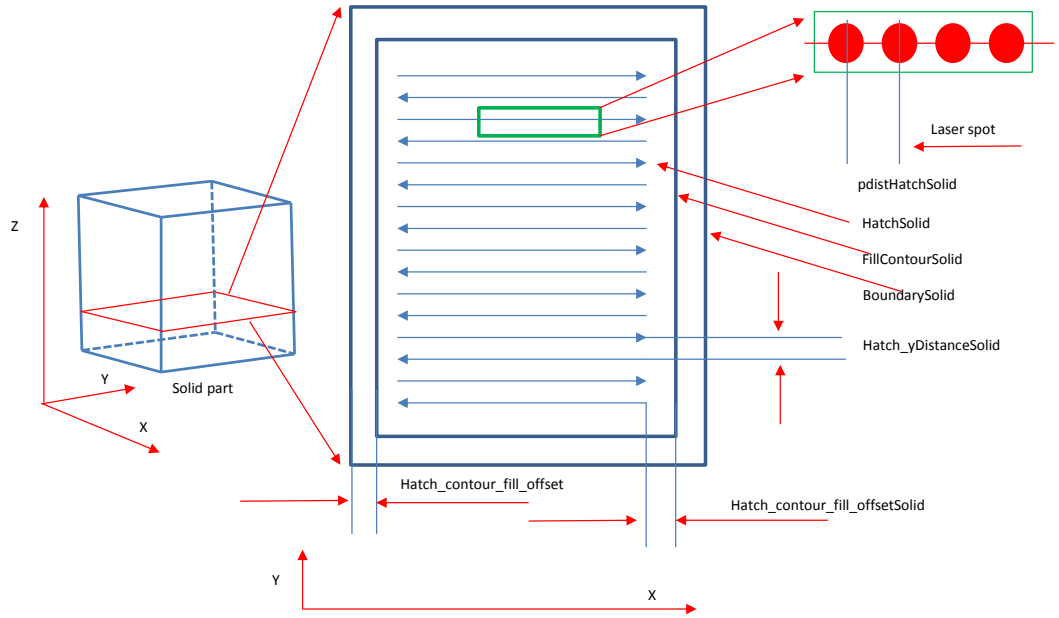

Figure B 1 Notation used in material file for a solid part

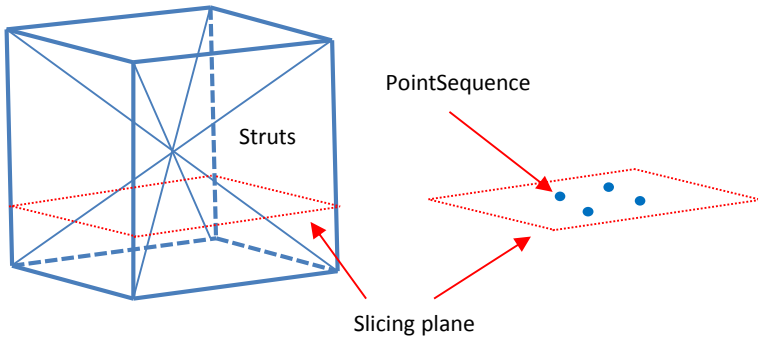

Figure B 2 Notation used in material file for a strut structure

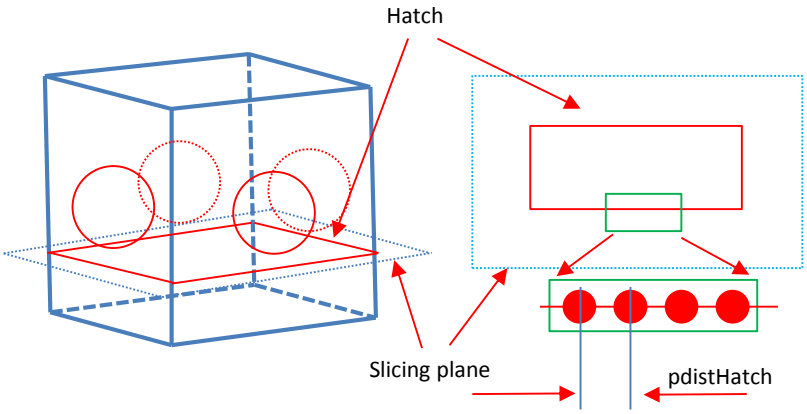

Figure B 3 Notation used in material file for a VS

APPENDIX C

BUILD FILE (.fas file)

[MODELS]

count=4 ***Total number of parts on substrate*

Model0=E:\Build files\Part0.f&s ***Part file path*

OffsetX0=20 ***X coordinate of part0 on substrate*

OffsetY0=20 ***Y coordinate of part0 on substrate*

OffsetZ0=0 ***Z coordinate of part0 on substrate*

Shiftslices0=0

Model1=E:\Build files\Part1.f&s

OffsetX1=20

OffsetY1=-40

OffsetZ1=0

Shiftslices1=0

Model2=E:\Build files\Part2.f&s

OffsetX2=-40

OffsetY2=-40

OffsetZ2=0

Shiftslices2=0

Model3=E:\Build files\Part3.f&s

OffsetX0=-40

OffsetY0=20

OffsetZ0=0

Shiftslices3=0

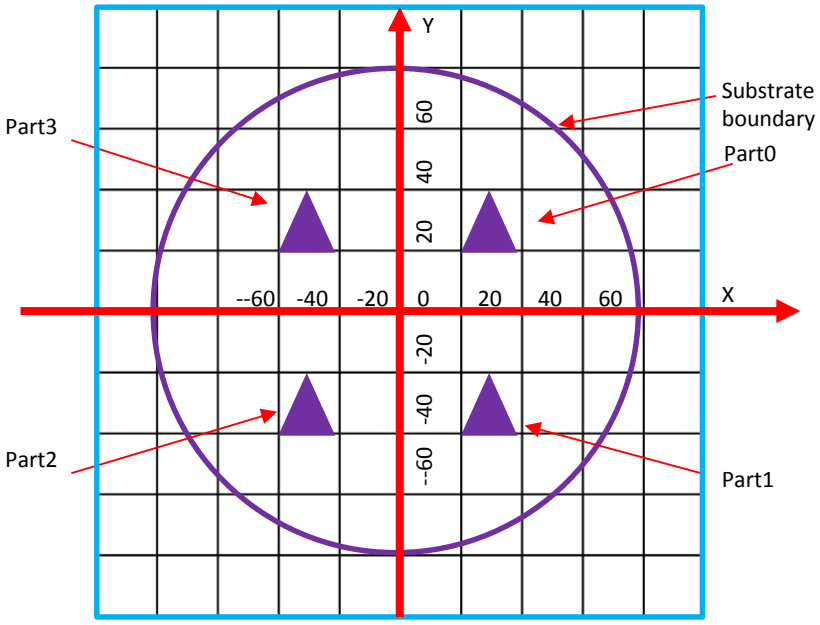

Figure C 1 Notation used for the build file definition

APPENDIX D

ORTHOPAEDIC IMPLANTS WITH VAULTED STRUCTURES

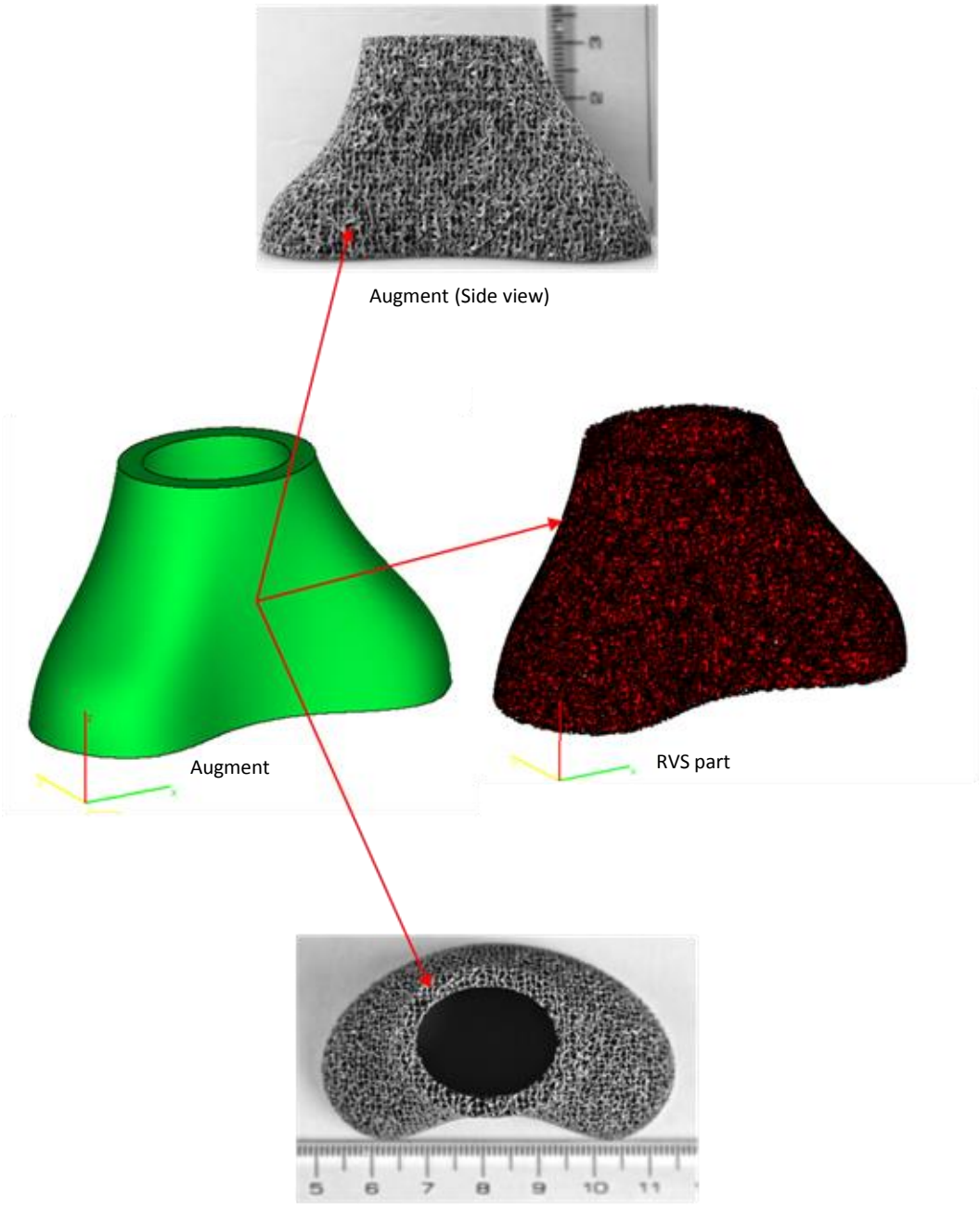

Figure D 1 An augment filled with VS fabricated by SLM 100

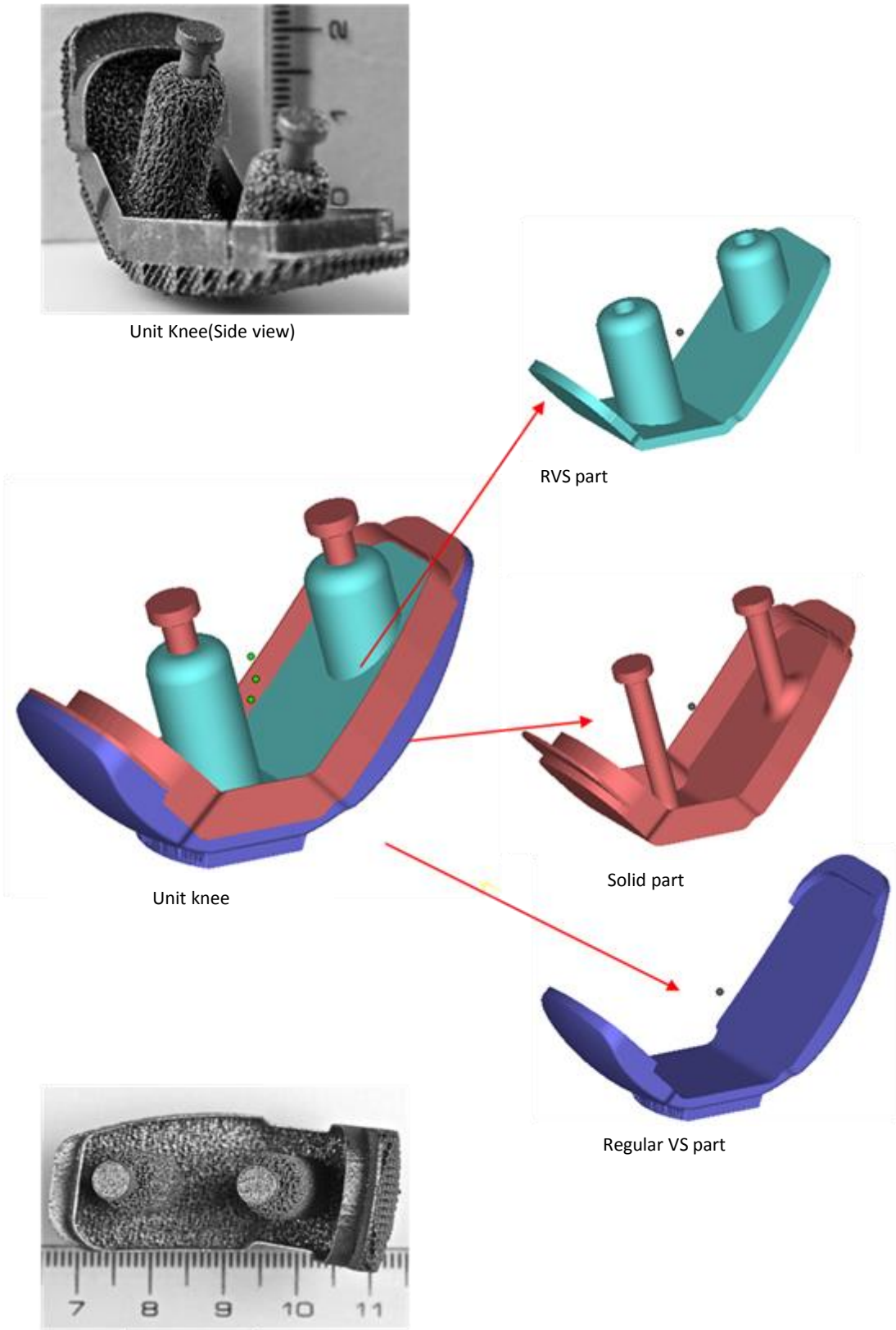

Figure D 2 A unit knee with three sections fabricated by SLM 100

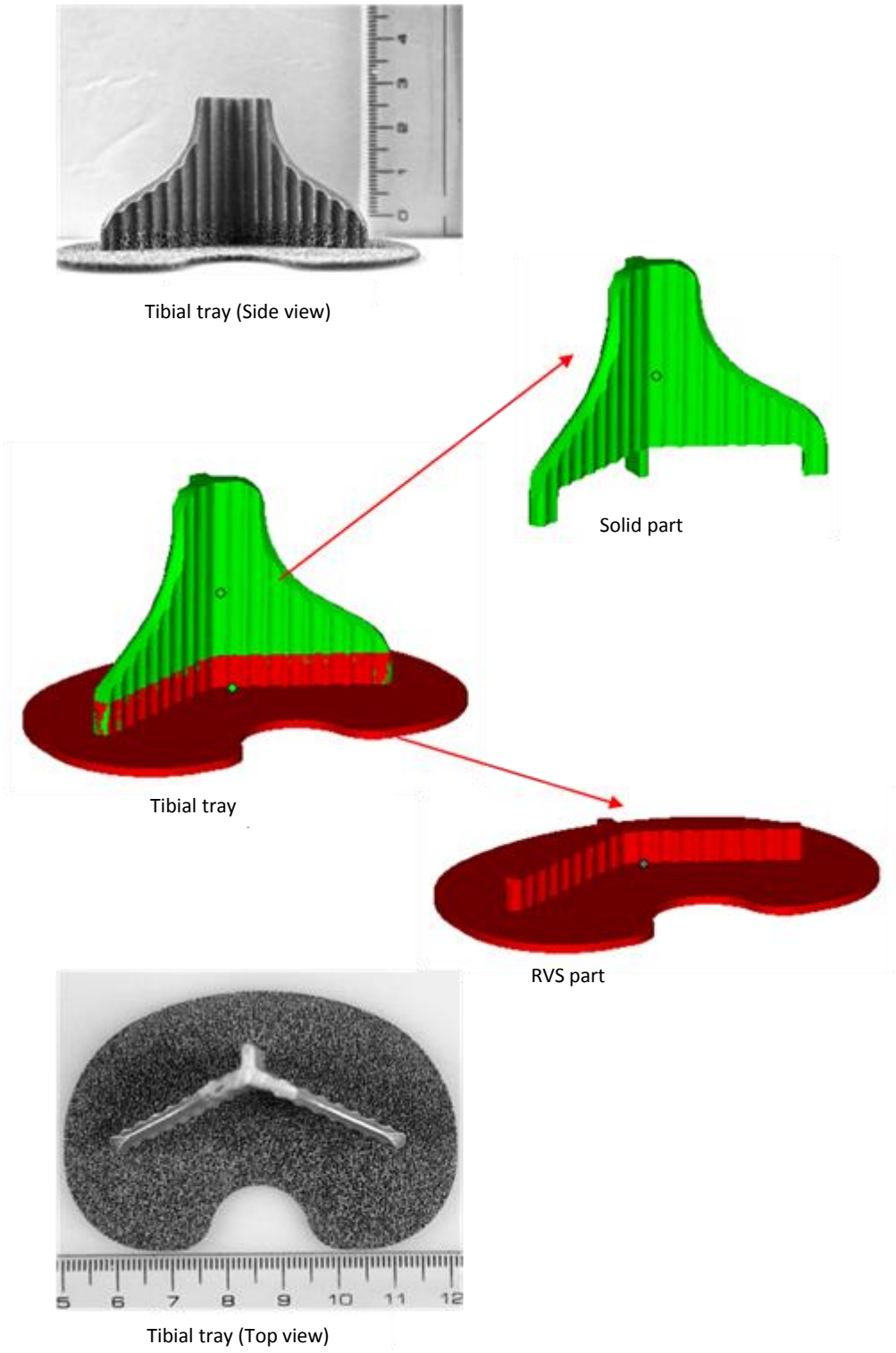

Figure D 3 A tibial tray with two sections fabricated by SLM 100

APPENDIX E

EXPERIMENT DATA

The effect of hole size in regular vault structure		
Number of samples 6×5		
Hole size, R/H, %	Compressive strength, σ, MPa	Porosity, ρr, %
0	184±1.68	70±0.31
20	178±1.56	72±0.34
40	165±4.84	70±0.37
60	102±2.99	72±0.23
80	41±1.16	80±0.42

The effect of platelet thickness in regular vault structure		
Number of samples 6×5		
Hole size, R/H, %	Compressive strength, σ, MPa	Porosity, ρr, %
0	15±1.32	80±0.58
20	14±1.08	87±0.33
40	10±0.74	84±0.20
60	9±0.16	86±0.31
80	9±0.30	86±0.30
0	184±1.68	70±0.31
20	178±1.56	72±0.34
40	165±4.84	70±0.37
60	102±2.99	72±0.23
80	41±1.16	80±0.42

The effect of cell size effect in regular vault structure		
Number of samples 6×5		
Hole size, R/H, %	Compressive strength, σ, MPa	Porosity, ρr, %
0	224±1.94	60±0.54
20	218±3.16	62±0.54
40	205±5.32	60±0.23
60	142±5.63	62±0.29
80	81±4.73	70±0.30
0	184±1.68	70±0.31
20	178±1.56	72±0.34
40	165±4.84	70±0.37
60	102±2.99	72±0.23
80	41±1.16	80±0.42

Regular vault structure isotropy		
Aspect ratio:1:1:1		
In plane direction		
Number of samples 6×5		
Hole size, R/H, %	Compressive strength, σ, MPa	Porosity, ρr, %
0	184±1.68	70±0.31
20	178±1.56	72±0.34
40	165±4.84	70±0.37
60	102±2.99	72±0.23
80	41±1.16	80±0.42
Regular vault structure isotropy		
Aspect ratio:1:1:1		
Out plane direction		
Number of samples 6×5		
Hole size, R/H, %	Compressive strength, σ, MPa	Porosity, ρr, %
0	151±2.34	58±0.23
20	183±4.74	54±0.26
40	178±1.98	55±0.44
60	131±0.20	62±0.02
80	61.8±0.93	72±0.11

Regular vault structure isotropy		
Aspect ratio:2:2:1		
In plane direction		
Number of samples 6×5		
Hole size, R/H, %	Compressive strength, σ, MPa	Porosity, ρr, %
0	33±0.14	80±0.20
20	37±0.11	77±0.08
40	47±0.19	77±0.88
60	30±1.74	77±0.20
80	23±0.21	80±0.02
Regular vault structure isotropy		
Aspect ratio:2:2:1		
Out plane direction		
Number of samples 6×5		
Hole size, R/H, %	Compressive strength, σ, MPa	Porosity, ρr, %
0	311±1.41	61±0.88
20	296±5.65	56±1.03
40	280±7.07	56±0.88
60	227±3.53	60±0.97
80	115±7.07	62±0.88

Regular vault structure isotropy		
Aspect ratio:1:1:2		
In plane direction		
Number of samples 6×5		
Hole size, R/H, %	Compressive strength, σ, MPa	Porosity, ρr, %
0	133±2.31	60±0.14
20	160±2.70	57±0.62
40	165±0.07	57±0.56
60	142±0.80	60±0.23
80	126±0.87	63±0.05
Regular vault structure isotropy		
Aspect ratio: 1:1:2		
Out plane direction		
Number of samples 6×5		
Hole size, R/H, %	Compressive strength, σ, MPa	Porosity, ρr, %
0	132±3.13	79±0.20
20	153±4.65	76±0.20
40	150±0.41	76±0.42
60	131±2.05	78±0.76
80	107±2.08	81±0.44

Randomised effect on compressive strength and porosity of vault structure		
Number of samples 6×5		
Percentage of randomisation, *rand*, %	Compressive strength, σ, MPa	Porosity, ρr, %
20	36±0.22	80±0.41
40	32±0.77	81±0.37
60	28±0.60	80±0.23
80	27±0.35	78±0.18
100	30±0.63	76±0.20

The effect of platelet thickness in randomised vault structure		
Number of samples 6×5		
Percentage of randomisation, *rand*, %	Compressive strength, σ, MPa	Porosity, ρr, %
20	184±9.09	50±0.51
40	156±11.77	54±0.79
60	157±16.50	50±0.39
80	176±8.82	47±0.43
100	199±15.02	44±1.04
20	36±0.22	80±0.42
40	32±0.70	81±0.37
60	28±0.60	80±0.23
80	27±0.35	78±0.18
100	30±0.63	76±0.20

The effect of hole size in randomised vault structure		
Number of samples 6×5		
Percentage of randomisation, *rand*, %	Compressive strength, σ, MPa	Porosity, ρr, %
20	36±0.22	80±0.41
40	32±0.70	81±0.37
60	28±0.60	80±0.23
80	27±0.35	78±0.18
100	30±0.63	76±0.20
20	217±5.74	59±0.41
40	193±5.93	56±0.62
60	182±2.73	51±0.92
80	183±5.05	48±0.63
100	216±8.64	47±1.45

The effect of cell size in randomised vault structure		
Number of samples 6×5		
Percentage of randomisation, *rand*, %	Compressive strength, σ, MPa	Porosity, ρr, %
20	217±5.74	59±0.41
40	193±5.93	56±0.62
60	182±2.73	51±0.92
80	183±5.04	48±0.63
100	216±8.64	47±1.45
20	41±3.00	81±0.42
40	37±2.42	79±0.43
60	37±1.69	77±0.36
80	39±2.28	75±0.41
100	46±4.72	73±0.92

Randomised vault structure isotropy		
Aspect ratio:1:1:1		
In plane direction		
Number of samples 6×5		
Percentage of randomisation, *Rand*, %	Compressive strength, σ, MPa	Porosity, ρr, %
20	65±2.23	74±0.79
40	66±2.87	68±1.18
60	56±4.23	72±1.12
80	71±1.01	66±0.91
100	91±7.36	62±1.98
Randomised vault structure isotropy		
Aspect ratio:1:1:1		
Out plane direction		
Number of samples 6×5		
Percentage of randomisation, *Rand*, %	Compressive strength, σ, MPa	Porosity, ρr, %
20	36±0.22	80±0.41
40	32±0.70	81±0.37
60	28±0.60	80±0.23
80	27±0.35	78±0.10
100	30±0.63	76±0.20

Randomised vault structure isotropy		
Aspect ratio:2:2:1		
In plane direction		
Number of samples 6×5		
Percentage of randomisation, *Rand*, %	Compressive strength, σ, MPa	Porosity, ρr, %
20	99±5.89	66±2.27
40	92±4.46	64±2.04
60	94±4.06	62±0.35
80	100±5.21	59±1.36
100	116±6.16	57±1.56
Randomised vault structure isotropy		
Aspect ratio:2:2:1		
Out plane direction		
Number of samples 6×5		
Percentage of randomisation, *Rand*, %	Compressive strength, σ, MPa	Porosity, ρr, %
20	184±10.86	66±0.68
40	175±1.54	64±1.09
60	163±0.32	62±0.71
80	171±11.61	60±0.38
100	176±2.51	57±0.76

Randomised vault structure isotropy		
Aspect ratio:1:1:2		
In plane direction		
Number of samples 6×5		
Percentage of randomisation, *Rand*, %	Compressive strength, σ, MPa	Porosity, ρr, %
20	67±0.60	80±0.35
40	45±0.70	78±0.32
60	41±0.05	74±0.32
80	51±0.62	70±0.44
100	60±0.13	67±0.38
Randomised vault structure isotropy		
Aspect ratio:1:1:2		
Out plane direction		
Number of samples 6×5		
Percentage of randomisation, *Rand*, %	Compressive strength, σ, MPa	Porosity, ρr, %
20	29±0.59	80±0.35
40	32±0.94	77±0.23
60	39±0.56	73±0.23
80	47±0.73	70±0.26
100	61±1.18	67±0.14